Good Practice Guidelines for

1. Atmospheric Inversions to Support Greenhouse Gas Emission Reporting
2. Evaluating Emission Inventories Using Inverse Modelling Results

DELIVERABLE 5.10 (EYE-CLIMA) | DELIVERABLE 6.1 (AVENGERS)

Authors (in alphabetical order):	Tuula Aalto[1], Lara Abou Chehade[2], Antoine Berchet[3], Gregoire Broquet[3], Philippe Ciais[3], Audrey Fortems-Cheiney[4], Christine Groot Zwaaftink[5], Lukas Häffner[6], Sander Houweling[7], Ignacio Pisso[5], Thomas Kaminski[8], Nalini Krishnankutty[5], Anteneh Getachew Mengistu[1], Christian Mielke[6], Seyed Omid Nabavi[9], Marko Scholze[10], Rona Thompson[5], Aki Tsuruta[1], Martin Vojta[9], Rebecca Ward[1], Hannes Witt[11] and Margreet van Zanten[11,12]
Date of submission:	23-10-2026
Version:	1.0
Responsible partners:	1. FMI, 2. CMCC, 3. LSCE, 4. SP, 5. NILU, 6. UBA, 7. VUA, 8. The Inversion Lab, 9. UNIVIE, 10. ULUND, 11. RIVM, 12. WUR
Deliverable due date:	31-08-2026
Dissemination level:	Public

Call:	HORIZON-CL5-2022-D1-02
Topic:	Climate Sciences and Responses
Project Type:	Research and Innovation Action
Lead Beneficiary:	NILU (EYE-CLIMA), Lund University (AVENGERS)

Document History

Version	Date	Comment	Modifications made by
1.0	23-10-2026	Complete version based on merging documents	

Preface

This document is a common deliverable from the two Horizon Europe projects AVENGERS and EYE-CLIMA, both funded under the same call HORIZON-CL5-2022-D1-02. Both AVENGERS and EYE-CLIMA had as a deliverable the preparation of good practice guidelines for the use of atmospheric inversion based emission estimates to support national greenhouse gas inventories. Producing two separate guidelines and deliverable reports was considered as problematic as this would lead to two competing guidelines and possible ambiguity. To circumvent this problem it was decided to produce joint guidelines in collaboration between the two projects. This document is the joint guidelines encompassing the following:

1. Good Practice Guidelines for Atmospheric Inversions to Support Greenhouse Gas Emission Reporting: this document is for those wanting to set-up or run inversions and explains the inversion methodology, sources of error and specific considerations for different greenhouse gases. It also describes in detail the methodology for comparing inversions to national inventories.
2. Good Practice Guidelines for Evaluating Emission Inventories Using Inverse Modelling Results: this document is aimed at those who want to use information from atmospheric inverse modelling to evaluate and improve their national inventory and is less technical than document (1).

The EYE-CLIMA and AVENGERS projects were funded from the European Union's Horizon Europe research and innovation programme under grant agreement No.s 101081395 and 101081322

1. Good Practice Guidelines for Atmospheric Inversions to Support Greenhouse Gas Emission Reporting

Authors: Rona Thompson[1], Gregoire Broquet[2], Tuula Aalto[3], Antoine Berchet[2], Philippe Ciais[2], Audrey Fortems-Cheiney[4], Christine Groot Zwaaftink[1], Sander Houweling[5], Ignacio Pisso[1], Nalini Krishnankutty[1], Anteneh Getachew Mengistu[3], Martin Vojta[6], Aki Tsuruta[3], Seyed Omid Nabavi[6], Rebecca Ward[3], Hannes Witt[8] and Margreet van Zanten[8,9]

Responsible partners: 1. NILU, 2. LSCE, 3. FMI, 4. SP, 5. VUA, 6. UNIVIE, 7. IIASA, 8. RIVM, 9. WUR

Document History

Version	Date	Comment	Modifications made by
0.1	01-03-2026	First draft	Rona Thompson[1], Gregoire Broquet[2], Tuula Aalto[3], Antoine Berchet[2], Philippe Ciais[2], Audrey Fortems-Cheiney[4], Christine Groot Zwaaftink[1], Sander Houweling[5], Ignacio Pisso[1], Nalini Krishnankutty[1], Anteneh Getachew Mengistu[3], Martin Vojta[6], Aki Tsuruta[3], Seyed Omid Nabavi[6], Rebecca Ward
0.2	15-06-2026	Internal review	Andreas Stohl[6], Philippe Peylin[2], Wilfried Winiwarter[7]
0.3	30-09-2026	Second draft complete	Rona Thompson[1], Gregoire Broquet[2], Tuula Aalto[3], Antoine Berchet[2], Philippe Ciais[2], Audrey Fortems-Cheiney[4], Christine Groot Zwaaftink[1], Sander Houweling[5], Ignacio Pisso[1], Nalini Krishnankutty[1], Anteneh Getachew Mengistu[3], Martin Vojta[6], Aki Tsuruta[3], Seyed Omid Nabavi[6], Rebecca Ward[3], Hannes Witt[8] and Margreet van Zanten[8,9]
1.0	16-10-2026	Final formatted version	Monika Strasser Englund[1], Rona Thompson[1].

This project has received funding from the European Union's Horizon Europe research and innovation programme under grant agreement No 101081395

Summary

This deliverable describes good practice for atmospheric inversions to support monitoring of greenhouse gases, especially on national scales. The aim of these guidelines is to improve the quality and reliability of emissions estimates derived from atmospheric inversions for use in emissions monitoring and in support of national greenhouse gas inventories. These guidelines also describe how inversion results can be benchmarked and what information should be reported with an inversion result to aid its interpretation and comparison with inventory estimates. Furthermore, these guidelines detail how inversion estimates may be compared to inventory estimates to ensure that estimates from each method are in fact comparable. These guidelines are intended to be a living document in the sense that they should be refined as the field of atmospheric inverse modelling evolves.

This project has received funding from the European Union's Horizon Europe research and innovation programme under grant agreement No 101081395

Table of Contents

DOCUMENT HISTORY 2

SUMMARY 3

1. INTRODUCTION 8

1.1. Why we need good practice guidelines 8

1.2. The purpose of these guidelines and what is covered 9

2. METHODOLOGY 10

2.1. A brief introduction to atmospheric inversion 10

2.2. Model operators 11
2.2.1. Observation operators 12
Linearized model operators 13
2.2.2. Adjoint operators 13
2.2.3. Operator input and output 14

2.3. Inversion theory 14

2.4. Inversion implementation 16
2.4.1. Resolution, discretization and aggregation 16
2.4.2. Domain, initial and boundary conditions 18
2.4.3. Prior fluxes 20

2.5. Methods to solve the inverse problem 21
2.5.1. Analytical solution 22
2.5.2. Kalman Filters 23
2.5.3. Gradient methods 24
2.5.4. Ensemble methods 27
2.5.5. Overview of methods 35

2.6. Determining the covariance matrices B and R 36

3. CO_2 INVERSIONS FOR LULUCF 39

3.1. Focusing on LULUCF fluxes in CO_2 inversion frameworks 39

3.2. Prior and fixed estimates of the fluxes 40

3.3. Spatial and temporal resolution of the controlled flux variables 45

3.4. Other variables of the control vector and boundary conditions 45

3.5. Observation vector definition and selection of the observations 46

3.6. Configuration of the prior and observation error covariances 47

This project has received funding from the European Union's Horizon Europe research and innovation programme under grant agreement No 101081395

4. CH_4 INVERSIONS 48

4.1. Prior fluxes and consideration of sectors to be optimized 48

4.2. Boundary and initial mixing ratios 52

4.3. Uncertainties associated with fluxes 55

4.4. Atmospheric sinks 59

4.5. Inclusion of isotopic information 60

5. N_2O INVERSIONS 65

5.1. Prior fluxes and uncertainties 65

5.2. Boundary conditions and the atmospheric sink 69

6. F-GAS INVERSIONS 70

6.1. Prior emissions and uncertainties 71

6.2. Boundary conditions 73
6.2.1. Boundary mixing ratios 73
6.2.2. Optimization of the boundary mixing ratios 74

6.3. Observations and observation uncertainties 75

6.4. Atmospheric chemistry 76

7. ATMOSPHERIC OBSERVATIONS 77

7.1. Ground-based observations 77
7.1.1. Types of observations 77
7.1.2. Data selection and averaging 78
7.1.3. Model representation and uncertainty 78
7.1.4. Calibration scales and data quality 79

7.2. Satellite observations 79
7.2.1. Context 79
7.2.2. Representation in atmospheric transport models for inversions 81
7.2.3. Data processing and uncertainty propagation for inversions 84

8. UNCERTAINTY QUANTIFICATION 85

8.1. Purpose, scope and what must be reported 85

8.2. Sources of uncertainty and the role of sensitivity analysis 85

8.3. Statistical posterior uncertainty 87

8.4. Statistical diagnostics 89

8.5. Systematic components 90

This project has received funding from the European Union's Horizon Europe research and innovation programme under grant agreement No 101081395

8.5.1 Prior fluxes 90
8.5.2 Boundary and initial mixing ratios 91
8.5.3 Transport 91
8.5.4 Observations 92
8.5.5 System settings 92

8.6. From grid-cell uncertainty to regional and national uncertainty 92

8.7. Total uncertainty 93

8.8. Uncertainty reporting levels 94

9. EVALUATION AND BENCHMARKING OF INVERSION RESULTS 95

9.1. Purpose, evaluation strategy and definitions 95

9.2. Assessing the degree of dependence from the prior: uncertainty reduction, DoFS, averaging kernels, covariance between regions 95

9.3. Deciding where and when results can be used 98

9.4. Evaluation with independent observations 99

9.5. Interpreting sensitivity and ensemble results 101

9.6. Plausibility checks 102

9.7. Benchmarking against archived inversion output 103

9.8. Reporting requirements and lessons learned 104

10. COMPARISONS TO NGHGIS 105

10.1. Introduction to inventories 105

10.2. CO_2 LULUCF 107
10.2.1. Assumptions on fossil fuel emissions 108
10.2.2. Sampling for managed land 108
10.2.3. Adjusting CO_2 fluxes from "traditional" inversions for lateral C transport by crop and wood products trade and rivers 109
10.2.4. Recombining the flux components from inversions that account for the lateral fluxes 111

10.3. CH_4 fluxes 111
10.3.1. Comparing inversions with NGHGI estimates for managed peatlands 112

10.4. N_2O fluxes 114

10.5. General considerations when comparing inversion fluxes with NGHGIs 115
10.5.1. From gridded to regional estimates 115
10.5.2. Interpretating inversion results 116

11. EPILOGUE 119

12. ACKNOWLEDGEMENTS 119

This project has received funding from the European Union's Horizon Europe research and innovation programme under grant agreement No 101081395

13. GLOSSARY 120

14. REFERENCES.....122

This project has received funding from the European Union's Horizon Europe research and innovation programme under grant agreement No 101081395

1. Introduction

Rona Thompson

1.1. Why we need good practice guidelines

Atmospheric inversion (which is shorthand for "atmospheric chemistry and transport inverse modelling") refers to the methodology of estimating the surface-atmosphere fluxes of a gas (or aerosol) based on observations of mixing ratios (or concentrations) in the atmosphere (or, for aerosols, of atmospheric deposition) and a model relating the fluxes to the measurements, i.e., a model of atmospheric transport and, where relevant, atmospheric chemistry. The *inversion* relates to the fact that to estimate the fluxes, the relationship between a change in the flux and the change in atmospheric mixing ratio needs to be effectively inverted to relate the observations to a correction to the original (or *prior*) estimate of the fluxes.

Atmospheric inversion is becoming increasingly used in estimating emissions (and removals) of greenhouse gases (GHGs) to support emissions inventories and in monitoring emissions at global to national, and even facility scales. The methods employed for this are often derived from those used for data assimilation in, for example, numerical weather prediction. The methodology is also referred to in the Intergovernmental Panel on Climate Change (IPCC) Guidelines for National Greenhouse Gas Inventories and, specifically, is mentioned in the 2019 refinement to the guidelines as a way of verifying an inventory using independent data.

As a result, a few countries are starting to use atmospheric inversions to support their emission inventories and are including these as annexes to their National Inventory Reports (NIRs) (IG^{3}IS National-scale Applications of the Science-based Quantification of Emissions and Removals Workshop[1]). This has also led to the WMO Integrated Global Greenhouse Gas Information System (IG^{3}IS) to produce a set of guidelines for estimating national-scale GHG emissions using atmospheric observations[2]. These guidelines, however, do not provide any technical guidance on how to set-up an inversion framework.

In addition to national efforts, there is also a growing interest in atmospheric inversions to provide "near-real-time" global information on greenhouse gas fluxes, including natural sources and sinks, which are not considered in national emission inventories. In an emerging application, inversions updated every few months to include recent observations from ground-based networks and satellites are being used to trace developments in emissions as well as in the variability of natural sources and sinks (Ke et al., 2024).

With the increasing interest and reliance on atmospheric inversion estimates, there is a critical need to formulate a good practice to reduce errors and improve confidence in the emission estimates obtained. As with any methodology, if it is not well implemented the

[1] https://wmo.int/media/update/science-based-greenhouse-monitoring-can-complement-national-efforts-meet-mitigation-targets-and?book=24971

[2] https://library.wmo.int/records/item/69714-integrated-global-greenhouse-gas-information-system-good-practice-guidance-for-estimating-national-scale-greenhouse-gas-emissions-using-atmospheric-observations

This project has received funding from the European Union's Horizon Europe research and innovation programme under grant agreement No 101081395

results obtained may be erroneous and misleading. Atmospheric inversion is a reasonably complex methodology and requires careful consideration of how the input data and settings are chosen, and how the results may depend on those choices.

Over the past approximately three decades, the use of atmospheric inversion in the scientific community has grown substantially with improvements in atmospheric transport models and in inversion systems. Recently within the framework of the EYE-CLIMA and AVENGERS projects, substantial effort has been made to further refine the methodology. These guidelines are written based on scientific literature as well as the experience and results from EYE-CLIMA, AVENGERS and earlier projects. Up to now, a document summarizing the atmospheric inversion methodology and expert knowledge of how to implement it has been lacking - the aim of these guidelines is to help fill that gap.

1.2. The purpose of these guidelines and what is covered

These guidelines are aimed at anyone who uses or plans to use the atmospheric inversion methodology for estimating fluxes. As a companion to these guidelines, there is a separate document (Good Practice Guidelines on Evaluating Emission Inventories Using Inverse Modelling Results), which is aimed at those who simply wish to use atmospheric inversion results.

These guidelines assume the reader has basic knowledge of atmospheric modelling and statistics. However, no prior knowledge of inversion theory is required and an introduction to the methodology and its implementation (as well as references for further reading) are provided in Section 2.

The focus in these guidelines is on long-lived greenhouse gases for which there are reporting obligations under the United Nations Framework Convention on Climate Change (UNFCCC), specifically carbon dioxide (CO_2), methane (CH_4), nitrous oxide (N_2O) and the group of synthetic fluorinated gases together referred to as F-gases. For CO_2, the focus of atmospheric inversions is largely on land ecosystem emissions and removals, and this will be the focus for CO_2 in these guidelines as well. Some parts of these guidelines are also relevant to other gases (and particles). In addition, particular focus is paid to regional-scale inversions, especially with the aim of supporting national emission inventories, but the guidelines are also applicable to global scale inversions.

These guidelines aim to make the reader aware of how important the set-up of the inversion is. More specifically, how the choice of input data, the treatment of observations, and the uncertainty settings can lead to varying results and to provide guidance on these choices. In addition, guidance is provided on how to estimate the uncertainties and what additional diagnostics are available to assess the robustness of the results. Finally, recommendations are given on what information should be provided along with the inversion results to enhance transparency and confidence in the flux estimates.

Although much of the methodology is common to all long-lived atmospheric gases, there are some specific considerations for the different gases, hence Sections 3 to 6 deal with these specifics respectively for CO_2 (i.e. land ecosystem emissions and removals), CH_4, N_2O and F-gases. Section 7 discusses different types of atmospheric observations

This project has received funding from the European Union's Horizon Europe research and innovation programme under grant agreement No 101081395

including those from ground-based platforms and those from satellite remote sensing. Section 8 presents methods for estimating the posterior uncertainty and sensitivity to different input data, and Section 9 discusses diagnostic tools and benchmarking of inversion results. Lastly, Section 10 examines how the flux estimates obtained from inversions differ from what is reported in emission inventories and how the two can be compared in a consistent and meaningful way.

2. Methodology

Rona Thompson

2.1. A brief introduction to atmospheric inversion

Atmospheric inversion has been used since the 1980s to study surface-atmosphere fluxes of varying gases based on observations in the atmosphere (e.g. Fung et al., 1991; Keeling et al., 1989; Prinn et al., 1990; Tans et al., 1989). The method relies on using a model to describe the relationship between fluxes and observations of mixing ratios in the atmosphere. With a given estimate of the fluxes, the model simulates the mixing ratios at observation points (see Figure). The inversion part of the method, uses the mismatch between the modelled and observed mixing ratios to correct the original (or prior) estimate of the fluxes. To make the correction, the mismatch has to be related to a change in fluxes, and this is done by effectively inverting the relationship between the fluxes and mixing ratios. Different types of observations may be used, also in combination, such as atmospheric column observations from satellites, and observations from ground-based stations.

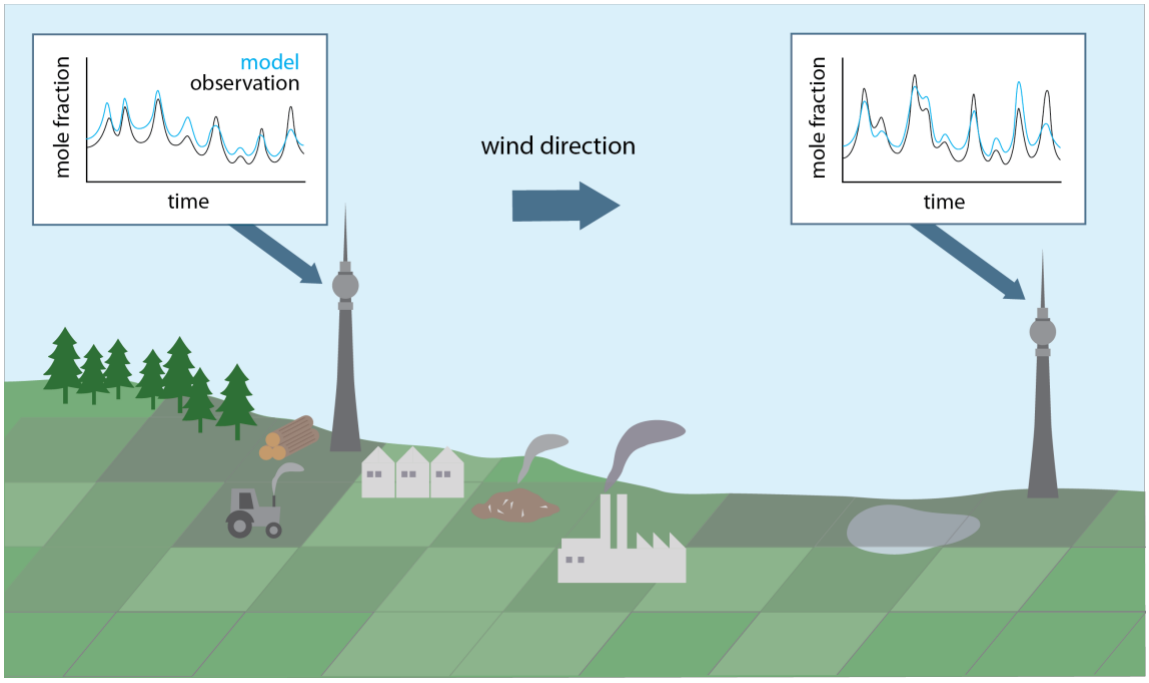


Figure 2.1: Simplified representation of the principal of atmospheric inversion showing two observation sites with a timeseries of observed and modelled mole fractions of a gas. The mole fractions at each site are a function of the fluxes and the atmospheric transport. The shading on the ground indicates the combined (from both sites) modelled sensitivity of the observations to the fluxes on a regular grid with darker shading indicating a stronger sensitivity.

This project has received funding from the European Union's Horizon Europe research and innovation programme under grant agreement No 101081395

The atmospheric inversion methodology has a statistical basis, and often is derived from Bayes' Theorem. The theoretical aspects are presented in Section 2.2.

2.2. Model operators

To run an inversion, one needs a model relating the fluxes (or the variables of interest) to atmospheric mixing ratios (or the observations). The problem of predicting the results of observations given an estimate of the fluxes is called *the forward problem*, while the problem of using the actual observations to infer the variables of interest (the fluxes) is called *the inverse problem*. In the forward problem, the model (or operator) required to relate the variables of interest, x, also known as the control (or state) variables, to the observed variables, y, is called the *observation operator*, H, and can be written as:

$$H: x \rightarrow y$$

or

$$y^m = H(x)$$

where y^m is the model output (e.g. mixing ratio). The control variables can be thought of as a subset of the *control space*, and the observation variables can be thought of as a subset of the *observation space*. Then the operator, H can be thought of as providing a mapping from the control to the observation space.

In the inverse problem, the relationship is in reverse in the sense that mixing ratios (or more generally observations) are the input and the fluxes (control variables) are the output. In this problem, the operator used is often called the *adjoint operator* (H^*) and has as input the difference between the modelled and observed mixing ratios and the sensitivity to the variables of interest (fluxes) is the output and is written as:

$$H^*: y^* \rightarrow x^*$$

where * indicates adjoint variables (see Section 2.2.2 for more about adjoint operators and variables). Note that these guidelines follow the notation for data assimilation as described by Ide et al. (1997) and the key variables are summarized in Table 2.1.

Although in reality the fluxes are continuous in space and time, it is generally not possible to solve for continuous variables [3]. Therefore, the fluxes (or control variables) are described as discrete variables and are from here on represented by the vector $\boldsymbol{x}$. Similarly, the observations are represented by the vector $\boldsymbol{y}$.

Table 2.1. Summary of the notation used in these guidelines.

Variable	Description
y	Variable in the observation space
x	Variable in the state space
H	Observation operator, $H: x \longrightarrow y$
H^*	Adjoint operator, $H^*: y^* \longrightarrow x^*$
M	Forecast model operator, $M: x_t \longrightarrow x_{t+1}$ (where t is the time step)
$P(\cdot)$	Probability density function
$E[\cdot]$	Expected value

[3] Unless the variables are parameters of a continuous function, however, it should be noted that input data (such as meteorological variables) are always discrete variables.

This project has received funding from the European Union's Horizon Europe research and innovation programme under grant agreement No 101081395

$J(\cdot)$	Cost function
R	Observation error covariance matrix
B	Background (prior) error covariance matrix
P	Analysis (posterior) error covariance matrix (for Kalman methods **P** is used for both prior and posterior covariance matrices)
G	Gain matrix
K	Kalman gain matrix
A	Averaging kernel matrix
$(\cdot)^a$	Analysis (posterior) variable
$(\cdot)^b$	Background (prior) variable
$(\cdot)^o$	Observation variable
$(\cdot)^m$	Model output variable (in the observation space)
$(\cdot)^t$	A variable representing the true state
$(\cdot)^*$	Adjoint variable

2.2.1. Observation operators

The observation operator describes the complete mapping of the control variables (which can be fluxes as well as other variables) into the observation space. Generally, it consists of a model of atmospheric transport (and where relevant, chemistry) and possibly also contains other operation, such as spatial and/or temporal interpolation of flux variables or averaging of simulated mixing ratios. The transport (and chemistry) model used can be of varying complexity. In the atmospheric transport community there are essentially two classes of models used: i) Eulerian models in which the coordinate system is fixed in space and the equations solved (at least in theory) conserve energy, momentum and mass, and ii) Lagrangian models in which the frame of reference is moving with the flow. In practice, this is done by calculating the trajectories of virtual particles as they move through the atmosphere.

In general, Lagrangian models tend to be preferred when modelling atmospheric transport at high resolution and on regional domains because they have arbitrary resolution as individual particles are followed at, in principle, infinite resolution. They also exhibit less numerical diffusion compared to Eulerian models and because of this they generally better capture tracer filaments generated by atmospheric dispersion (Pisso et al., 2019) and fine structures in tracer mixing ratios resulting from long-range transport (Rastigejev et al., 2010). On the other hand, Eulerian models may be preferred for global budgets and long-term studies, and when assimilating satellite observations (for more about this see Section 7.2). Hybrid Eulerian-Lagrangian models have also been used, for example Ganshin et al. (2012) used a global Eulerian model to provide 3D fields of mixing ratios that were used as initial conditions for a Lagrangian model run at high spatial and temporal resolution.

The observation operator may cover different spatial domains, i.e., it may be global or regional, and may cover different temporal domains, i.e., the time period which the model is run. For instance, Lagrangian models are typically run in a backwards in time mode when used in atmospheric inversions, where virtual particles are released at the spatiotemporal coordinates of the observations and are followed back in time (reversing the transport), typically for several days but in some cases up to 1 to 3 months (Vojta et

This project has received funding from the European Union's Horizon Europe research and innovation programme under grant agreement No 101081395

al., 2024; Püschel et al., 2025). Longer backwards runs become computationally expensive and each additional calculation day provides progressively less information. In the Lagrangian case, the temporal domain of the model differs for each temporal coordinate of the observations. For atmospheric gases with lifetimes that approach, or are longer, than the length of the backwards calculation, an estimate of the contribution to the measured mixing ratio at the end of the backwards calculation is required - this is often referred to as the *background mixing ratio* (see Section 2.4 for methods how this can be estimated). If the spatial domain of the model is global, then the particle trajectories can end anywhere in the global atmosphere. However, if it is regional, then the particle trajectories end either within the domain or at its borders. Therefore, how the background mixing ratio is calculated depends on the model's spatial domain. In the Eulerian case, the model temporal domain covers the full period of the inversion, however, an estimate for the 3D field of mixing ratio is needed at the start of the inversion period – this is often referred to as the *initial mixing ratio*. For regional domain models, the mass fluxes at the lateral and top borders of the domain need to be accounted for. For this, estimates of the mixing ratios at the borders need to be provided throughout the time of the model simulation.

In these guidelines, we will refer to inputs at the spatial limits of the model domain as the *boundary conditions* and the input at the start of the temporal domain(s) as the *initial conditions*.

Linearized model operators

Some atmospheric inversion methods make use of a *linearized model operator*. The linearized model operator is the gradient of the observation operator and describes the sensitivity of an observation to a change in flux. The linearized model operator is in fact a Jacobian matrix with each element given by $\partial H(x)_j/\partial x_k$ for the jth observation and the kth control variable. Lagrangian models run backwards in time directly derive a linear operator, which is only applicable in cases where there is a linear dependence of the mixing ratios on the fluxes. This linear operator is often called the source-receptor relationship (SRR) (for a detailed description of how the SRR is derived see (Seibert and Frank, 2004).

This Jacobian matrix may also be generated from Eulerian models by integrating the model forward in time with a perturbation to each control variable (or flux grid cell) and deriving for each observation the term $\partial H(x)_j/\partial x_k$. This approach was used by e.g. (Fung et al., 1991; Rayner et al., 1999) and more recently (Patra et al., 2016) . In principle, atmospheric transport (in the absence of non-linear chemistry) is linear but in practice numerical models generate non-linearity between the fluxes and the concentrations when dealing with numerical problems, especially discretization, in Eulerian models.

2.2.2. Adjoint operators

While the observation operator relates the fluxes to the observations, the adjoint operator relates the model-observation differences to a sensitivity to the fluxes. To understand the adjoint operator, it helps to first consider the model sensitivity, i.e., the perturbation of the output (mixing ratio) given a perturbation in the input (flux variables), which can be represented as:

$$\delta y_j^m = \sum_k^K \frac{\partial H(x)_j}{\partial x_k} \delta x_k \qquad (2.1)$$

This project has received funding from the European Union's Horizon Europe research and innovation programme under grant agreement No 101081395

where δx_k is the perturbation to the k^{th} flux variable and, $\partial H(x)_j/\partial x_k$ is an element of the linear(ized) model operator (for simplicity, in the following $H(x)_j$ is replaced by y^m_j). To assess the performance of the forward model different criteria may be used, but a particularly useful quantity is the mean square model error, represented here by *J:*

$$J_j = \frac{1}{2\sigma_j^2}\left(y_j^m - y_j^o\right)^2 \quad (2.2)$$

where σ_j is the observation error. The sensitivity of the mean square error (also called the *cost*), δJ to a perturbation in the outputs (mixing ratios) is:

$$\delta J = \sum_j^M \frac{\partial J}{\partial y_j^m}\delta y_j^m \quad (2.3)$$

However, a more useful measure is the sensitivity of the cost to the input (fluxes), $\partial J/\partial x$ (this sensitivity is used in the solution to the inverse problem, see Section 2.5). This sensitivity can be derived efficiently using the adjoint operator as in the following:

$$\frac{\partial J}{\partial x_j} = \sum_k^K \frac{\partial H(x)_k}{\partial x_j}\frac{\partial J}{\partial y_k^m} \quad (2.4)$$

Note, in equation (2.4) the indices are reversed with respect to (2.1) since the roles of input and output are reversed and the Jacobian, $\partial H(x)_k/\partial x_j$ is the transpose of the Jacobian in (2.1) and is the *adjoint* of the linear(ized) model operator, denoted H^*. Using the definition of J in (2.2) and inserting this in (2.4) gives the sensitivity of the cost with respect to the fluxes based on the model-observation error:

$$\frac{\partial J}{\partial x} = H^*\mathbf{R}^{-1}(y^m - y^o) \quad (2.5)$$

Where **R** is the observation error covariance matrix with the variances σ^2 as the diagonal terms. A good introduction to adjoint models can be found in (Errico, 1997) and their derivation is described in (Giering and Kaminski, 1998).

Note that not all inversion methods explicitly require an adjoint operator, such as ensemble methods, which are discussed in Section 2.5.4. Moreover, if the observation operator can be expressed as a matrix operator, **H**, then the adjoint operator is simply the matrix transpose, $\mathbf{H}^T$. This is the case for Lagrangian models run backwards in time, even when they include first-order chemical reactions or deposition processes. For this reason, Lagrangian models are said to be *self-adjoint*.

2.2.3. Operator input and output

The input to the observation operator (where here the operator is the mathematical mapping from the control space to the observation space) is the vector of fluxes (and/or other variables that one wants to improve the knowledge about). The output of the observation operator is a vector of mixing ratios (or concentrations).

The input to the adjoint operator is the vector of the model-observation discrepancy weighted by the observation error. The output of the adjoint operator is the gradient, $\partial J/\partial x$ or in other words the sensitivity of the cost to the fluxes (see Equation 2.5).

2.3. Inversion theory

This section provides the theoretical basis for how the posterior control vector (fluxes and/or other variables) can be derived. The problem of estimating the fluxes based on the

This project has received funding from the European Union's Horizon Europe research and innovation programme under grant agreement No 101081395

observations is most often not well-constrained, therefore, it is not possible to derive an exact solution for the control variables. There may be variables in the control vector, $\boldsymbol{x}$ to which the observations are insensitive and thus perturbations to these variables will result in the same predicted values (such variables are said to lie in the null space of the observation operator). For this reason, the inverse problem cannot simply be solved as:

$$\boldsymbol{x} = \mathbf{H}^{-1}\boldsymbol{y}$$

even if **H** would in principle be invertible (and generally it is not) since **H** is most likely ill-conditioned (meaning that its inverse may be numerically unstable and inaccurate). Solving the problem using simple least squares is also problematic because $\mathbf{H}^{\mathrm{T}}\mathbf{H}$ is most likely also ill-conditioned and because the control variables are often correlated[4]. Therefore, a method of regularization is needed to make the poorly constrained (or ill-posed) problem solvable. There are different approaches to do this, either by modifying the matrix to be inverted to decrease its *condition number*, such as the Tikhonov regularization (Tikhonov and Arsenin, 1977), or by using prior information about control variables and consideration of probability. In these guidelines, the latter approach is used, but regularization methods can be used to derive a similar solution.

In the probabilistic approach, Bayes' Theorem provides a method to derive the posterior probability distribution function (PDF) for the control vector combining information from the observations and prior PDF of the control vector. The posterior probability of the control vector, $\boldsymbol{x}$ given the observations, $\boldsymbol{y}^o$ is the conditional probability, $P(\boldsymbol{x}|\boldsymbol{y}^o)$ and is proportional to the conditional probability of making the observations given some value of the control vector (also known as the likelihood), $P(\boldsymbol{y}^o|\boldsymbol{x})$, multiplied by the prior probability of the control vector, $P(\boldsymbol{x})$:

$$P(\boldsymbol{x}|\boldsymbol{y}^o) \propto P(\boldsymbol{y}^o|\boldsymbol{x})\, P(\boldsymbol{x}) \qquad (2.6)$$

Note that although P is used to denote all the PDFs they are not the same function. The best estimate of $\boldsymbol{x}$ (called the analysis or posterior, $\boldsymbol{x}^a$) is usually taken to be the mean or mode of $P(\boldsymbol{x}|\boldsymbol{y}^o)$. (From here on, we use the terminology *posterior*). The solution corresponding to the mode, i.e., the maximum of the posterior PDF is called the maximum a posterior probability (MAP) and is most commonly used (at least for Gaussian PDFs). When the likelihood, $P(\boldsymbol{y}^o|\boldsymbol{x})$ and prior probability, $P(\boldsymbol{x})$ are Gaussian PDFs, then the posterior PDF is also Gaussian and the MAP solution is the same as the mean and median of this PDF.

The prior PDF, $P(\boldsymbol{x})$ describes the knowledge about the control variables before observations are considered and can be expressed as the deviation around the prior estimate of $\boldsymbol{x}^b$, $P(\boldsymbol{x} - \boldsymbol{x}^b)$ (if P is defined for all $\boldsymbol{x} - \boldsymbol{x}^b$). If the PDF is Gaussian this can be written as being proportional to:

$$P(\boldsymbol{x}) \propto \exp\left(-\frac{1}{2}\left(\boldsymbol{x}-\boldsymbol{x}^{\boldsymbol{b}}\right)^{\mathrm{T}}\mathbf{B}^{-1}\left(\boldsymbol{x}-\boldsymbol{x}^{\boldsymbol{b}}\right)\right) \qquad (2.7)$$

Where **B** is the error covariance described by:

$$\mathbf{B} = \mathrm{E}\left[\left(\boldsymbol{x}-\boldsymbol{x}^{\boldsymbol{b}}\right)\left(\boldsymbol{x}-\boldsymbol{x}^{\boldsymbol{b}}\right)^{\mathrm{T}}\right] \qquad (2.8)$$

[4] The least squares problem minimizes the equation: $argmin\|H(\boldsymbol{x}) - \boldsymbol{y}^{\boldsymbol{o}}\|^2$ and, if $\mathbf{H}(\boldsymbol{x})$ can be expressed as a matrix operation, the least squares problem can be computed by solving: $\boldsymbol{H}^T\boldsymbol{H}\boldsymbol{x} = \boldsymbol{H}^T\boldsymbol{y}^{\boldsymbol{o}}$

This project has received funding from the European Union's Horizon Europe research and innovation programme under grant agreement No 101081395

Conditional probability $P(\boldsymbol{y}^o|\boldsymbol{x})$ describes the probability of making the observations, $\boldsymbol{y}^o$ given a particular value of $\boldsymbol{x}$. Again, assuming a Gaussian PDF, this can be written as being proportional to:

$$P(\boldsymbol{y}^o|\boldsymbol{x}) \propto \exp\left(-\frac{1}{2}(H(\boldsymbol{x})-\boldsymbol{y}^o)^{\mathrm{T}}\mathbf{R}^{-1}(H(\boldsymbol{x})-\boldsymbol{y}^o)\right) \quad (2.9)$$

where **R** is the observation error covariance described by:

$$\mathbf{R} = \mathrm{E}\left[\left(\boldsymbol{y}^o - H(\boldsymbol{x}^t)\right)\left(\boldsymbol{y}^o - H(\boldsymbol{x}^t)\right)^{\mathrm{T}}\right] \quad (2.10)$$

where $H(\boldsymbol{x}^t)$ is the model output given the true fluxes, $\boldsymbol{x}^t$. Note that **R** formulated this way accounts for the error introduced in the observation operator.

By inserting (2.7) and (2.9) into the expression for Bayes' theorem (2.6) and taking the natural logarithm we can derive the function (termed the *cost function*):

$$J(\boldsymbol{x}) = -\ln P(\boldsymbol{x}|\boldsymbol{y}^o) \propto \frac{1}{2}\left(\boldsymbol{x}-\boldsymbol{x}^b\right)^{\mathrm{T}}\mathbf{B}^{-1}\left(\boldsymbol{x}-\boldsymbol{x}^b\right) + \frac{1}{2}(H(\boldsymbol{x})-\boldsymbol{y}^o)^{\mathrm{T}}\mathbf{R}^{-1}(H(\boldsymbol{x})-\boldsymbol{y}^o) \quad (2.11)$$

The $\boldsymbol{x}$ that minimises this cost function corresponds to the maximum of the posterior probability (i.e., the mode of the distribution).

If the posterior PDF is in the same probability distribution family as the prior PDF, then these are said to be conjugate distributions with respect to the likelihood function, and prior PDF is said to be the conjugate prior of the likelihood function. The corollary of this, is that choosing a conjugate prior for the likelihood function, means the posterior PDF will be the same family as the prior PDF and will have a closed form expression, which enables direct calculation of posterior moments and a clear relationship between prior and posterior parameters. In these guidelines, generally Gaussian PDFs will be used unless otherwise stated.

2.4. Inversion implementation

This section introduces the general considerations needed to set-up an atmospheric inversion. Advice for specific species are provided in Sections 3 to 6.

2.4.1. Resolution, discretization and aggregation

Although in reality the fluxes are continuous in space and time it is impossible to solve these as such. Therefore, the variables (and the model) need to be discretized in space, such as on a grid, and in time, such as averages over a given time interval. The variables may alternatively represent parameters in a function describing the fluxes. The model resolution and how the variables are discretized can have a significant influence on the results, and this choice should be given some attention.

2.4.1.1. Errors associated with model transport and resolution

The observation and adjoint operators have a finite resolution (for practical reasons, even for Lagrangian models the output SRR needs to be discretized in space and time). This represents the finest resolution at which the influence of the fluxes on the observations can be resolved, and the choice of this resolution is important in two contexts: 1) The representation of atmospheric transport. This can be especially important for observations in complex terrain where the finite resolution of model orography can result in large differences between the model surface elevation and the

This project has received funding from the European Union's Horizon Europe research and innovation programme under grant agreement No 101081395

actual elevation of an observation. Furthermore, owing to the limited resolution (also of the meteorological fields used to drive the transport model), the model may not capture atmospheric flows that are important locally for the observations, such as mountain valley circulations, or for coastal sites, land-sea breezes e.g. (Geels et al., 2007; Pillai et al., 2011; Wang et al., 2017). Even at high-resolution, model errors occur and can be due to errors in the wind fields used or due to the model parameterizations e.g. (Katharopoulos et al., 2023) . 2) The importance of subscale variability in the fluxes. For instance, if an observation is sensitive to the distribution of fluxes within the unit of discretization (e.g. grid cell and/or time interval) since the distribution is not represented it will result in a modelling error. Together, these types of error are called *model representation error*. Model representation error is challenging to estimate and, as discussed above, there are different causes of this error.

There are different approaches for estimating the first type of error, i.e., model transport error, and three of these will be discussed here (in no specific order). 1) The first approach involves examining the spatial and/or temporal variability in the model around the observation point (such as the gradient between horizontally and vertically adjacent grid cells) and using this as a proxy for the transport error (e.g. Bergamaschi et al., 2005; Rodenbeck et al., 2003). 2) The second approach involves comparing the modelled and observed mixing ratio (or concentration) of a species for which the fluxes are assumed to be well-known. There are very few species (if any) for which this assumption can be made, but one species that has been used in several studies is Radon-222 (Broquet et al., 2011; Koffi et al., 2016). However, this method is also limited by: i) uncertainties in the Radon fluxes (Karstens et al., 2015), and ii) the fact that there may be differences in the spatiotemporal distribution between the fluxes of interest and the fluxes of Radon, affecting the simulation of both species, as well as due to the half-life of Radon-222 (3.8 days) which limits the approach to the influence of the past few days. 3) The third approach uses the difference in mixing ratios simulated by different models or model set-ups (including one or more of meteorological forcing, boundary conditions, resolution and parameter choice). The difference in mixing ratios from the different models or model set-ups is used as a proxy for the transport error (e.g. Munassar et al., 2023; Pillai et al., 2012; Wang et al., 2017; Steiner et al. 2024b).

A method for estimating the second type of error, i.e., due to the lack of sub-grid scale flux variability, is presented by Bergamaschi et al. (2010). Their method uses the influence of the prior emission in the grid cell where the observation is located as a proxy and assumes that the emission is instantaneously mixed within the boundary layer and calculates the influence as the integrated signal over a timescale of horizontal advection of air mass.

2.4.1.2. Errors associated with control vector discretization

Another consideration is the resolution of the variables (e.g. fluxes) to be optimized and how these are discretized, namely how the control vector is specified. It is not necessary that the control variables are at the same spatiotemporal resolution as the model and there may be good reasons for aggregating the variables in space and/or time. For instance, variables may need to be averaged to reduce the size of the control vector for computational reasons. Another reason is because the observations may not provide sufficient information to constrain the variables at the resolution of the model, resulting in strongly correlated errors between the posterior variables.

This project has received funding from the European Union's Horizon Europe research and innovation programme under grant agreement No 101081395

When averaging the variables, it is important to consider their variability in space and time, and how sensitive the observations are to this. Specifically, when the variables are averaged, not resolving their variability will result in model error - this type of error is called *aggregation error* (see Figure 2.2). A good overview of aggregation error is given by Kaminski et al. (2001) who also describe a method for estimating the aggregation error in the observation space. The spatial and temporal pattern on which the variables are averaged should be chosen to minimise the aggregation error. One approach is choosing regions (and time intervals) over which the variability is minimized. This may be e.g. ecosystem type and geographic region for CO_2 land biosphere fluxes as used in Chevallier et al. (2006) and Peters et al. (2007). Another approach is to aggregate in areas where the linearized model operator is not very sensitive, i.e., where the fluxes have only a weak influence on the observations. This approach has been used by e.g. Thompson and Stohl (2014) and Gómez-Ortiz et al. (2024) who based the aggregation on the SRRs derived from a Lagrangian model. Bocquet et al. (2011) present a formal optimization of the aggregated grid using various criteria.

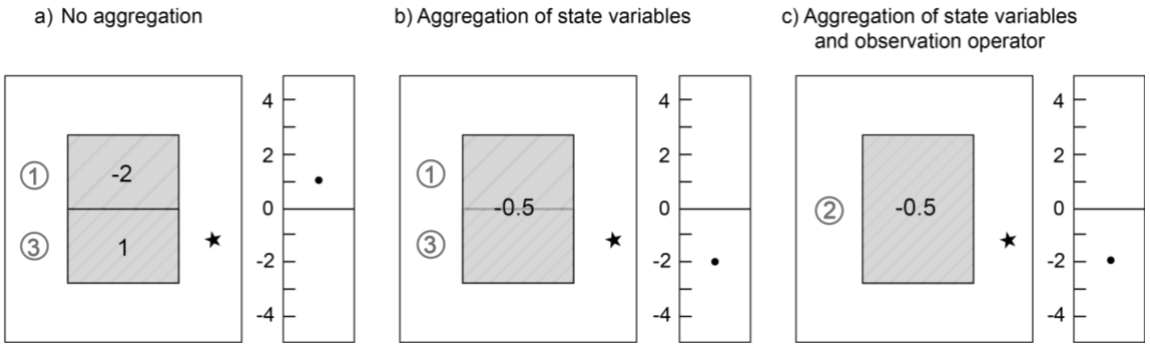


Figure 2.2: Schematic illustrating aggregation error for a two variable case. The boxes with grey hatching represent the control variables and the corresponding observation operator (or SRR). The values of the observation operator are given by the numbers in circles and the numbers in the boxes are the values of the fluxes. The star represents the observation location. The black points in the vertical bars on the right indicate the observed value (observation units), which is the integral of the fluxes and the observation operators. a) case with no aggregation, b) with aggregation of the state variables (mean value of the two flux variables), and c) aggregation of the state variables and observation operator (mean values of both) with the observation operator now applying to the area equivalent to two boxes. Note that in each case (a) the resulting modelled value in the observation space (black dot) is different to cases (b) and (c).

2.4.2. Domain, initial and boundary conditions

The choice of the inversion domain size, where the boundaries are located, and the boundary conditions warrant consideration. Generally, the smaller the inversion domain is, the more important the boundary conditions will become.

Related to the boundary conditions, are the so-called *background mixing ratios*. The background mixing ratios describe the influence of fluxes and atmospheric transport (and chemistry) at the observation points from outside the spatiotemporal domain of the model. Note that not all inversion frameworks need an estimate of the background mixing ratios as input (e.g. Eulerian models only need an estimate of the initial conditions and the mixing ratios at the boundaries), however, it is still a useful quantity for evaluating an inversion.

An estimate of the background mixing ratios is required for Lagrangian models and is used when comparing the model output (e.g. mixing ratios) with observations:

$$\boldsymbol{y^m = \mathbf{H}x + y^{bg}}$$

This project has received funding from the European Union's Horizon Europe research and innovation programme under grant agreement No 101081395

Where $\boldsymbol{y}^{bg}$ is a vector of background mixing ratios (note here the observation operator is given as a matrix as is the case for observation operators based on SRRs). A number of methods have been proposed to estimate the background mixing ratio: 1) Based on a filtering of the observations to approximate the signal which is assumed to represent the background, such as the REBS (Robust Extraction of Baseline Signal) method (Ruckstuhl et al., 2012) . 2) Using measurements, such as from aircraft or a "clean" background station to sample air presumed to represent the background. 3) By calculating it through coupling the end points of the Lagrangian model's backwards trajectories to an estimate of the 3D mixing ratio field, such as from a global coarser resolution model, such as the Global Distribution Based (GDB) method (Thompson and Stohl, 2014; Vojta et al., 2022). In the case the trajectories are calculated beyond the inversion domain, the contribution from fluxes outside the domain also needs to be estimated, using for example a global prior estimate of the fluxes.

A detailed comparison of methods (1) and (3) is given in Vojta et al. (2022) and they argue against using method (1). In principle, the longer backwards in time that the trajectories are calculated, the smaller the amount of variability in the observations that is explained by the background. However, method (1) does not account for this, which can lead to biases in the posterior fluxes (see Figure 2.3). There are also further issues with method (1) for continental sites (or for sites close to sources) for which there may be no instances when the observation represents the background signal. Method (2) may be suitable for small domains and inversions over short time periods for which the boundary mixing ratios can be sampled, and when the locations of the boundaries are chosen such that the mixing ratios at the boundaries do not vary strongly. This method, however, is not plausible for inversions covering longer time periods and/or larger domains.

For regional Eulerian models, there are also a couple approaches for dealing with the influence from outside the spatial (and temporal) domain. One is the "2-step" method proposed by Rodenbeck et al. (2009), which describes coupling a regional model to the output of a global model. In this method a global model is run forwards in time with (optimized) fluxes but with fluxes over the regional inversion domain set to zero. The mixing ratios from this global run are sampled at the observation points to determine the background mixing ratios. One drawback of this method is that the background is only calculated using the coarse global modelled transport. Alternatively, the mixing ratios from a global model can be provided at each model time step at the boundaries of the regional model (e.g. Nesser et al., 2025). This approach uses the higher resolution model to determine the influence of the boundary conditions at the observation points.

This project has received funding from the European Union's Horizon Europe research and innovation programme under grant agreement No 101081395

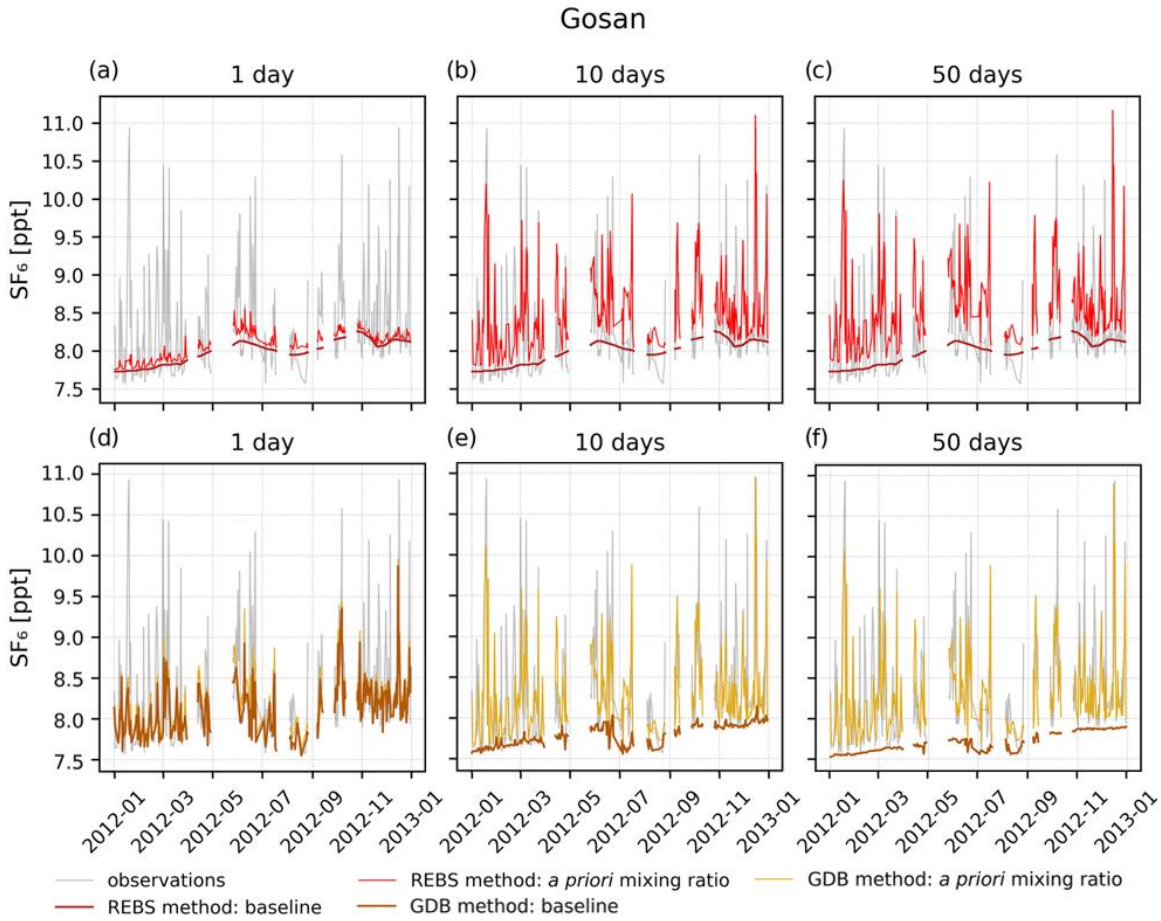


Figure 2.3: Comparison of background calculation methods for SF_6 at the example site, Gosan showing: (a to c) the REBS method and (d to f) the GDB method, both with Lagrangian backwards in time calculations for 1, 10 and 50 days. Note that for the GDB method, the background contribution decreases with increasing backward calculation time, while the flux contribution increases. For the REBS method, the background remains constant, thus producing a negative bias for short backward calculation times and a positive bias for longer ones.

2.4.3. Prior fluxes

Prior fluxes used in atmospheric inversions may be based on e.g. process-based models, empirical models, emission inventories, or a combination of these. These different types of methods that are not based on atmospheric observations are often collectively referred to as *bottom-up* methods because they involve scaling-up small-scale processes in physical or empirical models to gridded, regional, national and global flux estimates. Prior fluxes should be viewed as first guess estimates that provide some constraint based on existing knowledge, such as the spatial and temporal patterns, rather than as accurate representations of true fluxes (Enting, 2002).

There are some considerations on what can be used for the prior fluxes. First, Bayes' Theorem requires that the prior estimate is independent of the observations. Thus, the prior cannot be based on a previous result that relies on the same observations as used in the inversion (or a subset of these) (e.g. Rodgers, 2000). Second, the prior fluxes should be, as far as possible or practical, an unbiased estimate of the true fluxes. Thus, they should represent as close as possible the flux variables in the inversion that are targeted in the optimization.

This project has received funding from the European Union's Horizon Europe research and innovation programme under grant agreement No 101081395

A discussion of priors, and their uncertainties, for specific species is given in Sections 3 to 6 as well as example datasets used for defining priors. Section 2.6 discusses methods for evaluating and optimizing the parameters defining the prior error covariance matrix.

2.5. Methods to solve the inverse problem

To find the estimate of $\boldsymbol{x}$ that corresponds to the maximum a posterior (MAP) solution, one needs to find $\boldsymbol{x}$ that minimises the cost function (2.11). If the forward model is linear or close to linear, and given the quadratic form of (2.11), the solution is that for which the gradient of (2.11) is equal to zero:

$$\nabla J(\boldsymbol{x}) = \mathbf{B}^{-1}\left(\boldsymbol{x} - \boldsymbol{x^b}\right) + H^{*}\mathbf{R}^{-1}(H(\boldsymbol{x}) - \boldsymbol{y^o}) \quad (2.12)$$

Note in (2.12) that the adjoint operator H^* is used to determine the gradient of cost function with respect to $\boldsymbol{x}$ in the observation space, as derived in Section 2.1.2. If the observation operator can be expressed as a matrix, **H**, then the adjoint is the matrix transpose $\mathbf{H}^{\mathrm{T}}$. There are different methods of solving (2.12) and which one is chosen depends on a number of considerations. If the observation operator can be stored as matrix, **H**, then an analytical solution is possible. If not, then other solutions, such as gradient methods or ensemble approaches are required. If the model is not close to linear, then there are a couple of options, such as: 1) using a linearized model operator, which is called from an outer loop over the non-linear model, or 2) using Monte Carlo methods (see Section 2.5.4.1).

In addition, considerations such as computational efficiency play a role in which method is most suited for a specific problem. Particularly important for this is the size of the control and observation vectors. The size of the control vector (dimension *N*) obviously also determines the size of the error covariance matrix **B** (*N* × *N*) and calculating the inverse of this matrix may be a computationally demanding step for large *N*. The observation vector (dimension *M*) may also be very large, although often diagonal **R** matrices are used (and for some methods this is required) meaning the calculation of the inverse is fast. However, there are cases when correlations between observations should be accounted for. (For more about **B** and **R** matrices, see Section 2.6).

In the case of a linear or linearized model, the posterior error covariance matrix can be found from the second derivative of the cost function (Fisher and Courtier, 1995):

$$\mathbf{P} = (\nabla^2 J)^{-1} = (\mathbf{B}^{-1} + \mathbf{H}^{\mathrm{T}}\mathbf{R}^{-1}\mathbf{H})^{-1} \quad (2.13)$$

If the observation operator can be expressed as a matrix, there is the possibility to easily calculate a number of inversion diagnostics. Rodgers (2000) presents a number of useful inversion diagnostics. One diagnostic is the averaging kernel, **A**, which quantifies the sensitivity of the posterior fluxes to the prior estimates, and is derived as follows:

$$\boldsymbol{x^a} = \boldsymbol{x^b} + \mathbf{G}\left(\boldsymbol{y^o} - \mathbf{H}\boldsymbol{x^b}\right) \quad \text{where } \mathbf{G} = (\mathbf{H}^{\mathrm{T}}\mathbf{R}^{-1}\mathbf{H} + \mathbf{B}^{-1})^{-1}\mathbf{H}^{\mathrm{T}}\mathbf{R}^{-1} \quad (2.14)$$

$$\boldsymbol{x^a} = \boldsymbol{x^b} + \mathbf{G}\left(\mathbf{H}\left(\boldsymbol{x^t} - \boldsymbol{x^b}\right) + \boldsymbol{\varepsilon}\right) \quad \text{where } \boldsymbol{\varepsilon} \text{ is the observation error} \quad (2.15)$$

$$\boldsymbol{x^a} = \boldsymbol{x^b} + \mathbf{A}\left(\boldsymbol{x^t} - \boldsymbol{x^b}\right) + \mathbf{G}\boldsymbol{\varepsilon} \quad \text{where } \mathbf{A} = \mathbf{GH} \quad (2.16)$$

$$\boldsymbol{x^a} = (\mathbf{I} - \mathbf{A})\boldsymbol{x^b} + \mathbf{A}\boldsymbol{x^t} + \mathbf{G}\boldsymbol{\varepsilon} \quad (2.17)$$

This project has received funding from the European Union's Horizon Europe research and innovation programme under grant agreement No 101081395

It follows from (2.17) that the posterior fluxes are a weighting between the true fluxes and the prior fluxes with some error. The weighting, described by **A**, *depends on the degree of observational constraint, and the error is proportional to the observation space error. This is the case no matter what method is chosen to solve the inverse problem.*

In the following sections a brief introduction to a number of different methods is provided and key references are given for further reading. The methods presented in this section are those that are currently most commonly used in the atmospheric inversion community but there are also other methods for solving the inverse problem, which are not presented here.

2.5.1. Analytical solution

The analytical solution refers to directly solving (2.12) for $\boldsymbol{x}$ using matrix inversion (see Figure 2.3). Theoretically, this is the most accurate method to solve the inversion problem. However, in practice limited numerical accuracy can sometimes lead to problems in matrix inversion. By setting (2.12) to zero and applying some algebra (for a full derivation see Chapter 2 of Rodgers (2000)) one can derive the following expression for $\boldsymbol{x}^a$:

$$\boldsymbol{x^a} = \boldsymbol{x^b} + (\mathbf{H}^{\mathrm{T}}\mathbf{R}^{-1}\mathbf{H} + \mathbf{B}^{-1})^{-1}\mathbf{H}^{\mathrm{T}}\mathbf{R}^{-1}\left(\boldsymbol{y^o} - \mathbf{H}\boldsymbol{x^b}\right) \quad (2.18)$$

By further rearrangement one can derive an alternative but equivalent expression for $\boldsymbol{x}^a$:

$$\boldsymbol{x^a} = \boldsymbol{x^b} + \mathbf{B}\mathbf{H}^{\mathrm{T}}(\mathbf{H}\mathbf{B}\mathbf{H}^{\mathrm{T}} + \mathbf{R})^{-1}\left(\boldsymbol{y^o} - \mathbf{H}\boldsymbol{x^b}\right) \quad (2.19)$$

The important difference between these two expressions is the matrix in parentheses, which needs to be inverted. In (2.18) this matrix is $\mathbf{H}^{\mathrm{T}}\mathbf{R}^{-1}\mathbf{H} + \mathbf{B}^{-1}$, which has dimensions ($N \times N$) and (2.18) is sometimes referred to as the N-form, whereas in (2.19) the matrix that needs to be inverted, ($\mathbf{H}\mathbf{B}\mathbf{H}^{\mathrm{T}} + \mathbf{R}$), has dimensions ($M \times M$) and (2.19) is sometimes referred to as the M-form. For large matrices, calculating the inverse can be computationally demanding, therefore, the choice of the N-form or the M-form can make a large difference in computational efficiency. However, the condition number of these matrices can differ to the extent that one equation may lead to a poorer result than the other. In some cases, results can even become numerically unstable.

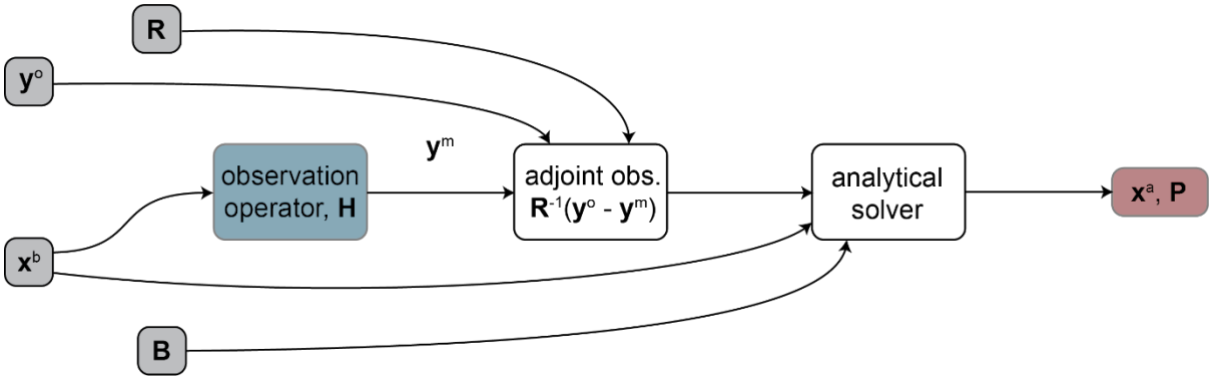


Figure 2.4: Schematic of analytical solution. The grey boxes indicate inputs to the inversion and the red box indicates output from the inversion.

In summary, the analytical method is easy to implement if the observation operator is linear (or can be linearized) and can be expressed as a matrix and kept in memory (note

This project has received funding from the European Union's Horizon Europe research and innovation programme under grant agreement No 101081395

determining **H** can be challenging for Eulerian models). This method also allows direct calculation of the posterior error covariance matrix as well as other useful diagnostics (see Section 9 for more on diagnostics).

2.5.2. Kalman Filters

The Kalman Filter (Kalman, 1960) is used in many smoothing, filtering, and data prediction applications. The advantage of the Kalman Filter (KF) is that it does not require the full observation matrix in memory since it assimilates observations, or batches of observations, sequentially, updating the estimate of the control vector and its uncertainty in each iteration (see Figure 2.5). The KF is recursive in the sense that only the estimated control vector from the previous step and the observation in the current step are needed to compute the update. The KF and its variants have been used in several atmospheric inversion studies (e.g. Brunner et al., 2012; Prinn et al., 2005; Varon et al., 2023) and is straight forward to implement.

In the KF, the prior estimate of the control vector, $\boldsymbol{x}$ (dimension N) at time step t can be defined by propagating forward the control vector from the previous timestep with a *state transition operator*, $\mathbf{F}$ ($N \times N$) and accounting for error in this operator, $\boldsymbol{w}$ (N):

$$\boldsymbol{x}_{t|t-1} = \mathbf{F}\boldsymbol{x}_{t-1|t-1} + \boldsymbol{w} \tag{2.20}$$

where $t|t$-1 signifies that this is the prior estimate for timestep t and is based on observations up to and including time t-1, whereas t-1$|t$-1 signifies the posterior estimate for timestep t-1. The error in the state transition is Gaussian distributed with covariance, $\mathbf{Q}$ ($N \times N$):

$$\mathbf{Q} = \mathrm{E}[\boldsymbol{w}\boldsymbol{w}^{\mathrm{T}}] \tag{2.21}$$

The observation at timestep t can be modelled according to:

$$\boldsymbol{y}_t = \mathbf{H}_t\boldsymbol{x}_{t|t-1} + \boldsymbol{v}_t \tag{2.22}$$

where $\boldsymbol{v}_t$ is the observation error with known covariance and is independent of $\boldsymbol{w}$.

$$\mathbf{R} = \mathrm{E}[\boldsymbol{v}\boldsymbol{v}^{\mathrm{T}}] \tag{2.23}$$

The update to $\boldsymbol{x}$ is calculated by combining the prior estimate with the new observation:

$$\boldsymbol{x}_{t|t} = \boldsymbol{x}_{t|t-1} + \mathbf{K}_t\left(\boldsymbol{y}_t^o - \mathbf{H}_t\boldsymbol{x}_{t|t-1}\right) \tag{2.24}$$

where $\mathbf{K}_t$ is the Kalman gain matrix and the term $\boldsymbol{y}^o_t - \mathbf{H}_t\boldsymbol{x}_{t|t\text{-}1}$ is called the *innovation* (note for a single observation the innovation is scalar and $\mathbf{K}_t$ has dimension ($N \times 1$)).

The Kalman gain is calculated as:

$$\mathbf{K}_t = \mathbf{P}_{t|t-1}\mathbf{H}_t^{\mathrm{T}}\left(\mathbf{H}_t\mathbf{P}_{t|t-1}\mathbf{H}^{\mathrm{T}} + \mathbf{R}_t\right)^{-1} \tag{2.25}$$

where $\mathbf{P}_{t|t\text{-}1}$ is the prior error covariance matrix ($N \times N$):

$$\mathbf{P}_{t|t-1} = \mathrm{E}\left[\left(\boldsymbol{x}_t^t - \boldsymbol{x}_{t|t-1}\right)\left(\boldsymbol{x}_t^t - \boldsymbol{x}_{t|t-1}\right)^{\mathrm{T}}\right] \tag{2.26}$$

and can be obtained by propagating forward the error covariance matrix from the previous timestep:

$$\mathbf{P}_{t|t-1} = \mathbf{F}\mathbf{P}_{t-1|t-1}\mathbf{F}^{\mathrm{T}} + \mathbf{Q} \tag{2.27}$$

This project has received funding from the European Union's Horizon Europe research and innovation programme under grant agreement No 101081395

The update to give the posterior error covariance matrix is:

$$\mathbf{P}_{t|t} = (\mathbf{I} - \mathbf{K}_t\mathbf{H}_t)\mathbf{P}_{t|t-1} \quad (2.28)$$

The KF sequentially assimilates observations at each timestep by looping over the propagation and update steps.

If the model is perfect and the covariances are known exactly, then the KF provides the best non-biased estimate of the state variables. In reality though, this is unlikely the case, and choosing appropriate covariances **R** and **Q** is essential to having a successful KF set-up. Brunner et al. (2012) use a maximum likelihood approach for determining the parameters of **R** and **Q** which is a common approach in KF applications (Harvey, 1990; Simon, 2006).

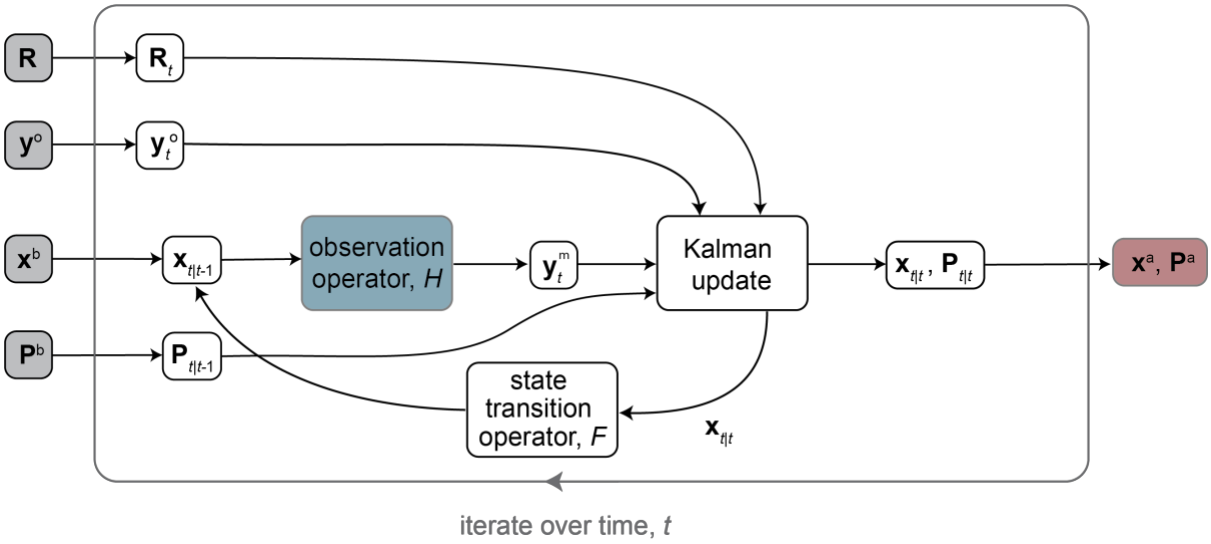


Figure 2.5: Schematic of the Kalman Filter.

2.5.3. Gradient methods

Gradient methods provide a solution to the gradient equation (2.12) without the need for specifying the observation operator, *H*, as a matrix (see Figure 2.6). Because of this, gradient methods are widely used in atmospheric inversion (e.g. Berchet et al., 2021; Bergamaschi et al., 2009; Chevallier et al., 2005; Thompson et al., 2025; Villalobos et al., 2021).

Gradient methods fall into the category of *variational assimilation*, which solve the inversion problem using all observations in the assimilation period at once (Rabier and Liu, 2003). According to this definition, the analytical solution given in Section 2.5.1 is also a variational (Var) method and can be defined as a 3D-Var approach as the observation operator, *H*, considers variations in 3D space. An extension of this is the 4D-Var approach, in which the observation operator also includes a dynamical model to evolve the atmospheric state in time. Variational methods are widely used in numerical weather prediction, and their use in atmospheric inversions largely stems from this application.

This project has received funding from the European Union's Horizon Europe research and innovation programme under grant agreement No 101081395

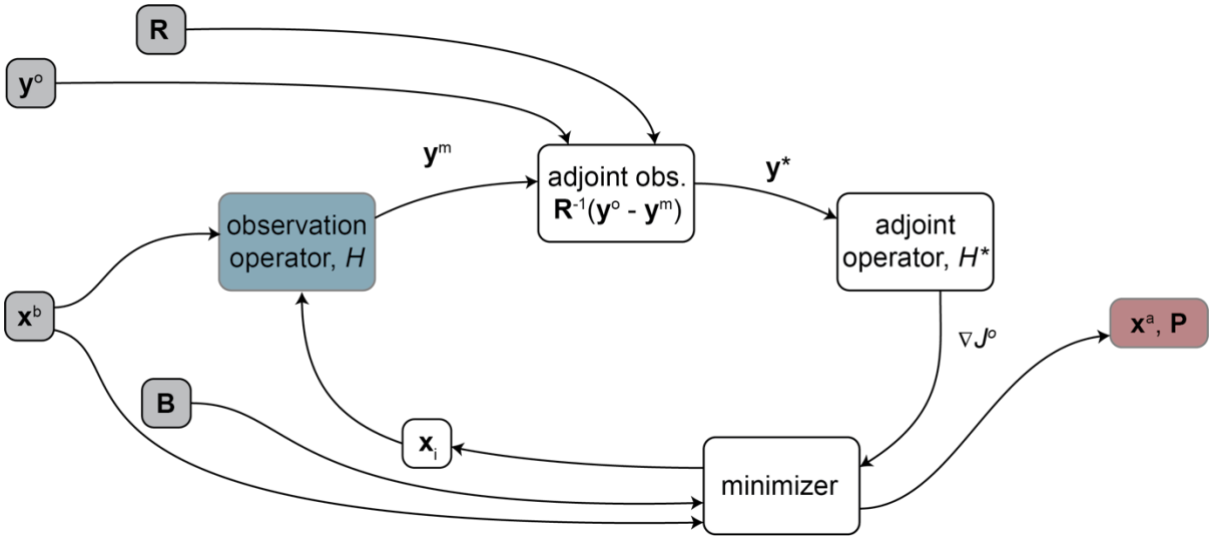


Figure 2.6: Schematic of the generalized gradient method. This is an iterative method with a loop around the observation operator, the calculation of the adjoint observation, adjoint operator and minimizer.

Gradient methods solve the gradient equation iteratively (using all observations at once), by calculating the gradient for the current value of the control vector, $\nabla J(\mathbf{x}_i)$, which gives the direction of steepest increase in $J(\mathbf{x}_i)$, then proceeding in the opposite direction, $-\nabla J(\mathbf{x}_i)$, i.e., the direction of steepest descent, for a given step size, α. Gradient methods differ principally in how they determine the step size. The gradient of the cost function $\nabla J(\mathbf{x}_i)$ can be determined without the need for explicitly stating $\mathbf{H}^T$ by using the adjoint operator as discussed in Section 2.1.2. An excellent introduction to gradient methods, and especially the conjugate gradient method, is provided by (Schewchuk, 1994).

The gradient method solves equations of the form:

$$\nabla J(\boldsymbol{x}) = \mathbf{A}\boldsymbol{x} - \boldsymbol{b} \tag{2.29}$$

where **A** is a symmetric positive definite matrix.

The steps in the generalized gradient method can be summarized as follows:

i) Start with a first (prior) estimate of the control vector, $\mathbf{x}_i = \mathbf{x}^b$. Apply the observation operator to calculate the observation-model mismatches ($H(\mathbf{x}_i) - \mathbf{y}^o$).
ii) Calculate the gradient of the cost function, $-\nabla J(\mathbf{x}_i)$ using the adjoint operator.
iii) Find the optimal step size, α_i.
iv) Update the estimate of the control vector according to:

$$\boldsymbol{x}_{i+1} = \boldsymbol{x}_i - \alpha_i \nabla J(\boldsymbol{x}_i) \tag{2.30}$$

v) Check for convergence, if not converged repeat.

2.5.3.1. Conjugate gradient method

In the conjugate gradient method, each descent direction is chosen such that it is orthogonal to the previous descent direction guaranteeing that it is linearly independent (Schewchuk, 1994). Choosing the descent direction as the gradient $-\nabla J(\mathbf{x}_i)$ fulfils this requirement.

By relating the gradient of the cost function (2.12) to equation (2.29), it can be seen that **A** is the matrix: $(\mathbf{B}^{-1} + \mathbf{H}^T\mathbf{R}^{-1}\mathbf{H})$, which is also the Hessian of the cost function and is

This project has received funding from the European Union's Horizon Europe research and innovation programme under grant agreement No 101081395

symmetric and positive definite. This makes the conjugate gradient method an ideal choice for solving the gradient equation.

The conjugate gradient can be summarized as follows:

i) Choose the first descent direction:

$$\boldsymbol{d}_i = -\boldsymbol{g}_i = -\nabla J(\boldsymbol{x}_i) \tag{2.31}$$

ii) Calculate the step size as:

$$\alpha_i = \frac{\boldsymbol{d}_i^{\mathrm{T}} \boldsymbol{d}_i}{\boldsymbol{d}_i^{\mathrm{T}} J'' \boldsymbol{d}_i} \tag{2.32}$$

iii) Calculate the new estimate:

$$\boldsymbol{x}_{i+1} = \boldsymbol{x}_i + \alpha_i \boldsymbol{d}_i \tag{2.33}$$

iv) Calculate the gradient at the new estimate:

$$\boldsymbol{g}_{i+1} = \boldsymbol{g}_i + \alpha_i J'' \boldsymbol{d}_i \tag{2.34}$$

v) Calculate the new descent direction as:

$$\boldsymbol{d}_{i+1} = -\boldsymbol{g}_{i+1} + \beta_i \boldsymbol{d}_i \qquad \text{where} \qquad \beta_i = \frac{\boldsymbol{g}_{i+1}^{\mathrm{T}} \boldsymbol{g}_{i+1}}{\boldsymbol{g}_i^{\mathrm{T}} \boldsymbol{g}_i} \tag{2.35}$$

vi) Check for convergence, and if not converged repeat.

In (2.32 and 2.34) $J''\boldsymbol{d}_i$ is the Hessian of the cost function applied to the descent direction, which, following (Fisher, 1998), can be approximated as:

$$J''\boldsymbol{d}_i = \frac{1}{\tau}(\nabla J(\boldsymbol{x}_0 + \tau \boldsymbol{d}_i) - \boldsymbol{g}_0) \tag{2.36}$$

where τ is a small number, but large enough to avoid problems with numerical rounding errors. Equation (2.36) requires calculation of ∇J for the vector $\boldsymbol{x}_0 + \tau \boldsymbol{d}_i$. Thus, for each iteration, the gradient needs to be recalculated, which involves applying the observation operator and adjoint operator. Fortunately, the conjugate gradient algorithm converges quickly minimizing the computational cost.

2.5.3.2. Quasi-Newton methods

Quasi-Newton methods are derived from the Newton method for finding the extrema of a function and have some similarities to gradient methods. In the Newton method, a second order Taylor expansion around an iterate is used to find the minimum of $J(\boldsymbol{x})$:

$$J(\boldsymbol{x} + \Delta \boldsymbol{x}) \approx \left(J'(\boldsymbol{x})\right)^{\mathrm{T}} \Delta \boldsymbol{x} + \frac{1}{2} \Delta \boldsymbol{x}^{\mathrm{T}} J'' \Delta \boldsymbol{x} \tag{2.37}$$

where J'' is the Hessian matrix of the cost function. Calculating the gradient of (2.37) and setting this to zero, provides the Newton step:

$$\Delta \boldsymbol{x} = -(J'')^{-1} J'(\boldsymbol{x}) \tag{2.38}$$

And then $\boldsymbol{x}$ is updated as:

$$\boldsymbol{x}_{i+1} = \boldsymbol{x}_i + \Delta \boldsymbol{x}_i \tag{2.39}$$

In quasi-Newton methods, the Hessian matrix is not used (as this can be computationally expensive to calculate) but instead an approximation of it, **V** where the definition of this matrix distinguishes the different quasi-Newton methods. In the BFGS variant of the algorithm, **V** is updated at each iteration as:

This project has received funding from the European Union's Horizon Europe research and innovation programme under grant agreement No 101081395

$$\mathbf{V}_{i+1} = \mathbf{V}_i + \frac{\boldsymbol{z}_i \boldsymbol{z}_i^{\mathrm{T}}}{\boldsymbol{z}_i^{\mathrm{T}} \Delta \boldsymbol{x}_i} - \frac{\mathbf{V}_i \Delta \boldsymbol{x}_i (\mathbf{V}_i \Delta \boldsymbol{x}_i)^{\mathrm{T}}}{\Delta \boldsymbol{x}_i^{\mathrm{T}} \mathbf{V}_i \Delta \boldsymbol{x}_i} \qquad \text{where} \qquad \boldsymbol{z}_i = J'(\boldsymbol{x}_{i+1}) - J'(\boldsymbol{x}_i) \qquad (2.40)$$

The quasi-Newton method can be summarized as follows:

i) Choose an initial approximation for **V**, for the first guess of the control vector, $\boldsymbol{x}_i = \boldsymbol{x}^b$ and calculate the gradient
ii) Update the control vector:
$$\boldsymbol{x}_{i+1} = \boldsymbol{x}_i - \alpha_i \mathbf{V}_i^{-1} J'(\boldsymbol{x}_i) \qquad (2.41)$$
where α_i is the step size and satisfies the *Wolfe conditions*[5].
iii) Calculate the gradient of the new control vector $J'(\boldsymbol{x}_{i+1})$
iv) Calculate the new approximation to the Hessian, $\mathbf{V}_{i+1}$
v) Check for convergence, if not repeat from step (ii)

2.5.3.3. Pre-conditioning

The rate of convergence for gradient and quasi-Newton methods can be further improved by *pre-conditioning*, i.e., by transforming the matrix **A** to improve its condition number.

In preconditioning, the equation **Ax** = **b** is multiplied by some matrix, $\mathbf{M}^{-1}$:

$$\mathbf{M}^{-1}\mathbf{A}(\mathbf{M}^{-1})^{\mathrm{T}}\boldsymbol{\chi} = \mathbf{M}^{-1}\boldsymbol{b} \qquad \text{where } \boldsymbol{\chi} = \mathbf{M}^{\mathrm{T}}\boldsymbol{x} \qquad (2.42)$$

Where the transformed matrix $\mathbf{M}^{-1}\mathbf{A}(\mathbf{M}^{-1})^{\mathrm{T}}$ is also symmetric positive definite but has a smaller condition number, meaning that the solution can be reached in fewer iterations. A useful choice for $\mathbf{M}^{\mathrm{T}}$ is the square root of the inverse of the prior error covariance matrix such that $\boldsymbol{\chi} = \mathbf{B}^{-½}\mathbf{x}$, which has been used by e.g. Chevallier et al. (2005).

2.5.4. Ensemble methods

Ensemble-based approaches also have the advantage that they can be used in the case that the observation operator cannot be expressed as a matrix or kept in memory and have the additional advantage that they do not require an adjoint operator. Furthermore, ensemble methods may be also used to solve inversions for which the model is non-linear (the degree of non-linearity that can be handled depends on the specific method). These methods are also generally simple to code, although some of them can be computationally demanding limiting their application on large problems. Here, only two ensemble approaches will be presented, both of which have been used in atmospheric inversion studies.

2.5.4.1. Markov Chain Monte Carlo methods

Markov Chain Monte Carlo (MCMC) methods generate sequences of samples (or in statistical terminology "events"), the probability of which depends on the previous sample. Here, only one MCMC algorithm will be discussed, and that is the Metropolis algorithm (MA), which has been used in atmospheric inversion studies e.g. (Ganesan et al., 2014; Rigby et al., 2011). This method is appropriate to use also for non-linear problems where there may be local minima.

The MA works by first drawing a sample from a distribution (here this will be referred to as the prior distribution, $P^b(\mathbf{x})$). This sample is then accepted or rejected based on the acceptance probability, and if it is accepted a new sample, $\mathbf{x}_i$ is generated by drawing

[5] The Wolfe conditions are a set of inequalities for performing inexact line search especially in quasi-Newton methods, first published by (Wolfe, 1969).

This project has received funding from the European Union's Horizon Europe research and innovation programme under grant agreement No 101081395

from a conditional probability distribution, $Q(\mathbf{x}_i|\mathbf{x}_{i-1})$ given the previously accepted sample, $\mathbf{x}_{i-1}$. The distribution Q is called the *proposal density* or *jumping distribution* and is commonly a Gaussian distribution (as was also used by Rigby et al. (2011) and Ganesan et al. (2014)). In this way, the MA generates a Markov chain of samples (see Figure 2.7). The sequence of all accepted samples defines the posterior PDF, $P^a(\mathbf{x}|\mathbf{y}^o)$ (or in statistical terminology, the *target distribution*). As the number of samples increases the closer the distribution becomes to the posterior PDF.

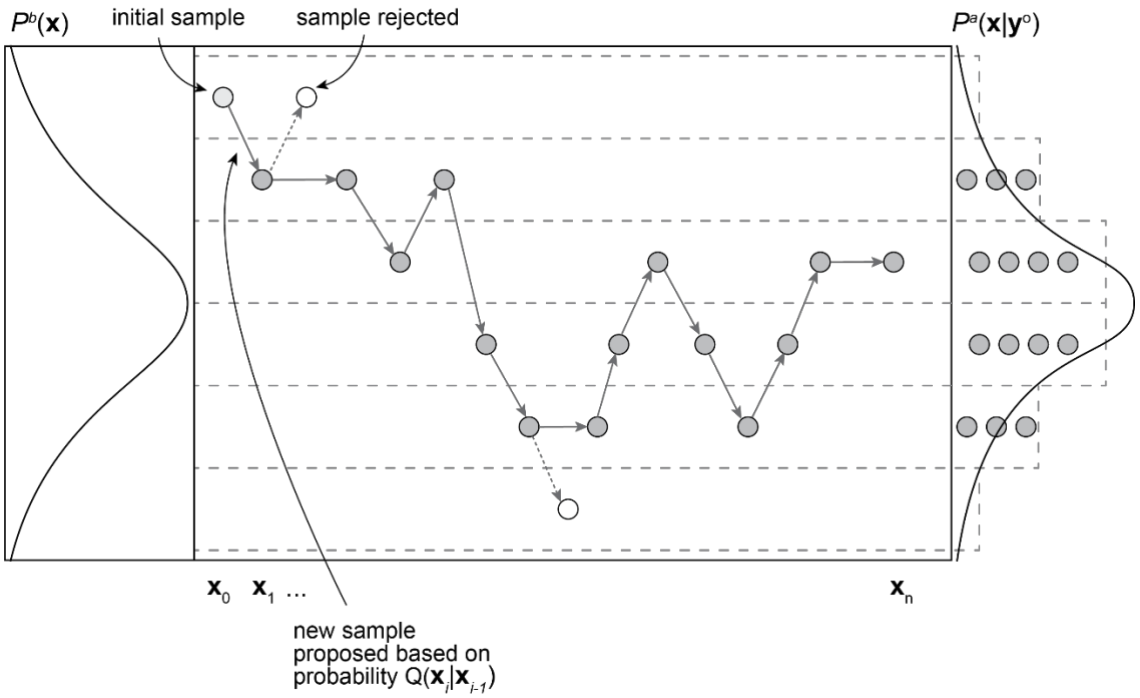


Figure 2.7. Metropolis algorithm showing a sample drawn from a prior distribution and a random walk generating a sequence of samples forming the posterior distribution.

The derivation of the MA stems from the fact that the probability for new samples must fulfil the condition of *detailed balance*, i.e., the probability, P^t of transitioning from $\mathbf{x}_{i-1}$ to $\mathbf{x}_i$ must equal that of transitioning from $\mathbf{x}_i$ to $\mathbf{x}_{i-1}$:

$$P^t(\boldsymbol{x}_i|\boldsymbol{x}_{i-1})P^a(\boldsymbol{x}_{i-1}|\boldsymbol{y}^o) = P^t(\boldsymbol{x}_{i-1}|\boldsymbol{x}_i)P^a(\boldsymbol{x}_i|\boldsymbol{y}^o) \quad (2.43)$$

Using this condition, and the definition of the transition probability:

$$P^t(\boldsymbol{x}_i|\boldsymbol{x}_{i-1}) = Q(\boldsymbol{x}_i|\boldsymbol{x}_{i-1})A(\boldsymbol{x}_i, \boldsymbol{x}_{i-1}) \quad (2.44)$$

where $A(\mathbf{x}_{i-1},\mathbf{x}_i)$ is the acceptance distribution, then inserting (2.44) into (2.43) gives:

$$\frac{A(\boldsymbol{x}_i,\boldsymbol{x}_{i-1})}{A(\boldsymbol{x}_{i-1},\boldsymbol{x}_i)} = \frac{P^a(\boldsymbol{x}_i|\boldsymbol{y}^o)Q(\boldsymbol{x}_{i-1}|\boldsymbol{x}_i)}{P^a(\boldsymbol{x}_{i-1}|\boldsymbol{y}^o)Q(\boldsymbol{x}_i|\boldsymbol{x}_{i-1})} \quad (2.45)$$

The acceptance probability, A is chosen such that the condition in (2.43) is fulfilled, and in the Metropolis algorithm it is chosen to be:

$$A(\boldsymbol{x}_i, \boldsymbol{x}_{i-1}) = \min\left(1, \frac{P^a(x_i|y^o|)Q(x_{i-1}|x_i|)}{P^a(x_{i-1}|y^o|)Q(x_i|x_{i-1}|)}\right) \quad (2.46)$$

Equation (2.46), is the generalized MA (often referred to as the Metropolis-Hastings algorithm), in which the proposal density, Q, does not need to be symmetric (Chib and Greenberg, 1995). In the case that Q is symmetric (2.46) simplifies to:

This project has received funding from the European Union's Horizon Europe research and innovation programme under grant agreement No 101081395

$$A(\boldsymbol{x}_i, \boldsymbol{x}_{i-1}) = \min\left(1, \frac{P^a(\boldsymbol{x}_i|\boldsymbol{y}^o)}{P^a(\boldsymbol{x}_{i-1}|\boldsymbol{y}^o)}\right) \quad (2.47)$$

and from (2.47) it is easy to see that if the probability, P^a, of the proposed sample, $\mathbf{x}_i$ is greater than that of $\mathbf{x}_{i-1}$ then $A(\mathbf{x}_i|\mathbf{x}_{i-1}) = 1$. This sample is then finally accepted or rejected based on the following criteria where u is a uniform random number $u \in [0, 1]$:

if $u \leq A(\mathbf{x}_i|\mathbf{x}_{i-1})$, accept the new sample

if $u > A(\mathbf{x}_i|\mathbf{x}_{i-1})$, reject the new sample

Although in the above equations, the ratio of $P^a(\mathbf{x}_i|\mathbf{y}^o)$ to $P^a(\mathbf{x}_{i-1}|\mathbf{y}^o)$ is used, in fact only a function, let's call it $f(\mathbf{x})$, is needed, where $f(\mathbf{x})$ is proportional to P^a since the normalizing constant for P^a cancels out.

Although the MA is easy to implement, there are a number of important considerations before choosing the MA for the application of atmospheric inversion:

1) Burn-in period

The samples early in the Markov chain may not represent the posterior (or target) distribution, which is especially true if the initial sample has a low probability. Therefore, it is usual to have a "burn-in" period in which the samples are discarded to achieve independence from the initial sample. The number of samples discarded may need to be quite large, e.g. Ganesan et al. (2014) discarded the first 25,000 samples in their burn-in period.

2) Autocorrelation

The samples in the Markov chain are correlated with each other and, as a result, may not accurately represent the posterior distribution. To achieve independence among the samples, and thereby improve the representation of the posterior distribution, the samples can be selected, e.g., by choosing only every nth sample, where n is determined from the autocorrelation length of the samples.

3) Computational cost

To achieve an accurate representation of the posterior PDF, a large number of samples is often needed. For instance, Rigby et al. (2011) used 10^5 samples in their study with a control vector of size N = 322. For each sample, the calculation of the acceptance probability, A, requires calculation of the cost, which requires the applying the observation operator to compute $\boldsymbol{y}^m$. Thus, unless the observation operator calculations are very fast, the MA (and MCMC methods in general) come at considerable computational cost.

2.5.4.2. Ensemble Kalman Filters

The Ensemble Kalman Filter (EnKF) was developed by (Evensen, 1994) and can be considered as a Monte Carlo implementation of the KF. The main advantage of the EnKF is that it can handle very large inversion problems with many control variables and, additionally, it is relatively straight forward to implement. While there are many variants of the EnKF, only one of them will be presented here, i.e., the Ensemble Square Root Filter (EnSRF), which is one variant that is commonly used in atmospheric inversions at present (e.g. Laan-Luijkx et al., 2017; Peters et al., 2005; Steiner et al., 2024a; Thanwerdas et al., 2025) (see Figure 2.8). A clear and comprehensive explanation of the EnKF and EnSRF is

This project has received funding from the European Union's Horizon Europe research and innovation programme under grant agreement No 101081395

given in Thanwerdas et al. (2025) based on earlier work (Houtekamer and Mitchell, 2001; Peters et al., 2005; Whitaker et al., 2002). Therefore, only a brief description of the algorithm is presented here.

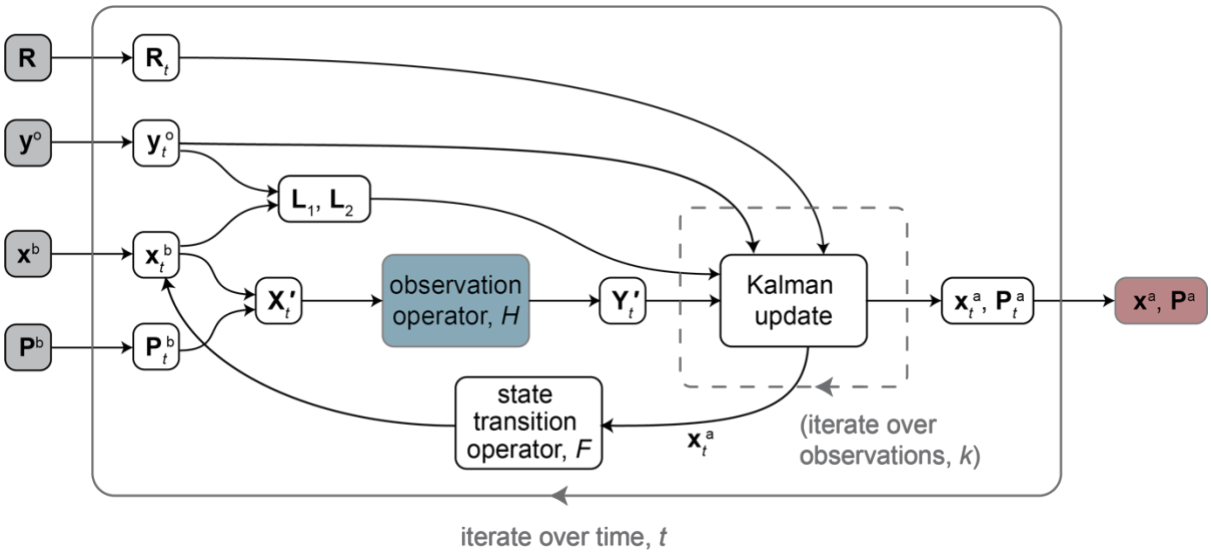


Figure 2.8: Schematic of the EnKF. In the sequential filter (described below) the algorithm iterates over each observation in the assimilation time window. There is also an outer loop over the assimilation time windows. The matrices L_1 and L_2 are localization matrices (described below).

In the EnKF, the uncertainty of the control vector is represented by an ensemble, with the ensemble mean representing the best estimate of the control vector and the ensemble covariance representing the error covariance. (Note, alternatively, the ensemble can be described as perturbations from the mean control vector and, in this case, the mean of the ensemble is zero and this is the implementation described below). The error covariance, **P** is approximated in fewer dimensions than the control vector using an ensemble of size *S*:

$$\mathbf{P} = \frac{1}{S-1}\mathbf{X}'\mathbf{X}'^{\mathrm{T}} \tag{2.48}$$

(note that the matrix **P** approaches the true error covariance matrix as $S \rightarrow \infty$). The matrix **X′** has as its columns *S* individual vectors, which are deviations from the mean:

$$\mathbf{X}' = (\boldsymbol{x}_1', \boldsymbol{x}_2', \ldots, \boldsymbol{x}_S') \qquad \text{where } \boldsymbol{x}_i' = \boldsymbol{x}_i - \overline{\boldsymbol{x}} \tag{2.49}$$

The minimum covariance estimate of the mean control vector is given by the KF update equation:

$$\overline{\boldsymbol{x}^a} = \overline{\boldsymbol{x}^b} + \mathbf{K}\left(\boldsymbol{y}^o - H\overline{\boldsymbol{x}^b}\right) \tag{2.50}$$

Where $\overline{\boldsymbol{x}^a}$ and $\overline{\boldsymbol{x}^b}$ are the posterior and prior means of the ensemble, respectively, and **K** is the Kalman gain with dimension $N \times M$ (where *M* is the number of observations):

$$\mathbf{K} = \mathbf{P}^b\mathbf{H}^{\mathrm{T}}(\mathbf{H}\mathbf{P}^b\mathbf{H}^{\mathrm{T}} + \mathbf{R})^{-1} \tag{2.51}$$

The primary advantage of the EnKF is that Kalman gain matrix, **K** can be derived from the ensemble without requiring the matrix **H** to be stored in memory. This is because the *model-observation covariance matrix*, $\mathbf{PH}^{\mathrm{T}}$ and the *observation-observation covariance*

This project has received funding from the European Union's Horizon Europe research and innovation programme under grant agreement No 101081395

matrix $\mathbf{HPH}^{\mathrm{T}}$ can be approximated from integrations of the forward model with the ensemble:

$$\mathbf{PH}^{\mathrm{T}} = \frac{1}{S-1}\mathbf{X}'\mathbf{Y}'^{\mathrm{T}}$$

$$\mathbf{HPH}^{\mathrm{T}} = \frac{1}{S-1}\mathbf{Y}'\mathbf{Y}'^{\mathrm{T}} \quad (2.53)$$

where $\mathbf{Y}' = (H(\boldsymbol{x}_1'), H(\boldsymbol{x}_2'), \dots, H(\boldsymbol{x}_S'))$

The update to the ensemble is analogous to the update for the ensemble mean:

$$\mathbf{X}'^{a} = \mathbf{X}'^{b} + \widehat{\mathbf{K}}(\boldsymbol{y}'^{\boldsymbol{o}} - \mathbf{H}\mathbf{X}'^{b}) \quad (2.54)$$

Note in (2.54) $\widehat{\mathbf{K}}$ is used and not **K**. In the stochastic EnKF, the observations are represented by another ensemble, with the mean as the actual observation and the variance as the observation error. Thus, $\boldsymbol{y}'^{\boldsymbol{o}}$ is randomly drawn from the PDF of observation errors (Burgers et al., 1998). In this case, the ensemble members are updated with slightly differing observations reflecting the observation uncertainty and this is represented in the spread of the analysis (or posterior) ensemble and $\widehat{\mathbf{K}}$ = **K**. The stochastic EnKF can be interpreted as a Monte Carlo method.

In the deterministic implementation, the observations are not represented by an ensemble and each member of the ensemble is updated with the same observations, in other words the perturbation to the observations is zero, i.e., $\boldsymbol{y}'^{\boldsymbol{o}}$ = 0. In this case (2.54) reduces to:

$$\mathbf{X}'^{a} = \left(\mathbf{I} - \widehat{\mathbf{K}}\mathbf{H}\right)\mathbf{X}'^{b} \quad (2.55)$$

Considering the definition of the error covariance given in (2.48) substituting value of $\mathbf{X}'^{a}$ into (2.55) the posterior error covariance is:

$$\mathbf{P}^{a} = \left(\mathbf{I} - \widehat{\mathbf{K}}\mathbf{H}\right)\mathbf{P}^{b}\left(\mathbf{I} - \widehat{\mathbf{K}}\mathbf{H}\right) \quad (2.56)$$

However, this definition omits the influence of the observation error covariance and underestimates $\mathbf{P}^{a}$ (Burgers et al. 1998). This problem can be resolved by seeking a definition of $\widehat{\mathbf{K}}$ that satisfies the equivalence of the definition of $\mathbf{P}^{a}$ with that in the KF expression for $\mathbf{P}^{a}$ (see 2.28), that is:

$$\left(\mathbf{I} - \widehat{\mathbf{K}}\mathbf{H}\right)\mathbf{P}^{b}\left(\mathbf{I} - \widehat{\mathbf{K}}\mathbf{H}\right) = (\mathbf{I} - \mathbf{K}\mathbf{H})\mathbf{P}^{b} \quad (2.57)$$

This expression can be solved for $\widehat{\mathbf{K}}$ (see (Andrews, 1968)) giving:

$$\widehat{\mathbf{K}} = \mathbf{P}^{b}\mathbf{H}^{\mathrm{T}}(\mathbf{H}\mathbf{P}^{b}\mathbf{H} + \mathbf{R})^{-\frac{1}{2}}\left((\mathbf{H}\mathbf{P}^{b}\mathbf{H} + \mathbf{R})^{\frac{1}{2}} + \mathbf{R}^{\frac{1}{2}}\right)^{-1} \quad (2.58)$$

This is the EnSRF as presented by (Whitaker et al., 2002). Note, however, that the matrix square roots in (2.58) are not unique. The expression of $\widehat{\mathbf{K}}$ can also be written without the need for formulating **H** as:

$$\widehat{\mathbf{K}} = \frac{1}{S-1}\mathbf{X}'\mathbf{Y}'^{\mathrm{T}}\mathbf{D}^{-\frac{1}{2}}\left(\mathbf{D}^{\frac{1}{2}} + \mathbf{R}^{\frac{1}{2}}\right)^{-1} \quad (2.59)$$

Where **D** is the *innovation matrix*:

$$\mathbf{D} = \frac{1}{S-1}\mathbf{Y}'\mathbf{Y}'^{\mathrm{T}} + \mathbf{R} \quad (2.60)$$

This project has received funding from the European Union's Horizon Europe research and innovation programme under grant agreement No 101081395

For a large number of observations, calculating the square root of **D** and the inverse of $\mathbf{D}^{1/2} + \mathbf{R}^{1/2}$ can be computationally expensive, thus, the serial EnSRF was developed in which the observations are assimilated sequentially and **D** and **R** reduce to scalars. In this case, a constant, α can be defined such that $\widehat{\mathbf{K}} = \alpha\mathbf{K}$, where α is:

$$\alpha = \left(1 + \sqrt{\frac{\mathbf{R}}{\mathbf{D}}}\right)^{-1} \tag{2.61}$$

(see Whitaker et al. (2002) and references therein for the derivation). Sequential processing of observations only works if all correlated observations are processed in the same batch (i.e., correlated observations should not be processed sequentially). In the sequential implementation, after each observation (or batch of observations) assimilated, the ensemble mean, the ensemble of control vectors, the ensemble mean in observation space and the ensemble of deviations in the observation space all need to be updated. A detailed description of the implementation of the serial EnSRF is provided in Thanwerdas et al. (2025) and will not be repeated here.

As in the KF, the prior control vector for time step t+1 is forecast from the analysis of the previous time step, t (see 2.20). The prior control vector, $\boldsymbol{x}_{t+1}$, may be defined as a weighting, w, between the prior information for t+1 and posterior control vector from the time step t, with the rationale that the analysis from the previous time step may also be a good estimate for the truth for time t+1 and gives the filter a "learning" effect (Kim et al., 2014; Laan-Luijkx et al., 2017; Steiner et al., 2024a; Thanwerdas et al., 2025). Considering only the posterior control vector of the last window, the prior control vector for t+1 can be estimated as:

$$\boldsymbol{x}_{t+1}^{b} = w_t \boldsymbol{x}_t^{a} + (1 - w_t)\boldsymbol{x}_{t+1}^{b} \tag{2.62}$$

Although the EnKF is in principle straightforward to implement, there are some important considerations, which should be tested in any new set-up:

1) Ensemble size

In EnKF, **P** has a maximum rank of S-1, thus if $S \ll N$, has a greatly reduced rank compared to the full error covariance matrix, and the information of the observations is projected to S-1 directions in the state space. For the EnKF to work well, the ensemble size must be large enough to accurately represent the mean and covariance otherwise spurious correlations between control variables can arise. The error associated with a small ensemble can be reduced to some extent by using covariance localization (see below). For further discussion of ensemble size see Houtekamer and Zhang (2016) and Peters et al. (2005).

2) Covariance localization

To address the rank problem (see above) the assimilation can be effectively split into quasi-independent local problems, for which the S-1 local directions of the ensemble are more likely to provide a reasonable estimate of the true covariance. This localization (called covariance localization) is critical to successful implementation of the EnKF for large problems (Houtekamer and Zhang, 2016). In the sequential EnKF, the localization can be implemented using a smooth function of distance, $l(d)$ between: i) the model and observation coordinates, which is applied to the model-observation covariance matrix

This project has received funding from the European Union's Horizon Europe research and innovation programme under grant agreement No 101081395

and can be described as a matrix, $\mathbf{L}_1$, and ii) the different observations, which is applied to the observation-observation covariance matrix and can be described as a matrix, $\mathbf{L}_2$:

$$\widehat{\mathbf{K}}_{loc} = \mathbf{L}_1 \circ \mathbf{P}\mathbf{H}^{\mathrm{T}}(\mathbf{L}_2 \circ \mathbf{H}\mathbf{P}\mathbf{H}^{\mathrm{T}} + \mathbf{R})^{-1} \quad (2.63)$$

Where ∘ indicates the Hadamard (element-wise) matrix product. The dimensions of $\mathbf{L}_1$ and $\mathbf{L}_2$ are $N \times M$ and $M \times M$, respectively. The function over distance is usually either the Gaussian function (Steiner et al. 2024), the exponential function (Peters et al. 2005), or the 5th order piecewise function proposed by Gaspari and Cohn (1999).

3) Time window of assimilation and lag

In the EnKF, the assimilation is run over a given number of time windows, which are cycled through with some lag (i.e. the number of times the control variables are optimized). The procedure is illustrated in Figure. 2.9 based on Thanwerdas et al. (2025). There are a few important considerations when choosing the time window of assimilation and the degree of lag. A longer assimilation window means there are more variables to estimate and, hence, a larger error covariance matrix is required. This in turn requires more ensemble members to represent accurately. On the other hand, a longer assimilation window means more observations are used to estimate the variables. Peters et al. (2005) used a cycle of 12 weeks that optimizes weekly fluxes window sliding 1 week at a time. In their set-up, each week of fluxes is optimized 12 times (i.e. lag of 12) using observations up to 12 weeks after the flux time. They find that 90% of the variance in the final flux estimate is obtained after estimating the flux 8 times. Thanwerdas et al. (2025) tested using a cycle of 20 days optimizing 10-day resolved fluxes with lags of 1 to 3 and found that as the number of lags increased so did the uncertainty reduction and the degrees of freedom of signal. However, increasing the number of lags has the drawback of increasing the computation time due to the longer integrations of the forward model.

This project has received funding from the European Union's Horizon Europe research and innovation programme under grant agreement No 101081395

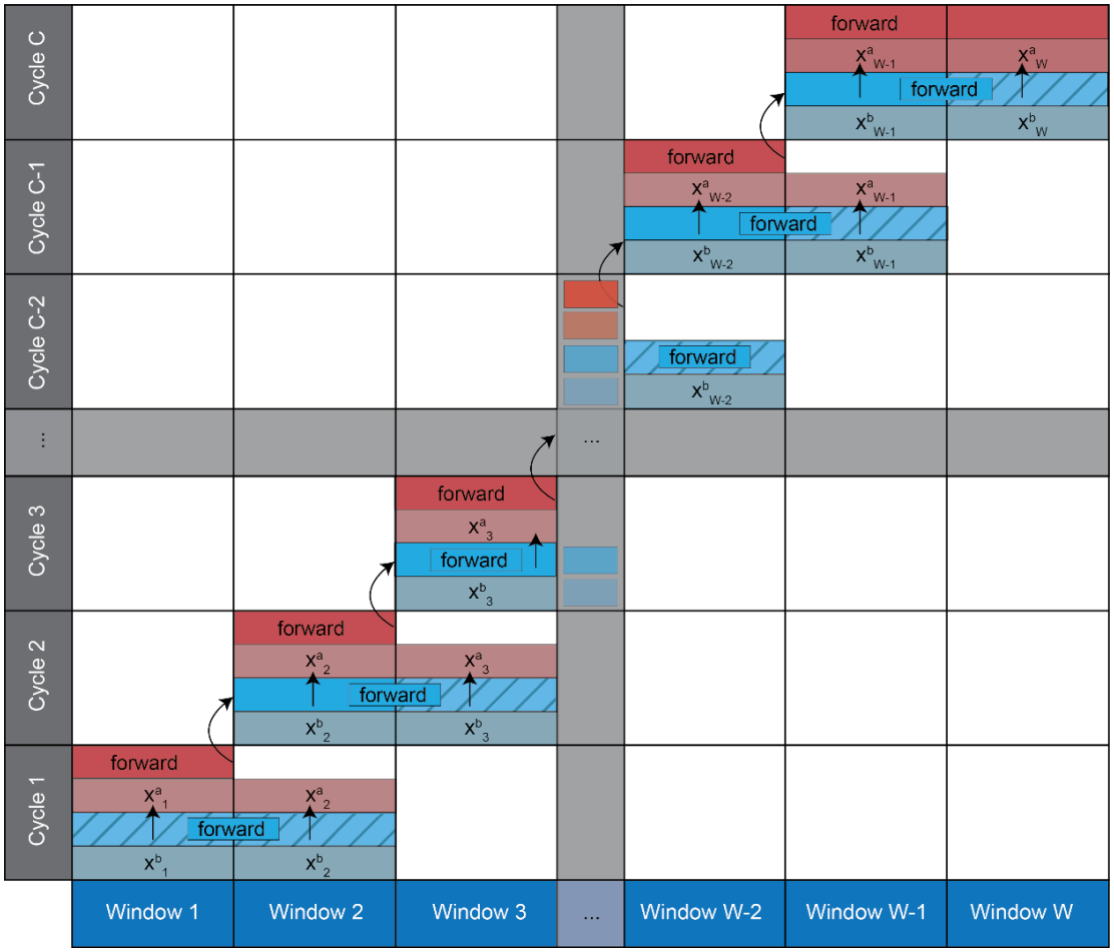


Figure 2.9: Schematic showing the iterations over time windows in the EnSRF (based on Thanwerdas et al. 2025). Blue colours indicate prior fluxes and prior forward simulations, while red colours indicate posterior fluxes and posterior forward simulations. The grey diagonal shading indicates time steps for which observations are assimilated. The posterior fluxes from the first window in each cycle (e.g. Cycle 1, Window 1) are used in a forward simulation to provide the initial mixing ratios for the start of the next time window. Also, only the posterior fluxes from the first window in each cycle, which have been estimated based on the assimilation of all observations in a cycle, are included in the posterior control vector. The posterior fluxes from the last window (W) are estimated using only observations up to the end of the assimilation period.

This project has received funding from the European Union's Horizon Europe research and innovation programme under grant agreement No 101081395

2.5.5. Overview of methods

Table 2.2 presents an overview of the methods to solve the inverse problem discussed in these guidelines. Note that these guidelines describe only the most commonly used methods in the community but other methods also exist and may be equally suitable.

Table 2.2: Overview of inversion methods presented in these guidelines.

Method type	Advantages	Disadvantages/Limitations
Analytical	• Simple to implement • Very accurate if the matrix to be inverted is well-conditioned • Simple to calculate useful diagnostics	• Only applicable in cases where the observation operator can be described by a matrix (linear or linearized problems only) and can be kept in memory • Limited to Gaussian PDFs • Can become slow for large problems • Possibly poor results if the matrix to be inverted is poorly conditioned
Kalman Filter	• Simple to implement • Can be used for problems with a large number of observations since these can be used sequentially • Applicable also to problems with non-Gaussian PDFs	• Only applicable in cases where the observation operator can be described by a matrix (linear or linearized problems only) • Sensitive to the definition of the observation error covariance **R** and the state transition error covariance **Q**.
Gradient	• Computationally efficient and can be used for very large problems • Preconditioning can be used to improve the condition number and the rate of convergence • Applicable to problems with non-Gaussian PDFs and with some non-linearity as long as the problem remains convex	• If the observation operator cannot (easily) be described by a matrix then the adjoint model of atmospheric transport (and chemistry) is required. Adjoint models can be challenging to code and debug.
MCMC	• Simple to implement • Can be used on non-linear and non-Gaussian problems	• Computationally inefficient in the case when the forward model (observation operator) takes considerable time.
Ensemble Kalman Filter	• Simple to implement • Can be used for problems with a large number of observations as these can be used sequentially • Does not need the adjoint model	• Standard implementations are limited to Gaussian PDFs • Sensitive to the ensemble size and the degree of localization when the rank of the problem is greatly reduced

This project has received funding from the European Union's Horizon Europe research and innovation programme under grant agreement No 101081395

2.6. Determining the covariance matrices B and R

The dependence of the posterior control variables on the prior is described by the averaging kernel matrix, **A** (see equation 2.17). The matrix **A**, is in fact, the ratio:

$$\mathbf{A} = \frac{\mathbf{H}^{\mathrm{T}}\mathbf{R}^{-1}\mathbf{H}}{(\mathbf{H}^{\mathrm{T}}\mathbf{R}^{-1}\mathbf{H}+\mathbf{B}^{-1})} \quad (2.63)$$

Thus, the dependence of the posterior on the prior, is determined by the balance of the observation space error covariance, **R** and the prior error covariance, **B**. Therefore, the optimal choice of **R** cannot be found independently of **B**, and vice-versa. It is not easy to check the appropriateness of the choices for **R** and **B**, i.e., if the observational uncertainties and/or model uncertainties are over- or under-estimated, or if the prior uncertainties are over- or under-estimated. The aim of this section is to provide some guidance on defining appropriate matrices for **R** and **B**.

Variance and covariance in B

The diagonal terms of the **B** matrix correspond to the variances of the control variables and the off-diagonal terms correspond to the covariance of errors between control variables. The choice of the variances and covariances can have an important influence on the accuracy of the inversion. In the absence of better information, it is common practice to set the square root of the variance (i.e., the standard deviation) as proportional to the prior flux. If multiple choices for the prior are available (different inventories or model estimates), then the standard deviation of these may be used.

The correlation between errors is normally assumed to decay over distance in space and time. Different decay models can be used, but a common choice is exponential decay (e.g. Rödenbeck et al., 2003) where the correlation between the *i*th and *j*th variables, r_{ij}, is governed by the distance between them, Δd_{ij} and the correlation length, D:

$$r_{ij} = exp\left(-\frac{\Delta d_{ij}}{D}\right) \quad (2.64)$$

The correlation length is intended to represent the spatial scales over which uncertainties are expected to be coherent, for example, due to ecosystem types, emission factors, or climate.

The control of flux variables at relatively high spatial and temporal resolution is sometimes hampered by the use of large spatial and temporal correlation lengths in the configuration of **B**. Long correlation lengths reflect homogeneity in the uncertainties in the prior flux estimates, which should prohibit controlling the flux at fine scales. Consistency should thus be found between the assumptions made for the selection of the control variable resolution and the configuration of **B**, namely in the choice of spatial and temporal correlation lengths.

Variance and covariance in R

The variances of the matrix, **R** should reflect both the observation (or measurement) uncertainty as well as the model representation error (see Section 2.4.1.1 for a discussion of this).

A number of methods for solving the inverse problem assume **R** to be diagonal (e.g., the serial implementation of the EnSRF (Section 2.4.4.2) and the gradient methods (Section 2.4.3), and would be greatly complicated or become computationally inefficient if **R**

This project has received funding from the European Union's Horizon Europe research and innovation programme under grant agreement No 101081395

would not be diagonal. In practice though, observation errors may be strongly correlated, especially in the case of satellite retrievals (see also Section 7.2). Moreover, errors in modelling atmospheric transport may introduce further correlations between errors in the observation space. Therefore, it is useful to consider how the effect of correlated errors may be accounted for in a diagonal **R** matrix. Chevallier et al. (2007b) examine different methods for handling error correlation while maintaining a diagonal **R**, namely: i) neglecting the correlations, ii) data thinning, and iii) error inflation. They found the latter (iii) to be the better approach. Typically, an error inflation factor is sought, to multiply the variances to account for the missing covariances in the diagonal matrix. There are various methods to find the inflation factor, but their discussion is beyond the scope of these guidelines.

Posterior residuals

A simple guide to the appropriateness of the choice of **R** and **B** in an inversion, is to examine the misfit (or residual) at the minimum of the cost function, i.e., the cost for posterior control vector (see equation 2.11). For problems with Gaussian PDFs, the minimum of the cost function follows a chi-square distribution with the number of degrees of freedom, k, equal to the dimension of the observation space (Tarantola, 2005) . Thus, if the uncertainties (in both the observation and control spaces) are optimally chosen, the value $\chi^2 = 2J(\boldsymbol{x})/k$ will have a value close to one. Very large values of χ^2 suggest an under-estimation of the uncertainty, whereas very small values of χ^2 suggest an over-estimation of the uncertainty (Tarantola, 2005) but it is not possible from this statistic alone to determine if this is due to **R**, or **B**, or both.

Maximum Likelihood estimation

Michalak et al. (2005) describe a method to determine the covariance parameters of **R** and **B** given the observations, $\boldsymbol{y}$, the prior fluxes, $\boldsymbol{x_b}$, and the transport matrix, **H**. In the simplest case that **R** and **B** are both diagonal matrices, the parameters to be found are the variances of both matrices and a PDF, θ can be defined for the covariances parameters as $\theta(\sigma^2_{R,1},\ldots, \sigma^2_{R,M}, \sigma^2_{B,1},\ldots, \sigma^2_{B,N})$. If it is assumed that there is no prior knowledge about the parameters, then the posterior PDF, $P(\theta \mid \mathbf{H}, \boldsymbol{x_b}, \boldsymbol{y^o})$ is simply proportional to the likelihood function $P(\boldsymbol{y} \mid \mathbf{H}, \boldsymbol{x_b}, \theta)$. An expression for the posterior PDF can be derived (see Michalak et al., (2005) for the full derivation):

$$P(\theta|\mathbf{H}, \boldsymbol{x_b}, \boldsymbol{y^o}) \propto P(\boldsymbol{y^o}|\mathbf{H}, \boldsymbol{x_b}, \theta)$$

$$\propto |\mathbf{HBH}^{\mathrm{T}} + \mathbf{R}|^{-1/2}\exp(-\tfrac{1}{2}(\boldsymbol{y^o} - \mathbf{H}\boldsymbol{x_b})^{\mathrm{T}}(\mathbf{HBH}^{\mathrm{T}} + \mathbf{R})^{-1}(\boldsymbol{y^o} - \mathbf{H}\boldsymbol{x_b})) \qquad (2.65)$$

Where $|\cdot|$ indicates the determinant. The optimal covariance parameters are those for which the logarithm of (2.65) is minimized and is equivalent to their maximum likelihood estimates:

$$L_\theta = \tfrac{1}{2}\ln|\mathbf{HBH}^{\mathrm{T}} + \mathbf{R}| + \tfrac{1}{2}(\boldsymbol{y^o} - \mathbf{H}\boldsymbol{x_b})^{\mathrm{T}}(\mathbf{HBH}^{\mathrm{T}} + \mathbf{R})^{-1}(\boldsymbol{y^o} - \mathbf{H}\boldsymbol{x_b}) \qquad (2.66)$$

In general, to solve (2.66) an iterative method is needed (see Michalak et al. (2005) for such a method). The maximum likelihood values of the covariance parameters can be assessed by performing the inversion for the control vector, $\boldsymbol{x}$, and the posterior residual (see above) can be used to check that the maximum likelihood covariance parameters do not over- or under-estimate the uncertainty.

This project has received funding from the European Union's Horizon Europe research and innovation programme under grant agreement No 101081395

The drawbacks of this method, however, are that it requires that: i) the observation operator can be stored in memory as the matrix **H**, and ii) that the covariance matrices are diagonal, which at least for **B** is not usually the case.

The marginalized Bayesian inversion

Berchet et al. (2015) further examine the impact of the choice of **R** and **B** on the posterior control vector by expressing the posterior PDF as a marginalized probability, i.e., as the sum of conditional probabilities:

$$P(\boldsymbol{x}|\boldsymbol{y^o}) = \int_{(\mathbf{R},\mathbf{B})} P(\boldsymbol{x}|\boldsymbol{y^o},\mathbf{R},\mathbf{B}) \times P(\mathbf{R},\mathbf{B}|\boldsymbol{y^o})\, d(\mathbf{R},\mathbf{B}) \quad (2.67)$$

$$\propto \int_{(\mathbf{R},\mathbf{B})} \mathcal{N}\left(\widetilde{\boldsymbol{x^a}},\widetilde{\boldsymbol{P^a}}\right) \times P(\mathbf{R},\mathbf{B}|\boldsymbol{y^o})\, d(\mathbf{R},\mathbf{B}) \quad (2.68)$$

where $\tilde{\cdot}$ indicates a dependency on (**R**, **B**).

Similarly to Michalak et al., (2005), Berchet et al., (2015), used diagonal **R** and **B**, and solve for the maximum likelihood for these matrices, $\mathbf{R}_{max}$, $\mathbf{B}_{max}$. Berchet et al., (2015) then go a step further to derive PDFs for the diagonal terms of **R** and **B** assuming that these follow a χ^2 distribution with k degrees of freedom with the averages of the distributions being the diagonal terms of $\mathbf{R}_{max}$ and $\mathbf{B}_{max}$ (see Berchet al., (2015) for details). They then carry-out a Monte Carlo sampling of the posterior PDF, $\mathcal{N}\left(\widetilde{\boldsymbol{x^a}},\widetilde{\boldsymbol{P^a}}\right)$ by running an ensemble of inversions each with different **R** and **B** drawn from the χ^2 distributions.

The limitation of their method is similar to that of Michalak et al., (2005), namely, it requires that **H**, **R**, and **B** are small enough to compute the maximum likelihood values of **R** and **B** without excessive computational cost, but additionally, to compute the ensemble of inversions. Berchet et al., (2015) reduce the dimensionality of their problem by carrying-out a projection of the control vector of fluxes to aggregated regions, and by sampling the observations to only assimilate those corresponding to the daily mixing ratio minimum when the planetary boundary layer is well-mixed.

Hierarchical Bayesian inversions

Ganesan et al. (2014) include parameters to define **R** and **B** in the optimization simultaneously with the control variables. This approach estimates *hyperparameters* that characterize the PDFs of **R** and **B**, which have their own prior distributions called *hyperpriors*.

The Hierarchical model, which seeks to find the posterior joint PDF, $P(\boldsymbol{x}, \boldsymbol{\theta} \mid \boldsymbol{y})$, i.e., the joint probability of $\boldsymbol{x}$ and $\boldsymbol{\theta}$ given the observations, $\boldsymbol{y}$, can be formulated as follows:

$$P(\boldsymbol{x},\boldsymbol{\theta}|\boldsymbol{y}) \propto P(\boldsymbol{y},\boldsymbol{x}|\boldsymbol{\theta})P(\boldsymbol{x},\boldsymbol{\theta}) \quad (2.69)$$

$$\propto P(\boldsymbol{y}|\boldsymbol{x},\boldsymbol{\theta})P(\boldsymbol{x}|\boldsymbol{\theta})P(\boldsymbol{\theta}) \quad (2.70)$$

where $\boldsymbol{\theta}$ is the hyperparameter and $P(\boldsymbol{\theta})$ is the hyperprior.

In the study of Ganesan et al., (2014), the hyperparameters that are optimized are the mean, $\boldsymbol{\mu_x}$ and standard deviation, $\boldsymbol{\sigma_x}$ of the PDF represented by **B**, and the standard deviation, $\boldsymbol{\sigma_y}$ of the observation error covariance matrix, **R**, and a temporal correlation scale length, τ describing the correlation of observation errors. For each hyperparameter, a hyperprior needs to be specified. The full posterior PDF sought by Ganesan et al., (2014) is:

This project has received funding from the European Union's Horizon Europe research and innovation programme under grant agreement No 101081395

$$P(\boldsymbol{x}, \boldsymbol{\mu_x}, \boldsymbol{\sigma_x}, \boldsymbol{\sigma_y}, \tau | \boldsymbol{y}) \propto P(\boldsymbol{y} | \boldsymbol{x}, \boldsymbol{\sigma_y}, \tau) P(\boldsymbol{x} | \boldsymbol{\mu_x}, \boldsymbol{\sigma_x}) P(\boldsymbol{\mu_x}) P(\boldsymbol{\sigma_x}) P(\boldsymbol{\sigma_y}) P(\tau) \quad (2.70)$$

Ganesan et al., (2014) solve problem using Monte Carlo method, however, if the logarithm of the expression for posterior PDF is differentiable, then gradient methods could also be used. Once again, the computational cost for finding the posterior PDF may be significant, especially if Monte Carlo sampling methods are used (see Section 2.4.4.1).

3. CO_2 inversions for LULUCF

Gregoire Broquet and Audrey Fortems-Cheiney

3.1. Focusing on LULUCF fluxes in CO_2 inversion frameworks

Atmospheric observations of CO_2 integrate signals from all CO_2 sources and sinks. In principle, the CO_2 atmospheric inversions should thus primarily quantify CO_2 the total net surface fluxes. However, first, the total flux estimates are not directly relevant for studies on the carbon cycle or to support national inventories. A separation is needed, at least, between the fossil fuel emissions and the ocean and terrestrial ecosystem fluxes. Second, depending on the study area, observation network and inverse modelling framework for a specific application, the results can be highly dominated by one type of flux (Peylin et al., 2013; Balsamo et al., 2021). The reason is not only that the observed variations in the mixing ratios are dominated by a type of flux (making it difficult to get information on the other types of fluxes), but also that inversion configurations generally focus the filtering and processing of the signal towards one type of flux. Therefore, even if, eventually, CO_2 inversions should aim to address jointly all types of fluxes, they generally target only one or a few of them.

This section is dedicated to CO_2 atmospheric inversions targeting the quantification of terrestrial ecosystem fluxes and, more specifically, those associated with human management, which should be reported as part of the Land Use, Land Use Change and Forestry (LULUCF) sector of the national inventories under UNFCCC. This component of the anthropogenic CO_2 emissions and removal is also one of the most uncertain sectors and its quantification should strongly benefit from the atmospheric inversion approach (McGrath et al., 2023). The estimates of terrestrial ecosystem fluxes via atmospheric inversions coincide more or less with the definitions from ecosystem modellers of Net Ecosystem Exchange (NEE) or Net Biome Production (NBP), with some ambiguities (as detailed below) which are now better tackled in inverse modelling frameworks (Broquet et al., 2026; Deng et al., 2022).

In the 1990s, the first CO_2 atmospheric inversions were conducted at global scale and targeted the large-scale quantification of the ocean and terrestrial sinks of CO_2. Such global scale CO_2 atmospheric inversions have kept on being the main reference for the monitoring of CO_2 fluxes until the early 2010s, as illustrated in the first comparison of main global inversion systems in Peylin et al., (2013). However, the development of regional scale inversion systems, the general increase in the spatial resolution of the inverse modelling systems and the increasing density of ground-based and space-borne CO_2 observation systems have led to the development of applications targeting CO_2 fossil emissions (Balsamo et al., 2021) and the discrimination between the ecosystem fluxes associated to managed versus unmanaged land (Chevallier, 2021). The

This project has received funding from the European Union's Horizon Europe research and innovation programme under grant agreement No 101081395

atmospheric monitoring of CO_2 fossil emissions raise specific considerations and requires specific strategies (e.g. with the co-assimilation of co-emitted species or isotopic tracers such as radiocarbon, ^{14}C, with the detection and inversion of plumes from emission hotspots etc.) even though the overall principle of such inversions is similar to that for the monitoring of the land ecosystem fluxes (Janssens-Maenhout et al., 2020). The uncertainty in the CO_2 land ecosystem fluxes is much larger than that in the CO_2 fossil emissions, and it dominates the variations of the misfits between the atmospheric simulations and the CO_2 observations currently assimilated in global and regional scale CO_2 inversions (Broquet et al., 2023; Marshall et al., 2023). Therefore, most of CO_2 inversions are thus still conducted to derive the land biosphere fluxes assuming that the CO_2 fossil emission maps provided as input to the transport models are accurate, or that the uncertainties in these maps have a limited impact on the retrieval of the land ecosystem fluxes (Byrne et al., 2023; Crowell et al., 2019; McGrath et al., 2023).

CO_2 inversions are also conducted assuming CO_2 is a passive tracer and neglecting the CO_2 atmospheric production (from oxidation of CO and hydrocarbons), even when conducting inversions at global scale over several decades (Fortems-Cheiney, 2025) .

The split between the land ecosystem fluxes associated to managed and unmanaged land, which supports the comparisons to national inventories, primarily relies on land use maps (Deng et al., 2022). The coupling between atmospheric inversions and process models (Carbon Cycle Data Assimilation System – CCDAS, whose detailed presentation is out of the scope of these guidelines) could be used for a direct connection between the need to correct for flux estimates and parameters associated to land management (Bacour et al., 2023; Kaminski et al., 2013).

3.2. Prior and fixed estimates of the fluxes

In the following, all the fluxes are defined as positive when CO_2 is emitted from the surface to the atmosphere. Traditionally, the land ecosystem flux components have been described in atmospheric inversions as: i) the NEE, with or without an explicit split between the gross flux components of NEE, namely Gross Primary Production (GPP) and autotrophic and ecosystem heterotrophic respiration (R_a and $R_{h,eco}$) or between Net Primary Production (NPP = GPP + R_a) and the heterotrophic respiration and ii) the biomass burning emissions (BB) (Byrne et al., 2023; Monteil et al., 2020; Tolk et al., 2011). Such NEE and BB fluxes have been complemented by fossil CO_2 emission estimates to define the total land fluxes. However, such a decomposition of the land fluxes implicitly creates ambiguity between the NEE (strictly speaking: NPP + $R_{h,eco}$) and the NBP (accounting for other processes emitting the carbon that has been absorbed by the ecosystem via the NPP), and more critically ignoring the lateral transfer of carbon through harvest (wood and crops) and emission of CO_2 from the harvested products and their consumption and decay (including the livestock and human respiration), and via river discharge to the sea (together often referred to as *lateral fluxes*; see Figures 3.1, 3.2 and 3.3). The latter has a critical impact on the spatial distribution of the total land fluxes within the study areas but also across its boundaries through import and export (Ciais et al., 2020b, 2021; Deng et al., 2022; McGrath et al., 2023). However, the ecosystem models tend to better simulate the complexity of the land carbon cycle, which, together

with the availability of complementary databases on the carbon lateral transfer supports the derivation of prior estimates for such components of the land fluxes, and recent analysis (Broquet et al., 2026) promotes decomposing the land fluxes used as input to the inversions, as:

- NEE, decomposed or not into GPP (or NPP), R_a and $R_{h,eco}$
- BB
- Sources from wood / crop harvest products
- Sources from river, lake and estuaries discharge
- Fossil emissions (mainly from fossil fuel combustion, but also from cement and other carbonate decomposition process)

with the GPP (and thus NEE) implicitly consistent with the harvest of wood and crop, and the transfer of carbon from ecosystems to rivers via leaching and using suitable spatial (and as much as possible, temporal) distribution for these different components (see Figures 3.1 and 3.2). Disturbance fluxes due to land use change are mainly associated to deforestation from fires and are thus accounted for in the BB fluxes. The residual component of land use change fluxes (F_{LUC}, mainly from non-fire deforestation or reforestation) is here implicitly aggregated into NEE.

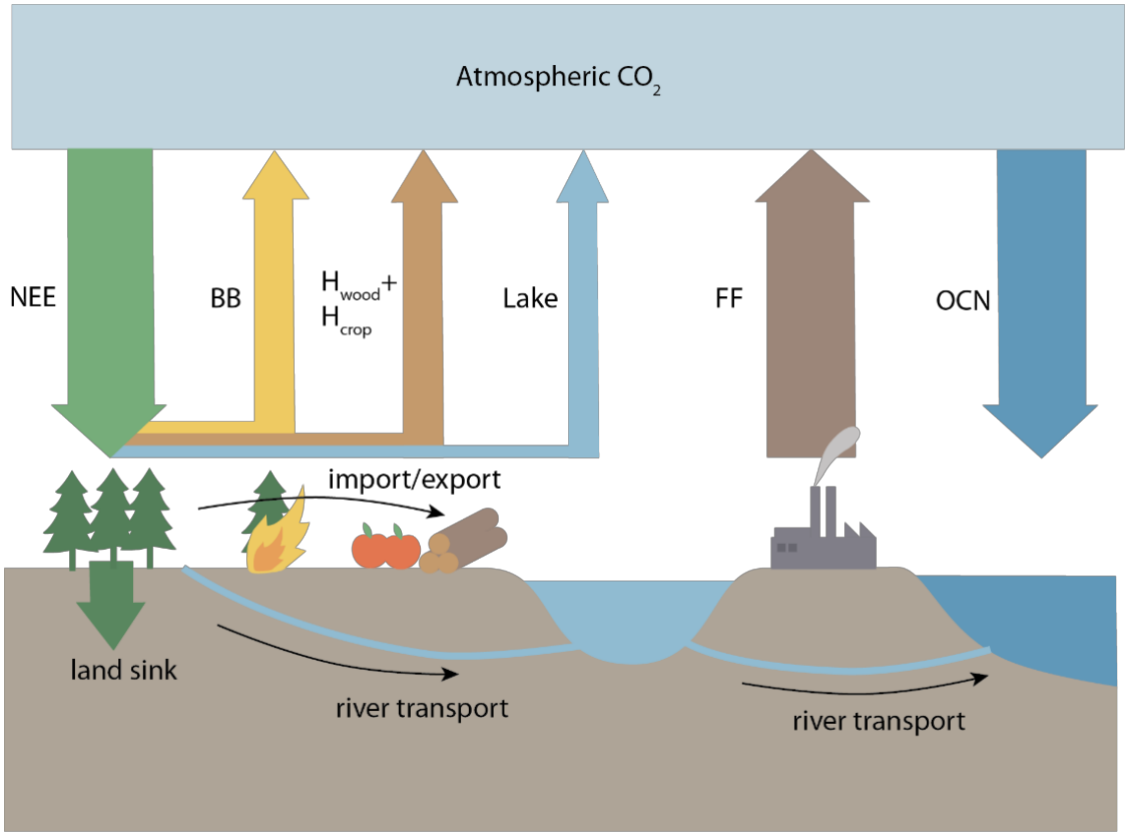


Figure 3.1: Schematic showing the principal CO_2 flux components. (NEE: Net Ecosystem Exchange, BB: Biomass Burning, H_{wood} + H_{crop}: emissions from Harvest Wood and Crop products, Lake: emissions from rivers, lakes and estuaries discharge FF: Fossil Fuel, OCN: Ocean).

This project has received funding from the European Union's Horizon Europe research and innovation programme under grant agreement No 101081395

Such a decomposition facilitates the comparisons to the bottom-up national inventories reported to the UNFCCC, via suitable re-combinations of these land fluxes that are consistent with the assumptions and scope underlying such inventories. For example, the subsampling over managed lands and the correction of the NEE to account for the loss of carbon due to harvest and river drainage, and the addition of BB fluxes should lead to an estimate of the change in the carbon stock of the managed ecosystems that is consistent with the UNFCCC national inventories of LULUCF emissions (excluding the Harvested Wood Products sector) in European countries (Ciais et al., 2022).

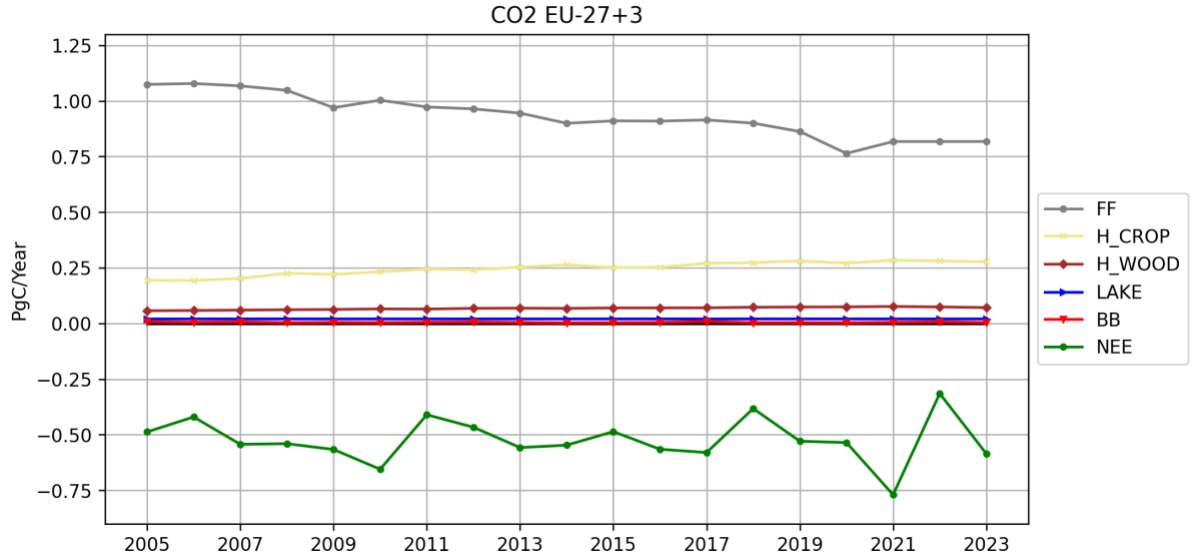


Figure 3.2: Times series of annual estimates for the different land fluxes used as input to the inversions in Broquet et al. (2026), in PgC/year, from 2005 to 2023 for the EU27+3 (Norway, UK and Switzerland) area. The labelling of the fluxes follows that of Figure 3.1.

The land fluxes should be complemented by ocean fluxes, when applicable. These fluxes should encompass both open ocean and coastal fluxes with distinct types of spatialization and temporal dynamics, and sometimes distinct products of bottom-up estimates. However, while the split into these two components could bring significant impact to the flux estimates from the inversions, they keep on being generally taken together as the ocean flux (Byrne et al., 2023; Chau et al., 2022; McGrath et al., 2023).

Of note is that the joint assimilation of observational tracers, such as $^{14}CO_2$ in CO_2 inversions (Basu et al., 2020) could support the split of net NEE and ocean fluxes, into gross fluxes with distinct signatures for this tracer, such as NPP and $R_{h,eco}$, and ocean-to-atmosphere and atmosphere-to-ocean fluxes (Gómez-Ortiz et al., 2024; Potier et al., 2022). However, such a co-assimilation is currently orientated towards the monitoring of fossil CO_2 emissions and is thus out of the scope of this document.

The definition of the control vector for CO_2 inversions primarily relies on the selection of the flux components: i) to be controlled by the inversion, for which the estimate from models and data independent to the atmospheric observations will only be used as prior estimate, and ii) those not controlled by the inversion, for which the estimate will be kept fixed in the inversion process. The inversion should primarily control the main targeted component of the land fluxes, i.e. the NEE (decomposed or not into subcomponents). A joint control of NEE with F_{LUC} (the latter being aggregated to the former above and

This project has received funding from the European Union's Horizon Europe research and innovation programme under grant agreement No 101081395

hereafter) makes sense in practice since the two fluxes are strongly linked in the process models used to generate the prior estimates (MacBean et al., 2022) and since it can be difficult to distinguish between them with the available observations. Much of the biomass burning (BB) as well as wood/crop harvest and river sources are relatively localized, heterogeneous in space and usually distant from the stations of the existing global and continental CO_2 ground-based observation networks (see Figure 3.2). Their control is thus relatively challenging compared to that of NEE (see the strategies to monitor BB based on CO observations, e.g. Basso et al., 2023) and the uncertainties in these fluxes projected into the atmospheric observation space is small compared to the observed atmospheric CO_2 signals and to the projection of uncertainties in NEE over long timescales, typically over more than few days (see Figure 3.3). For these different reasons, all these components can be kept fixed in the inversions as usually done for BB (Thompson et al., 2020) . However, some improvements could be foreseen if expertise and methods are developed for a joint control of all the CO_2 flux components, especially in a context of regular increase of the spatial resolution for the transport and inverse models, of the observation density, and of the use of satellite observations at high resolution and high frequency. In some cases, at large scale, BB emissions are controlled together with NEE as total land ecosystem fluxes (e.g., Net Biosphere Exchange (Byrne et al., 2023)). Traditionally, the ocean fluxes are controlled as well as the land NEE, even for regional inversions whose targets are focused on the latter (Byrne et al., 2023; Monteil et al., 2020) .

The prior estimates of NEE (and of GPP, R_a and $R_{h,eco}$) are generally derived from simulations with process-based dynamical vegetation models or diagnostic vegetation flux models with various levels of complexity (Monteil et al., 2020; Petrescu et al., 2021). Products upscaling eddy covariance GPP and ecosystem respiration flux measurements can also be used (Upton et al., 2024). BB estimates are based on products derived from satellite observations regarding the fire activity, burnt areas and vegetation type and density (Kaiser et al., 2012; Werf et al., 2025). Note that these BB products usually partly overlap with NEE estimates from process-based models, for instance for savannahs that burn every year with subsequent regrowth. In that case, the BB estimates for these particular components should be complemented with a regrowth flux. A few datasets provide information regarding the sources and sinks associated to wood/crop harvest (based, e.g., on FAO statistics) and riverine fluxes (Ciais et al., 2020c; Liu et al., 2024). They mainly support the fixed estimate of the sources. However, they can also be used to adjust the prior estimate of NEE to achieve consistency between the carbon in harvested products and that taken up in NEE. Although process-based vegetation models include harvest processes, the resulting wood/sink harvest can be positively/negatively biased with respect to estimates based on inventories (e.g. on FAO statistics (Petrescu et al., 2021)), which leads to similar biases in the corresponding NPP and thus NEE. Similarly, the NPP and NEE from process-based models that ignore the loss of carbon from the ecosystems due to leaching to rivers should be adjusted when accounting for river sinks to ensure that there is a realistic carbon balance between the

This project has received funding from the European Union's Horizon Europe research and innovation programme under grant agreement No 101081395

different components included in the prior flux estimates, leading to realistic variations of the carbon stock in the ecosystems (Broquet et al., 2026; Deng et al., 2022).

Estimates of fossil CO_2 emissions are derived from gridded global or regional emission inventories that usually disaggregate in space and time the country-scale and annual sectoral emissions from national inventories using spatial proxies (e.g., population maps, road traffic data, etc.) and typical temporal cycles for the underlying activities, and complement them with additional information on international emissions (Crippa et al., 2024; Kuenen et al., 2022; Urraca et al., 2024) . In practice, these inventories can combine different products and sources of data: national – annual budgets from a given product, spatial distributions and sub-annual temporal variations from a combination of other products (Soulie et al., 2024; Steinbach et al., 2011; Woude et al., 2023) . Such inventories generally also provide biofuel emission estimates. However, these estimates partially overlap with the databases of sources associated to the wood/crop harvest products, and choices have to be made to select which ones are the most suitable product in terms of amplitude or spatial and temporal distribution (Ciais et al., 2020a).

Some land CO_2 fluxes are generally ignored due to the lack of suitable products to infer reliable estimates and due to their relatively low magnitude (as of present), such as the emissions from geological weathering and the sinks associated to artificial carbon dioxide removals (Ciais et al., 2022).

A key criterion for the selection of prior estimates, besides their known reliability, quality and accuracy, has often been their spatial and temporal resolution. The main concern has generally been the spatial resolution of the gridded inventories used to prescribe the estimate of the fossil CO_2 emissions, expecting them to be at least that of the atmospheric transport model underlying the inversion system. The reason is that this estimate is generally kept fixed in the inversion, and these emissions are highly heterogeneous in space, with strongly emitting hotspots whose distance to the observation location can have a critical impact of the variations of the observed mixing ratios, and whose dilution at coarse resolution in the model could lead to strong biases for specific observation sites. Major sources of uncertainties arise when strong point sources are mislocated (or kept active while the corresponding site has been closed), or more generally due to the limitation of the approach used to disaggregate the national emissions spatially using affordable proxies in gridded inventories (Guevara et al., 2023; Oda et al., 2018). The spatial resolution of the prior estimate of the ecosystem and ocean fluxes has generally been seen as less critical since these fluxes are rather diffuse and homogeneous (except for the disturbance fluxes). However, with the growing interest in the mapping of the land ecosystem fluxes at high spatial resolution (targeting budgets at scales smaller than the administrative regions in Europe) or on linking the flux estimates to specific types of ecosystems, the need for prior estimates with a precise spatial distribution at fine scales, and if possible at the transport model resolution, has increased (Kuhlmann et al., 2020; Potier et al., 2022) .

In terms of temporal resolution, the 3-hour to 1-hour scale has generally been targeted, considering that it is critical to solve for the diurnal cycle of the fluxes, especially since

This project has received funding from the European Union's Horizon Europe research and innovation programme under grant agreement No 101081395

the global to regional scale inversions assimilate surface observations over specific daytime or nighttime windows (depending on the measurement stations) and since satellite observations based on passive instruments are limited to daytime (Munassar et al., 2024). Global to regional scale inversion systems generally work with hourly inputs and would not make use of a finer temporal resolution. Of note is that the traditional estimates of the sub-annual temporal variations associated to bottom-up inventories of the fossil emissions are based on the repetition of typical average month-to-month, weekday versus weekend, and diurnal cycles (Crippa et al., 2020). However, the temporal variations of the fossil emissions are known to vary in a much more heterogeneous way and products of actual day-to-day variations are emerging, so inversions should use combined fossil emission products with real daily, if not hourly, resolution, if available (Liu et al., 2020).

3.3. Spatial and temporal resolution of the controlled flux variables

The spatial and temporal resolution of the atmospheric transport model and of the controlled flux variables should be much finer than the targeted scales for the analysis of the land terrestrial fluxes to minimize the impact of model and aggregation errors on this analysis. The spatial resolution is generally set as close as possible to that of the transport model, but some inversion frameworks can limit it technically (Thompson et al., 2020). The specific considerations for the monitoring of the land ecosystem fluxes have been that of the scale of homogeneity of these fluxes depending on the regions, providing some flexibility to coarsen this spatial resolution. Ecoregions have been considered as a basis for the control of NEE in Europe (Peters et al., 2010) and some regions such as the Amazon forest had sometimes been seen as relatively homogeneous (Basso et al., 2023). However, the significant impact of spatial variations in the soils structure and properties (impacting gross carbon fluxes) and meteorological forcing have pushed for increasing the control vector spatial resolution everywhere. The temporal resolution of the control vector should allow, somehow, to adjust the diurnal cycle of the fluxes, since this cycle is highly uncertain in the estimates from process models. This has led for control vector resolution of ≤6-hour resolution in regional inversions (Broquet et al., 2011). A trade-off has been made in regional and global inversions by splitting the control vector into sub-daily time steps (e.g. 3 to 12 hours) which represent averages of a specified number of days (usually in the order of a few days to 1-2 weeks, Chevallier et al., 2010).

3.4. Other variables of the control vector and boundary conditions

Variables which contribute to large uncertainties when propagated into the atmospheric observation space should ideally be included in the control vector to allow for this source of error to be better accounted for, compared to adding a statistical characterization of these uncertainties in the observation error covariance matrix, **R**.

The CO_2 lateral boundary conditions of regional inversion configurations are increasingly controlled as well as the CO_2 initial conditions of both global and regional scale inversions, especially since an increasing number of studies document their large

This project has received funding from the European Union's Horizon Europe research and innovation programme under grant agreement No 101081395

impact on regional inversions (Munassar et al., 2023; Nesser et al., 2025). Two types of products have generally been considered to provide prior or fixed estimates of the initial and boundary conditions for the inversions, as illustrated by two types of CO_2 global products distributed by the CAMS services: CO_2 4D fields from relatively coarse global atmospheric inversions (Chevallier et al., 2010) and finer scale forecasts of CO_2 4D fields without the assimilation of CO_2 data (Agustí-Panareda et al., 2014, 2016). While the former should bear relatively low biases at the spatial or temporal boundaries of the inversions, the latter offer relatively good variations at fine scale due to its higher spatial resolution and to that of its input flux products (Agusti-Panareda et al., 2019). The selection of the best type of products, therefore, depends on the location of the boundaries in the regional inversion systems (e.g. in the ocean where fine scale variations are assumed to be small or across regions where numerous plumes from fossil fuel emission hotspots could arise, far from the main area of interest and of observations in the inversion domain, etc.) and on the assumed ability of the inversion to control the large scale biases or small scale variations at its boundaries. The use of nested regional inversion configurations lessens the need for fine scale boundary conditions (Lian et al., 2021).

The control of the meteorological forcing of the parameters of the atmospheric transport is regularly discussed but it remains challenging and there are still few practical examples of such control in the frame of large dimensional global or regional scale inversion problems (Vanderbecken et al., 2023).

3.5. Observation vector definition and selection of the observations

There have not been any major specific strategies for the definition of the observation vector in CO_2 inversions. In situ continuous measurements at ground-based stations are usually assimilated as hourly to 3-hourly mean observations. They are usually selected only during daytime (mainly afternoon, during well-mixed conditions in the planetary boundary layer) at low altitude stations and during nighttime at high-altitude stations. This selection aims to avoid transport modelling biases associated to the dynamics of the boundary layers and the poor representation of mountain sites with a limited resolution of the topography (Broquet et al., 2011). The wide spread of CO_2 fluxes exacerbates the issues associated with the modelling of mountain sites (e.g., with specific CO_2 signals arising from neighbouring valleys) or of coastal sites (being represented by either fully sea or fully land grid-cells in transport models). This encourages adaptative strategies (Pillai et al., 2011). Concepts for more elaborated definitions of the observation vectors which limit the weight of uncertainties in the transport model, boundary conditions etc. are regularly tested (e.g., the use of differences between stations (Breon et al., 2015)) but they have hardly been generalized for global and regional scale inversions until now, and such developments usually aim to tackle problems that are common to all GHGs. The same applies to the assimilation of satellite observations (see Section 7.2).

This project has received funding from the European Union's Horizon Europe research and innovation programme under grant agreement No 101081395

3.6. Configuration of the prior and observation error covariances

The characterization of the prior error covariances for land ecosystem fluxes usually follows two types of approaches. They are often derived from a general knowledge of the uncertainties associated to the ecosystem models used to provide the prior flux estimates. Alternatively, it is often based on commonly accepted levels of uncertainties on the large-scale estimate of the land carbon sink, which are then disaggregated in space and time. In both cases, standard assumptions are usually made on the error spatial and temporal correlations. Specific studies with the comparisons between ecosystem model simulations and eddy covariance flux measurements (or products based on the upscaling of these measurements) have allowed for improving the characterization of the level of uncertainties at different spatial and temporal scales, and of the typical temporal and spatial correlations of uncertainties as a function of the spatial and temporal resolution (Chevallier et al., 2012; Kountouris et al., 2015; Visser and Bousserez, 2024), but in general the modelling of the prior error covariance matrices remains relatively simple.

At the spatial and temporal resolution of the control variables, the most usual principle remains to define an uncertainty that is somehow proportional to the corresponding flux, but since NEE can be positive or negative, and since a small NEE could actually reflect a balance between high NPP and $R_{h,eco}$, the prior uncertainty, whether the inversion controls NEE or its subcomponent, is generally defined as proportional to one of the gross fluxes: $R_{h,eco}$, GPP, or NPP (Broquet et al., 2011; Monteil et al., 2020) .

The spatial and temporal correlations of the uncertainties in the prior estimate of the land carbon fluxes from process-based or statistical models arise from model structural errors (missing processes, wrong process representation etc.), which follow the spatial distribution of the different types of ecosystems, from the meteorological forcing (typically at synoptic scales) etc. Therefore, they likely bear complex and anisotropic structures, e.g. including potential negative correlations between the NEE in summer and the NEE in the dormant season (Broquet et al., 2013). However, in practice, the derivation of the spatial and temporal correlations usually follows simple models, which are isotropic and homogeneous in space and time, typically exponentially decaying functions (Chevallier et al., 2012), to facilitate the construction of valid (i.e., symmetric positive definite) error correlation matrices with diagonal values of 1, and elsewhere values between -1 and 1. New capabilities in terms of prior error covariance modelling and in terms of comparisons to independent data now allow for envisaging varying the spatial and temporal correlation length scales as a function of time and space (Visser and Bousserez, 2024). Importantly, the temporal correlations of the uncertainty in prior estimate of the NEE can be assumed to have relatively long temporal scales (the typical scale of 1 month is generally used, which, combined with exponentially decaying functions leads to a correlation of e^{-1} for a 1 month time lag) for a given window of the day but to be low across different windows of the day, due to the uncertainties in the diurnal cycle. Specific models of the prior uncertainties for NEE, therefore, split the temporal dimension into that of the sub-diurnal variations and day-to-day variations, with small correlation length scale for the former, and larger ones for the latter (Broquet et al.,

This project has received funding from the European Union's Horizon Europe research and innovation programme under grant agreement No 101081395

2013). In general, in 10 to 100 km resolution inversions, the typical correlation length scales for the prior uncertainties in NEE range from 100 to 500 km (Crowell et al., 2019; Monteil et al., 2020). The increasing accuracy of the ecosystem models, and resolution of inversion systems should lead to a decrease of these typical spatial and temporal scales of uncertainty (Chevallier et al., 2012).

The configuration of the prior uncertainties for the ocean fluxes generally assumes relatively small and homogeneous uncertainties at the control resolution, and very large spatial and temporal correlation scales (Crowell et al., 2019). However, this should probably be reconsidered to better account for the impact of uncertainties in the relatively strong and localized coastal fluxes.

Even though the impact of uncertainties in the boundary conditions has received increasing attention, the characterization of the prior uncertainties for these conditions when they are controlled remain quite notional and based on general considerations about the amplitude and scales of the uncertainties in the CO_2 global simulations used as prior estimates (Broquet et al., 2026). These uncertainties should be more systematically extracted from the analysis conducted over the CO_2 global simulations and inversions.

The configuration of the observation error covariances (to characterize the uncertainties in the observation operator and the observations themselves) do not rely on specific approaches in the field of the CO_2 atmospheric inversions. Efforts have been made to characterize the separate impact of uncertainties in the CO_2 fossil emissions in addition to that of the boundary conditions (when they are not controlled by the inversion) and of the model limited accuracy and resolution as a function of time and observation conditions (Berchet et al., 2023; Broquet et al., 2011, 2013). New efforts could focus on the land flux subcomponents that are kept fixed in the inversion framework (such as emissions from BB, rivers and harvested products).

4. CH_4 inversions

Aki Tsuruta, Anteneh Mengistu, Rebecca Ward, and Rona Thompson

4.1. Prior fluxes and consideration of sectors to be optimized

The prior methane fluxes provide first-guess representations of the spatial, temporal, and sectoral distribution of fluxes for use in atmospheric inversion systems. The prior fluxes should ensure complete source coverage, and, when coupled to atmospheric transport models, generate realistic mole fractions that can be compared to observations. Methane fluxes arise from a wide range of anthropogenic and natural processes, each governed by distinct physical drivers and exhibit differing spatial and temporal variability.

For anthropogenic sources, prior CH_4 fluxes are typically derived from disaggregated emission inventories (see Table 4.1), or national inventories. National inventories usually provide emissions as aggregated country-level totals. For use in atmospheric transport models, these emissions must be spatially disaggregated to the model grid using appropriate proxies (e.g., population density, activity data, and infrastructure mapping).

This project has received funding from the European Union's Horizon Europe research and innovation programme under grant agreement No 101081395

Table 4.1. Datasets and models used to construct prior CH_4 fluxes

Source category	Dataset / Model	Description	Reference
Anthropogenic emissions	EDGAR	Global gridded anthropogenic CH_4 emissions by sector	(Crippa et al., 2020)
	GAINS	Global/regional emissions based on activity data	(Höglund-Isaksson et al., 2020)
	CEDS	Harmonized global anthropogenic emissions	(Hoesly et al., 2017)
	CAMS-REG	Regional gridded emissions for Europe	(Kuenen et al., 2022)
	National inventories (NGHGIs)	Country-level reported totals; require spatial disaggregation	UNFCCC 2023 reports
Wetlands	JSBACH–HIMMELI	Process-based wetland CH_4 model	(Raivonen et al., 2017)
	ORCHIDEE	DGVM with wetland CH_4 module	(Krinner et al., 2005)
	LPJ-GUESS	DGVM with CH_4 wetland processes	(Smith et al., 2014)
	LPJ-wsl	DGVM with land use and land cover change and forest demography	(Calle and Poulter, 2021)
	CLM4.5/CLM5	Land component of the Community Earth System Model	(Lawrence et al., 2019)
	WetCHARTs	Ensemble wetland CH_4 emission dataset	(Bloom et al., 2017)
Biomass burning	GFAS	Satellite-based fire emission dataset	(Kaiser et al., 2012)
	GFED	Global fire emissions database	(van der Werf et al., 2017)
Others	Geological emissions	Global geological methane seepage	(Etiope et al., 2019)
	Ocean–atmosphere fluxes	Marine methane emissions	(Weber et al., 2019)
	Termites	Biogenic methane emissions from termites	(Saunois et al., 2020)
	Inland water	Fresh water emission from rivers and lakes	(Johnson et al., 2022)

In addition to these anthropogenic sources, prior methane fluxes also need to account for natural emissions. Process-based models are commonly used to prescribe natural CH_4 fluxes from wetlands (see Table 4.1). Emissions from biomass burning are typically taken from fire emission datasets such as GFAS (Kaiser et al., 2012) or GFED (Werf et al., 2025). Additional natural source terms are frequently included based on estimates from

This project has received funding from the European Union's Horizon Europe research and innovation programme under grant agreement No 101081395

empirical studies, such as geological emissions (Etiope et al., 2019) , ocean–atmosphere methane fluxes (Weber et al., 2019) and emissions from termites (Saunois et al., 2020) (see Table 4.1).

To enable meaningful comparisons with national inventories and to support monitoring of emissions, priors must distinguish all major anthropogenic methane sources: agriculture (enteric fermentation, rice cultivation and manure management), fossil fuel production and use (coal, oil, and natural gas), waste and wastewater management, combustion-related emissions from residential, industrial, and transport energy use, and industrial processes. Natural methane sources include wetlands (often grouped together as peatlands, inundated and wet soil emissions), inland waters, termites, ocean fluxes, geological seepage, mineral soil uptake, and biomass burning. It should be noted, however, that the distinction between natural and anthropogenic methane sources is not always clear-cut, as several sources traditionally classified as natural can be indirectly influenced by human activities and climate change (e.g., wetlands, inland waters, reservoirs, permafrost, and biomass burning). (Saunois et al., 2025), therefore, distinguish *direct anthropogenic* from *natural and indirect anthropogenic* sources rather than treating the separation as absolute.

Within this framework of comprehensive source representation, estimates of total methane emissions provide an important consistency check on the aggregated prior fluxes. For the 2010–2019 period, global methane emissions estimated using bottom-up methods are approximately 669 Tg CH_4 yr^{-1}, with a range of 512–849 Tg CH_4 yr^{-1} (Saunois et al., 2025). When aggregating prior CH_4 fluxes, care must be taken to avoid double counting. For example, biomass burning emissions from agricultural fires may already be included in agricultural source categories (Kirschke et al., 2013; Saunois et al., 2020) . Another example is the possible overlap of ocean fluxes and ocean geological seeps – the estimates of which are often given by different models and approaches. Although in principle including both estimates would represent a double counting, in practice some approaches may miss certain components of the flux, which may be better represented in a different dataset using a different approach. Thus, when considering if two different datasets overlap, and if so, to what extent (e.g. ocean fluxes and ocean geological seeps) a more thorough investigation of the approaches and what they cover is needed.

In atmospheric inversions, the total net CH_4 flux is commonly optimized, as has been frequently done in the past, e.g. (Bergamaschi et al., 2007; Maasakkers et al., 2019; Saunois et al., 2020) . However, many studies have also optimized fluxes by groups of source categories e.g. (Chen et al., 2022; Mengistu et al., 2026; Tenkanen et al., 2024) , in particular, separating natural from anthropogenic sources provides more pertinent information for monitoring emissions, evaluating inventories, and supporting policy decisions. Although the diverse sources could be grouped in various ways, a useful inversion set-up for policy purposes requires defining source sectors that can be compared with aggregates of sectors as reported by national greenhouse gas inventories (i.e. IPCC sectors). A further consideration in defining source categories to use in the control vector, is whether or not isotopic data (such as the *isotopologue* $^{13}CH_4$) are included in the inversion (Basu et al., 2022b). If so, then the categories need to be aligned with the characteristic *source signatures* of the isotopologues (see Section 4.5).

This project has received funding from the European Union's Horizon Europe research and innovation programme under grant agreement No 101081395

A key factor in defining prior CH_4 fluxes and inversion control variables is the pronounced source-dependent variability of CH_4 emissions in both space and time. This variability shapes the observed atmospheric CH_4 signals and should, as far as possible, be reflected in process-based models and inventories. Different source sectors exhibit distinct temporal characteristics. Wetland emissions vary strongly on seasonal and inter-annual time scales in response to climate drivers such as temperature, precipitation, and inundation extent (Bloom et al., 2017; Saunois et al., 2020). Fossil fuel emissions often show relatively stable spatial patterns but can experience large short-term fluctuations driven by episodic leaks and super-emitter events that are poorly captured by inventories (Alvarez et al., 2018; Scarpelli et al., 2020). Biomass burning is particularly irregular, characterised by short-lived but intense emission pulses with limited spatial extent (Kaiser et al., 2012; Werf et al., 2017).

The spatial and temporal resolution of prior CH_4 fluxes should be aligned with the resolution of the atmospheric transport model, as this consistency underpins the ability of the model to represent the observations and, hence, for the inversion to extract meaningful information from the observation-model comparison. Although prior emissions may be specified at fine spatial scales (e.g. the EDGAR inventory provides global emission estimates at 0.1°), the inversions (especially global ones) typically have coarser resolution owing to limitations in the resolution of the atmospheric transport model, and the limited observational coverage, which does not allow the fluxes to be resolved at high spatial (and temporal) resolutions. If the control variables (i.e. those representing fluxes) are at coarser resolution than the transport model and are defined in such a way that there is in reality significant variability within the spatial and/or temporal domain of each variable, this can lead to aggregation error, as is discussed in Section 2.3.1.2 and in (Berchet et al., 2013; Bocquet et al., 2011; Kaminski et al., 2001) .

Depending on the study objectives and the available observational constraints, the control variables for fluxes can be defined to either optimise the total CH_4 source or to optimise by source sector. Optimising the total source reduces the number of degrees of freedom (DOF), where the DOF represents the number of elements estimated to obtain a comprehensive understanding of the system and is, therefore, appropriate when the primary objective is to quantify the total CH_4 budget. In contrast, sector-specific optimisation is especially relevant for CH_4 because of its strong relevance to emissions monitoring and policy decisions. Owing to the distinct spatial and temporal characteristics of some source sectors, such as wetlands versus fossil fuel emissions there can be some observational constraint on the sources by sector (Jacob et al., 2016) . If this temporal and spatial variability is not adequately represented in prior fluxes or in the definition of the control variables, aggregation errors may arise, weakening the inversion's ability to correctly attribute observed atmospheric signals to individual sources.

In practice, constraints on computational cost and the size of the control vector, especially in ensemble-based inversions, often necessitate grouping source categories, such as combining oil and gas emissions or grouping waste sources. When doing so, similarities in temporal variability and spatial patterns should be considered to preserve interpretability and reduce aggregation errors (Jacob et al., 2016). This issue is especially critical when emissions are estimated at coarse temporal or spatial resolution, or when sectors with fundamentally different variabilities are grouped together. Biomass burning

This project has received funding from the European Union's Horizon Europe research and innovation programme under grant agreement No 101081395

and fossil fuel methane emissions are particularly challenging in this regard. Their sporadic nature and incomplete representation in bottom-up inventories contribute to large prior uncertainties and limit the ability of inversions to capture their true variability (Alvarez et al., 2018; Saunois et al., 2020). Notably, unlike for CO_2, fossil fuel CH_4 emissions are considered highly uncertain reflecting the incomplete representation of leaks and episodic emissions in many bottom-up inventories (Alvarez et al., 2018; Scarpelli et al., 2020). For this reason, CH_4 fossil fuel emissions are often optimized as a distinct category.

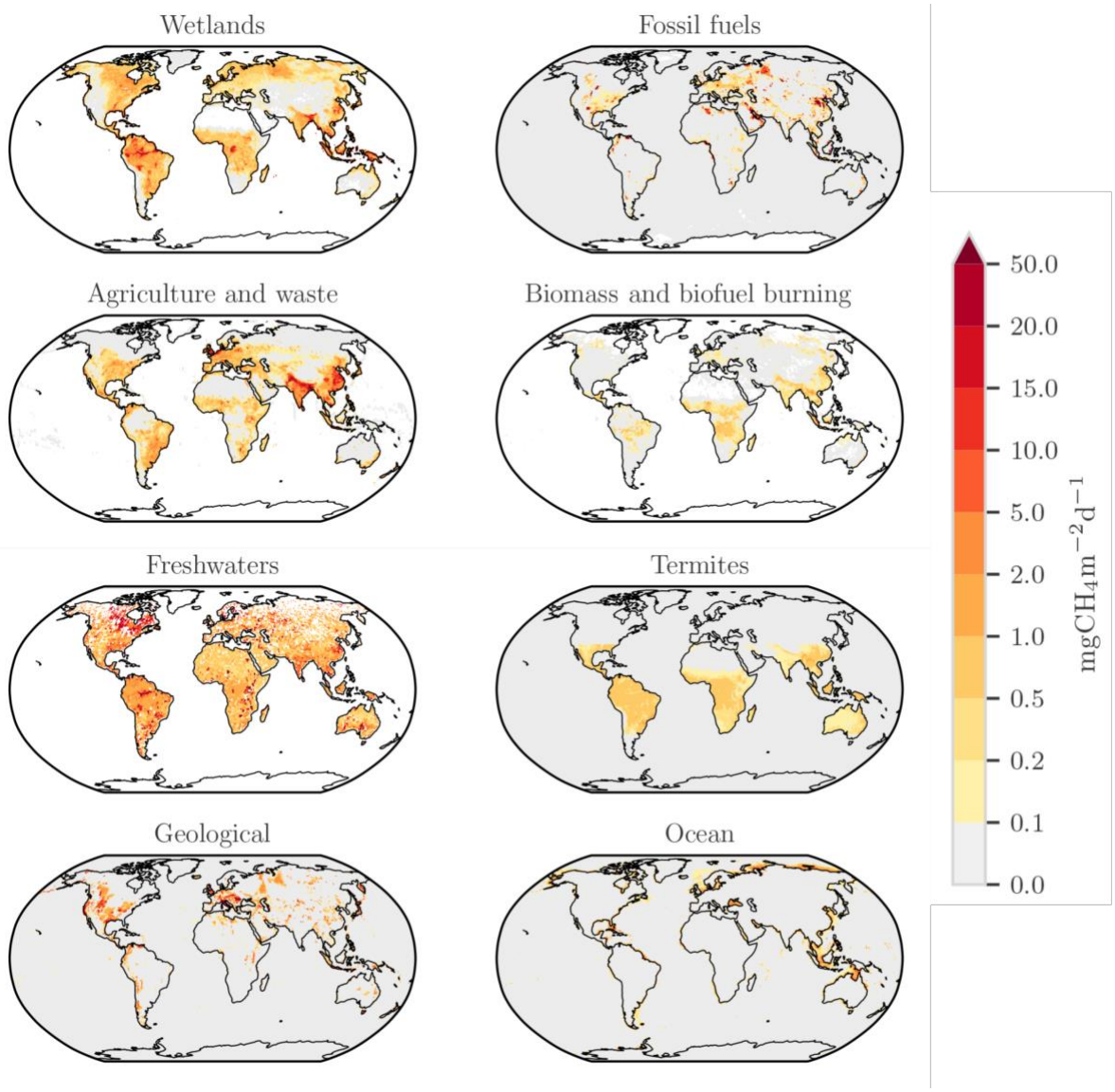


Figure 4.1. Methane emissions from eight source categories taken from biogeochemical models and inventories: natural wetlands (excluding lakes, ponds, and rivers), biomass and biofuel burning, agriculture and waste, fossil fuels, inland freshwaters (including lakes, ponds, reservoirs and stream and rivers), geological sources, termites, and oceans for the 2010–2019 decade (in mg CH_4 m^{-2} d^{-1}). (Figure courtesy of Saunois et al., 2025)

4.2. Boundary and initial mixing ratios

Boundary and initial mixing ratios are a key element in inversions. The initial mixing ratios define the initial mass of trace gases in the domain of interest at the beginning of the inversion window. For regional inversions, boundary conditions drive the mass of CH_4

This project has received funding from the European Union's Horizon Europe research and innovation programme under grant agreement No 101081395

entering the domain (at the domain lateral boundaries, as well as from the roof of the domain in case of limited-vertical-extent transport models), as well as the evolution of CH_4 mixing ratio within the domain. In regional inversions, the contribution to the variability in the observed mixing ratios from outside the inversion domain may be significant and, in some cases, may be comparable to the magnitude of the variability from in-domain fluxes (e.g., Lauvaux et al., 2012; Lauvaux et al., 2016; Nesser et al., 2025).

Boundary and initial mixing ratios may be prescribed using CH_4 mixing-ratio fields output from a global atmospheric transport model (see Table 4.2), ideally optimized using global satellite or in situ observations (e.g., Agusti-Panareda et al., 2023; Groot-Zwaaftink et al., 2018). These models provide spatially and temporally resolved CH_4 fields that capture seasonal and inter-annual variations and are constrained through the assimilation of atmospheric observations. These fields can be coupled to the regional domain spatial and temporal boundaries to ensure consistency between the rest of the global atmosphere and the regional flux optimisation. Global reference simulations should be properly set-up to limit the propagation of uncertainties to regional inversions. One key aspect to account for is adequate spin-up periods in the global model to limit the impact of improperly specified global initial conditions (Gurney, 2002; Peters et al., 2005; Thanwerdas et al., 2024). In general, global inversions should ensure that the spin-up period (usually several years) leads to a realistic horizontal and vertical distribution of CH_4 mixing ratio.

Even properly prescribed global inversions diverge in their simulated mixing ratio fields (Saunois et al., 2025), which when used as initial/boundary conditions for regional inversions can lead to discrepancies. Since any errors in the boundary/initial mixing ratios will distort surface flux adjustments (Rödenbeck et al., 2009) it is crucial to carefully assess the accuracy of these mixing ratios and ideally include variables to optimize these in the control vector (see also Section 2.3.2). Two main approaches are used in the community to deal with boundary conditions: i) the so-called “two-step” approach by Rödenbeck et al. (2009), and ii) the direct optimization of boundary conditions. The Rödenbeck et al. (2009) approach has already been described in Section 2.3.2. The direct optimization of boundary conditions can be done in different ways, mostly depending if a Lagrangian or Eulerian transport model is used and its domain of coverage.

In Lagrangian frameworks, the influence of the outside-domain mixing ratios on the observations may be estimated using the end points of the backward trajectories. Thompson et al. (2017) used backwards trajectories calculated globally (over 10 days) and coupled their end points to global mixing ratios fields representing a coupling in the time domain. This allows for a smooth integration of the influence of initial mixing ratios, as well as fluxes outside the regional domain, into a background mixing ratio estimate for each observation. Longer backward trajectories of 30 to 60 days are now routinely used to fully account for the hemispheric transport of background air masses (e.g., Vojta et al., 2025). For regional Eulerian models, the initial mixing ratios determine the atmospheric CH_4 field at the beginning of a simulation. Similarly to Lagrangian models, initial conditions can be retrieved by interpolated global models. Boundary conditions to regional Eulerian models include background mixing ratios at the top and sides of the domain of simulation (e.g., Fortems-Cheiney et al., 2021).

This project has received funding from the European Union’s Horizon Europe research and innovation programme under grant agreement No 101081395

Table 4.2: Examples of global model products of CH_4 mixing ratio

Product/Model	Model Type	Spatial/ Temporal Resolution	Data Assimilation/ Inversion	Meteo-rological Forcing	Reference
CAMS EGG4	Reanalysis (global CTM)	0.75° × 0.75°, 3-hourly	4D-Var assimilation of satellite & in-situ observation	ECMWF IFS	(Inness et al., 2019)
CAMS TM5-4DVar	Flux inversion system	1° × 1°, monthly fluxes	4D-Var inversion of surface & satellite	ECMWF ERA-Interim / ERA5	(Pandey et al., 2022)
FLEXPART CTM (now FLEXPART LCM)	Lagrangian particle dispersion model	Depends on setup	Transport only, not inversion	ERA5 / ECMWF	(Zwaaftink et al., 2018)
NOAA CarbonTracker	Inversion (EnKF with TM5)	3° × 2° global (nested regional ~1°) ; 3-hourly / 30-min met fields	Ensemble Kalman Filter inversion	ECMWF processed meteorology	(Carbon-Tracker CH4 2025)
MOZART-4 /GEOS-5	Chemistry-transport model	1.9° × 2.5°, hourly–daily	CTM forward simulation	NASA GEOS-5	(Emmons et al., 2010)
GEOS-Chem CH_4 fields	3D CTM	2° × 2.5°, 72 levels	Forward CTM simulation (used as observation operator in inversions)	NASA GEOS (e.g., GEOS-FP, MERRA-2) Goddard Earth Observing System	(Bindle et al., 2021)

The structure and uncertainties assigned to variables used to optimize the initial or background CH_4 mixing ratios needs to be carefully considered to avoid trade-off with surface flux adjustments. Regarding the structure of the control variables, the objective is to leave sufficient degrees of freedom to adjust the atmospheric signal entering the domain of interest, while limiting the inflation in the number of unknown variables to be optimized. Optimizing the global dataset used for boundary and/or initial conditions at grid cell resolution would dramatically increase the number of unknowns and lead to ill-posed problems, so is typically not practical. To limit this issue, previous studies usually optimize scalars for aggregates of the background/initial conditions. For the boundary conditions of Eulerian models, the aggregation can be by boundary side or sections of boundaries of the regional domain (e.g., Steiner et al., 2024a; Sicsik-Paré et al., 2025). Likewise, for the initial mixing ratios, these can be optimized as aggregated regions, either for the total column, or with some vertical resolution (e.g. lower troposphere, upper troposphere and stratosphere). Aggregation should also be made in the temporal dimension to limit the number of control variables related to the optimization of the boundary conditions while keeping sufficient degrees of freedom to adjust large-scale

This project has received funding from the European Union's Horizon Europe research and innovation programme under grant agreement No 101081395

discrepancies. Daily to weekly adjustments are usually done to allow for synoptic scale adjustments to background conditions. For Lagrangian models, Thompson et al., (2017) optimized the initial mixing ratios (coupled to the trajectory endpoints) by aggregating these into latitudinal bands, and later also vertical layers (Thompson et al., 2025) with a temporal resolution in the order of weekly to monthly.

Regarding uncertainties, proper balance between flux and boundary/initial errors are critical to avoid under- or over-correction of the boundary/initial conditions. Too small uncertainties will lead to over-correction to the fluxes whereas too large uncertainties in the boundary/initial conditions may lead to too much attribution of model-observation mismatches to the background (see also Sections 6.2 and 8.5.2). Approaches for specifying the prior error covariance matrix **B** include objective diagnostics based on innovation statistics, tuning of spatial and temporal correlation structures according to transport characteristics, and deriving variability estimates from ensembles of prior states. They are not specific to background optimization but can serve this purpose. They include χ^2 diagnostics, Desroziers schemes (Desroziers et al., 2005), maximum-likelihood optimization (Berchet et al., 2013) or hyper-parameter optimization (Berchet et al., 2015; Ganesan et al., 2015) (see also Section 2.5).

4.3. Uncertainties associated with fluxes

Despite their detailed sectoral representation, bottom-up estimates of CH_4 fluxes remain subject to substantial uncertainties arising from incomplete process understanding, sparse or incomplete activity data, and limited representation of episodic or poorly monitored sources, e.g. in emission factors, leading to inconsistencies across inventories and spatial scales.

Prior uncertainties define the variances (diagonal elements) of **B** corresponding to the control variables targeted in the optimization. The control variables in an inversion can take different forms, such as the fluxes themselves, scaling factors applied to the prior fluxes and offsets from a prior flux field. As such, there is not a single 'correct' way to assign the variances, but the square root of the variance needs to be in the same units as the corresponding control variable. Prior uncertainties for CH_4 fluxes may be prescribed based on expert knowledge, previous studies or inventory-provided estimates, or combination of these. They can be defined as a fraction of the prior flux (e.g. Bergamaschi et al., 2013; Tsuruta et al., 2017) , based on the differences between alternative prior flux estimates (e.g. Tenkanen et al., 2024) or derived from bottom-up assessments of inventories or process-model errors (e.g. Niwa et al., 2025). When the different CH_4 source sectors (see also Section 4.1) are optimised separately, sector-specific uncertainty values need to be applied.

For fluxes from wetlands, inland waters, and soil sinks derived from process-based models, prior uncertainties are typically large. These uncertainties reflect current limitations of the models, including missing or poorly represented processes, uncertain parameterizations, and errors in wetland and inland water surface area and inundation dynamics. Large uncertainty values give the inversion sufficient freedom to adjust both the magnitude and spatial distribution of emissions. For example, Bergamaschi et al., (2013) applied uncertainties of 100% of the prior wetland fluxes and (Bloom et al., 2017) found large uncertainties (approximately 100% of the fluxes) across all regions in the WetCHARTs model ensemble. More recently, process-based models are providing

This project has received funding from the European Union's Horizon Europe research and innovation programme under grant agreement No 101081395

their own uncertainty estimates, for example through ensembles of model configurations using different wetland extent maps and parameter perturbations (Aalto et al., 2026) . Tenkanen et al., (2025) applied spatially and temporally varying wetland prior uncertainties derived from the inter-quartile range of a 6-model ensemble in the framework of the Global Carbon Project, capped between 10% and 500%. Even when large errors are used for wetland emissions, it is good practice to test alternative prior flux estimates in sensitivity experiments.

Uncertainties in anthropogenic prior fluxes are generally smaller than those for wetland process models, reflecting the use of bottom-up inventories with activity data and spatial attribution (e.g. oil and gas infrastructure, urban areas, landfills). Inventory developers have produced uncertainty assessments, providing guidance for the interpretation and appropriate use of their data, e.g. EDGAR (Solazzo et al., 2021), GAINS (Winiwarter et al., 2024) and CAMS-REG (Super et al., 2026). Significant differences can be found across anthropogenic CH_4 emission estimates, reflecting key methodological choices, such as use of Tier 1 methods, which use default values for emissions factors and global datasets (used often in global estimates such as EDGAR) and Tiers 2 and 3, which use national emissions values and/or models (Lamb et al., 2025) . Uncertainties are generally smaller for fugituve emissions due to well-reported activity data, but missing ultra-emitters in bottom-up inventories can increase regional uncertainty in regions of extensive of fossil fuel extraction (Tibrewal et al., 2024). When anthropogenic emissions are optimised as a single aggregated source, a key choice is whether to use a more conservative uncertainty reflecting the most uncertain sub-sector, or a weighted uncertainty that reflects the combination of uncertainties.

Biomass burning priors can be expected to have moderate uncertainties. Errors are driven by multiple sources, including uncertainties in burned area detection, fuel consumption and emission factors (Kaiser et al., 2012; Van der Werf et al. 2017). Small fires that occur below the detection limits of satellite products such as MODIS lead to an underestimation of burned area and, therefore, emissions. Advances in higher resolution products are expected to reduce uncertainties in future inventories. Fuel consumption (dependent on vegetation type and density, moisture, fire type and combustion completeness) and emission factors, are limited by sparse and unrepresentative field observations, which are biome-specific and extrapolated globally, introducing further uncertainties.

Fluxes from geological seepage are poorly constrained with sparse observational data and incomplete or unknown seep locations and magnitudes, and large uncertainties associated with scaling-up the few observations available to regional and global estimates (Etiope et al., 2019). Furthermore, independent studies using ice-core CH_4 isotopes have indicated that pre-industrial geological methane emissions were small, ~15 Tg/y (Petrenko et al., 2017) . As geological emissions should be roughly constant over time, this implies that present-day inventories could be strongly overestimated (Hmiel et al., 2020; Petrenko et al., 2017). Thus, geological seep emissions are commonly given large uncertainties and/or scaled to match global top-down estimates.

The off-diagonal elements of **B** describe spatial and temporal correlations in prior flux uncertainties. These represent assumptions about the spatial and temporal coherence of prior errors across neighbouring grid-cells and/or regions and must be specified according to the resolution and definition of corresponding control variables. Temporal

This project has received funding from the European Union's Horizon Europe research and innovation programme under grant agreement No 101081395

correlations should also be included in **B** (when the inversion extends over more than one time step) to represent the persistence of prior flux errors between consecutive time steps, dependent on the temporal resolution of the inversion.

A spatial correlation length is the distance over which errors in two locations are assumed to be related in **B.** They are typically defined using distance-based functions, such as exponential decay with distance, e.g. (Peters et al., 2005). For high-resolution regional inversions with dense station networks, such as over Europe, short spatial correlation lengths are appropriate over land, e.g. 50 km (Henne et al., 2016). Inversions with coarser grids or region-based control variables typically use longer spatial correlation lengths over land e.g. 100 km – 500 km (Tenkanen et al., 2024; Thompson et al., 2017; Wittig et al., 2023). Oceanic source regions typically show lower flux magnitudes and lower short-term variability than many land sources. For this reason, relatively long spatial correlation lengths are used over oceans regardless of the observing network, e.g. 1000 km – 2000 km (Tenkanen et al., 2025; Thompson et al., 2017). It has previously been common to not use separate spatial and temporal correlations by source sector, as with the above studies. However, it is recommended to use different spatial and temporal correlations for different source sectors to better constrain the sources using independent information on the expected error correlations in each sector (Szénási et al., 2021) . Table 4.3 provides examples of methane inversion studies that use source-specific spatial and temporal correlations.

Errors in wetland emissions are often assumed to be spatially coherent on the scale of basins and continents (Bloom et al., 2017). Alternatively, Monteil et al. (2025) derived spatial correlation lengths from ensembles of the LPJ-GUESS models, finding low correlations above 250 km and Niwa et al. (2025) directly built the prior error covariance matrix, **B**, from an ensemble of VISIT simulations. Meirink et al. (2008) and Bergamaschi et al. (2022) applied zero temporal correlation to wetlands and other strongly seasonally varying sources (such as rice cultivation and biomass burning) as emissions from these categories vary strongly in time. However, Bloom et al. (2017) show that wetlands have strongly temporally correlated prior errors, despite strong seasonal emission variability, based on uncertainties in carbon decomposition rates and the wetland extent between different wetland models. Whilst Monteil et al. (2025) found low temporal correlations (<0.4 after 200 days) in their ensemble.

Anthropogenic emissions from inventories may have systematic biases; the temporal persistence depends on source type, from relatively short-term for fugitive emissions (e.g. leaks in gas installations) to more seasonal for microbial sources such as agriculture and waste. Due to the episodic and localised nature of biomass burning events (van der Werf et al., 2025), relatively short spatial and temporal correlation lengths are appropriate. As a poorly constrained source, geological seepage uncertainties are associated with large sedimentary basins, incomplete inventories and limited observations (Etiope et al., 2019), longer spatial and temporal correlation lengths are appropriate. Thus far, the discussion has focused on inversions with a fixed prior error covariance structure. However, there is no uniquely optimal choice for the prior error covariance matrix. For CH_4, methods such as hierarchical Bayesian inversions infer prior uncertainty probability distribution functions (PDFs) and model error jointly with emissions, while other approaches have used an ensemble of prior PDFs and inversion setups to define posterior uncertainty (East et al., 2025).

This project has received funding from the European Union's Horizon Europe research and innovation programme under grant agreement No 101081395

Table 4.3: Example prior uncertainties, spatial correlation lengths and temporal correlation lengths used in methane inversion studies that apply different correlation lengths to different sources.

Study	Inversion description	Separately optimised sources	Prior uncertainties	Spatial correlation lengths	Temporal correlation lengths
(Niwa et al., 2025)	Global 4D-Var inversion using NISMON-CH_4.	Anthropogenic, biomass burning, wetlands (incl. rice cultivation, soil uptake), other natural.	Wetlands from ensemble of process-model (VISIT) simulations. Percentages of prior fluxes. 50% for anthropogenic, 100% for biomass burning and other natural.	Ensemble-derived covariances from the VISIT process model used directly to construct **B**. No spatial correlation for other sources.	No temporal correlations.
(Meirink et al., 2008)	Global 4D-Var inversion, 6°×4° (with higher resolution zoom regions) spatial and monthly temporal resolution.	11 different source categories.	Percentages of prior fluxes. Enteric fermentation 30%, wetlands and biomass burning 80%, other categories 50%.	500 km for all categories.	9.5 months for all categories except wetlands, rice cultivation and biomass burning, with temporal correlation of 0.
(Bergamaschi et al., 2022)	Regional European CH_4 4D-Var inversion using FLEXVAR. 7km x 7km spatial and monthly temporal resolution.	Wetlands, rice, biomass burning, all remaining sources.	Percentages of prior fluxes. For all sources uncertainties set to 100%.	For all sources 200 km.	12 months for "all remaining sources", zero for other sources with pronounced seasonal cycles.
(McNorton et al., 2018)	Global inversion using TOMCAT. 2.8°×2.8° spatial and monthly temporal resolution.	Agriculture, biomass burning, energy, Rice, waste, wetlands	Percentages of prior fluxes. All sources set to 50%.	No spatial correlation.	1-month lag, 0.5 for energy sector. Zero for other sources.
(Monteil et al., 2025)	Regional northern Europe inversion using LUMIA. 0.25° spatial and daily temporal resolution.	Two "super-categories": wetlands and non-wetlands.	Wetlands: derived from LPJ-GUESS process-model ensemble spread multiplied by annual scaling factor of 0.5 Tg CH_4/yr. Non-wetlands: annual scaling factor of 5 Tg CH_4/yr (≈15 % of the annual emissions)	Wetlands: uses average correlation lengths of LPJ-GUESS ensemble spread. Non-wetlands: 500 km.	Both categories: 30 days.

This project has received funding from the European Union's Horizon Europe research and innovation programme under grant agreement No 101081395

4.4. Atmospheric sinks

About 90% of CH_4 in the atmosphere is lost due to oxidation by the hydroxyl radical (OH). The atmospheric sink due to this chemical reaction mostly occurs in the troposphere, removing around 503–554 Tg yr^{-1} globally (Saunois et al., 2025). Therefore, one must account for the atmospheric sink in regional and global inverse modelling of CH_4 fluxes. However, the effect of the atmospheric sink decreases with shorter time and smaller spatial scales of the model transport operator, and it could even be ignored for very short-temporal (hours to a few days) and local (up to a few hundreds of kilometres) operators. In those cases, the atmospheric removal should be taken into account in the background estimates or boundary conditions.

There are also other atmospheric sinks that are important to take into account, namely that due to the oxygen radical, $O(^1D)$, and the chlorine radical, Cl, in the stratosphere, and the reaction with Cl in the marine boundary layer. Globally, it is estimated that the stratospheric loss accounts for about 4-7% of the total chemical loss removing 28–43 Tg yr^{-1} globally (Saunois et al., 2025). These losses can play an important role especially when assimilating and comparing the estimates to satellite data or data from the stratosphere, because they strongly affect the vertical profiles and stratospheric seasonal cycles of the estimated CH_4. Although the effects may be minor for regional models assimilating only ground-based observations, the effects must be taken into account in the background estimates or boundary conditions, as for OH. The contribution of tropospheric Cl to the total CH_4 sink is minor (only 1-2 %, Saunois et al., 2025) but produces strong isotopic fractionation which can have a significant effect when assimilating isotopic data (see Section 4.5).

Chemical reactions can be included in the atmospheric transport model either by using prescribed fields (precalculated from a chemistry model) e.g. (Bergamaschi et al., 2005; Thompson et al., 2017; Tsuruta et al., 2025; Ward et al., 2024; Zhao et al., 2019) or by calculating the reactions including production and losses of OH within the model (e.g. CAMS v24r2 onwards[6]). The former is more straight-forward and easier to implement but ignores possible non-linearities, while the latter requires a chemistry transport model, which is more computationally expensive.

There are varying estimates of atmospheric OH concentrations and reaction rates of CH_4 and OH (Zhao et al. 2019; see also Table 4.4). OH is a radical that is inherently instable and thus extremely reactive. Measurements are not spatially representative, therefore, approximations and modelling are needed for estimation of global atmospheric OH. The different approaches include empirical approaches inferring OH concentrations based on other species such as methyl chloroform (CH_3CCl_3) e.g. (Montzka et al., 2011; Patra et al., 2021b; Prinn et al., 2005) , hydrofluorocarbons (HFCs) (Liang et al., 2017; Thompson et al., 2023) and ^{14}CO (Krol et al., 2008; Quay et al., 2000) , modelling using atmospheric chemistry transport models e.g. (Anderson et al., 2021; He et al., 2021; Lelieveld et al., 2016; Nicely et al., 2017; Voulgarakis et al., 2013) and data assimilation (Naus et al., 2021) . The OH estimates can vary significantly in horizontal, vertical and

6 https://confluence.ecmwf.int/display/CKB/Description+of+the+CH4+inversion+production+chain#DescriptionoftheCH4inversionproductionchain-Atmosphericlossrates

This project has received funding from the European Union's Horizon Europe research and innovation programme under grant agreement No 101081395

temporal dimensions (Zhao et al., 2019), and as a result, the estimated atmospheric CH_4 and, thus posterior fluxes, can differ for different OH estimates even if one uses the same transport model (Zhao et al., 2020) . This effect can be seen already in the forward model, so it is strongly recommended to test first the forward run and see if the growth rate and seasonal cycle of atmospheric CH_4 roughly matches the observations. It is strongly recommended to include at least seasonally varying OH concentrations, and for multi-year inversions, annual variations can also be included (Saunois et al., 2025). Similarly, monthly varying concentrations (either climatological or also including annual variations) are recommended for reactions with Cl and $O(^1D)$.

It is possible to include parameters to optimize the atmospheric sinks in the control vector. When optimizing them simultaneously with the fluxes and the effect of methane levels themselves on sinks are considered, it makes the inversion problem non-linear. Therefore, some inversion methods cannot be used, but the quasi-Newton method (Section 2.4.3.2) or ensemble methods (Section 2.4.4) remain to handle not strongly non-linearly problems. Although, since most observations are most sensitive to the lower troposphere (especially ground-based observations), their constraint on the sink may be limited and, therefore, a balance is needed so that there is not a trade-off between correcting the atmospheric sinks versus the fluxes (Maasakkers et al., 2019; Peng et al., 2022; Qu et al., 2024) .

Table 4.4: Examples of global datasets for OH, Cl, and $O(^1D)$.

Gas	Data type	Model	References
OH	Concentrations	CAMS	https://confluence.ecmwf.int/display/CKB/Description+of+the+CH4+inversion+production+chain
	Concentrations		(Huijnen et al., 2010; Spivakovsky et al., 2000)
	Concentrations	INCA	(Thanwerdas et al., 2023; Zhao et al., 2022)
	Concentrations	GEOS-Chem ESM	(Hu et al., 2018)
	Concentrations	GEOS-Chem CTM	(Prather et al., 2012)
	Concentrations	MOZART-4	(Emmons et al., 2010)
Cl	Reaction rates	ECHAM	(Jöckel et al., 2006)
	Reaction rates*	MPI	Brühl and Crutzen, 1993
$O(^1D)$	Reaction rates	ECHAM	(Jöckel et al., 2006)
	Reaction rates*	MPI	(Brühl and Crutzen, 1993)

*Combined reaction rates of Cl and $O(^1D)$.

4.5. Inclusion of isotopic information

For better separation of source sectors, it is useful to add information from isotopologues – molecules that differ in their isotopic composition. Methane has two singly substituted isotopologues, $^{13}CH_4$ and $^{12}CH_3D$, and information regarding the ratio

This project has received funding from the European Union's Horizon Europe research and innovation programme under grant agreement No 101081395

of ^{12}C to ^{13}C and hydrogen (H) to deuterium (^{2}H or D) isotopes are most commonly used in CH_4 flux inversion studies. The isotope ratios are defined as:

$$\delta^{13}C = \left(\frac{\left({}^{13}CH_4 / {}^{12}CH_4 \right)_{sample}}{\left({}^{13}CH_4 / {}^{12}CH_4 \right)_{reference}} - 1 \right) 1000 \quad (4.1)$$

$$\delta D = \left(\frac{\left({}^{CH_3D}/_{CH_4} \right)_{sample}}{\left({}^{D}/_{H} \right)_{reference}} - 1 \right) 1000 \quad (4.2)$$

where in (4.1) the reference is the international standard, Vienna Pee Dee Belemnite (VPDB) and in (4.2) it is the Vienna Standard Mean Ocean Water (VSMOW). The VPDB for $^{13}C/^{12}C$ is 1123.72×10^{-5} (Craig, 1957) and VSMOW for D/H is 155.76×10^{-6} (Hagemann et al., 1970).

The isotopic ratios vary depending on the source type (Menoud et al., 2022; Sherwood et al., 2017) (see Figures 4.2 and 4.3) and are referred to as the *isotopic signature* of the source. The isotopic signatures for thermogenic sources such as fossil fuel combustion are more enriched in $\delta^{13}C\text{-}CH_4$ and $\delta D\text{-}CH_4$ compared to biogenic sources, and biomass burning is the most enriched in $\delta^{13}C\text{-}CH_4$ (Figure 4.2 and 4.3). Using this information, it is possible to gain further constraints on the origin of the methane fluxes from the atmospheric measurements of the isotopic ratios. Currently, most of the inversion studies are limited to using only $\delta^{13}C$ e.g. (Basu et al., 2022b; Chandra et al., 2024; Lan et al., 2021; Thompson et al., 2018; Zhang et al., 2021a) but there are an increasing number of studies that also assimilate $\delta D\text{-}CH_4$ (Dasgupta et al., 2026; Fujita et al., 2020, 2025; Thanwerdas et al., 2023; Warwick et al., 2016) . The studies using $\delta D\text{-}CH_4$ are limited mainly due to a lack of observations, which is associated with challenges in measurement techniques and difficulties incorporating the information owing to their scarcity.

The "isotope inversion" (atmospheric inversion assimilating isotopic data) requires several additional data and modifications to transport models: 1) separation of fluxes into sources categories corresponding to the characteristic source signature of each source, 2) isotope fraction information from each source category (i.e., the source signatures) and 3) atmospheric chemistry transport models that can handle the different reaction rates of the isotopologues.

There are increasing number of CH_4 isotope measurements for $\delta^{13}C\text{-}CH_4$ and $\delta D\text{-}CH_4$ globally and over Europe from tall towers, aircraft and other means (Sellmaier et al., 2025; Team et al., 2022; Umezawa et al., 2025). However, isotope measurements are more challenging to make compared to CH_4 mixing ratios because isotopologues are far rarer compared to $^{12}CH_4$ ($^{13}CH_4$ is only 1% of total CH_4, and CH_3D less than 0.1%). Therefore, the inversion should be set up according to data availability (location and frequency). For example, if there are $\delta^{13}C\text{-}CH_4$ isotope measurements only from a remote non-urban location, it would not have strong constraint on separating fossil fuels and agriculture emissions. It is also important to note that the data may be subject to systematic bias when using data from various laboratories due to differences in calibration scales (Dasgupta et al., 2025; Umezawa et al., 2018) and need to be corrected to a common scale before assimilation in the inversion (see also Section 7.1).

This project has received funding from the European Union's Horizon Europe research and innovation programme under grant agreement No 101081395

The isotopic source signature values are needed to estimate the ratio of isotopologue emissions. Using those values, the amount of isotopologue emitted from each source category is estimated and using the atmospheric transport model, the isotope ratios are estimated from the model to be compared to the observations (see Section 4.1). It is especially important to distinguish the soil sink from the wetland emission source because they have distinct isotopic signature values (King et al., 1989; Reeburgh et al., 1997) . The soil sink may be accounted for in an atmospheric model using deposition velocity as the soil sink also depends on the mixing ratio of CH_4, similar to the atmospheric sinks. The landfills can have much enriched $\delta^{13}C$ source signatures compared to agricultural sources depending on the types of waste and condition of the landfills (Menoud et al., 2022), and the $\delta^{13}C$ source signatures from rice cultivation can have strong temporal variation. On the other hand, the $\delta^{13}C$ isotopic signatures from biogenic sources are relatively similar, so can be combined (e.g. wetlands + enteric fermentation and manure management + rice cultivation + termites).

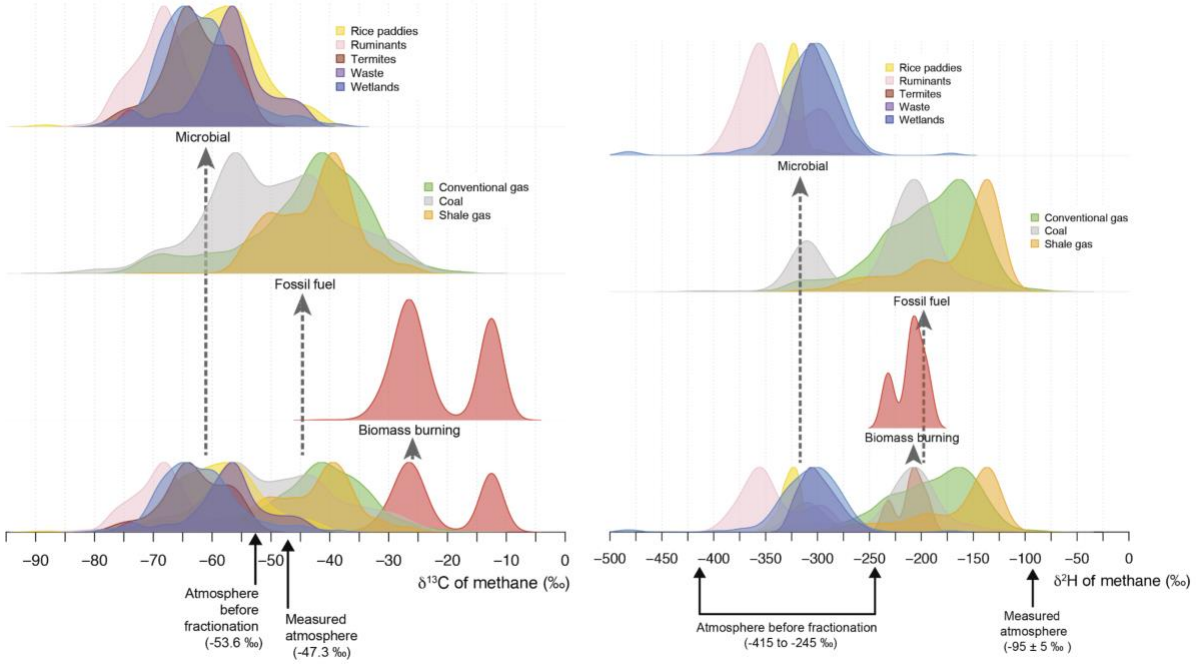


Figure 4.2: Isotopic source signatures of $\delta^{13}C$-CH_4 (left) and δD-CH_4 (right) showing the normalized probability density functions from the global inventory by Sherwood et al., (2017). (Figure courtesy of Sherwood et al., 2017).

There are various global source signature estimates published (Basu et al., 2022a; Douglas et al., 2020; Etiope et al., 2019; Feinberg et al., 2018; Ganesan et al., 2018; Lan et al., 2021; Oh et al., 2022; Sherwood et al., 2017; Warwick et al., 2016) but the source signatures are highly heterogeneous and can vary temporally depending on the emission sources (Menoud et al., 2022). Therefore, where available, it is strongly recommended to include detailed spatial and temporal information of the source signature values. In regional inversions, it would be important to use region specific source signature values. The regional differences are large for wetlands where northern peatlands have more depleted $\delta^{13}C$ compared to the tropics depending on types of wetlands, including soil properties, plant species, methanogenic communities and water availability (Fisher et al., 2017; Ganesan et al., 2018). The wetland and rice paddy emissions can have strong seasonal cycles of the isotopic signatures depending on transport pathways (France et

This project has received funding from the European Union's Horizon Europe research and innovation programme under grant agreement No 101081395

al., 2022; Jentzsch et al., 2024; Li et al., 2025) and agricultural practices (Marik et al., 2002). For enteric fermentation and manure management, $\delta^{13}C$ signature varies mainly depending on diets (Carranza et al., 2022). The landfills can have distinctive isotopic signatures depending on the types of waste, cover condition and other management activities (Bakkaloglu et al., 2021). It would be important to take into account the decay rate in non-active landfills (Börjesson et al., 2007).

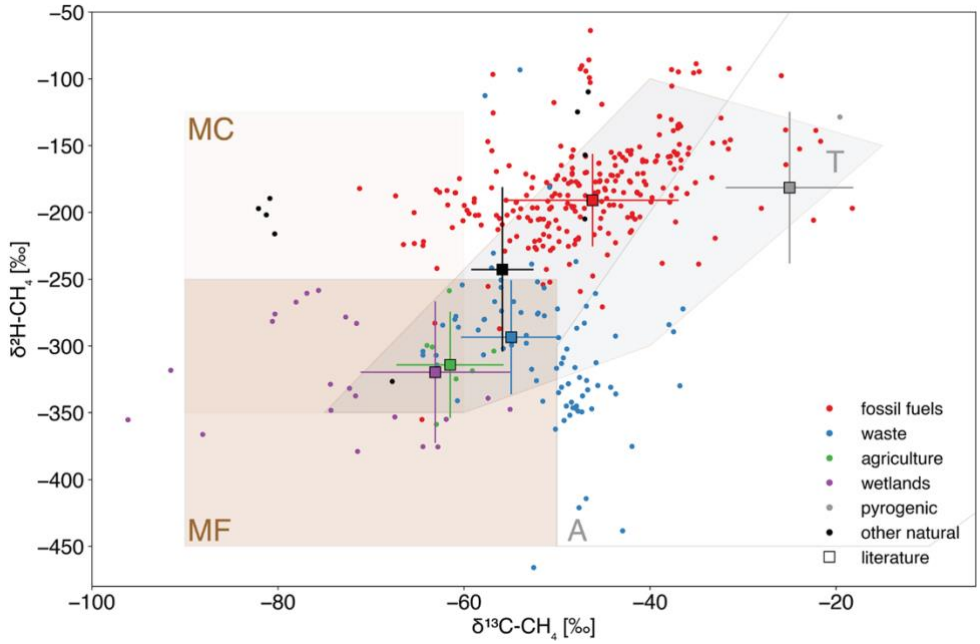


Figure 4.3: Dual isotope plot from European measurements by Menoud et al., (2022). (Figure courtesy of Menoud et al., 2022).

The atmospheric reactivity of isotopologues differs and is important to consider in the isotope inversion. Each isotopologue has a different reaction rate for their chemical reactions in the atmosphere leading to the so-called *kinetic isotopic effect* (KIE). The KIE arises due to the difference in the molar mass – reactions with heavier isotopologues ($^{13}CH_4$ and $^{12}CH_3D$) are slower compared to $^{12}CH_4$. The KIEs vary depending on the isotopologues and reactions (see Table 4.5).

Although oxidation by OH is the principle atmospheric sink process (see Section 4.4), in the isotope inversion tropospheric Cl plays a significant role in the estimation of $\delta^{13}C$ owing to the large KIE of this reaction (Strode et al., 2020; Thanwerdas et al., 2022) (see Table 4.5). For limited temporal domain observation operators, such as those based on Lagrangian transport models, the loss of CH_4, and thus the change in $\delta^{13}C$ starts to become non-negligible if the back trajectories extend beyond approximately 20 days (see Figure 4.4).

It is important to note that the soil sink also has a KIE and the sink depends on the mixing ratio of CH_4 at the surface. Therefore, the soil sink is often represented in transport models using a deposition velocity, which removes CH_4 from the atmosphere. The estimates of soil sink, accounting for about 30 Tg CH_4 yr^{-1} globally (Saunois et al., 2025), can be obtained from process-based models and inventories (e.g. Kleinen et al., 2020, Ito and Inatomi, 2012; Murguia-Flores et al., 2018). It is represented as negative flux to

This project has received funding from the European Union's Horizon Europe research and innovation programme under grant agreement No 101081395

the atmosphere, i.e. flux from atmosphere to soils, which can be considered as the deposition velocity at the surface layer of the transport models. Estimates of the KIE for the soil sink vary significantly and depend on the soil oxidation processes and ecosystems (Snover and Quay, 2000; Tyler et al., 2000).

In atmospheric transport models, the different isotopologues are transported as separate species due to their different ratios in emissions and their different reaction rates. In the isotope inversion, observations of $\delta^{13}C$ and δD are, therefore, converted into corresponding $^{13}CH_4$ and $^{12}CH_3D$ mixing ratios using (4.1) and (4.2). Furthermore, the source signatures are converted into fractions, e.g. $^{13}CH_4/^{TOT}CH_4$ and $^{12}CH_4/^{TOT}CH_4$ and applied to the emissions to calculate the emissions of $^{13}CH_4$ and $^{12}CH_4$, respectively. The modelled mixing ratios are typically converted back to $\delta^{13}C$ and δD in the model output.

Table 4.5: List of estimates for the kinetic isotopic effects.

	Reaction	**KIEs**	**Reference**
k_{C12}/k_{C13}	Loss to OH	1.0039 ± 0.0004 1.0054 ± 0.0009 1.0056[a] ± 0.0001	(Saueressig et al., 2001) (Cantrell et al., 1990) (Chen et al., 2026)
	Loss to Cl	1.0430 1.066 ± 0.002 1.0621+0.0001	(Saueressig et al., 2001) (Crowley et al., 1999) (Tyler et al., 2000)
	Loss to $O(^1D)$	1.0130	(Saueressig et al., 2001)
	Soil sink	1.0621 ± 0.0001 1.0173 ± 0.001 (grassland) 1.0181 ± 0.0004 (forest) 1.022 - 1.025 (boreal forest) 1.022 ± 0.004 (temperate forest)	(Tyler et al., 2000) (Snover and Quay, 2000) (Snover and Quay, 2000) (Reeburgh et al., 1997) (Tyler et al., 1994)
k_H/k_D	Loss to OH	1.18 1.294 ± 0.018 1.31 ± 0.01 1.319[a] ± 0.004	(DeMore, 1993) (Saueressig et al., 2001) (Joelsson et al., 2016) (Chen et al., 2026)
	Loss to Cl	1.508 1.474 ± 0.020	(Saueressig et al., 2001) (Tyler et al., 2000)
	Loss to $O(^1D)$	1.06	(Saueressig et al., 2001)
	Soil sink	1.066 ± 0.007 (forest) 1.099 ± 0.030 (grassland)	(Snover and Quay, 2000) (Snover and Quay, 2000)

[a] Chen et al. (2026) determined a temperature dependent KIE the value given here is for standard atmospheric temperature.

Another important aspect is that initial atmospheric mixing ratios for isotopologues should be stabilized before carrying out inversions. For this, longer spin-up (~30 years) may be needed to obtain stable initial mixing ratios using Eulerian transport models due

This project has received funding from the European Union's Horizon Europe research and innovation programme under grant agreement No 101081395

to longer lifetime of the heavier isotopologues (Chandra et al., 2024; Fujita et al., 2020; Kangasaho et al., 2022).

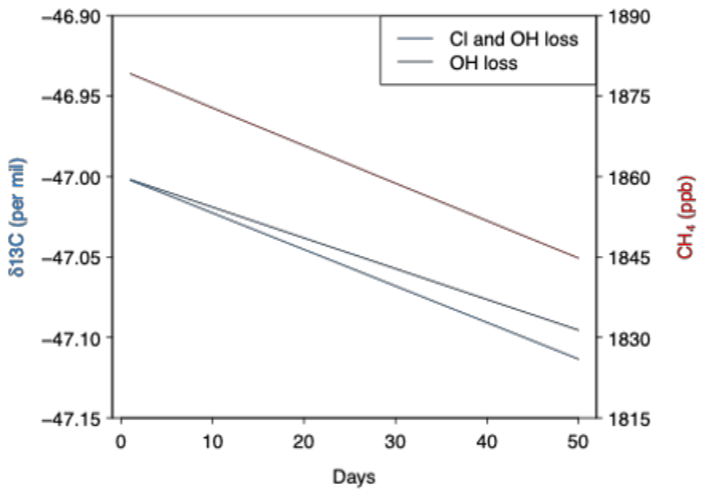


Figure 4.4: Box model calculation of the change in $\delta^{13}C$ and CH_4 due to reactions with OH and Cl up to 50 days assuming standard atmospheric temperature (273.15 K), global mean OH (Spivakovsky et al., 2000) and Cl (Allan et al., 2007) concentrations (molecule/cm^3), and $k_{OH} = 3.703\times10^{-15}$ (Atkinson, 2003) and $k_{Cl} = 6.606\times10^{-14}$ (Allan et al., 2007) (cm^3/molecule/s) and $KIE_{OH} = 1.0054$ and $KIE_{Cl} = 1.066$.

The isotopic signatures and KIEs play significant roles in estimating isotopic ratios using atmospheric transport models. Small changes in these can lead to significant differences in the estimated values, thus the model representation errors for isotopologues are deemed larger compared to total CH_4. Therefore, the transport model errors (included in the covariance matrix **R**) must be adjusted carefully depending on the inversion set-up. It is also possible to co-optimize the source signatures and KIEs (Fujita et al., 2025; Thanwerdas et al., 2024), although this introduces non-linearity and additional challenges regarding the assignment of uncertainties.

5. N_2O inversions

Rona Thompson and Nalini Krishnankutty

5.1. Prior fluxes and uncertainties

Anthropogenic N_2O emissions globally are dominated by agricultural soils e.g. (Tian et al., 2020, 2024). In particular, N_2O is produced in soils via the microbial processes of nitrification and denitrification - naturally occurring processes that are enhanced by the anthropogenic additions of reactive nitrogen (N) to soils (e.g. through N fertilizers, livestock manure and legume crops) (e.g. Butterbach-Bahl et al., 2013; Firestone and Davidson, 1989). Emissions from agricultural soils caused by N additions constitute the *direct* agricultural emission of N_2O, which is about 56% of the global total anthropogenic emissions (Tian et al. 2024). In addition, N_2O is also emitted from other soils that are not directly fertilized, as well as from inland waters and coastal areas as reactive N is transported from agricultural soils by atmospheric dispersion and deposition and through waterways. This constitutes the *indirect* emission of N_2O and accounts for 18% of the global total anthropogenic emissions (Tian et al. 2024). Other more minor anthropogenic sources of N_2O include waste, especially wastewater management, 5%,

This project has received funding from the European Union's Horizon Europe research and innovation programme under grant agreement No 101081395

and industrial processes (especially adipic and nitric acid production) and combustion of fossil fuels, together 17% (Tian et al. 2020; 2024; Global Nitrous Oxide Assessment, 2024) (see also Table 5.1).

Natural sources of N_2O include soils under natural vegetation, especially important in tropical forests, natural outgassing from inland waters, and the coastal and open ocean, as well as biomass burning (Tian et al. 2020; 2024; Global Nitrous Oxide Assessment, 2024). The processes responsible for N_2O production in natural soils, waste water, inland waters and the ocean, are the same as those responsible for emissions from agricultural soils, namely nitrification and denitrification (Global Nitrous Oxide Assessment, 2024).

Table 5.1: Examples of global datasets that can be used for prior flux estimates (this list is not exhaustive and higher resolution regional model estimates may be preferred for regional inversions).

Source	Method/Model	Description	References
Natural soils	Process-based models: e.g. VISIT DLEM OCN LPJ-GUESS ORCHIDEE LPX-Bern CLASSIC ISAM ELM	Models that parameterize biogeochemical processes leading to production of N_2O and its flux to the atmosphere	(Tian et al., 2019)
Agricultural soils	Process-based models (see above)	(see above)	(Tian et al., 2024)
	Inventories: e.g. EDGAR CEDS	Use emission factors and activity data	(Crippa et al., 2021)
Industrial processes, fossil fuel combustion, and waste	Inventories: e.g. EDGAR CEDS	Use emission factors and activity data	(Crippa et al. 2021)
Inland waters	Process-based and data-driven models	Use combinations of data-driven and process-based approaches	(Lauerwald et al., 2019) (Yao et al., 2019) (Maavara et al., 2019)
Biomass burning	Inventories: e.g. GFED GFAS	Use satellite detected fires with maps of land-cover and emission factors	(Kaiser et al., 2012) (Werf et al., 2017)
Ocean	Process-based models: e.g. NEMO-PlankTom Bern-3D NEMO-PISCES UVic	Ocean circulation models that include biochemistry leading to production and fluxes of N_2O	(Tian et al., 2024)

Unlike for other species, the discrimination between natural and anthropogenic emissions is not clear for N_2O. Soils not directly under human management can receive

This project has received funding from the European Union's Horizon Europe research and innovation programme under grant agreement No 101081395

reactive N of anthropogenic origin through atmospheric deposition and/or through water transport leading to enhanced (i.e. above some natural baseline) N_2O emissions. Furthermore, soils under human management may also emit N_2O in the absence of anthropogenic N input. Land-use change also influences N_2O fluxes, e.g., following deforestation soils may produce a pulse of N_2O emission followed by a decline, and in the absence of anthropogenic N input may eventually emit less than in the state before deforestation (Tian et al., 2020; 2024).

In UNFCCC reporting, only anthropogenic emissions are reported. For soils, these are calculated for managed land, with indirect emissions extrapolated from the direct additions of reactive N. Direct agricultural soil emissions are calculated using emission factors multiplied by corresponding N inputs, where the emission factors are based on flux measurements considering the flux above a natural background. Indirect emission extrapolations use assumptions on the amount of reactive nitrogen transferred via atmospheric or aqueous transport and use similar emission factors to those for direct emissions.

It is not often feasible to cleanly distinguish between natural soil emissions and anthropogenic soil emissions (or emission enhancements), as both arise from the same microbial processes and respond to the same environmental drivers, and can occur in the same grid cells (Tian et al., 2020). Owing to this, most inversion systems choose to optimise total N_2O fluxes, and sectoral information is used only for the construction of prior fluxes and the evaluation of the results (Thompson et al., 2019). (Note, not all process-based models provide separate estimates for anthropogenic and natural soil emissions). On the other hand, non-soil emissions, such as the point emissions from industrial processes, may possibly be optimized as a separate category but the constraint on industrial emissions versus other sources will strongly depend on the resolving power on the inversion, the density and location of the observations relative to the industrial emissions, and the strength of the industrial emissions relative to surrounding non-industrial emissions.

When combining different estimates, such as anthropogenic inventories and process-based model estimates, care must be taken to avoid double-counting. For example, agricultural waste burning is often a source in bottom-up inventories and should be excluded if a fire emission dataset that includes this is used. Similarly, if combining process-based model estimates for soil emissions and an inventory for the anthropogenic emissions, care must be taken not to double count e.g. agricultural soil emissions. Moreover, some inventories and models report fluxes of N_2O in using the mass of N_2O, whereas others report using the mass of N, which results in a factor of 44/28 difference between the two units. The molar mass (N or N_2O) used in the estimates must always be carefully checked.

Oceanic N_2O fluxes amount to 25% of the global total source (Tian et al., 2024). However, given the fairly limited sensitivity of the atmospheric observing networks to oceanic N_2O, these fluxes are typically weakly constrained by the inversion (Tian et al., 2020; Thompson et al., 2014). There are some measurement platforms, however, that do have an oceanic signal. In particular, regular shipboard measurements across the Pacific Ocean have indicated variability in tropospheric N_2O owing to inter-annual variations in ocean N_2O fluxes corresponding to ENSO (Ishijima et al., 2009) and measurements at

This project has received funding from the European Union's Horizon Europe research and innovation programme under grant agreement No 101081395

Trinidad Head in California are sensitive to coastal upwelling and outgassing of N_2O (Lueker et al., 2003; Nevison et al., 2004).

When prescribing prior fluxes for N_2O inversions, it is important to consider the temporal and spatial variability of these fluxes and the resolution of the model used. Soil fluxes of N_2O are very heterogeneous and are characterised by "hot-spots" and "hot-moments" (Butterbach-Bahl et al., 2013). In particular, emissions of N_2O from agricultural soils can be very significant after N-fertilizer application, following rainfall, and from fallow cropland. In high spatial resolution models, it is important to use an appropriate temporal resolution to capture the highly variable and often short-lived emission events. In coarser regional and global datasets, the influence of high spatial and temporal variability is smoothed. Atmospheric observation sites that are remote from these emissions will receive an integrated signal and may not be sensitive to the highly heterogenous emissions, meaning that the coarse resolution (e.g. monthly) of the fluxes may not introduce significant model representation error. On timescales of the order of a week to a month, seasonal variability in soil emissions is important, as these respond strongly to temperature and soil moisture, and in seasonally frozen soils, freezing and thawing can also influence the emissions (Butterbach-Bahl et al., 2013). Similarly, ocean fluxes are seasonal and ideally seasonality should be represented in the prior used in the inversion.

The uncertainty on the total net N_2O flux can be described by considering the uncertainties of the various sources and may be prescribed as an emission weighted sum of the individual source uncertainties. The uncertainties may be ascertained by considering the spread of an ensemble of models, or via error propagation. In inventories, the emission factor uncertainties usually contribute the most to the total uncertainty. For direct and indirect soil emissions the estimated uncertainty (corresponding to 95% confidence when the distribution is Gaussian) is around 70% (Solazzo et al., 2021). For industrial sources, the uncertainty is less, about 20%, and a bit larger for combustion of fuels and waste, about 50% (Solazzo et al., 2021).

Process-based model estimates of N_2O soil fluxes differ substantially due to variations in process parameterisations, N-fertilization rates, meteorological forcing and other input data (Tian et al., 2019). Globally, agricultural soil estimates differ by about 30%, while natural soil estimates differ by about 37% but locally and regionally the differences can be larger (Tian et al., 2024). Ocean flux estimates include those from coastal shelves, which vary globally by about 41%, and from the open ocean, which vary by about 31% (Tian et al., 2024).

Correlations in the prior error covariance matrix further control how flux adjustments are distributed in space and time. Horizontal correlation lengths are intended to represent the spatial scales over which uncertainties are expected to be coherent, for example, due to management practices, emission factors, or meteorology. For N_2O soil fluxes, temporal correlations of several weeks to a few months are appropriate for N_2O, reflecting soil moisture, management and meteorology. However, long temporal correlations may prevent the inversion from correcting seasonal biases.

This project has received funding from the European Union's Horizon Europe research and innovation programme under grant agreement No 101081395

5.2. Boundary conditions and the atmospheric sink

Nitrous oxide is a long-lived gas with a lifetime of around 116 ± 9 years (Prather et al., 2015) and its only atmospheric sink is in the upper stratosphere where it undergoes photolysis (~90% of the loss) and oxidation by O^1D radicals (10% of the loss) (Crutzen, 1970; Minschwaner et al., 1993; Ravishankara et al., 2009). Owing to the dependency of the reactions on sunlight they vary strongly with latitude and time-of-the-year.

Although the loss of N_2O occurring within the residence time of N_2O within a regional domain (such as for a sub-continent) is minimal (especially if the regional model does not include the upper stratosphere) it is vital, however, that the influence of N_2O loss is represented in the boundary conditions, as the global annual loss of N_2O is around 13.4 TgN/y compared to a total source of around 18.3 TgN/y (Tian et al., 2024).

The loss of N_2O in the stratosphere also results in a strong mixing ratio gradient across the tropopause, and the largely seasonal mixing between the stratosphere and troposphere (stratosphere-troposphere exchange, STE) has a significant influence on tropospheric N_2O (Nevison et al., 2024). The seasonal cycle of N_2O especially at mid to high latitude sites is determined by the seasonal STE and propagation of the signal from the tropopause to the lower troposphere as well as the seasonality of the surface fluxes (Ishijima et al., 2010; Thompson et al., 2014b). Together this results in a minimum in N_2O in August-September in the Northern Hemisphere and in April-June in the Southern Hemisphere ((Sun et al., 2024), see also Figure 5.1).

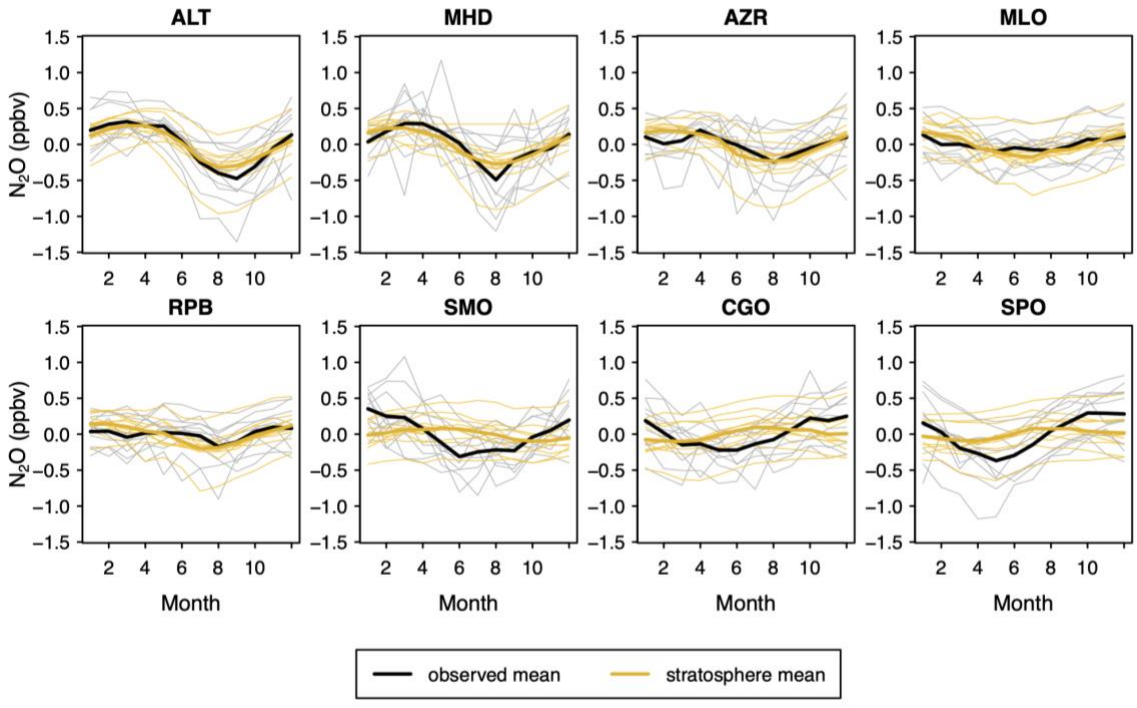


Figure 5.1. Components of the seasonal cycle of N_2O in the lower troposphere at 8 example sites at different latitudes (in order north to south from left to right). The thin black lines are the observed seasonal cycles for 10 years (2013 to 2022) from NOAA flask network data and the thick black line is the mean. The thin yellow lines are the modelled stratospheric influence at each site (using the model LMDz-v6).

Furthermore, inter-annual variations in STE also have an impact on tropospheric N_2O variability, in particular, due to the Quasi-Biannual Oscillation (QBO), which produces a

This project has received funding from the European Union's Horizon Europe research and innovation programme under grant agreement No 101081395

periodicity of around 2 years in the tropospheric N_2O growth rate (Ruiz et al., 2021). Correct representation of atmospheric circulation to capture the variations in tropospheric N_2O is important for an inversion to be able to correctly constrain the surface fluxes and otherwise the seasonal and inter-annual variations in N_2O fluxes will contain artefacts. Thus, having an accurate vertical mixing ratio gradient and representation of STE in models is crucial to simulating tropospheric N_2O in both global and regional models. The representation of the gradient in a global model can be improved by using a spin-up period of several years (the length of spin-up needed will depend on the accuracy of the initial mixing ratios used).

In regional inversions, the boundary mixing ratios, or background mixing ratios, as with other long-lived species, will have an important influence on the posterior flux estimation. Therefore, as also stated in Section 2.3.2, it is strongly recommended to include variables for the optimization of the boundary or background mixing ratios. The same strategies to do this for other species can also be used for N_2O (see Section 4.2).

6. F-gas inversions

Martin Vojta and Omid Nabavi

Fluorinated gases (F-gases) are a family of different substance classes containing fluorine, specifically hydrofluorocarbons (HFCs), perfluorocarbons (PFCs), sulfur hexafluoride (SF_6), and nitrogen trifluoride (NF_3). Their lifetimes vary, e.g., from 1.5 years for HFC-152a to about 900 years for SF_6 and 50.000 years for perfluoromethane (CF_4). Most of these gases are purely human-made and used, for instance, in refrigeration, air-conditioning, aluminum smelting, etc. For some of these gases, very small natural sources may exist but can be ignored for the purpose of inverse modelling. F-gases have high radiative efficiency and are chemically related to chlorofluorocarbons (CFCs) and hydrochlorofluorocarbons (HCFCs), which also contain other halogen atoms than fluorine and lead to stratospheric ozone destruction.

For F-gases, atmospheric transport is generally considered less challenging to model than for e.g. CO_2 for which the diurnal variations in the fluxes are correlated with variations in boundary layer dynamics. Except for a few HFCs, with substantial losses due to oxidation by OH in the troposphere, most F-gases undergo only very slow chemical removal in the stratosphere or above, which in many cases can even be neglected. In addition, because F-gas emissions originate from well-defined anthropogenic sectors, there is no need to account for soil exchange, biogenic sources, or natural variability.

However, F-gas inversions face other important challenges. Observational coverage is much sparser than for CO_2, CH_4, or N_2O. Emissions are hard to quantify with bottom-up methods, due to numerous diffuse and sometimes unreported sources, resulting in substantial discrepancies in inventories that serve as prior information for the inversion, while the magnitude of emission uncertainties, as well as their spatial and temporal correlations are usually not provided by the inventories. Some F-gases originate almost exclusively from relatively few point sources, where they may be used as feed-stocks for the production of other gases or substances, while others have only sporadic emissions during certain events (e.g., fires in transformer stations). Furthermore, the influence of

This project has received funding from the European Union's Horizon Europe research and innovation programme under grant agreement No 101081395

boundary mixing ratios of most F-gases is relatively large compared to the episodic pollution events observed at monitoring sites, making the inversion results highly sensitive to the boundary mixing ratios. Furthermore, as is common in atmospheric inversions, many aspects of the optimization process rely on assumptions and expert judgment.

6.1. Prior emissions and uncertainties

Prior emissions of F-gases can be taken from bottom-up inventories such as EDGAR (Crippa et al., 2024) and GAINS (Purohit and Höglund-Isaksson, 2017), which provide gridded data. Another common approach is to use national emissions reported under the UNFCCC (where available) and distribute them on a spatial grid using proxy data such as population density or industrial activity e.g. (Stohl et al., 2009; Vojta et al., 2024). Depending on the species and region, bottom-up estimates can show large discrepancies, such as missing emissions or temporal irregularities in certain countries that are often caused by the varying availability of national emission reports. In poorly observed areas the inversion may be strongly influenced (or nearly entirely controlled) by the choice of prior emissions. Bottom-up inventories for F-gases are typically calculated on an annual basis, based on yearly reported activity data and emission factors. Generally, a temporal resolution of one year also provides a robust choice for F-gas inversions.

The uncertainties of the emissions used as prior information are largely unknown. A simple and robust approach to estimate the prior emission uncertainty is to specify this as a fraction of the emission values in each grid cell assuming that regions with higher reported emissions also carry proportionally larger uncertainties. When using this approach, it is recommended to prescribe a minimum prior uncertainty, ensuring that the inversion algorithm can adjust emissions even in grid cells with small or zero prior emissions. In a similar way, a maximum prior uncertainty may be prescribed to prevent unrealistically large uncertainty values from dominating the inversion. An alternative approach to estimating prior emission uncertainties is to base them on comparisons between different bottom-up emission inventories, which better reflects uncertainties arising from activity data, emission factors, and methodological choices. However, different inventories might not be fully independent and may share common assumptions or biases, potentially underestimating true uncertainty. In principle, top-down estimates can also be compared with bottom-up inventories, however, differences may also reflect uncertainties in atmospheric transport and observational systems, rather than emission uncertainties only.

For F-gas inversions, the results can be highly sensitive to the choice of the spatial correlation length used to calculate the prior error covariance matrix (Vojta et al., 2025). This choice may be guided by the dominant type of source for a chosen F-gas, for instance, whether emissions are mostly widespread (e.g., air-conditioning) or due to few individual industrial point sources. Increasing the correlation length generally allows observational information to influence a larger number of grid cells, but may come at the cost of reducing the inversion's ability to resolve spatial variability in the emissions (as illustrated in Figure 6.1). Conversely, a very small correlation length can result in an insufficient observational constraint at the grid-cell scale if the overall magnitude of the

This project has received funding from the European Union's Horizon Europe research and innovation programme under grant agreement No 101081395

prior covariance is kept fixed. In this case, the inversion problem can become ill-determined leading to noisy posterior fluxes and, in some cases, unrealistic negative emission estimates. Alternatively, the prior covariance can be rescaled, for example to maintain a consistent overall level of prior uncertainty.

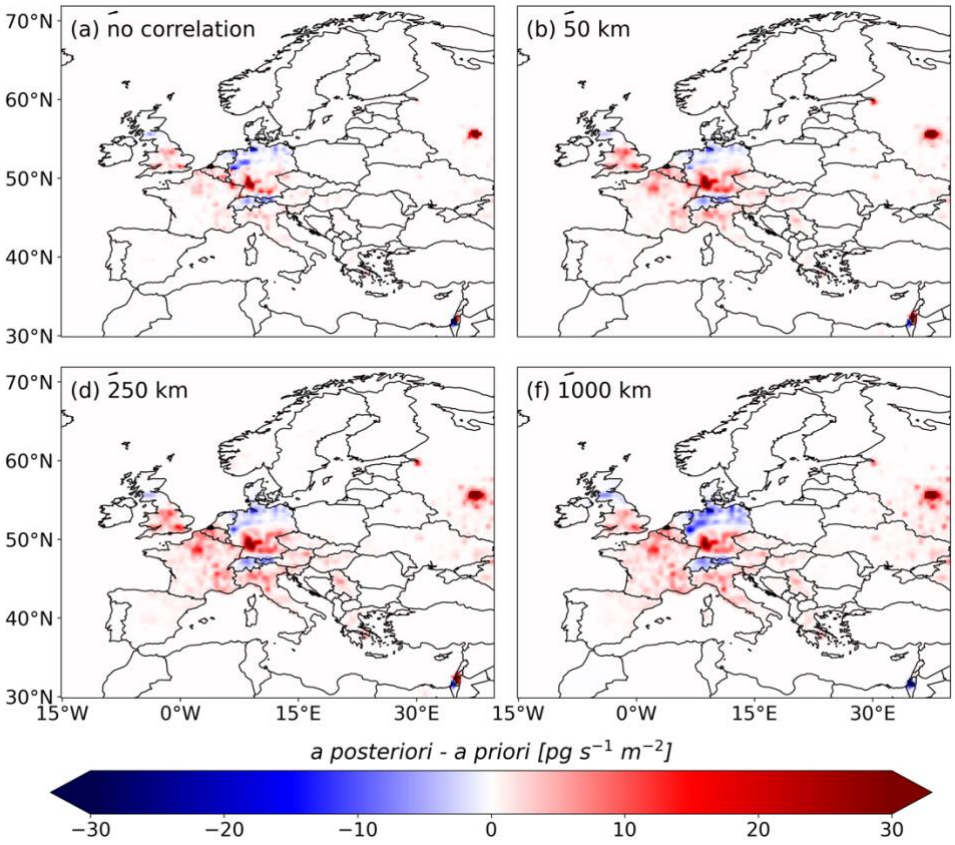


Figure 6.1: SF_6 inversion increments (posterior minus prior) under different spatial correlation lengths, when using an exponential decay function to account for uncertainty correlations. As the correlation length increases, the increments become less localized as observational information is spread over larger areas.

If the state vector is temporally resolved, as in multi-year or seasonal inversions, including temporal correlations in the prior errors can also improve inversion results. Longer temporal correlation lengths help to stabilize the inversion against spurious temporal variability (arising from, e.g. temporally uneven observational coverage). However, too long correlations can reduce the ability to resolve temporal variations in emissions.

Bottom-up F-gas fluxes are typically strictly positive, with many small values and a few large ones, forming a distribution well approximated by a lognormal distribution (as illustrated in Figure 6.2 for the EDGAR SF_6 inventory), strongly suggesting that the errors follow a lognormal distribution as well.

If nevertheless, Gaussian prior errors are assumed, the inversion can produce negative posterior fluxes on a grid-cell basis, because these values can still lie within the prescribed uncertainties. Therefore, it is recommended to apply some non-negativity constraint. If the posterior error covariance matrix can be computed (and stored in memory), the truncated-Gaussian method of Thacker (Thacker, 2007) can be used,

This project has received funding from the European Union's Horizon Europe research and innovation programme under grant agreement No 101081395

which enforces non-negativity as an inequality constraint. Here, the adjusted fluxes, $\boldsymbol{x}^{a,p}$ are calculated as

$$\boldsymbol{x}^{a,p} = \boldsymbol{x}^{a} + \mathbf{P}\mathbf{T}^{\mathrm{T}}(\mathbf{T}\mathbf{P}\mathbf{T}^{\mathrm{T}})^{-1}(\boldsymbol{c} - \mathbf{T}\boldsymbol{x}^{a}) \quad , \qquad (6.1)$$

where $\boldsymbol{x}^{a}$ is the original posterior estimate, $\mathbf{P}$ the posterior error covariance matrix, $\mathbf{T}$ the operator identifying negative fluxes, and $\boldsymbol{c}$ the constraint vector.

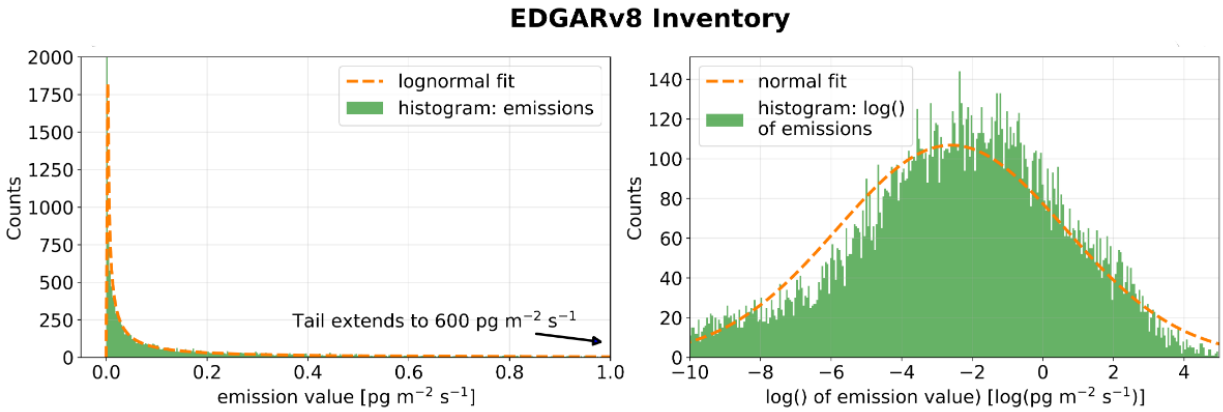


Figure 6.2: European SF_6 emission distribution derived from the gridded EDGAR (version 8) bottom-up inventory.

Another recommended approach is to use a log-normal distribution for the prior errors, which is defined only for positive control variable values and, therefore, ensures a positive posterior solution (Vojta, Thompson, and Pisso, 2026). In this case, however, the posterior error covariance matrix cannot be calculated analytically, and posterior uncertainties must instead be estimated from an inversion ensemble.

6.2. Boundary conditions

6.2.1. Boundary mixing ratios

Contrary to the major greenhouse gases, for most F-gases, global mixing ratio fields do not exist or are not readily available and, therefore, purely observation-based background estimators such as the Robust Estimation of Baseline Signal (REBS) method (Ruckstuhl et al., 2012) have typically been used to estimate the background in inversions that are based on Lagrangian transport models. However, as discussed in Section 2.3.2, it is highly recommended also for F-gases to estimate background mixing ratios by coupling the endpoints of the backwards trajectories to mixing ratios from a (coarse resolution) global model. This method is fully consistent with the length of the Lagrangian backwards simulation period and avoids the systematic biases inherent in observation-filtering approaches, which do not incorporate any model information (Vojta et al., 2022). However, this requires to first create global mixing ratio fields, for example by adopting a method such as described in (Zwaaftink et al., 2018) or (Vojta et al., 2022, 2024). In this approach, mixing ratios are simulated with a Lagrangian model operated in a global domain-filling mode, while a nudging routine relaxes the model fields towards atmospheric observations. In principle, any global model may be used, provided that the background fields are free of significant biases, since such biases (if not corrected-for in the inversion) will directly propagate into the posterior emissions. While coupling at the trajectory endpoints offers a robust approach for both global and regional inversions, coupling at the spatial boundaries of the regional domain e.g. (Ganesan et al., 2017; Lunt

This project has received funding from the European Union's Horizon Europe research and innovation programme under grant agreement No 101081395

et al., 2016; Ramsden et al., 2022; Say et al., 2019) provides a suitable alternative for regional inversions. In Eulerian inversion frameworks, similarly, boundary mixing ratios for a regional domain are typically prescribed from a global model at the edges of the domain, ensuring consistency with large-scale background mixing ratios e.g. (Rödenbeck et al., 2009).

6.2.2. Optimization of the boundary mixing ratios

Even if global mixing ratio fields are constrained by observations, some residual biases will always remain. This is particularly true for F-gases, for which far fewer observations exist than for the major greenhouse gases and thus uncertainties in the background are relatively larger. Therefore, it is important to include the optimization of boundary (or background) mixing ratios as part of the inversion, and this is again especially pertinent for F-gases, for which the posterior emissions are highly sensitive to errors in the boundary mixing ratios. This adjustment can be implemented by optimizing scalars of the boundary or initial mixing ratios resolved on a coarse grid e.g. (Thompson and Stohl, 2014). For this, it is necessary to specify appropriate uncertainties for the scalars and to choose suitable spatial and temporal resolutions and correlation lengths for the optimization.

- **Uncertainty**: F-gas inversion results are typically highly sensitive to the prescribed uncertainty in variables controlling the optimization of the boundary, initial or background mixing ratios. Although the true uncertainty is unknown, scalars defined on a coarse grid can usually be well constrained, meaning that underestimating the uncertainty is generally more problematic than overestimating. (Vojta et al., 2025) demonstrated that increasing the uncertainty on scalars can improve inversion outcomes, but that results tend to stabilize once the uncertainty exceeds a certain threshold, as illustrated in Figure 6.3. It is, therefore, recommended to perform sensitivity tests for the uncertainty to ensure that it is not underestimated.
- **Spatial resolution**: Many F-gases exhibit a large inter-hemispheric gradient in atmospheric mixing ratios, therefore, potential biases in the modeled fields likely differ between the Southern and Northern Hemispheres. Thus, it is recommended to optimize the background in at least two latitudinal bands, while using four bands generally provides a robust choice (Vojta et al., 2025). When a finer subdivision of the background is required, spatial correlation between respective scalars might be applied to improve the constraint.
- **Temporal resolution**: The temporal aggregation interval for the background optimization typically has only a minor influence on inversion results (Vojta et al., 2025). A 30-day interval represents a reasonable and commonly effective choice. As for the spatial case, temporal correlations may be imposed to further constrain the scalars where additional regularization is required.

This project has received funding from the European Union's Horizon Europe research and innovation programme under grant agreement No 101081395

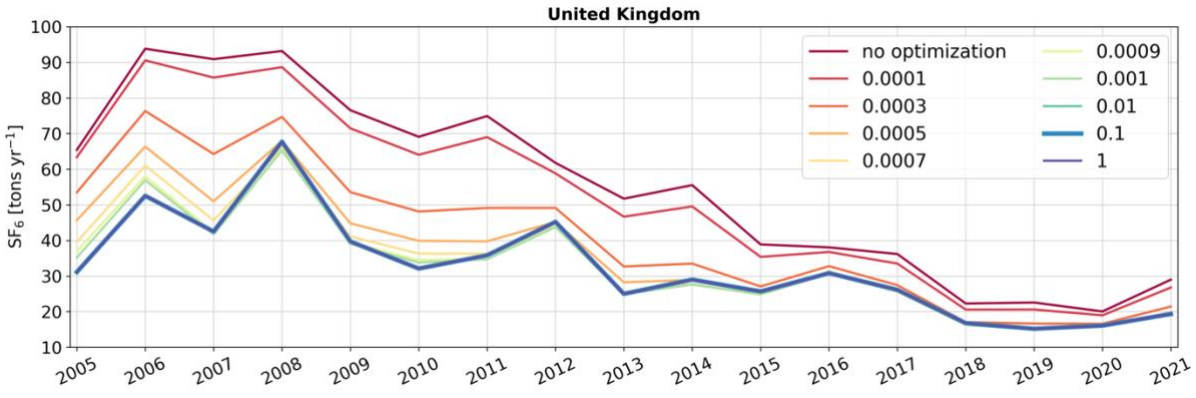


Figure 6.3: Inversion results for varying uncertainty settings regarding the optimization of boundary mixing ratios, illustrated for constraining annual SF_6 emissions in the UK. Increasing the prescribed uncertainty has a substantial effect on the inferred emissions, however, the sensitivity decreases at higher uncertainty levels, and the results stabilize once the uncertainty exceeds a certain threshold between 1 and 10%.

6.3. Observations and observation uncertainties

Observation datasets are discussed in detail in Section 7.1. However, here it is worth noting that the choice of datasets, including data selection, filtering, and averaging, can also significantly influence inversion results for F-gases (Vojta et al., 2025). For low-altitude stations, afternoon observations may be selected to focus on periods with a well-mixed planetary boundary layer, when model errors are expected to be smallest. At mountain stations, nighttime observations may be preferred to reduce errors associated with daytime small-scale upslope winds in complex terrain, which are not resolved by the model. Especially when observation error correlations are not explicitly considered, also averaging observations over predefined time intervals (e.g. 3 hours to daily) may be considered to prevent an overestimation of the impact of high-frequency measurements, while at the same time reducing representation errors and short-term variability that are not resolved by the model. However, decisions on observation selection and temporal averaging should be based on the ability of the model to represent the observations (e.g. spatial and temporal resolution of the model and input wind fields) while ensuring that sufficient information is retained to constrain the inversion.

Depending on the data provider, measured F-gas mole fractions are calibrated to different reference scales, such as the Scripps Institution of Oceanography (SIO), World Meteorological Organization (WMO), or National Institute for Environmental Studies (NIES) scales. When combining datasets, it is, therefore, crucial to convert all measurements to a common calibration scale to ensure consistency. This is especially important for species with low atmospheric abundances and rapid growth rates (e.g., HFC-32, HFC-365mfc), where small absolute calibration offsets correspond to large relative differences, which can bias inversion results.

Observation uncertainties, including measurement and model representation errors, are difficult to quantify. An estimation based on model residuals (the difference between observed and simulated mole fractions) at the measurement stations e.g. (Henne et al., 2016; Stohl et al., 2009) is problematic as it violates the independence of the prior and observations spaces, and residuals also include emission errors, leading to an overestimation of uncertainty. Such approaches should therefore be used with caution and can only serve as a rough estimate of model error magnitude. Transport ensemble

This project has received funding from the European Union's Horizon Europe research and innovation programme under grant agreement No 101081395

approaches with multiple transport realizations have been presented to estimate model errors e.g. (Diaz-Isaac et al., 2019) and idealized experiments have shown that incorporating temporally varying, flow-dependent model uncertainties can improve emission estimates (Steiner et al., 2024b). However, these approaches are computationally demanding and not always feasible. Approaches for determining whether uncertainties are appropriately chosen are presented in Section 2.5.

6.4. Atmospheric chemistry

For hydrogen containing F-gases (HFCs) reaction with the OH radical is the dominant atmospheric removal process, which occurs primarily in the troposphere. Stratospheric loss, including photolysis and reactions with electronically excited oxygen, $O(^1D)$, is much slower and is usually negligible, except for some long-lived HFCs (e.g., HFC-125, HFC-143a), contributing a few percent to total loss (Ko et al., 2013). CFCs are removed primarily via stratospheric photolysis, leading to lifetimes of decades to a century, whereas highly fluorinated species such as NF_3, PFCs, and SF_6 are extremely stable, with upper atmospheric loss processes so slow that their atmospheric lifetimes extend to centuries or millennia.

Long-term (months to years) simulations of HFCs within Eulerian inverse modelling frameworks should include OH reactions to accurately represent the decay of atmospheric mixing ratios. In contrast, when using Lagrangian models to simulate emission sensitivities, OH-induced chemical loss is generally negligible over typical backward simulation periods (e.g. ~10 - 50 days) for most species. Consequently, except for the most short-lived ones, HFCs can be treated as inert when constructing the sensitivity matrix with Lagrangian models, which simplifies the workflow without introducing significant error. When simulating mixing ratio fields of HFCs for coupling to Lagrangian models to provide the background, OH-induced chemical loss should, however, be included.

For HFCs, the rate constant k(T) of OH-induced chemical loss may be calculated using the Arrhenius-type formulation

$$k(T) = A \exp\left(-\frac{D}{T}\right) \tag{6.2}$$

where A (cm^3/molecule/s) and D (K) are species-specific constants, with $D = E_a R^{-1}$ representing the activation energy E_a divided by the gas constant, R, and T is the absolute temperature (Atkinson, 1997). Global OH datasets are listed in Table 4.4, while species-specific constants can be taken from literature. Table 6.4 gives an overview about relevant HFCs, showing the lifetime, species-specific parameters, together with the corresponding reaction rate constants at 298 K, and their associated uncertainties.

This project has received funding from the European Union's Horizon Europe research and innovation programme under grant agreement No 101081395

Table 6.1 Atmospheric lifetimes (Forster et al., 2021), species-specific constants (HFC-125, HFC-143a, HFC-134a, and HFC-32 from (Wilson, et al., 2007) and HFC-23 from (Hampson et al., 1989), corresponding reaction rate constants, and associated uncertainty factors at 298 K for relevant HFCs.

Species	Atmospheric lifetime (y)	A (cm^3 $molec^{-1}$ s^{-1})	D (K)	k (298 K) (cm^3 $molec^{-1}$ s^{-1})	Uncertainty factor at 298 K
HFC-134a	14	1.5×10^{-12}	1750	4.2×10^{-15}	1.2
HFC-143a	51	1.8×10^{-12}	2170	1.2×10^{-15}	2.0
HFC-23	228	1.5×10^{-12}	2650	2.1×10^{-16}	1.5
HFC-32	5.4	1.9×10^{-12}	1550	1.1×10^{-14}	1.2
HFC-125	30	5.6×10^{-13}	1700	1.9×10^{-15}	2.0

Depending on the species, uncertainties of OH reaction rate constants of HFCs can be considerable (up to a factor of 2) and represent an additional source of uncertainty alongside uncertainties in the OH fields.

Highly fluorinated species (e.g., PFCs, SF_6, NF_3) can generally be treated as inert due to their extremely long lifetimes and negligible chemical loss.

7. Atmospheric observations

Antoine Berchet, Christine Groot Zwaaftink, Aki Tsuruta and Rona Thompson

7.1. Ground-based observations

7.1.1. Types of observations

In-situ observations are based on samples of air and are collected on a variety of platforms. They foremost include ground-based observations from tall towers and near-surface stations but can also be made on moving platforms such as aircraft, drones, weather balloons, or ships. Historically, measurements of CO_2 have been mainly based on non-dispersive infrared (NDIR) absorption techniques and measurements of CH_4 and N_2O based on gas chromatography (GC). However, more recently, GC measurements of CH_4 and N_2O are increasingly being replaced by different spectroscopic instruments with extended path lengths (Zellweger et al., 2016) . Observations can be made at high temporal frequency (continuous observations) or low temporal frequency (such as flask samples, which are typically weekly to biweekly). Although the flask sampling method limits temporal frequency, the sampled air can be later analyzed (in a central laboratory) for multiple species and for isotopic composition. Moreover, since the infrastructure required for flask sampling is much simpler than that for in-situ instruments, flask samples can be taken at remote sites where running and maintaining gas analysis instruments is challenging.

National and international monitoring networks of GHG measurements have been established over the past approximately four decades and include for instance the NOAA Global Greenhouse Gas Reference Network (https://gml.noaa.gov/ccgg/about.html), the Integrated Carbon Observation System (ICOS) network (https://www.icos-cp.eu/) and the Advanced Global Atmospheric Gases Experiment (AGAGE; https://www-

This project has received funding from the European Union's Horizon Europe research and innovation programme under grant agreement No 101081395

air.larc.nasa.gov/missions/agage/global-network). Data from several networks are archived at the World Data Centre for Greenhouse Gases (WDCGG, https://gaw.kishou.go.jp/) and EBAS (https://ebas.nilu.no/).

7.1.2. Data selection and averaging

The location of the observation site and timing of the observations are critical for determining their representativeness. That is, a near-surface observation might only be representative of local fluxes while observations from tall towers (typically in the order of 50 to 400 m height) are generally set-up to sample the well-mixed boundary layer and their *footprints* can extend up to many 1000s of km^2 to obtain regional coverage e.g. (Bakwin et al., 1998a; Gloor et al., 2001). Moreover, a large difference in the representativeness of nighttime and daytime observations might be seen. At mountain sites, daytime observations can be strongly influenced by local fluxes due to valley breezes and upslope winds, which at the typical resolution of most transport models cannot be accurately represented (see also Section 2.3.1). It is, therefore, usually preferable to use nighttime values (e.g. 0 – 4 AM local time) at mountain sites, when there is subsidence over the mountains and downslope winds prevail. For other sites, however, it is preferable to use daytime afternoon (e.g. 12 - 16 local time) values, when the atmospheric boundary layer is well developed (Bakwin et al., 1998b; Steiner et al., 2024b), its height well captured in meteorological data sets and vertical gradients in mixing ratios minimal inside the boundary layer. In inverse modelling, observations can be averaged to reduce computational cost and noise as well as to find a meaningful balance between modelled and observed resolutions. Any averaging interval has to preserve the information relevant for flux estimation while not underestimating errors or introducing biases. It is important to consider the variability meant to be captured in the top-down estimates and this will vary depending on the modelled region and greenhouse gas. For several species, a common set-up is to use daily mean afternoon values at least for non-mountain sites.

7.1.3. Model representation and uncertainty

An issue with mountain sites, is the representation of the observations in model simulations. Complex terrain may not be well captured in a model owing to the finite resolution to which the topography is averaged (smoothed) over each grid cell. This can lead to significant differences between the model and actual elevation of an observation site and thus significant transport error. For instance, if the site's vertical coordinate in the model is given as the height above ground level, this may place the site too low if the model topography is lower than in reality. On the other hand, if the vertical coordinate is given as the height above sea level this may place the site too high above the model surface. This error can be reduced by adjusting the height used to represent an observation in the simulation to one that is more representative of the observation. A common approach is to use the average between the model surface altitude and the site's actual altitude e.g. (Henne et al., 2016) .

Another issue can arise with coastal sites, which when represented by the closest grid cell (in a Eulerian model) to the site's coordinates may incorrectly place the site in the ocean depending on the model resolution and land-sea boundary. This can result in an inaccurate representation of the site by the model. Thus, for coastal sites it is important to check if the grid cell selected is the most appropriate. Furthermore, observations at

This project has received funding from the European Union's Horizon Europe research and innovation programme under grant agreement No 101081395

coastal sites may be influenced by land/sea breeze oscillations that may not be well captured by a model, and thus some data selection may be needed to assimilate only observations, which the model can represent (Ahmadov et al. 2007).

Further discussion on how to account for observation space uncertainties is given in Sections 2.3.1 and 2.3.2.

7.1.4. Calibration scales and data quality

Calibration can be an important source of uncertainty, especially for gases with very low ambient levels and for isotopes. Small calibration offsets between laboratories or from a single laboratory over time can be misinterpreted as signals and impact emission quantification and trend estimation, (e.g. Levin et al., 2012). Umezawa et al. (2018) reported significant offsets of δ^{13}C-CH_4 (0.5 ‰) and δD-CH_4 (up to 13 ‰) measurements among data sets from different laboratories and Dasgupta et al. (2025) provide calibration scale correction factors and data on a harmonized calibration scale. Several calibration scales for N_2O exist with average differences up to 0.23% (Hall et al., 2007). Guillevic et al. (2018) provided calibration standards for halogenated greenhouse gases showing differences up to 9% to existing scales. Given these large differences between observations from multiple networks and laboratories, correction of data by offsets or calibration scales is required to reduce bias and uncertainty of posterior emission estimates in atmospheric inversions.

Data quality can also be a significant issue for some species, especially those that are technically more challenging to measure, such as N_2O. This problem, especially for N_2O, is exacerbated by the fact that the mixing ratio gradients in the atmosphere (the signal) are relatively small compared to the precision and repeatability (noise) of the observations, resulting in a low signal-to-noise ratio. Some datasets provide quality flags indicating problematic observations, and these should be used to remove invalid observations. However, often there can still be problematic observations that have not been flagged, therefore, all observation timeseries should be checked for physically improbable values, e.g., values far below the baseline in a long-lived gas, or step jumps in the baseline and filtered.

7.2. Satellite observations

7.2.1. Context

Driven by sustained and substantial investments from major space agencies (most notably NASA, ESA, and JAXA) satellite-based monitoring of greenhouse gas (GHG) mixing ratios has undergone rapid and transformative progress over the past decade. What was once an experimental capability has evolved into a mature and increasingly operational component of the global GHG observing system. Satellite “flux mappers” now routinely provide measurements of atmospheric CO_2 and CH_4 atmospheric column mixing ratios with spatial resolution, accuracy, and coverage that are directly relevant for regional-to-global monitoring applications (Jacob et al., 2022). These observations support the quantification of emissions and sinks, trend detection, and the independent verification of national and sub-national inventories (Byrne et al. 2023; Deng et al. 2025).

The first generation of space-based GHG instruments emerged in the early 2000s with missions such as SCIAMACHY and IASI, which demonstrated the feasibility of retrieving

This project has received funding from the European Union’s Horizon Europe research and innovation programme under grant agreement No 101081395

column-averaged CH_4 mixing ratios from space (see Figure 7.1). This capability was significantly advanced in the 2010s through dedicated missions including GOSAT-1 and GOSAT-2 (CH_4 and CO_2), OCO-2 and OCO-3 (CO_2), and the imaging spectrometer TROPOMI (CH_4). These missions marked a step change in data quality, spatial coverage, and retrieval precision. The current and upcoming decade is characterized by further expansion and consolidation of this observing capacity. New missions such as Sentinel-5, GOSAT-GW, MicroCarb, and the next-generation IASI (all launched in 2025) are extending observational continuity, spectral capability, and spatial detail. Looking ahead, planned missions including CO2M and MERLIN will further enhance the ability to monitor anthropogenic CO_2 and CH_4 emissions with unprecedented sensitivity and revisit frequency. In contrast to CO_2 and CH_4, current satellite retrievals of N_2O remain too imprecise and too insensitive to the lower troposphere to be useful for atmospheric inversions for flux estimation (Bösch et al. 2026).

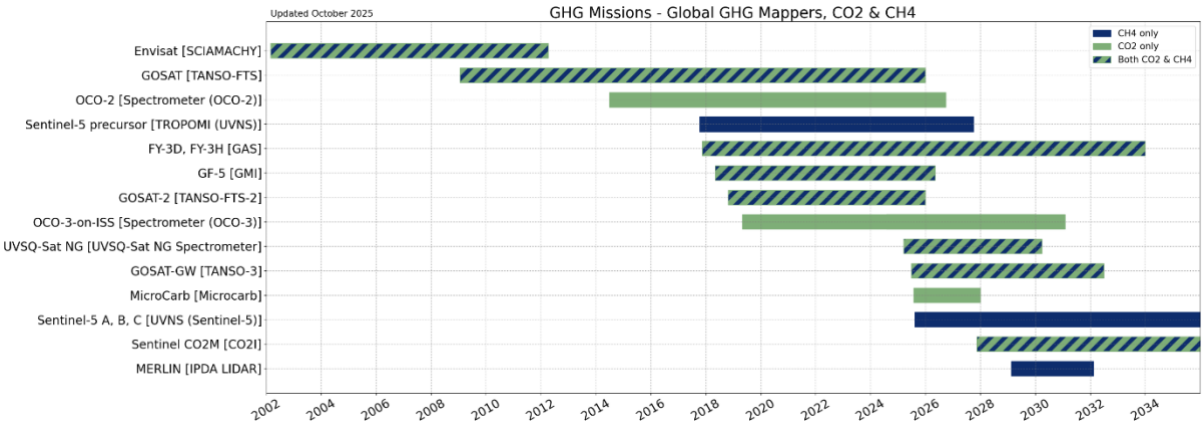


Figure 7.1: Overview of GHG monitoring satellite missions from years 2000s to 2030s (from the Committee on Earth Observation Satellites; https://database.eohandbook.com/ghg/).

Across successive generations of instruments, the spatial resolution has improved dramatically from sparse sampling with large footprints separated by several hundred kilometers to imaging at kilometer-scale resolution. At the same time, swath widths have expanded to several hundred or even thousands of kilometers, enabling near-global daily coverage (Jacob et al., 2022). Advances in spectroscopy, calibration, and retrieval algorithms have also led to steadily improving accuracy and precision, increasing confidence in the robustness and policy relevance of satellite-derived GHG data. Together, these developments signal a transition toward a sustained, reliable, and increasingly operational satellite-based capability for greenhouse gas monitoring at scales relevant to climate science, emissions reporting, and international climate policy.

In contrast to ground-based in situ observations, satellite remote-sensing platforms do not measure GHG mixing ratios directly. Instead, satellite observations rely on the analysis of high-resolution spectra of solar radiation that is reflected by the Earth's surface or scattered within the atmosphere. These spectra contain absorption features associated with specific gases, from which atmospheric composition can be inferred. The retrieval of greenhouse gas information from satellite measurements is performed using radiative transfer models that simulate the interaction of radiation with the atmosphere and the surface. These models require detailed ancillary information on atmospheric state variables, including pressure, temperature, water vapour, aerosols,

This project has received funding from the European Union's Horizon Europe research and innovation programme under grant agreement No 101081395

cloud properties, surface albedo and the concentrations of multiple trace gases (Schneising et al. 2019). Retrieval algorithms then iteratively adjust the atmospheric parameters, specifically the vertical mixing ratio distribution of the species of interest, to minimize the mismatch between simulated and observed spectrograms. However, the information content of the measured spectra is typically limited to the total column abundance of the target gas. In most cases, the number of independent degrees of freedom contained in a spectrum is not enough to resolve the vertical structure of greenhouse gas concentrations. As a result, satellite datasets usually do not address the vertical profile. The vertical profile that is used in the retrieval relies primarily on a priori assumptions. Because of this, satellite data products generally report vertically integrated quantities, such as total or column-averaged dry-air mixing ratios (equivalently mole fractions (e.g., XCO_2 or XCH_4)), rather than full vertical profiles. These column products are not directly comparable to model-simulated mixing ratios or point-based in situ observations, and such comparisons require appropriate processing of model or observed data. Further details on the comparison between atmospheric models and satellite observations are provided in Section 7.2.2.

The sensitivity of a satellite retrieval to mixing ratios at different altitudes is characterized by the so-called averaging kernel. Averaging kernels provide a compact, approximately linear representation of how true atmospheric mixing ratios are mapped onto retrieved quantities by the inverse retrieval algorithm process. However, averaging kernels depend on the specific retrieval algorithm, spectral configuration, and assumptions used, and are, therefore, not directly comparable across different satellite products or even retrievals from the same product. Recognizing these challenges, significant efforts have been undertaken in recent years to harmonize data formats, retrieval diagnostics, and documentation to facilitate the use of satellite GHG products by the atmospheric modelling and inverse modelling communities. Notably, initiatives such as the ESA Greenhouse Gas Climate Change Initiative (GHG-CCI) (e.g. Buchwitz et al., 2015) have played a central role in standardizing retrieval outputs and uncertainty characterization. These advances have made it possible to robustly and efficiently integrate satellite-derived greenhouse gas datasets into atmospheric inversion systems for GHG flux estimation and monitoring.

7.2.2. Representation in atmospheric transport models for inversions

The satellite GHG retrievals are sensitive to various inputs and set-ups of the retrieval methods, which need to be considered carefully when the retrievals are assimilated in atmospheric inversions. As mentioned in Section 7.2.1, the retrieval products have different temporal, spatial and vertical resolutions, error characterization, averaging kernels, surface pressure and sensitivities to e.g. albedo. All these affect the flux inversion results because they influence the retrieved column mixing ratios and hence the model-observation mismatches (Patra et al., 2021a; Schuh et al., 2019; Sicsik-Paré et al., 2025; Tsuruta et al., 2025; Ward et al., 2025). Therefore, it is recommended, wherever possible, to test inversions with different retrieval datasets to obtain a robust estimate of the fluxes.

Data filtering before assimilation is also important to avoid misattribution of the fluxes by poor quality data or model representation. The satellite retrieval data often provide metrics to help data filtering, and it is recommended to take only the best quality data. In

This project has received funding from the European Union's Horizon Europe research and innovation programme under grant agreement No 101081395

addition, there are a number of other considerations when comparing models with retrievals: 1) the surface pressure and pressure layers, 2) the retrieval averaging kernels (AKs), and 3) model transport and retrieval errors. These are discussed in more detail below.

1. Surface pressure and pressure layers: The retrieval surface pressure may be significantly different from that in an atmospheric transport model, especially in areas with very heterogeneous topography, or more generally high-altitude areas (Kiel et al., 2019). The differences in the surface pressure may lead to different total column mixing ratios between the retrievals and model estimates. Moreover, to apply the retrieval AKs (see point 2 below), the model vertical mixing ratio profiles need to be interpolated to match the retrieval pressure layers. The interpolation, and any difference between the retrieval and model surface pressure, may lead to changes in the model total column mixing ratio. Therefore, a correction should be applied to the modelled column mixing ratios to maintain mass balance. This correction, α, can be calculated according to:

$$\alpha = \frac{\langle \boldsymbol{v}_m, \boldsymbol{z}_m \rangle}{\langle \boldsymbol{v}_r, \boldsymbol{z}_r \rangle} \frac{\sum \boldsymbol{z}_{r,i}}{\sum \boldsymbol{z}_{m,i}} \quad (7.1)$$

where $\boldsymbol{v}_m$ is the model mixing ratio profile, $\boldsymbol{v}_r$ is the model mixing ratio profile interpolated to the retrieval pressure layers, $\boldsymbol{z}_m$ is a vector of the thicknesses of the model pressure layers, and $\boldsymbol{z}_r$ is a vector of the thicknesses of the retrieval pressure layers.

2. Averaging kernels: AKs from the retrievals are a key component that represents how dependent the retrieved column mixing ratio is on the prior profile used in the retrieval, and how strongly the retrieval of mixing ratios in different vertical layers in the atmosphere depend on mixing ratios in other layers (see also Section 7.2.1). Therefore, it is essential to take into account the AK when comparing retrievals with modelled total column mixing ratios e.g. (Rodgers and Connor, 2003) (see Figures 7.2 and 7.3). The modelled total column can be adjusted for comparison using:

$$c_m = c_{prior} + (\boldsymbol{w} \circ \boldsymbol{a})^T \left(\boldsymbol{v}_m - \boldsymbol{v}_{prior} \right) \quad (7.2)$$

where c_m is the adjusted modelled column value, c_{prior} is retrieved prior column value, $\boldsymbol{w}$ is a pressure weighting function, $\boldsymbol{a}$ is a column vector of averaging kernel profiles, $\boldsymbol{v}_m$ and $\boldsymbol{v}_{prior}$ are modelled and retrieved mole fraction values at each model or retrieval layer. The column AK can be derived from the full AK matrix by:

$$\boldsymbol{a}_i = \sum_j \mathbf{A}_{ij} \frac{\Delta z_i}{\Delta z_j} \quad (7.3)$$

where $\mathbf{A_{ij}}$ is the full averaging kernel matrix, Δz_i and Δz_j are the effective thickness of the pressure levels. To apply the AK, the model mixing ratio profile, $\boldsymbol{v}_m$ needs to be interpolated to retrieval layers (see point 1).

3. Model transport and retrieval errors: Despite significant recent developments in transport models and bias corrections of the retrieval data (e.g. Schneising et al., 2025), the transport model representations of tropopause height and stratospheric transport and chemistry may be poor (Krol et al., 2018; Tsuruta et al., 2023a) and the retrieval data may be subject to spatial or temporal biases due to lack of validation data (Lindqvist et al., 2024; Sha et al., 2021). These could lead to errors due to the differences between prior profiles, and large differences between the modelled and retrieved column values that can lead to erroneous corrections to the prior fluxes. There is no standard way to

This project has received funding from the European Union's Horizon Europe research and innovation programme under grant agreement No 101081395

handle such errors, but one could: i) apply regional or seasonal correction factors to the retrieval data (Houweling et al., 2017; Wang et al., 2022), ii) optimize multiple tracers simultaneously by ratio methods (e.g. CO_2:CH_4 using GOSAT; Palmer et al., 2021; Pandey et al., 2015) or iii) simply discard retrievals from the most problematic regions and/or times (Baray et al., 2021; Lu et al., 2022).

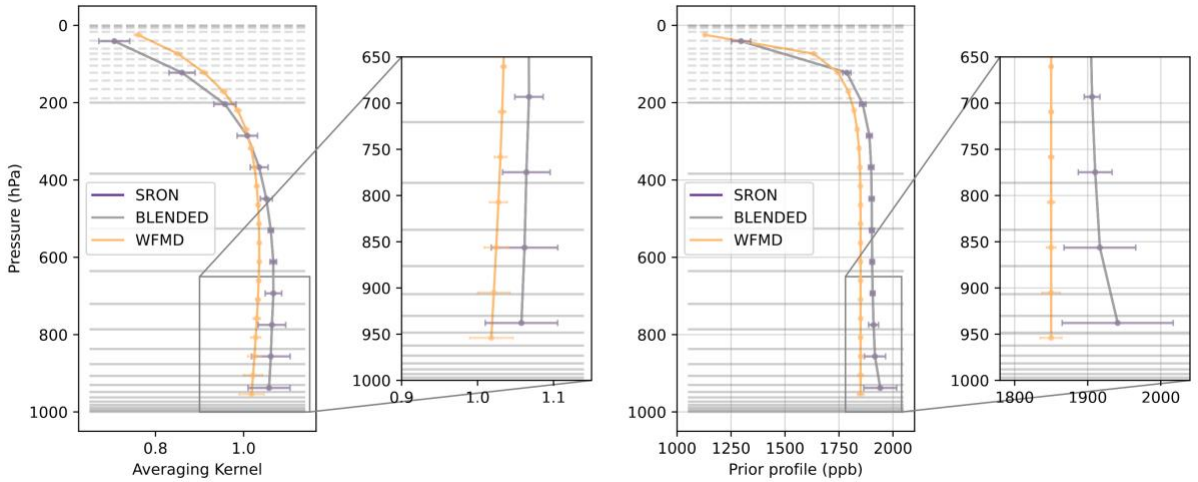


Figure 7.2: Example averaging kernels and prior profiles of different TROPOMI retrieval products, 2019 over Europe. The averaging kernel sensitivity tells that the retrievals are more sensitive to layers close to the surface. SRON and BLENDED retrieval products share exactly the same profile. The right panels of prior profiles illustrates that part of differences that appear in XCH4 values from different retrieval products come from the prior profiles of the retrievals. (Figure courtesy of Sicsik-Paré et al., 2025)

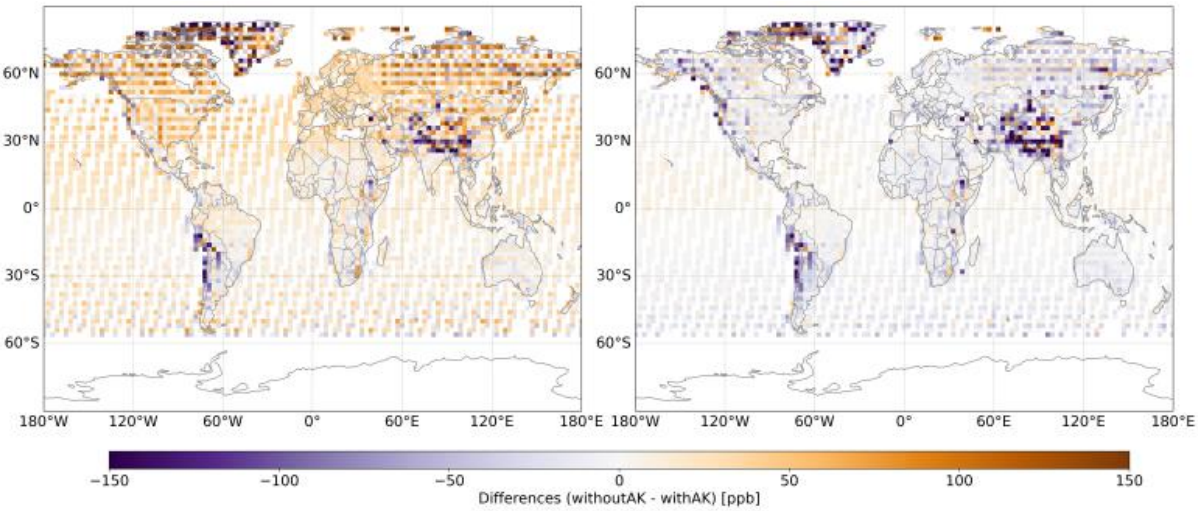


Figure 7.3: Example illustrating the effects of applying AKs to modelled total (left) and lower-tropospheric partial (right) column CH_4 against JAXA/EORC GOSAT v3.0 data. The positive values indicate higher modelled values without averaging kernels applied compared to those with averaging kernels.

This project has received funding from the European Union's Horizon Europe research and innovation programme under grant agreement No 101081395

7.2.3. Data processing and uncertainty propagation for inversions

As the number of retrievals in satellite data products are extensive, the inversion system may not be able to handle all the data, such that the system becomes computationally too expensive. In particular, for Lagrangian transport models, the inversion requires source-receptor-relationships (SRRs) (see Section 2.1.1) to be calculated for all the retrievals, which can be a very large number.

One effective and rather straight-forward way to reduce the computation cost is to average the retrievals. Averaged retrievals are sometimes called *super-observations*. This approach has been taken for assimilation of medium-resolution satellite data such as OCO-2 and TROPOMI. The level of aggregation may be subjective. For example, OCO-2 data have been averaged in time over 10 seconds (Baker et al., 2021; Crowell et al., 2019) while TROPOMI data have been averaged in space to 0.5° to 2.0° grid cells in line with atmospheric transport model resolutions (Chen et al., 2022; Tsuruta et al., 2023b; Ward et al., 2025). An alternative approach is to base the averaging on the heterogeneity of the retrieved mixing ratios leading to variable spatial resolution according to the variability of the mixing ratios (Thompson et al., 2025).

In addition, Thompson et al., (2025) introduced a new computationally efficient method to model total column observations, such as those from satellites, using a Lagrangian transport model, thus reducing the cost of assimilating satellite data into Lagrangian-based inversion frameworks. There is an urgent need for such solutions in all Lagrangian-based inversion frameworks considering the acceleration of the amount of satellite data in the future missions and the increasing resolution of the footprints.

Another concern in assimilating satellite data is the uncertainty propagation in observation space, i.e. definition of observation error covariance matrix, **R**. As mentioned in Section 2.5, **R** should contain both observations and transport model errors. Regarding the observation error, there are mainly two aspects to consider: 1) the uncertainty of the retrievals or super-observations and 2) how to account for correlated errors.

In super-observations (Rijsdijk et al., 2025), due to aggregation, the observation uncertainty may also be reduced if the retrieval errors are largely random, i.e., not correlated. In this case, the observation uncertainty is often calculated as the variance (square of the standard deviations) of the total or partial column values in each super-observation (Crowell et al., 2019; Tsuruta et al., 2023; Thompson et al., 2025) or by propagating the individual retrieval errors assuming some partial correlation between them (Baker et al., 2021; Vojta et al. 2026). It is also possible to estimate the errors using hierarchical Bayesian methods (Ward et al., 2025) (see also Section 2.5).

It is also the case that unlike the ground-based observations where the observation errors can be considered largely random, the errors in the satellite retrievals are often strongly correlated due to the underlying retrieval methods. However, as described in Section 2.5, it is not possible to include off-diagonal terms in the observation error covariance matrix, **R** for some inversion methods, and in others it could greatly increase the computational demand. In such cases, the observation error covariance matrix is a diagonal matrix, but inflation of the observation error variances can be used to account for correlated errors (Chevallier, 2007; Niwa et al., 2025).

This project has received funding from the European Union's Horizon Europe research and innovation programme under grant agreement No 101081395

8. Uncertainty quantification

Ignacio Pisso

8.1. Purpose, scope and what must be reported

This section explains how to quantify and report the uncertainty in the flux products obtained from an atmospheric inversion. It addresses the following question a user of these products may ask: how uncertain is the top-down estimate, and how was that uncertainty obtained? The mathematical framework, the notation and the inversion methods themselves are given in Section 2 and are not repeated here. The construction of the prior and observation error covariance matrices **B** and **R** is described in Section 2.6.

The uncertainty that matters for emission reporting is the uncertainty of the declared products, typically national or regional totals over a stated period, rather than the full posterior error covariance matrix of the control vector. A good practice is, therefore, to define the reporting products first, and then to decide which uncertainty estimates can be computed for them. Two distinct contributions have to be quantified. The first is the statistical posterior uncertainty implied by **B** and **R** (Section 8.3), whose validity depends on the statistical assumptions of the inversion. Whether these assumptions hold is addressed with the diagnostics of Section 8.4. The second is the systematic uncertainty associated with choices that **B** and **R** do not always represent, such as the prior fluxes, the boundary conditions, the transport model and the observation selection (Section 8.5). Both must be propagated to the spatiotemporal reporting scale (Section 8.6) before they can be combined into a total uncertainty (Section 8.7).

Throughout Sections 8 and 9, the *reference inversion* is defined as the configuration that uses the most plausible available priors, boundary conditions, observations and parameter settings, and whose results and posterior uncertainty are those reported. Sensitivity experiments including twin experiments and alternative configurations are defined and interpreted relative it. Section 8.8 sets out reporting levels that describe how completely the uncertainty of a given product has been characterised, and Section 9 illustrates how these products are used to judge whether, at which scales, and for which periods the results can be trusted.

8.2. Sources of uncertainty and the role of sensitivity analysis

The uncertainty of an inversion result has several distinct origins: the prior fluxes and their assumed error statistics, the observations and their treatment, the boundary and initial conditions, the atmospheric transport, and configuration choices made when setting up the inversion (e.g. resolution, background representation). Typically, only the first two are represented in **B** and **R** (transport is sometimes assumed to be part of **R**), and, therefore, only these are reflected in the formal posterior uncertainty. Before the formal uncertainty is computed, it is good practice to establish which of the remaining choices are relevant for the products being reported. Sensitivity experiments serve this purpose: by varying one element of the set-up at a time and examining the change in the reported aggregates, they identify the influential elements and provide ranges of variation. In practice, this step precedes the formal uncertainty calculation, because it

This project has received funding from the European Union's Horizon Europe research and innovation programme under grant agreement No 101081395

determines which components deserve quantitative treatment and how an ensemble should be designed. The formal posterior uncertainty of Section 8.3 nevertheless remains a standard product produced with a Bayesian estimate, and the two are complementary.

An important limitation must be clearly stated: a sensitivity experiment quantifies the dependence of the result on a choice. It may not on its own identify a bias. Establishing that a result is biased requires information from outside the inversion setup: the analysis of posterior fit residuals (Section 8.4), comparison with observations that were not assimilated (Section 9.4), or comparison with independent flux products and other inversion systems (Section 9.7). Varying parameters within the same modelling framework cannot reveal an error common to all of its configurations.

Ensemble approaches can be used to quantify systematic uncertainty by sampling over uncertain modelling parameters and configuration choices and examining the induced spread in the posterior fluxes. In this context, the ensemble is not primarily intended to represent random posterior covariance (as in ensemble Kalman methods), but rather to represent sensitivity to available choices in priors, boundary conditions, transport, observation selection, etc. This complements the posterior uncertainty estimate that is obtained from the formal random error propagation that the inversion method provides. For emission reporting, this ensemble spread should be interpreted and reported as a systematic uncertainty range unless the sampling design and parameter weighting support a probabilistic interpretation.

For the assessment of parametric uncertainties, Latin Hypercube Sampling (LHS) is a practical and efficient sampling strategy (Helton and Davis, 2003). LHS is a stratified, space-filling variant of Monte Carlo sampling that partitions each parameter's cumulative distribution function into N equiprobable intervals and draws one value from each interval, with the additional constraint that each interval is used exactly once per parameter (Lucas et al., 2017). This design improves coverage of the parameter space compared with simple random sampling and can reduce the number of samples needed to obtain stable uncertainty estimates for aggregated metrics.

Pilot sensitivity inversions are recommended to identify influential parameters and to derive realistic parameter ranges, so that the sampling reflects uncertainty rather than arbitrary variation. Parameter distributions should be chosen to reflect available information. For continuous parameters such as multiplicative uncertainties in prior emissions, boundary condition scaling, or selected observation error inflation factors, Gaussian or lognormal distributions are commonly used allowing realistic variability. For parameters that represent model choices or discrete configurations (for example, the number of control variables, the choice of boundary condition parameterisation, or alternative selections of optimised latitude bands for initial mixing ratio optimization), discrete uniform distributions may be appropriate when there is no basis for preferring one option over another. When discrete choices are included, it is good practice to ensure that the ensemble samples each category sufficiently and often to enable interpretation at the reporting scale.

No universal ensemble size can be recommended for all cases. The number of members should be justified by convergence of the reported aggregates, that is, by demonstrating that the estimated spread stabilises as members are added, and the achieved size and

This project has received funding from the European Union's Horizon Europe research and innovation programme under grant agreement No 101081395

the reason for it should be reported. Ensembles of the order of ten members or less, which computational cost often imposes, may be sufficient to indicate the magnitude of a spread but could give a poorly determined estimate of it, and should be presented with that caveat rather than as good practice.

8.3. Statistical posterior uncertainty

In a linear-Gaussian formulation the posterior error covariance is given by the inverse Hessian of the cost function at the optimum, equation (2.13). Whether it can be computed and stored depends on the solution method and on the dimension of the control vector so a good practice is to define in advance which uncertainty products required for reporting and evaluation, typically regional and temporal aggregates (Section 8.6) and compute those without assembling or archiving the full matrix. In all methods the usefulness of the resulting covariance depends on the specification of **B** and **R** and of the model error, and on the diagnostic checks of Section 8.4. Different equivalent expressions are commonly used:

$$\mathbf{P} = (\mathbf{B}^{-1} + \mathbf{H}^{\mathrm{T}}\mathbf{R}^{-1}\mathbf{H})^{-1} \tag{8.1}$$

$$= \mathbf{B} - \mathbf{B}\,\mathbf{H}^{\mathrm{T}}(\mathbf{H}\,\mathbf{B}\,\mathbf{H}^{\mathrm{T}} + \mathbf{R})^{-1}\mathbf{H}\,\mathbf{B} \tag{8.2}$$

$$= (\mathbf{I} - \mathbf{A})\,\mathbf{B} \tag{8.3}$$

The first form requires the inversion of an $N \times N$ matrix and the second of an $M \times M$ matrix, so the choice between them is computational, as it is for the state estimate in equations (2.18) and (2.19). The third expresses the posterior covariance in terms of the averaging kernel **A** of equation (2.16).

The degrees of freedom for signal (DoFS) quantify how many independent pieces of information the observations contribute about the control vector, and are obtained as the trace of the averaging kernel matrix **A** defined in equations (2.16) and (2.17), $\mathrm{DoFS} = \mathrm{tr}(\mathbf{A})$. Equivalently $\mathrm{DoFS} = n - \mathrm{tr}(\mathbf{B^{-1}P})$, where n is the dimension of the control vector, so that they can be evaluated from the prior and posterior error covariances where **A** is not formed explicitly. A closely related quantity is the uncertainty reduction, which for a given aggregate is defined as one minus the ratio of the posterior to the prior uncertainty. A value near zero indicates that the observations have added little to the prior, and a value approaching one that the posterior is determined almost entirely by the observations. Like the degrees of freedom for signal, it describes how strongly the result is constrained rather than constituting an uncertainty in its own right. Both are interpreted in Section 9.2.

This project has received funding from the European Union's Horizon Europe research and innovation programme under grant agreement No 101081395

Table 8.1: Posterior uncertainty products available from each method family. For the advantages and limitations of the methods themselves see Table 2.2.

Method family	**Posterior uncertainty product**	**Must be documented**
Matrix based analytical methods	**P** computed directly from (8.1) or (8.2), full matrix available	the form used (N- or M-form) and any linearisation
Sequential Kalman methods	**P** updated at each step (equation 2.28), available by construction	the model error covariance and the grouping of the observations
Gradient-based methods	**P** not assembled, approximated from Hessian-vector products in a reduced subspace	the approximation, the preconditioner, the iteration count and the stopping rule
Markov Chain Monte Carlo	posterior sampled directly, covariance and non-Gaussian features from sample statistics	burn-in discarded, treatment of autocorrelation, and effective sample size
Ensemble Kalman filters and smoothers	**P** approximated by the sample covariance of the analysis ensemble	ensemble size, localisation and inflation

In gradient-based methods the Hessian is never assembled, and the posterior covariance is recovered only within the subspace explored by the optimisation. Directions the iterations do not explore are not represented. Such estimates should therefore be reported with the approximation, the preconditioning and the stopping criterion stated, and checked for robustness against an alternative approximation. Preconditioning with a square root factor of **B** (Chevallier et al., 2005; see Section 2.5.3.3) improves the conditioning of the Hessian and reduces the number of iterations needed both for the optimisation and for any subsequent uncertainty calculation (Nocedal and Wright, 2006).

In sampling and ensemble methods the covariance is an empirical property of the sample rather than a quantity derived from the cost function. In each ensemble realisation, both the prior fluxes and the atmospheric observations are perturbed according to their prescribed uncertainties (as specified by **B** and **R**, respectively). The inversion is run for each perturbed member, producing an ensemble of posterior solutions. This allows non-Gaussian uncertainty to be represented where the sampling is adequate, but makes the estimate sensitive to the sample size: finite ensembles introduce sampling noise and spurious correlations, so localisation and inflation are commonly applied, and because these choices change the implied covariance they must be documented (Section 9.8).

A distinction has to be made between two uses of an ensemble of inversions started from different prior fluxes. If the priors are random draws consistent with the prior error covariance matrix, that is if their departures from an assumed truth sample $\mathcal{N}(0, \mathbf{B})$ while

This project has received funding from the European Union's Horizon Europe research and innovation programme under grant agreement No 101081395

the assimilated observations are perturbed consistently with $\mathcal{N}(0, \mathbf{R})$, then the spread of the resulting posterior estimates is an estimate of the statistical posterior uncertainty and is equivalent to the covariance given by equation (2.13). This Monte Carlo construction (Chevallier et al., 2007b) is the standard estimate of posterior uncertainty when the control vector is too large for the covariance to be computed explicitly, and it has been applied at European scale by, among others, Kadygrov et al. (2015). If instead the priors are in essence different products, such as alternative inventories or alternative process based models, they are not draws from a specified distribution. Their spread measures the sensitivity of the result to the choice of prior rather than its statistical uncertainty, and it is treated in Section 8.5. The two are complementary and should not be mixed into a single ensemble.

The distinction has a consequence that is useful for evaluation. If **B** is specified so as to cover a plausible range of priors, posterior estimates obtained from any plausible prior should fall within the posterior uncertainty derived from the reference inversion. Where they do not, either **B** is too narrow to represent the structural uncertainty in the prior, or one of the prior products is not consistent with the assumptions made in constructing **B**. Section 9.5 uses this comparison as an interpretation rule.

8.4. Statistical diagnostics

In the set-up of inversions several design choices have to be made on a priori and data uncertainties, for which limited information is available. Yet these choices are critical for the posterior solution that is obtained and the validity of the uncertainty that is computed using the methods described in the previous section. In the Bayesian inversion framework the posterior uncertainties are independent of the values of the a priori fluxes and the values of the measurements that are used, which is, therefore, true also for the errors in those values. Only if the assumed uncertainties reflect the statistics of these errors can the posterior uncertainty reliably reflect the error statistics of the posterior solution. To make sure that the assumed uncertainties reflect the statistics of the errors, statistical tests are available that should be used to check the statistical consistency of the inversion set-up.

The most common test to be used is the χ^2 test, which tests if the cost function value corresponds to the mean of the corresponding χ^2 distribution, which the cost function can be proven to obey (Section 2.6). If $J(\mathbf{x})$ is larger than its expected value, **R** and/or **B** are underestimated, so the posterior uncertainty is underestimated too (and conversely). Because many assumptions are only approximations, the χ^2 test should be seen as a consistency diagnostic, not a proof that the inversion is correct. The diagnostic should not be interpreted as exactly $2J/k = 1$; values of $2J$ around k are expected, with a spread of approximately $(2k)^{1/2}$, so the reduced value $2J/k$ should be assessed relative to its expected sampling variability, approximately $(2/k)^{1/2}$.

The logic of the χ^2 test can also be applied to subsets of the cost function to diagnose which subset of the data might not be fitted as expected from χ^2 statistics. It is advised to analyse fit residuals per measurement site. If the **R** matrix is assumed to be a diagonal matrix then the fit residuals are expected to be randomly distributed. Deviations from this assumption can point to problems in the inversion setup, or in the design of the **R** matrix. The same logical applies to the residuals between a posteriori and a priori fluxes in

This project has received funding from the European Union's Horizon Europe research and innovation programme under grant agreement No 101081395

relation to the **B** matrix. If the neglect of error-covariance in the **R** matrix is the cause of statistical inconsistencies, which is computationally prohibitive to repair then error inflation can be a solution (Chevallier, 2007a).

Additional guidance on the origin of deviations from the χ^2 test can be obtained following the diagnostic tests proposed by Desroziers et al. (2005). These diagnostic tests use the residuals between data and prior, data and posterior, and posterior and prior - that are readily available from inversion output - to separately verify and correct the **R** and **B** matrix contributions to the χ^2 test. Michalak et al. (2017) provides further information on diagnostic testing of inversion output.

A failed diagnostic is a reason to revise the set-up rather than to add an uncertainty term. The diagnostics reported for an inversion should be stated together with its results, and they are the first evidence considered when the evaluation of Section 9 is carried out.

8.5. Systematic components

Posterior uncertainty derived from the assumed prior and observation error covariances (**B** and **R**) quantifies the random component of uncertainty under the statistical assumptions of the inversion. In practical atmospheric inversions, additional error sources can introduce biases or correlated errors that are not adequately represented by **B** and **R** and, therefore, are not captured by the posterior error covariance. These systematic effects can arise from the prior flux estimates, from boundary conditions, from transport and mixing, from the observation operator (e.g., sampling, representativeness), and from biases in the observations themselves. A good practice is to treat the assessment of systematic errors as a complementary step to the formal posterior covariance calculation described in Section 8.1. The aim is to quantify how sensitive reported flux aggregates (Section 8.6) are to variations in key modelling elements and to communicate this sensitivity, using the same aggregated quantities that will be used for emission reporting. When reported flux products are specified (e.g., national annual totals) a systematic error assessment can be performed for these products. For each error source, the assessment can be based on a set of adequate perturbations. The resulting changes in the reported aggregates can then yield uncertainty ranges, separated by error category where possible.

8.5.1 Prior fluxes

Systematic errors related to the prior can be assessed by testing alternative available prior flux products, alternative temporal flux profiles, and alternative spatial distributions when these are known to be uncertain. This may include alternative inventories, alternative sector partitioning, or alternative treatments of temporal aggregation. For biospheric fluxes, this may include alternative process models or models run with alternative parameter sets. Where the inversion optimises flux multiple components simultaneously, systematic effects can also arise from imperfect separation of components (for example, compensation between anthropogenic and biogenic terms). Sensitivity tests can explore this partitioning and inform whether the flux totals are robust to alternative prior partitions.

This project has received funding from the European Union's Horizon Europe research and innovation programme under grant agreement No 101081395

8.5.2 Boundary and initial mixing ratios

A key systematic error source are the spatiotemporal time variability and biases in initial (background) conditions and boundary conditions especially for regional inversions. Particularly for long-lived gases where advected background and boundary mixing ratio variations in space and time can be comparable to local flux signals, differences in the input initial/boundary mixing ratios can be a major source of differences in the observation-model mismatch and hence the posterior fluxes. Systematic errors in boundary conditions can reflect biases or inadequate scaling in global model fields, errors in stratosphere–troposphere exchange, or limitations of the resolution used in the inversion. Sensitivity tests can quantify how robust flux estimates are to alternative initial/boundary mixing ratio products. Good practice includes: i) testing alternative boundary-condition products where available, ii) including boundary-condition parameters in the control vector when feasible (so that boundary corrections are estimated jointly with fluxes rather than imposed), and iii) evaluating boundary conditions using independent observations that are sensitive to background (e.g., background sites, aircraft profiles, or remote marine observations). The impact of boundary condition choices should be reported for the same aggregates used for emission reporting.

To test the sensitivity to the boundary mixing ratios, it is useful to examine the results using different values at the boundaries. The sensitivity distinguishes between standard posterior uncertainty and the additional sensitivity range induced by boundary condition alternatives. Boundary mixing ratio influences can be assessed using: i) differences in posterior grids and country totals between boundary condition alternatives and ii) differences in forward-model performance against independent observations when the boundary conditions are varied.

8.5.3 Transport

Transport uncertainty is an important contributor to systematic inversion differences, also for country/regional scale attribution. Sensitivity experiments and ensembles can quantify how posterior country totals and their covariances change when meteorological forcing is perturbed. This can be achieved through meteorological ensembles and model-model comparisons. Transport and mixing errors can have a large influence in atmospheric inversions. These errors affect both the model-observation mismatch and the correlations, and they can cause biases and spurious variability in flux estimates if not adequately represented in the **R** matrix.

The meteorological ensemble benchmarking reports the differences in posterior grids/country totals that can be attributed to meteorological variability. For reporting support, the resulting sensitivity range for national annual totals and for seasonal differences can be relevant.

Two complementary strategies are recommended. The first is the use of ensembles of meteorological drivers, for example by running the transport model with multiple wind field realisations or analyses and quantifying the spread in the posterior fluxes. This approach is valuable when the meteorological ensemble can represent uncertainty in synoptic flow, boundary-layer mixing, and transport pathways. The second is model–model comparison, in which inversions are repeated using different transport models or

This project has received funding from the European Union's Horizon Europe research and innovation programme under grant agreement No 101081395

different configurations of the same model (e.g., resolution, boundary-layer parameterisations, convection, sub-grid mixing).

8.5.4 Observations

Observation-related systematic errors can also be considered explicitly, especially when inversions combine different measurement types (in situ, aircraft, satellite), span heterogeneous sites, or combine measurements from different networks with different calibration scales. Biases can arise from calibration offsets, retrieval biases, site representativeness, or unresolved sub-grid variability. Good practice includes using independent information where available and exploring sensitivity to observation selection and filtering criteria. Where a persistent bias is suspected, one option is to include explicit bias parameters (e.g., site offsets or retrieval bias corrections) in the control vector e.g. (Corazza et al., 2011). Differences between surface and satellite data must be taken into account. The characterisation of these errors is described in Sections 7.1.4 and 7.2.3; what matters here is their propagation into the flux uncertainty. However, the risk of compensating errors remains, and the adopted strategy should be documented together with diagnostics showing that the bias treatment improves consistency with independent data.

8.5.5 System settings

A final group of systematic effects arises from the way the inversion problem is set-up rather than from its inputs: the resolution/discretisation of the control vector, the settings of the background (discretisation in space, transport time from sources), and the inversion framework and transport model themselves (see Sections 2.4.1.1 and 2.4.1.2). These choices are not represented in **B** or **R** and are the hardest systematic component to bound from within a single system, since a framework cannot readily explore configurations it does not support; in practice they are approached through comparison with other systems (Section 9.7), and where they cannot be quantified this should be stated explicitly (Section 8.8).

8.6. From grid-cell uncertainty to regional and national uncertainty

Inversions yield fluxes and uncertainties on a grid, whereas emission reporting usually requires totals for countries or regions over defined periods. The uncertainty of the aggregate is not the sum of the grid cell uncertainties, because the errors of neighbouring cells are correlated, and a good practice is to propagate the uncertainty explicitly rather than to combine grid cell standard deviations.

Aggregation is expressed as a linear operator. Let $\boldsymbol{w}$ be the vector whose elements give the contribution of each control variable to the aggregate, based on a country or region mask: for a country total these are the fraction of each grid cell lying within the country multiplied by the cell area, and zero elsewhere, with the corresponding weights for the time steps included in the reporting period. The aggregated flux is then $\boldsymbol{w}^{\mathrm{T}}\boldsymbol{x}$, and where the posterior error covariance matrix **P** is available the variance of the aggregate is

$$\sigma_{agg}^2 = \boldsymbol{w}^{\mathrm{T}}\mathbf{P}\,\boldsymbol{w} \tag{8.4}$$

which reduces to the sum of the elements of **P** weighted by the corresponding products of weights. Units must be consistent between $\boldsymbol{x}$ and $\boldsymbol{w}$: where $\boldsymbol{x}$ is a flux density, as

This project has received funding from the European Union's Horizon Europe research and innovation programme under grant agreement No 101081395

inversions usually deliver it, the grid cell area and the length of the reporting period are carried in $\boldsymbol{w}$ as described above; where $\boldsymbol{x}$ is instead the flux already integrated over the cell and over the period, $\boldsymbol{w}$ reduces to the mask fractions alone. Either convention is acceptable provided $\boldsymbol{w}^{\mathrm{T}}\boldsymbol{x}$ has the units of the reported total. Off-diagonal terms are essential. The uncertainty of an aggregate cannot exceed the sum of the grid cell standard deviations, and equals it only if the errors are perfectly correlated. Where the posterior errors of neighbouring cells are anti-correlated, as is common, it is smaller than their combination in quadrature as well. This is why aggregated estimates are more robust than gridded ones (see Section 10.5.2). The same construction gives the covariance between two aggregates. If $\boldsymbol{w}_a$ and $\boldsymbol{w}_b$ are the weight vectors of two regions, the posterior error covariance of their totals is $\boldsymbol{w}_a{}^{\mathrm{T}}\boldsymbol{P}\,\boldsymbol{w}_b$, which reduces to (8.4) when the two regions coincide. Collecting the weight vectors of all reporting regions as the columns of a matrix **W** gives the full region-region covariance matrix in a single operation,

$$\mathbf{P}_{reg} = \mathbf{W}^{\mathrm{T}}\mathbf{P}\,\mathbf{W} \qquad (8.5)$$

a $K \times K$ matrix whose diagonal elements are the variances of (8.5) and whose off-diagonal elements are the covariances between regions. The resulting country-country covariance matrix, or the correlation matrix derived from it, is interpreted in Section 9.2.

Where an explicit **P** is not available, the aggregation is performed on each ensemble member and the covariance of the aggregates is estimated from the resulting sample, as in equation 10.9. This applies equally to a posterior ensemble of random draws consistent with **B** and to a sensitivity ensemble of alternative configurations, but these are different: the first estimates the statistical posterior uncertainty, the second a systematic range (Sections 8.3 and 8.5).

Aggregation applies to every uncertainty component, not only to the statistical one. A total uncertainty for a national figure (Section 8.7) requires each component of Section 8.5 to be propagated to the same aggregate with the same operator. Second, the resolution of the control vector limits what can be aggregated meaningfully. For countries whose extent is comparable to the grid cell or smaller, a substantial fraction of the total comes from cells shared with neighbouring countries, and the information constraining them is shared in the same way. The correction estimated for such a country is therefore not separable from that of its neighbours, and both the total and its uncertainty depend strongly on the mask convention adopted. The choice of mask, including the treatment of fractional cells and of offshore areas, is discussed in Section 10.4.1 and should be reported with the results.

8.7. Total uncertainty

Users of inversion products, and in particular inventory compilers, generally need a single uncertainty attached to a reported figure as well as the individual contributions. Combining the components of Sections 8.3 and 8.5 into a total is, therefore, desirable but it requires assumptions that should be stated rather than implied.

The pragmatic approach is to add the components in quadrature, i.e., to take the square root of the sum of their squared standard uncertainties. This is adequate only when three conditions are met: the components are expressed as comparable standard uncertainties rather than as ranges or extreme cases, they refer to the same aggregate



This project has received funding from the European Union's Horizon Europe research and innovation programme under grant agreement No 101081395

and period, and they can be treated as mutually independent. The first two depend on the construction and are achieved by propagating every component to the reporting scale with the same aggregation operator (Section 8.6). The third is an assumption, and it is not always justified: the influence of the boundary conditions and that of transport, for example, both act through the simulated mixing ratios and need not be independent. Where components are known to be correlated, or where a component is a range over a small number of discrete alternatives rather than a standard deviation, quadrature may misrepresent the total and the components should be reported separately instead.

Whatever combination is adopted, the presentation should separate the formal posterior uncertainty obtained for the reference configuration (Section 8.3) from the systematic ranges assessed by category (prior, boundary conditions, transport, observations). If a combined total is provided, the combination rule and its assumptions should be stated explicitly.

8.8. Uncertainty reporting levels

Inversion systems differ in what they can afford to quantify, and a product that reports a single uncertainty is not necessarily better characterised than one that reports several components. To make the degree of characterisation explicit, and comparable between products, it is useful to state the level at which the uncertainty of a product has been reported. The levels below are cumulative: each includes what the previous one requires. They describe the completeness of the uncertainty characterisation, not the quality of the inversion, and they are not related to the tiers of the IPCC inventory guidelines.

- Level 0: central estimate only. Fluxes are reported without a quantified uncertainty. This is acceptable only for preliminary or exploratory results, it must be labelled as such, and it does not support quantitative statements about agreement or disagreement with an inventory.
- Level 1: statistical posterior uncertainty. The posterior uncertainty implied by **B** and **R** is reported for the declared products at the reporting scale (Section 8.3), propagated with a stated aggregation method (Section 8.6). The method used to obtain it, whether a posterior covariance matrix or an ensemble, and its assumptions are stated. The consistency diagnostics of Section 8.4 are reported with it.
- Level 2: quantified systematic components. In addition to Level 1, the sensitivity of the reported products to the main input choices is quantified separately and at the same aggregate: prior fluxes, boundary and background mixing ratios, transport and meteorology, and observation selection and filtering (Section 8.5). Each component is reported individually, with the alternatives that were tested.
- Level 3: combined total uncertainty. In addition to Level 2, a total uncertainty is reported for the declared products, with the combination rule and its assumptions stated (Section 8.7), together with an assessment (quantitative where possible, otherwise qualitative but explicit) of the components that remain hard to quantify, such as structural differences between inversion systems, non-Gaussian and nonlinear effects, and sectoral attribution.

This project has received funding from the European Union's Horizon Europe research and innovation programme under grant agreement No 101081395

Three rules should apply across the levels. First, constraint diagnostics (uncertainty reduction, degrees of freedom for signal, and averaging kernels where they can be computed) are not an uncertainty component but describe how strongly the result is constrained; they should be reported from Level 1 upwards and are used for interpretation in Section 9.2. Second, evidence from independent observations is evaluation evidence rather than uncertainty quantification and belongs to Section 9.4 (it does not by itself raise the level). Third, a product whose reported uncertainty cannot be reproduced from the accompanying documentation (the aggregation method, the masks, the ensemble definition and the versions of the inputs - Section 9.8) should be reported one level lower than the components alone would suggest.

9. Evaluation and benchmarking of inversion results

Ignacio Pisso and Sander Houweling

9.1. Purpose, evaluation strategy and definitions

Section 8 describes how uncertainty and sensitivity products are obtained. This section explains how to use them, together with atmospheric observations and results from other systems, to judge whether an inversion result can be trusted, at which spatial and temporal scales, and for which periods. The question it addresses is not whether the inversion is correct, which cannot be established directly, but whether the evidence available supports the use of a given product for a given purpose.

Three assessment types are distinguished here: i) Evaluation is the general assessment of whether a result is trustworthy and usable and covers everything in this section. ii) Benchmarking is used in the narrow sense of comparing a result against an agreed reference set, in practice an archive of results from other inversion systems (Section 9.7). Since no true flux field exists, such a comparison establishes whether a result lies within the range obtained by others, not whether it is right. iii) Sensitivity studies are the experiments described in Section 8.2 and 8.5, which quantify the dependence of the result on the choices made in the set-up. This section interprets their outcomes (Section 9.5) but does not describe how they are produced. Throughout, the reference inversion has the meaning defined in Section 8.1.

9.2. Assessing the degree of dependence from the prior: uncertainty reduction, DoFS, averaging kernels, covariance between regions

For emission reporting support, it is relevant to what extent posterior flux estimates are constrained by atmospheric observations or, in other words, to what extent they rely on the prior assumptions. Evaluation should, therefore, quantify the degree of dependence on the prior for both gridded fluxes and regional aggregations such as countries. In the linear Gaussian framework this dependence is described by the uncertainty reduction and by *degrees of freedom for signal* (DoFS), which are obtained as set out in Section 8.3, and by the averaging kernel matrix defined in Section 2 (equations 2.16 and 2.17).

The reference inversion (Section 8.1) is described by reporting the posterior uncertainty reduction relative to the prior and the DoFS, which together indicate the strength of the constraint provided by the observation network, at both grid and country scale.) The

This project has received funding from the European Union's Horizon Europe research and innovation programme under grant agreement No 101081395

variables and metadata that should accompany these products are listed in Section 9.8, and the reporting level they correspond to is defined in Section 8.8.

Where the posterior uncertainty is estimated from an ensemble of inversions started from priors drawn consistently with **B**, its spread is an estimate of the statistical posterior uncertainty rather than a sensitivity to the choice of prior. The distinction is set out in Section 8.3 and its consequences for interpretation in Section 9.5. Sensitivity to alternative plausible priors is quantified as described in Section 8.5 and interpreted as described in Section 9.5.

As an example of gridded estimates of uncertainty reduction, Figure 9.1 shows a European domain for N_2O, provided for a reference inversion for a selected year (a single year was selected owing to the computational cost of calculating the posterior uncertainty). These results were obtained using a Monte Carlo method with 50 ensemble members, see Section 8.3.

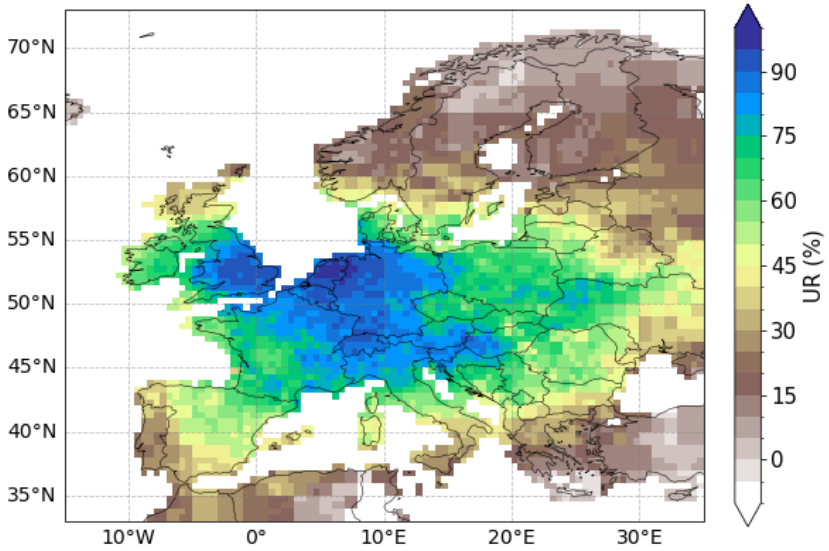


Figure 9.1: Uncertainty reduction for annual mean N_2O fluxes with a 50-member ensemble.

Estimates of uncertainty reduction on annual (or other time period) totals can also be provided aggregated by country. Figure 9.2 shows uncertainty reduction in CO_2 (NEE) fluxes for different countries in Western and Central Europe quantified using a Monte Carlo experiment with 10 ensemble members for a selected year. In this case, the uncertainties associated to the national and annual CO_2 NEE fluxes are strongly reduced by the surface-based inversions.

This project has received funding from the European Union's Horizon Europe research and innovation programme under grant agreement No 101081395



Figure 9.2: Uncertainty reduction in CO_2 (NEE) fluxes for different countries in Western and Central Europe quantified using a Monte Carlo experiment with 10 ensemble members

Results aggregated in space can be visualised also at higher temporal resolution than these annual examples, which may be important depending on the application of the results. This allows the assessment of the uncertainty of the fluxes at, for example seasonal or monthly time scales (Fig. 9.3).

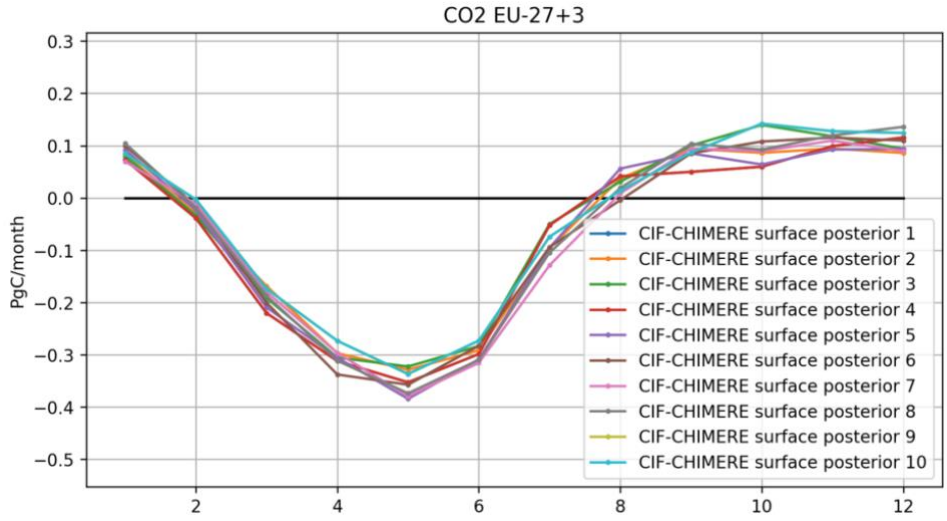


Figure 9.3: Ensemble plot for CO_2 (NEE) annual cycle in the European domain. The ensemble calculations yield estimates of the statistical posterior uncertainty of the inversion.

The dependence on the prior fluxes can be examined directly where plausible alternative priors are available. Figure 9.4 shows a comparison between a reference inversion based on GAINS fluxes and CAMS background and inversions based on alternative fluxes from the LPJ-GUESS and ORCHIDEE process-based models. Following Section 8.5, the differences between the posteriors obtained with alternative priors and the reference posterior should be compared against the posterior uncertainty of the reference inversion: differences falling within it indicate that the choice of prior is not a first-order concern for the aggregate concerned, whereas larger differences indicate either a systematic contribution to be reported under Section 8.5 or a prior error covariance too narrow to span the plausible priors.

This project has received funding from the European Union's Horizon Europe research and innovation programme under grant agreement No 101081395

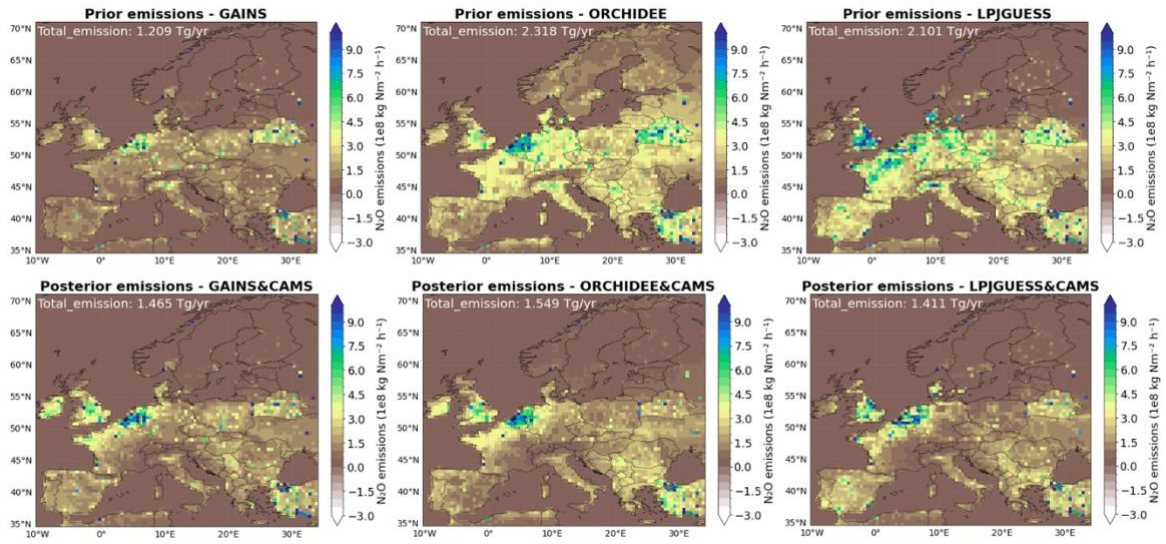


Figure 9.4: Prior and posterior N_2O fluxes for a comparison between a reference inversion using prior fluxes based on the GAINS model, versus using prior fluxes from the LPJGUESS and ORCHIDEE models.

For emission reporting support, the covariance structure between countries (or regions) can indicate whether the inversions compensate flux estimates between neighbouring countries (or regions). It is recommended that country-scale cross-correlations are reported alongside country totals. Section 10.5.2 discusses how covariance and averaging kernels are applied in the inventory comparison.

9.3. Deciding where and when results can be used

The diagnostics of Section 9.2 are descriptive but also inform on which parts of an inversion result should be used. Where the uncertainty reduction is small and the degrees of freedom for signal are low, the posterior remains close to the prior, and the estimate carries little independent information from the atmospheric observations. Reporting such a value as a top-down estimate, or comparing it with an inventory, can be misleading, particularly where the prior is itself derived from that inventory: the apparent agreement may be a property of the set-up rather than an observation constrained result.

A good practice is, therefore, to define an explicit criterion for the regions, scales and periods that are considered sufficiently constrained, and to justify this criterion, and to report it with the products. No universal threshold can be recommended, because the appropriate criterion depends on the gas, the density and type of the observation network, the resolution of the control vector and the intended use. A criterion adequate for identifying a long-term trend may not be adequate for an annual product. The criterion should be explicit rather than implicit, and that products which do not meet it should be excluded or flagged.

The same applies in time: observation networks change and the constraint on a given region may differ substantially between the beginning and the end of a long inversion. In such a case, periods of weaker constraint may be constrained more strongly by the prior estimate and thus lead to spurious results when regarding the trend over the full period of an inversion. Where the constraint varies over the period analysed, this should be

This project has received funding from the European Union's Horizon Europe research and innovation programme under grant agreement No 101081395

shown, for instance by reporting the uncertainty reduction as a time series alongside the fluxes, and taken into account when trends are compared with inventories.

Products that pass these checks can be compared with national inventories, for which the aggregation conventions, sectoral definitions and managed land considerations of Section 10.5 apply. The reporting level of Section 8.8 should be stated for each product carried forward.

9.4. Evaluation with independent observations

Comparison with atmospheric observations is of great importance for the evaluation of inversion results, but the observations used should be different from those used in the inversions in order to properly assess the performance of the posterior fluxes when projected with the transport operator into the observation space. Ideally independent observations should sample areas with different characteristics such as e.g. clean air/background versus airmasses more strongly influenced by fluxes. This allows to assess whether posterior simulations improve agreement relative to simulations based on the prior at these selected sites.

In addition, it informs on whether evaluation statistics such as bias, RMSE, correlation, seasonal cycle, amplitude and phase, and vertical gradient are sensitive to other elements in the inversion system such as the boundary mixing ratios, which can signal the relative importance of the background versus surface flux estimates. Vertical profile data (from e.g. aircraft and AirCore) can constrain the vertical structure absent in surface sites.

When comparing different results independent observation metrics can be used to select ensemble members, and system performance varies by region and by quantity (mean, trend, inter-annual variability), so a system good for one is not automatically good for another (van der Woude et al. 2026). There is a trade-off of observations to include for inversion and exclude for evaluation. For evaluation, it is recommended to use sites that have only short-time series and, if available, dedicated campaign data, and include sites with long records in the inversion.

As an example for N_2O, 14 sites were withheld from the reference inversion and used for independent evaluation, for two alternative boundary mixing ratios (CAMS and FPCTM) (see Fig. 9.5). The comparison between the upper and lower panels is the test such an evaluation has to pass: the fit of the posterior mixing ratios to the withheld observations must not be worse than the fit of the prior mixing ratios. In the example, the posterior mixing ratios provide better agreement but the difference is modest. Over 4518 daily station means the mean bias falls from −0.26 to −0.15 ppb and the RMSE from 0.54 to 0.50 ppb, with lower RMSE at most individual sites, while the correlation of daily variation is unchanged at 0.79, thus the inversion corrects the mean level of the simulated mixing ratios rather than their day-to-day variability. The choice of boundary mixing ratios has the larger effect: RMSE is lower with CAMS than with FPCTM at every site, in both prior and posterior, by more than the prior-to-posterior improvement.

Evaluation against flux measurements is generally not useful owing to scale mismatch (while eddy covariance samples ~1 km^2, inversions resolve ~10-100 km), but the comparison is occasionally still informative.

This project has received funding from the European Union's Horizon Europe research and innovation programme under grant agreement No 101081395

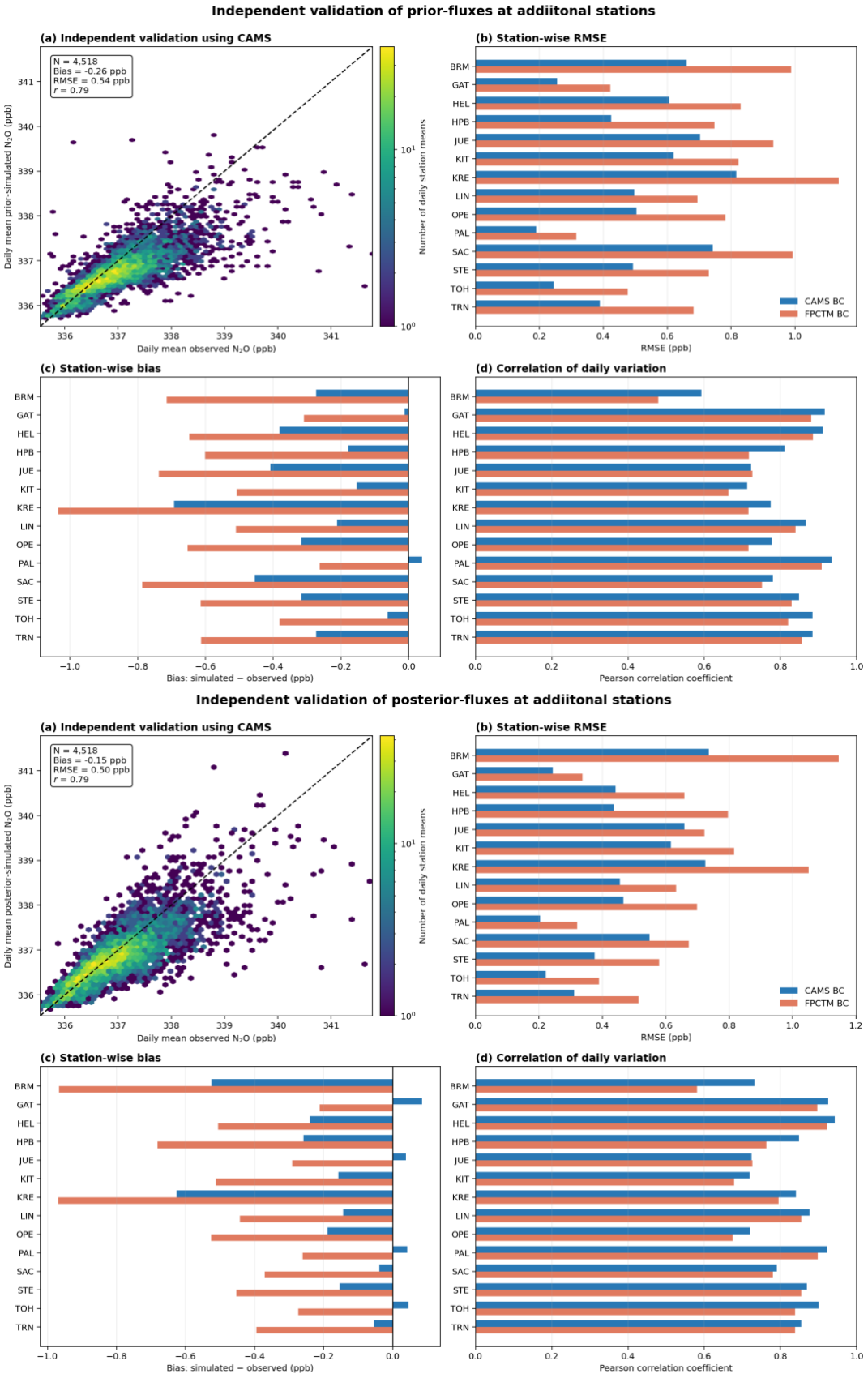


Figure 9.5: Independent evaluation of N_2O at 14 sites withheld from the reference inversion, with prior (upper) and posterior (lower) fluxes projected into observation space. In each panel: (a) daily mean simulated against observed mixing ratios for the CAMS boundary condition; (b) RMSE, (c) bias and (d) correlation of daily variation, per site, for the CAMS and FPCTM boundary mixing ratios. Statistics are over 4518 daily station means.

This project has received funding from the European Union's Horizon Europe research and innovation programme under grant agreement No 101081395

9.5. Interpreting sensitivity and ensemble results

Sensitivity experiments and ensembles produced as described in Section 8 yield a spread of posterior estimates. This section sets out how that spread should be read. Three kinds of ensembles occur in these guidelines and should be named explicitly whenever results are reported, because they support different conclusions. A posterior ensemble consists of inversions started from priors drawn at random consistently with **B**, with the observations perturbed consistently with **R**. Its spread estimates the statistical posterior uncertainty (Section 8.3). A sensitivity ensemble consists of inversions in which one element of the configuration is replaced by a plausible alternative, such as a different prior product, a different boundary condition or a different meteorological driver. Its spread is a systematic range (Section 8.5). An inter-comparison ensemble collects results from different inversion systems and is discussed in Section 9.7.

The basic rule for interpreting a sensitivity experiment is to compare the difference it produces against the posterior uncertainty of the reference inversion, at the same aggregate and for the same period. Where the difference between the alternative and the reference posterior is smaller than the posterior uncertainty, the configuration choice is not a first order concern for that reported quantity, although it may still matter at finer scales. Where it is comparable to or larger than the posterior uncertainty, one of two conclusions follows: either the element varied is a genuine systematic contribution, which should be quantified and reported under Section 8.5 and included in the total of Section 8.7, or the prior error covariance is too narrow to represent the structural uncertainty in that element (Section 8.3). Distinguishing between the two requires evidence from outside the inversion, in practice the diagnostic checks of Section 8.4 or comparison with independent observations (Section 9.4).

Differences should be reported both in absolute units and relative to the posterior flux and to the posterior uncertainty. The absolute field shows where the largest changes occur, which is generally where the fluxes themselves are largest. The relative field shows where the result is most sensitive to the choice being tested, which is the more informative quantity when deciding whether a given aggregate can be reported. Both should be shown for the reported aggregates as well as on the grid.

A sensitivity experiment answers a narrower question than it may appear to. It quantifies the dependence of the result on the alternatives actually tested, and the range obtained is bounded by the plausibility and the number of those alternatives. Testing two boundary condition products does not bound the uncertainty arising from boundary conditions in general. Where only a small number of alternatives is available, the result is better presented as the difference between named configurations than as an uncertainty range.

As example of sensitivity tests using boundary mixing ratios alternative to the reference inversions, Figure 9.6 shows the impact on the seasonal cycle of using FLEXPART-LCM instead of the CAMS global greenhouse gas inversion product v22r1. The figure contains also curves for CAMS-REG results instead of EDGARv8 fluxes for comparison. The three alternative inversions constrained with in-situ measurements show differences in the seasonal pattern that are closer together than with respect to the prior. This suggests that the influence of the alternative settings can be detected.

This project has received funding from the European Union's Horizon Europe research and innovation programme under grant agreement No 101081395

9.6. Plausibility checks

A result can be statistically consistent, well constrained and in reasonable agreement with independent observations, and still be physically implausible. Inversions are constrained by atmospheric mixing ratios and by the prior, but not by process understanding, thus an error in the transport, the boundary conditions or the observation treatment can be absorbed into fluxes that are inconsistent with process understanding (e.g. too large, too small or incorrectly distributed). Published top-down estimates have prompted further investigation on these grounds, for instance where an inferred regional land carbon sink was larger than independent process based and inventory evidence could support (Wang et al., 2020; Wang et al., 2022).

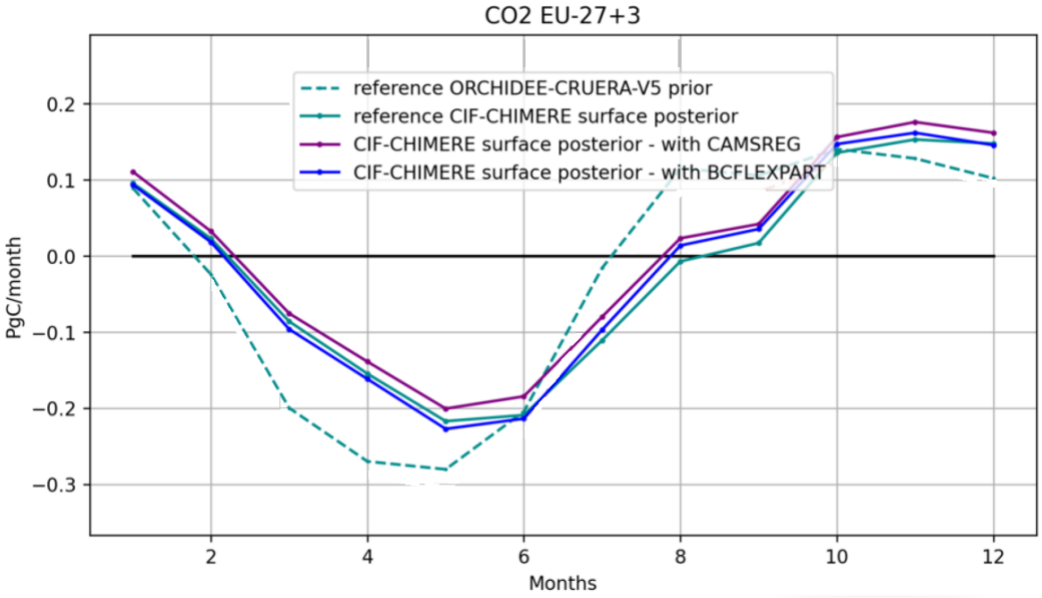


Figure 9.6: Total NEE flux for CO_2 monthly inversions in the European domain for 2019. The common prior is ORCHIDEE-CRUERA-V5. The reference inversion based on EDGARv8 is compared to alternative inversions based on CAMS-REG (alternative inventory fluxes) and FLEXPART-LCM (alternative background concentrations).

Figure 9.7 shows the transport uncertainty assessment for N_2O from an ensemble of 5 inversions where each member was run with transport driven by a different member of the IFS meteorological ensemble.

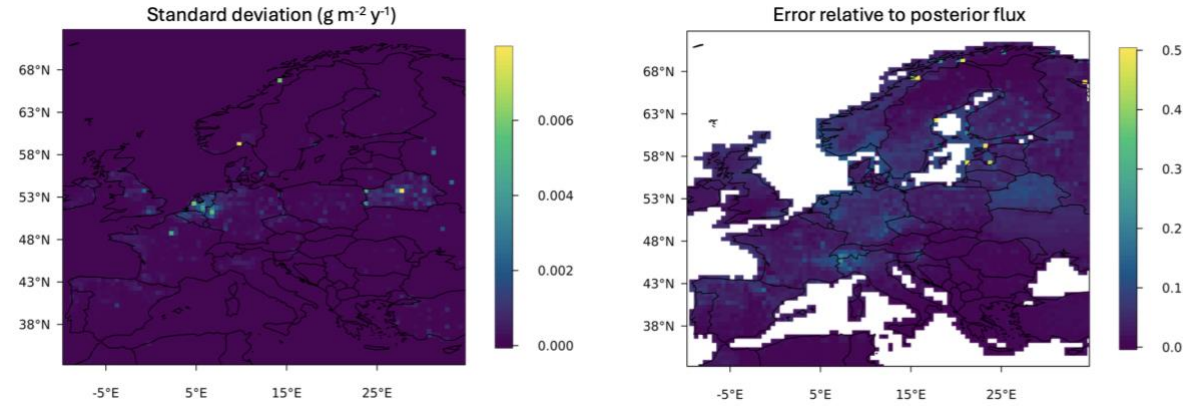


Figure 9.7: Posterior standard deviation on an ensemble of 5 N_2O inversions based on different IFS-ELDA meteorological fields. The rest of the parameters are as in the EYE-CLIMA reference inversion for N_2O.

This project has received funding from the European Union's Horizon Europe research and innovation programme under grant agreement No 101081395

It is good practice to compare posterior fluxes, at the scales reported, against the ranges that process knowledge and independent bottom-up evidence make plausible for the gas and region concerned using the gas specific guidance in Sections 3 to 5. Where a result falls outside those ranges, it should not be reported as a top-down estimate until the discrepancy has been investigated. Useful first steps are to check the consistency diagnostics of Section 8.4 for the sites and periods that drive the anomaly, to examine whether the feature persists under alternative boundary conditions and transport (Section 9.5), and to verify the corresponding simulated mixing ratios against independent observations (Section 9.4). An implausible result that survives these checks is a finding worth reporting. One that does not can be an artefact, and reporting it could damage confidence in the method.

9.7. Benchmarking against archived inversion output

The difficulty with inversions is that there is no true set of fluxes to evaluate against. Therefore, any performance assessment is necessarily indirect. In the absence of a "truth" it can be useful to check if the performance of an inversion is within the expected range of inversions that were performed by other researchers previously. Model inter-comparison archives are a useful resource to see how a new inversion estimate compares with the range of results in the inter-comparison.

This is complementary to other evaluations outlined in this chapter, but should not replace them. Note, however, that, the range of fluxes from an inter-comparison ensemble does not necessarily reflect the true uncertainty distribution and the ensemble mean is not necessarily closer to the truth. Inter-comparison spread mixes methodological differences with prior differences (if the priors are different) and is not an uncertainty. Nevertheless, an outlying result might point to implementation issues especially if different members start from the same prior. Assessing whether an apparent outlier is genuinely anomalous requires knowing which priors were used and what posterior uncertainties the individual systems report. Model-model differences being larger than the statistical uncertainties in practice cannot be assumed to hold generally.

A more informative comparison than flux against flux is one made in observation space. The mixing ratios simulated from each system's posterior fluxes are compared against the same set of observations, using the metrics defined in Section 9.4, so that systems are judged on how well their posterior fluxes reproduce the atmosphere rather than on how close their fluxes are to one another. Comparison with an ensemble also supports the selection of results. Not all systems perform equally well in every region, and performance can differ between the mean flux, the trend and the inter-annual variability, so the ensemble mean can be biased at regional scale (van der Woude et al., 2026). Where the observational coverage allows it, sub-selecting the ensemble members that agree with independent observations within a threshold can give a better regional estimate than the full ensemble mean.

If chosen inter-comparison study does not provide inversion output for the same domain, period or measurement dataset as the inversion under evaluation, it is advised to run a new inversion experiment for a setup that can be compared. Archiving and publishing own inversion results is strongly recommended to develop a growing archive that other developers can use and build on. Doing so supports the inversion community and

This project has received funding from the European Union's Horizon Europe research and innovation programme under grant agreement No 101081395

progress towards more reliable inversion results. Table 9.1 lists existing inversion archives that can be used for benchmarking.

For archiving future inversion output it is recommended to save the output following the Common Output Format (COF). The COF is a standard format based on the NetCDF file format and following the Climate and Forecast (CF) Metadata convention. This format has been already adopted by numerous European Commission funded projects.

The COF is used as a standard input format by the open-source post-processing analysis and intercomparison tool FLUXIE (FLUX Intercomparison Environment). FLUXIE is a set of Python scripts running in a Jupyter notebook that facilitates consistent post-processing of inversion output and enables easy and direct comparison of results against other output from inversion systems using the COF. FLUXIE also includes scripts for visualisation producing map and time-series plots of individual inversions as well as ensembles of inversions. (See: https://github.com/openghg/fluxie)

Table 9.1: Archives of inverse modelling output

Archive	Target gas	Application	URL
CAMS reanalysis	CO_2, CH_4, N_2O	Sub-continental trends and interannual variability	https://ads.atmosphere.copernicus.eu/datasets/cams-global-greenhouse-gas-inversion?tab=overview
CAMS facility scale	CH_4	Facility scale methane emissions from satellites	https://atmosphere.copernicus.eu/ghg-services/cams-methane-hotspot-explorer
GCP RECAPP2	CO_2, CH_4, N_2O	Sub-continental trends and interannual variability	https://www.globalcarbonproject.org/reccap/index.htm
ICOS-CP	CO_2, CH_4	National scale emissions for Europe	For CO_2: https://www.icos-cp.eu/data-products/G068-1T09 For CH_4: https://meta.icos-cp.eu/collections/eqtmTg6COhmsz2YAA_yDuqQy

9.8. Reporting requirements and lessons learned

The evaluation described in this section can only be carried out by a user of inversion output if that output is complete, traceable and consistently described. Experience from harmonising inversion products across systems shows that the obstacles are rarely conceptual: they are missing uncertainty fields, undocumented aggregation, ambiguous sign conventions and unversioned inputs, each of which prevents a user from

This project has received funding from the European Union's Horizon Europe research and innovation programme under grant agreement No 101081395

reproducing a country total or from knowing what an uncertainty refers to. Reporting requirements are, therefore, part of good practice rather than file format housekeeping. The following should accompany published inversion results:

- Prior and posterior fluxes, their uncertainties, and the simulated mixing ratios corresponding to both, under consistent variable names.
- Explicit units and sign convention, stating whether positive values denote emission to the atmosphere.
- Time bounds for every field, and the aggregation period to which reported totals refer.
- The country or region masks used, including the treatment of fractional cells and offshore areas, and the aggregation method, in sufficient detail for a user to reproduce the reported totals (Sections 8.6 and 10.5.1).
- The treatment of missing values, distinguished from zero flux.
- Versions and provenance of the prior fluxes, boundary conditions, transport and meteorological driver, and observation dataset, including the observation selection and filtering applied.
- For ensembles, the number of members, what was perturbed, and whether the ensemble is a posterior ensemble, a sensitivity ensemble or an intercomparison ensemble (Section 9.5).
- For every reported uncertainty, what it represents (statistical posterior uncertainty, a systematic range, or a combined total) and the reporting level of Section 8.8.
- The consistency and constraint diagnostics obtained (Sections 8.4 and 9.2).

Using a standard output format makes these requirements easier to meet consistently and enables direct comparison with other systems. Standards such as the Common Output Format described in Section 9.7 are recommended for this purpose. The general principle is that a user should be able to reproduce the reported totals and their uncertainties from the published output and its documentation alone, and should not have to infer what an uncertainty field represents.

10. Comparisons to NGHGIs

10.1. Introduction to inventories

Margreet van Zanten and Hannes Witt

This introduction provides some basic background on National Greenhouse Gas Inventories (NGHGIs) to help in interpreting differences between these and atmospheric inversion-based estimates. Here, general information is provided about the NGHGI system; for specific information on emissions from a certain country, it is recommended to check the National Inventory Documents of that country. Getting in contact with the compilers of such reports is recommended to make full use of the available knowledge, as this can greatly enhance the reconciliation. Involving inventory compilers early in the research process has been proven fruitful, as they often have specific user requirements that can be best taken into consideration already during the research design.

This project has received funding from the European Union's Horizon Europe research and innovation programme under grant agreement No 101081395

The main goal of NGHGIs is to produce robust, continuous and complete monitoring of anthropogenic emissions, rather than describing every physical detail of real world emission. This has led to some methodological choices in the IPCC guidelines for national greenhouse gas inventories (Publications - IPCC-TFI[7]), which need to be taken into account when evaluating inventory data. These will be discussed here in general, and in the sections below for specific gases and sectors.

For monitoring purposes, comparability of inventories is key. For that reason, inventory compilers are required to follow the instructions in the IPCC guidelines for NGHGIs and are subject to international reviews. These requirements aim to ensure that estimates of emissions and removals, even if uncertain, are genuine and unbiased, and that uncertainties are reduced as much as practicable given national circumstances.

Comparability is further ensured by the use of a few key concepts:

- Inventories deal with anthropogenic emissions and removals. The distinction between natural and anthropogenic emissions is based on the data used to quantify human activity. In the AFOLU sector, emissions and removals on managed land are used as a proxy for anthropogenic emissions and removals, and significant year-to-year variations in natural background emissions and removals are assumed to average out over time.
- Inventories include emissions that take place within their national territory and offshore areas over which the country has jurisdiction. Be sure to check whether this corresponds to exactly the same area in the inversion allocated to this country.
- Inventories should be complete; all anthropogenic emissions have to be reported. Missing sources should be documented, together with a justification for their exclusion.

Furthermore, consistency is an important concept. In an inventory, estimates for different years, gases and sources are made so that real changes in emissions are reflected in the data. As far as possible, annual trends should be derived using the same methods and data sources for all years and should aim to reflect true changes in the emissions rather than changes in the methodology.

The most common simple methodological approach is to combine information on the extent to which a human activity takes place (called activity data, or AD) with coefficients that quantify the emissions or removals per unit activity. These are called emission factors (EF). The basic equation is:

$$\text{Emissions} = AD \times EF$$

Besides this, some mass-balance methods are also used, for example the stock-change methods applied in the AFOLU sector[8].

The basic equation can be used with various levels of complexity, usually called *tiers*. Tier 1 relates to generic, default EF combined with AD applicable to the specific country.

[7] https://www.ipcc-nggip.iges.or.jp/public/2006gl/pdf/1_Volume1/V1_1_Ch1_Introduction.pdf
[8] https://www.ipcc-nggip.iges.or.jp/public/2006gl/pdf/4_Volume4/V4_01_Ch1_Introduction.pdf

This project has received funding from the European Union's Horizon Europe research and innovation programme under grant agreement No 101081395

In Tier 2, country-specific information is used to determine the EF, in addition to country-specific AD. Tier 3 requires the use of complex models or facility specific information to determine the emissions for a group of sources in a consistent way, e.g. for all emissions of the agricultural sector. Tier 1 methods in the guidelines are designed to use readily available national or international statistics and, therefore, should be feasible for all countries. In general, the higher tiers should result in more accurate emission estimates.

Besides reporting emissions, inventories are required to carry out a detailed uncertainty analysis, preferably using both error-propagation and Monte Carlo analysis. Details about the uncertainty analysis can be found in Volume 1, Chapter 3 of the IPCC guidelines and the respective National Inventory Documents. The uncertainty at the emission-source level has to be taken into account in a required key source analysis. The concept of key categories is used to identify those emissions that have a significant influence on a country's total inventory of greenhouse gases, in terms of the absolute level of emissions and removals, the trend therein, or its uncertainty. When an emission source is identified as a key source, a Tier 2 or Tier 3 method has to be used. Key source analyses can be a valuable source of information when comparing inversions with inventory data to identify emission sources with high uncertainties or high impact in the inventory.

10.2. CO_2 LULUCF

Philippe Ciais, Gregoire Broquet and Rona Thompson

Atmospheric inversions of CO_2 traditionally target net land-biosphere fluxes, which are considerably more uncertain than the CO_2 emissions from fossil carbon sources, namely fossil fuels and cement (see Section 3). Following the focus of Section 3, this section discusses the comparison and reconciliation of inversion estimates of net land-biosphere CO_2 fluxes with land-use land-use-change and forestry (LULUCF) reported emissions.

A variety of atmospheric inversion frameworks, both global and regional, have been used in previous carbon budget assessments, e.g. Global CO_2 Budget (Friedlingstein et al., 2025) and in comparisons with nationally reported LULUCF CO_2 emissions and removals (e.g. Byrne et al., 2023; Deng et al., 2022, 2025; McGrath et al., 2023) . Some inversion systems now provide low latency results used for fast-track updates of the Global CO_2 Budget based on OCO-2 satellite data (Ke et al., 2024) .

Traditionally, global and regional inversions targeting CO_2 land-biosphere fluxes, such as those contributing to the Global CO_2 Budget and national assessments (see references above), ignore the lateral fluxes associated with harvest products and transport through rivers to lakes and seas. Thus, the NEE defined in these inversions actually corresponds to the NBP following the definitions provided in Section 3 (specifically, they aggregate to the NEE all land fluxes other than fossil emissions). The NEE (or NBP) flux estimates from "traditional" inversions need to be post-processed to account for the lateral transfer of carbon and for the CO_2 emissions arising from this transfer or from the resulting products to be able to compare with NGHGIs. This post-processing is discussed in Section 10.2.3. The EYE-CLIMA project has proposed an alternative approach to the "traditional" inversions, by explicitly using estimates for the CO_2 emissions arising from lateral fluxes

This project has received funding from the European Union's Horizon Europe research and innovation programme under grant agreement No 101081395

as prior information in the inversions (see Section 3) and the post-processing of these inversions for comparison with NGHGIs is discussed in Section 10.2.4.

10.2.1. Assumptions on fossil fuel emissions

Most often inversions provide NEE (or NBP) fluxes as output. However, if only the total CO_2 flux (including fossil emissions) is provided then an estimate of the fossil CO_2 emissions[9] needs to be subtracted from the total to the obtain land-biosphere fluxes, assuming that the fossil emissions are well-known.

In general, uncertainties of fossil fuel CO_2 emissions for most countries are low (few percent), as emission factors follow directly from the carbon content of fuels.

If comparing multiple inversions that have used different fossil CO_2 emission estimates, then a more comparable estimate for the land-biosphere flux is often obtained by calculating the total emissions from each system and then subtracting a common fossil CO_2 emission estimate based on the assumption that the NEE (or NBP) estimated by each inversion will at least partially compensate for differences in the fossil emissions used in the inversion (Peylin et al., 2013) . However, it should be noted that since the differences in fossil emissions are not completely compensated for, this can still result in differences in NEE (or NBP) between inversions (Thompson et al., 2016).

10.2.2. Sampling for managed land

As defined in the IPCC Guidelines for NGHGIs (Paustian et al., 2006) , only CO_2 emissions and removals from managed land are reported in NGHGIs as a proxy for human-induced effects. It should be noted though, that this includes direct effects, such as forest management, and indirect effects, such as CO_2 fertilization and nitrogen deposition, as well as natural effects owing to e.g. climate variability. Inversions retrieve all CO_2 fluxes over all land types. Thus, for comparing inversion fluxes with NGHGIs, only the inversion's CO_2 flux ($F_{ML}^{inv\ NEE}$) over managed lands (ML) grid cells should be used (ML is defined here as all land except intact forests) because the fluxes over unmanaged land are not counted by NGHGIs. CO_2 fluxes over unmanaged land should be excluded from the land-biosphere CO_2 flux totals that will be compared with NGHGIs and can be calculated as proportional to the fraction of unmanaged land in each inversion grid cell. For some countries all land is considered to be managed land; this is the case for most European countries and for many developed countries.

New maps of non-intact forests have been compiled by Grassi et al. (Grassi et al., 2023) that can be used for this purpose (Figure 10.1). These maps include country official managed forest and other managed land areas for Canada and Brazil (as used for their NGHGIs) and the intact forest map of Potapov et al. (2017) as a substitute for unmanaged land where country-based information is not available. This approach assumes that non-intact forest areas can serve as a reasonably good proxy for managed forests reported in the NGHGIs (Grassi et al., 2021, 2023) . It is important to note that this approach is somewhat arbitrary, as highlighted in previous studies (Chevallier, 2021; Grassi et al., 2021; Ogle et al., 2018) . However, in the absence of a machine-readable

[9] Spatially (and temporally) resolved fossil fuel emission estimates are available from a number of datasets including GridFEDv2022 (Jones et al., 2022), and EDGAR (Crippa et al., 2000).

This project has received funding from the European Union's Horizon Europe research and innovation programme under grant agreement No 101081395

definition of managed plots in many NGHGIs, there is currently no better alternative available.

10.2.3. Adjusting CO_2 fluxes from "traditional" inversions for lateral C transport by crop and wood products trade and rivers

In addition to the extraction of managed land CO_2 flux, there are CO_2 fluxes from "traditional" inversions that are part of $F_{ML}^{inv\ NEE}$ but are not counted by NGHGIs. These fluxes are induced by: i) soil to river to ocean carbon export (F_{ML}^{rivers}) which has an anthropogenic and a natural component (Regnier et al., 2013), and ii) net anthropogenic import/export of crop and wood products across country boundaries ($F_{ant}^{crop\ trade}$ and $F_{ant}^{wood\ trade}$). It can be assumed that NGHGIs include CO_2 losses from fire (wildfire and prescribed fire) and other disturbances (wind, pests) and from domestic harvesting, as recommended by the IPCC reporting guidelines (Buendia et al., 2019; Paustian et al., 2006) , although some countries, such as Canada and Australia exclude some emissions from these disturbances, and the subsequent removals from the same areas (Grassi et al., 2023). The adjusted inversion NEE that can be compared with inventories, $F_{adj}^{inv\ NEE}$, is given by:

$$F_{adj}^{inv\ NEE} = F_{ML}^{inv\ NEE} - F_{ML}^{rivers} - F_{ant}^{crop\ trade} - F_{ant}^{wood\ trade} \leftrightarrow F_{ant}^{ni} \qquad (10.1)$$

where the sign ↔ means "comparable to", F_{ant}^{ni} is the anthropogenic CO_2 flux from NGHGIs, F_{tot}^{rivers} is the sum of the natural and anthropogenic CO_2 flux on land from CO_2 fixation by plants that is leached as carbon via soils and channelled to inland waters to be exported to the ocean or to another country. All countries export river carbon, but some countries also receive river inputs, e.g., Romania receives carbon from Serbia via the Danube River.

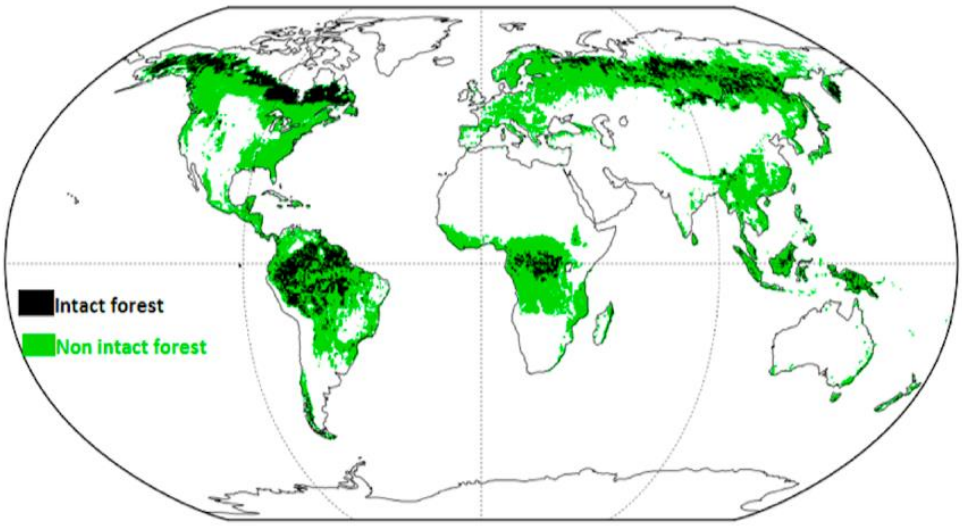


Figure 10.1. Map of managed and unmanaged forests. (Figure courtesy of (Grassi et al., 2023)).

Ciais et al. (2022) provide estimates for the lateral carbon export by rivers minus the imports from rivers entering each country, including dissolved organic carbon, particulate organic carbon and dissolved inorganic carbon of atmospheric origin distinguished from lithogenic carbon. In a country that only exports river carbon to the

This project has received funding from the European Union's Horizon Europe research and innovation programme under grant agreement No 101081395

ocean, the amount of carbon exported is equivalent to an atmospheric CO_2 sink, denoted as F_{ML}^{rivers} as in (10.1), ignoring burial, which is a small term. Over a country that receives carbon from rivers flowing into its territory, a small national CO_2 outgassing is produced by a fraction of this imported flux. In that case, we assumed that the fraction of outgassed to incoming river carbon is equal to the fraction of outgassed to soil-leached carbon in the RECCAP2 region to which a country belongs, estimated with data from Ciais et al., (2022).

$F_{ant}^{crop\ trade}$ is the sum of CO_2 sinks and sources induced by the trade of crop products. This flux is provided by Ciais et al., (2022) and is estimated from the annual trade balance of crop commodities calculated for each country from data from the United Nations Statistics Division of the Food and Agriculture Organization (FAOSTAT) combined with the carbon content values of each commodity (Xu et al., 2021). All the traded carbon in crop commodities is assumed to be oxidized as CO_2 in one year, neglecting stock changes of products, and the fraction of carbon from crop products going to waste pools and sewage waters after consumption, thus not necessarily oxidized to atmospheric CO_2.

$F_{ant}^{wood\ trade}$ is the sum of CO_2 sinks and sources induced by the trade of wood products (Zscheischler et al., 2017) . Ciais et al. (2022) provide an estimate of this flux based on a bookkeeping model to calculate the fraction of domestically produced and imported carbon in wood products that are oxidized in each country during subsequent years, with product lifetimes defined by Mason Earles et al. (2012). The underlying assumption in estimating CO_2 fluxes from wood harvest is that the emissions from domestically harvested wood, in addition to imported wood minus exported wood that is not allocated to wood product pools, are released into the atmosphere during the year of harvest. Conversely, wood allocated to wood product pools is gradually released into the atmosphere over time, based on their respective lifetimes. Domestic harvest is assumed to be balanced by an atmospheric CO_2 sink of equivalent magnitude, which is not necessarily the case given that harvest is rarely in equilibrium with forest increment, but inversions NEE will correct for this imbalance and can thus be compared with NGHGIs.

Included in the $F_{ant}^{crop\ trade}$ flux are also the CO_2 emissions from domestic animals consuming specific crop products delivered as feed. On the other hand, emissions of CO_2 from grazing animals and the decomposition of their manure are assumed to occur in the same grid box where grass is grazed, so that the CO_2 net flux captured by an inversion is comparable with grazed grasslands' carbon stock changes of inventories. Emissions of reduced carbon compounds (VOCs, CH_4, CO) are not included in this analysis (see Ciais et al., (2022) for a discussion of their importance in inversion CO_2 budgets).

In summary, the purpose of the adjustment of (10.1) is to make inversion output comparable to the NGHGIs that do not include F_{ML}^{rivers}, $F_{ant}^{crop\ trade}$ and $F_{ant}^{wood\ trade}$. The UNFCCC accounting rules (Paustian et al., 2006) assume that all the harvested wood products are emitted in the territory of a country that produces them, which is equivalent to ignoring $F_{ant}^{wood\ trade}$ as a national sink or source of CO_2, hence the need to remove $F_{ant}^{wood\ trade}$ from inversion NEE. The adjusted inversion fluxes from (10.1) depict the

This project has received funding from the European Union's Horizon Europe research and innovation programme under grant agreement No 101081395

national CO_2 stock change, which better matches the carbon accounting system boundaries of UNFCCC NGHGIs.

10.2.4. Recombining the flux components from inversions that account for the lateral fluxes

The fluxes from inversions following the recommendations from Section 3 should be more straightforward to post-process for the comparison to NGHGIs as compared to the "traditional" inversions. These "non-traditional" inversions use prior CO_2 land fluxes disaggregated into sub-components including the sources from lateral fluxes (following the EYE-CLIMA CO_2 inversion protocol, (Broquet et al., 2026)). Such inversions provide estimates of the NEE taken as the difference between the GPP and the autotrophic and ecosystem heterotrophic respiration fluxes, plus "non-fire" disturbance fluxes due to land use change (F_{LUC}, see Section 3).

The first post-processing step is to sample the NEE fluxes over managed land as described in Section 10.2.1. Then, if a "river sink" compensating the local soil to river carbon flux ($F_{ML}^{river\ sink}$) is included in the NEE estimate, following the reasoning detailed above, it should be subtracted from the inversion NEE fluxes. If it is explicitly taken as a separate term (as in the EYE-CLIMA CO_2 inversion protocol), it can be ignored.

The NEE should still be adjusted to remove the carbon sink compensating the harvests. Independent estimates of the local loss of carbon due to harvest (of crops and wood, $F_{ML}^{crop\ harvest}$ and $F_{ML}^{wood\ harvest}$) are needed for such a correction (such as that from Ciais et al., 2022). The sum of the resulting NEE+F_{LUC} flux and of the biomass burning F^{BB} flux corresponds to the change in the carbon stock of the ecosystems and it should be consistent with that from the NGHGIs, i.e., with the LULUCF fluxes from these inventories after excluding the Harvest Wood Product sector:

$$F_{adj}^{inv\ NEE+FLUC} = F_{ML}^{inv\ NEE+FLUC} + F_{ML}^{BB} + |F_{ML}^{crop\ harvest}| + |F_{ML}^{wood\ harvest}| \quad \Leftrightarrow \quad F_{ant}^{ni} \quad (10.2)$$

or if the river drainage has been accounted for as a separate sink:

$$F_{adj}^{inv\ NEE+FLUC} =$$

$$F_{ML}^{inv\ NEE+FLUC} + |F_{ML}^{river\ sink}| + F_{ML}^{BB} + |F_{ML}^{crop\ harvest}| + |F_{ML}^{wood\ harvest}| \Leftrightarrow F_{ant}^{ni} \quad (10.3)$$

if this is implicitly included in the NEE+F_{LUC} estimates.

10.3. CH_4 fluxes

Philippe Ciais and Tuula Aalto

Most atmospheric inversions derive total net CH_4 fluxes at the surface as it is difficult for them to disentangle overlapping fluxes from different sectors at the grid cell/regional scale based on atmospheric CH_4 observations only. However, some inversion systems solve for source categories, which, even if no isotopic data are included, are constrained to some extent using the different spatio-temporal distributions of fluxes in different sectors.

Where inversions explicitly solve for fluxes by source sector, the total anthropogenic CH_4 emission can be derived by summation of the anthropogenic sectoral fluxes. Otherwise,

This project has received funding from the European Union's Horizon Europe research and innovation programme under grant agreement No 101081395

the total anthropogenic emission can be found by subtraction of the natural fluxes from the total flux.

The inversions and NGHGIs can be compared on the total anthropogenic emissions or for super sectors, e.g. “fossil” (FF), “agriculture and waste” (AgW) and “biofuel and biomass burning” (BB). For the comparison, NGHGI emissions for the IPCC Common Reporting Format (CRF) sectors (1) “energy” and (2) “industrial processes and product use”, excluding biofuel emissions, are combined into the super sector of “fossil”. The sectors (3) “agriculture”, excluding agricultural waste burning (3F), and (5) “waste”, are combined into the super sector of “agriculture and waste”. The sector (3F) as well as residential biofuel combustion (e.g. stoves, boilers, fireplaces), are combined to the super sector “biofuel and biomass burning”.

It should be noted that in the inversions, the BB category includes CH_4 emissions from wildfires in forests, savannas, grasslands, peatlands, agricultural waste, as well as residential biofuel combustion (e.g. stoves, boilers, fireplaces), while in NGHGIs, emissions from wildfires are usually not included. To ensure consistency, bottom-up wildfire emissions are subtracted using estimates derived from e.g. GFED (Werf et al., 2025) or GFAS (Kaiser et al., 2012) datasets. However, because these also provide separate estimates for agricultural and waste fires, which are assumed to be reported in NGHGIs, these emissions should not be subtracted from the inversions, i.e., not included in the term $E_{wildfire}$ in (10.4).

The “fossil”, “agriculture and waste”, and “biomass and biofuel burning” sectors aggregate into total anthropogenic emissions which can be compared to inventories as follows:

$$E_{ant}^{inv} = E_{AgW}^{inv} + E_{FF}^{inv} + E_{BB}^{inv} - E_{wildfire} \leftrightarrow E_{ant}^{ni} \quad (10.4)$$

For inversions solving for net emissions only, the partition to source sectors can be created based on the fraction of each sectoral emission to the total emission in each grid cell in the prior emission estimates. For inversions solving for some source categories, a similar approach can be used to partition the solved categories into the five super sectors. However, such processing can lead to significant uncertainties since the fraction of the sectoral emissions in the prior may not be consistent with reality.

Deng et al. (2022) propose four methods to separate CH_4 anthropogenic emissions from inversions (E_{Anth}^{inv}) to compare them with national inventories (E_{Anth}^{ni}). The differences in the calculated results among the four methods were smaller compared to the variations observed in the inversions (see Figure 9 of Deng et al., 2022).

10.3.1. Comparing inversions with NGHGI estimates for managed peatlands

The areal extent of wetlands is still poorly constrained in the scientific literature. Multiple global wetland inventories derived from remote sensing and land-cover products show substantial inconsistencies, with estimates of total wetland area varying widely depending on the dataset and methodology used, highlighting major uncertainty in even broad-scale metrics. Examples of recent global and regional wetland maps include e.g. GLWD (Lehner et al., 2025) , WAD2M (Zhang et al., 2021b) , GIEMS-MC (Bernard et al., 2025) , BAWLD (Olefeldt et al., 2021) and European Wetland Map (Tegetmeyer et al.,

This project has received funding from the European Union’s Horizon Europe research and innovation programme under grant agreement No 101081395

2025). Combining these maps with more general land cover products needed as model input, like EU-Corine (EEA, 2021) or ESA CCI LC (Defourny et al., 2019) requires re-interpretation of land use classes and can be challenging. High-latitude wetlands are particularly challenging to quantify: peatlands and seasonally saturated soils dominate above ~50° N but are difficult to detect with coarse satellite data because organic soils and small, heterogeneous wetland features can be indistinguishable from surrounding land cover, ponds and lakes or masked by trees and snow and ice for much of the year. Current global mapping products may misestimate northern wetland area and misclassify wetland types, which in turn propagates uncertainty into estimates of methane emissions and carbon storage.

Because wetland extent is difficult to quantify, the identification of managed wetlands is likewise uncertain. Peatland management, most commonly involving drainage for forestry, agriculture (cropland or grassland) or peat extraction, can lead to a wide range of ecological and biogeochemical outcomes. In some cases, drainage is incomplete or ineffective, and peatlands remain waterlogged and continue to emit methane. They may contain trees and belong to e.g. transitional forest land use category. In other cases, drainage results in well-aerated soils that support dense, productive forests. In such well-drained peatlands, ecosystem respiration is enhanced, leading to progressive peat mineralization and long-term carbon loss e.g. (Tyystjärvi et al., 2024) . Methane is usually not emitted other than after prolonged rain periods/ flooding. However, drainage ditches emit methane and are included in NGHGIs. The designation of land as peatland typically requires the presence of a peat layer exceeding ~20–30 cm often with high organic carbon content, although exact thresholds vary among national definitions and soil classification systems. At the global scale, datasets such as those created by Fluet-Chouinard et al. (2023) have mapped drained peatlands and their historical development. Additionally, peatland management practices include rewetting and other interventions that alter hydrology, sometimes resulting in constructed wetlands or artificial waterbodies on peat soils, particularly following drainage or peat extraction. It is assumed that restored wetlands return in time close to the pristine state and, therefore, they are not always included in NGHGI. While land-cover products such as the EU CORINE inventory distinguish many of these categories, national-level information is often required to determine whether these land uses occur on peat soils. Tanneberger et al. (2021) has mapped the degraded peatlands across the EU and linked these results to CORINE land-use classes.

For atmospheric inversions and greenhouse gas assessments, it is important to distinguish between peatlands that are degraded and may no longer emit methane and those that remain pristine or maintain sufficiently high-water tables to support seasonal or persistent methane emissions. Some high-water table peatlands are located on managed lands and may therefore be eligible for emission reporting.

It should also be noted that the IPCC guidelines only provide a loose definition of land-use categories, which the countries can apply based on their national circumstances. This leads to ambiguity in the definition of land use categories. Water-saturated organic soil with mostly bushy of grassy vegetation could for example be categorized as wetlands or grass land in different countries, which complicates the inter-comparability of emission from different countries.

This project has received funding from the European Union's Horizon Europe research and innovation programme under grant agreement No 101081395

10.4. N_2O fluxes

Rona Thompson

In UNFCCC reporting, only anthropogenic N_2O emissions are reported. For N_2O, these are principally emissions from agriculture, chemical processing, wastewater treatment, and combustion of fuels.

For agriculture, emissions are reported for *direct* emissions, namely those that occur from nitrogen (N) applied directly to agricultural soils, and *indirect* emissions, namely those from soils as well as inland and coastal waters that receive anthropogenic N indirectly, that is, by atmospheric deposition, run-off and leaching. Direct agricultural soil emissions are calculated using emission factors multiplied by N-inputs. The emission factors (EF_i) represent the emission response to N-input (F_i) above a background level and are determined from measurements of emissions in a fertilized (or *treated*) plot (E_T^{N2O}) versus an unfertilized (or *control*) plot (E_C^{N2O}) (see equation 10.5). As such, the emission factor multiplied by N-input represents the enhancement due to N-input. Indirect emissions are also calculated based on emission factors multiplied by the fraction of N-input that is dispersed from agricultural soils (IPCC Guidelines, Chapter 11).

$$EF_i = \frac{E_T^{N2O} - E_C^{N2O}}{F_i} \quad (10.5)$$

In addition, to the emission response to N-input (from fertilizers, manure, etc.), inventories report the emissions from organic soils (E_{OS}^{N2O}), calculated per area of organic soil, and the emissions from urine and dung on grazed pasture (E_{PRP}^{N2O}). Thus the total reported emission from soils is the sum of direct, indirect, organic soil and pasture emissions:

$$E_{soil}^{N2O} = E_{Dir}^{N2O} + E_{Indir}^{N2O} + E_{OS}^{N2O} + E_{PRP}^{N2O} \quad (10.6)$$

Since atmospheric inversions most typically estimate the total net N_2O flux, the anthropogenic emissions can be determined by subtracting estimates of natural fluxes. The natural fluxes on land are from soils (E^{soil}_{nat}, this may be considered to be the equivalent of E_C^{N2O} in (10.5) if this emission is measured in a plot without indirect N-input), natural fluxes from wildfires ($E^{wildfire}_{nat}$) and inland waters, (E^{aq}_{nat}). Thus, the anthropogenic emission from inversions is:

$$E_{ant}^{inv} = E_{tot}^{inv} - E_{nat}^{soil} - E_{nat}^{aq} - E_{nat}^{wildfire} \quad (10.7)$$

This is similar to the equation of Deng et al. (2022), except of instead of $E^{inv}_{tot} - E^{soil}_{nat}$ they use E^{inv}_{mland}, which is the inversion sampled for only for managed land (MLAND). This, however, may not be a good approximation since on managed land, there may be some natural component to the emission (e.g., N-input from leaf litter in forests) and on unmanaged land there can be indirect emissions, especially if these are down-wind or downstream of agricultural land.

Estimates for the natural soil emission may be obtained from process-based models, such as those used in the Nitrogen Model Inter-comparison Project (NMIP) (see Table 5.1) (Tian et al. 2019). These models can estimate N_2O emissions in the absence of anthropogenic N-input but account for historic and current land-use and climate, which is an approximation of E^{soil}_{nat}. Natural emissions from inland waters, E^{aq}_{nat} may also be

This project has received funding from the European Union's Horizon Europe research and innovation programme under grant agreement No 101081395

provided by process-based models or from empirical or semi-empirical estimates (see Table 5.1). Wildfire emission estimates are based on satellite observations of fire activity and emission factors. These estimates, however, may also contain emissions from agricultural and waste burning, therefore, if these categories are included it is important to remove them from $E^{wildfire}_{nat}$ in (10.7).

UNFCCC Annex I countries are required to report their anthropogenic emissions according to the Common Reporting Table (CRT) format following IPCC guidelines. However, this does not include indirect emissions due to atmospheric N-deposition from NO_x and NH_3 from industrial and fuel combustion sources (E_{indep}). This is usually a small contribution, e.g., for France and Germany it is ~3% of the total anthropogenic emissions. In any case, for completeness this source should be added to the inventories for comparison with E^{inv}_{ant}. Estimates of E_{indep}, are available from some scientific inventories (e.g. EDGAR). Thus the full comparison of NGHGI versus inversion is:

$$E^{ni}_{ant} + E^{other}_{indep} = E^{ni}_{ant+} \Leftrightarrow E^{inv}_{ant} = E^{inv}_{tot} - E^{other}_{nat} \quad (10.8)$$

where "other" refers to other estimates than from NGHGIs or inversions, and E^{ni}_{ant+} refers to the total anthropogenic emissions bottom-up.

Non-Annex I countries are not required to report their emissions to the same level of detail as Annex I, but do submit National Communications (NCs) and Biennial Update Reports (BURs). However, these do not always report indirect emissions and, according to Deng et al. (2022), these emissions can amount to around 20% of the direct soil emissions. Therefore, if comparing to NCs or BURs, it is important to check what exactly is included.

Uncertainties in the anthropogenic emission source from an inversion can arise from uncertainties in the natural emissions estimates that are used in (10.7). The largest uncertainty will likely be from the natural soil emission estimate. Globally, natural soil emissions are estimated to be 6.4 (3.9 - 8.6) TgN/y or 35% of the total source, however, these emissions occur mostly in tropical and subtropical regions. The uncertainty due to the natural soil emissions should be estimated based on the comparison of different model estimates of this source, e.g., using NMIP model results. The inland waters source is globally quite small, 0.08 (0.05 - 0.14) TgN/y thus representing only ~0.4% of the total source (Tian et al. 2024). Thus, the contribution of uncertainty from this source is likely to be small, unless this source is regionally important, in which case, the uncertainty should be estimated based on the uncertainty estimate of E^{aq}_{nat}. The source from wildfires is more important, 0.8 (0.5 - 1.0) TgN/y or ~4% of the total source (Tian et al. 2024). Thus, the uncertainty due to this source should be assessed by comparing different wildfire emission datasets.

10.5. General considerations when comparing inversion fluxes with NGHGIs

Rona Thompson and Gregoire Broquet

10.5.1. From gridded to regional estimates

Since inversions generally provide fluxes on a spatial grid (typically in degrees of latitude and longitude), to compare with regional or country emission estimates it is necessary to integrate the gridded fluxes over the region of interest. For this, a spatial raster is needed

This project has received funding from the European Union's Horizon Europe research and innovation programme under grant agreement No 101081395

indicating the grid cells corresponding to the region. However, uncertainty in the regional estimate can arise due to how grid cells that border with another region (or sea) are handled. It is recommended to use a raster that includes the fractional area of each grid cell that occurs in the region, such that only the fraction of fluxes occurring within the region are included. Uncertainty arises due to the unknown distribution of fluxes within grid cells bordering regions. If multiple independent prior estimates of the fluxes exist at higher resolution than the inversion, this uncertainty may be estimated. This can be done by disaggregating the fluxes within each grid cell according to different higher-resolution prior estimates, and by applying the raster (at the same higher-resolution) to integrate the fluxes, and then taking, e.g., the standard deviation of these estimates, as the uncertainty due to the distribution of fluxes within border grid cells.

Another consideration is how to handle fluxes that occur off-shore but within a country's territory or Economic Exclusion Zone (EEZ). The EEZ is the maritime zone that extends up to 200 nautical miles (370 km) from the country's coastline. Countries are required to include emissions that occur within their EEZ in their NGHGIs. Thus, to compare inversion results with NGHGIs, the grid cells in the EEZ and any offshore territories should be included (or for the latter excluded from the inventory if the territory is outside the inversion domain). Spatial data for the EEZs are available (e.g. https://www.marineregions.org/, last access 9 July 2026).

10.5.2. Interpretating inversion results

Bayesian atmospheric inversions correct *prior* estimates of the fluxes to provide new *posterior* estimates. When comparing posterior fluxes to NGHGIs, it is very important to characterize the correction applied to the prior flux (i.e., the posterior minus prior flux difference), especially when the prior fluxes are partially or fully based on data from NGHGIs. The diagnostics of: i) the difference between the posterior and prior estimates, ii) the posterior uncertainties, and iii) the uncertainty reduction (calculated as one minus the ratio of the posterior to prior uncertainties) can support such a characterization (McGrath et al., 2023) (see also Section 2.5). Regions with high posterior uncertainty, usually corresponding to low uncertainty reduction, are where the inversion is not well constrained, thus the posterior fluxes there should be interpreted with caution. Moreover, it can be expected that in these poorly constrained regions the posterior fluxes remain close to the prior fluxes, but this cannot be interpreted to mean that the prior is correct in these regions (see Figure 10.2).

This project has received funding from the European Union's Horizon Europe research and innovation programme under grant agreement No 101081395

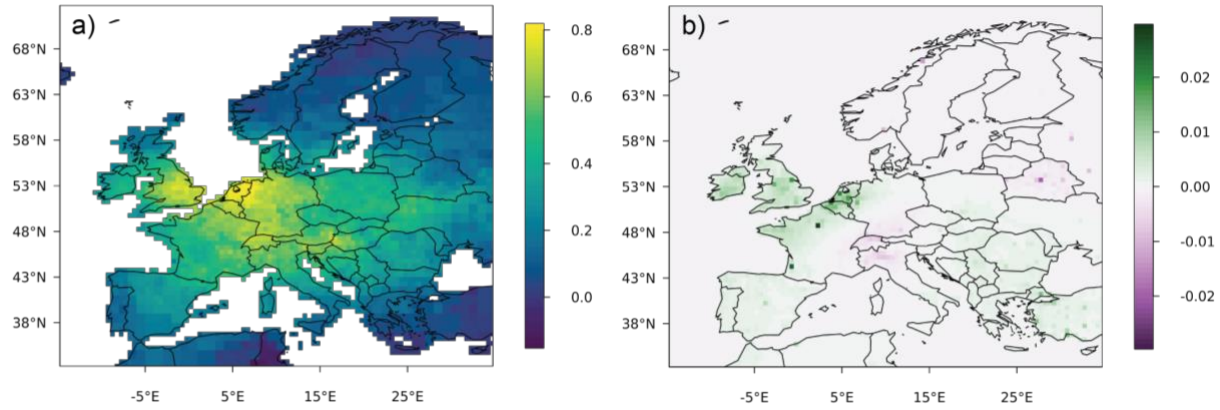


Figure 10.2: Uncertainty reduction (fraction of one) for the annual mean posterior flux of N_2O (a), and the posterior minus prior flux differences (g m^{-2} y^{-1}) for the same inversion (b). The flux differences over western Europe fall in an area of high uncertainty reduction and, therefore, can be considered well-constrained, whereas flux differences in e.g. Belarus fall in an area of low uncertainty reduction and have low confidence. (Example from the EYE-CLIMA project, inversion run with CIF-FLEXPART).

It is important to note that the uncertainties in the posterior fluxes from atmospheric inversions often have negative correlations between grid cells. This can be seen by examining the off-diagonal terms of the posterior error covariance matrix, if it is available. These negative correlations indicate where the inversion cannot independently constrain the fluxes at grid cell level. For this reason, posterior flux estimates become more certain the more they are aggregated in space and time. Hence, the most robust comparisons with NGHGIs are for large regions, countries and, where the inversion is well-constrained, sub-country regions. Moreover, atmospheric inversions generally provide only a weak constraint on emissions by sector, and thus comparisons with NGHGIs should bear this in mind and not focus on comparisons for highly resolved sectoral levels, but rather on "super sectors" (see Section 10.3).

In cases where the posterior error covariance matrix is not directly provided by the inversion algorithm, then an estimate of the posterior uncertainty should be provided based on an ensemble of inversions (see Section 8). In this case, the error covariance for regions or sectors ($\mathbf{P}_e$) can be obtained from the ensemble as:

$$\mathbf{P}_e = \frac{1}{N-1}(\mathbf{X}_e - \overline{\mathbf{X}}_e)(\mathbf{X}_e - \overline{\mathbf{X}}_e)^{\mathrm{T}} \qquad (10.9)$$

where $\mathbf{X}_e$ is a matrix of the regional (sectoral) emissions for each ensemble member and $\overline{\mathbf{X}}_e$ is a matrix of the ensemble mean regional (sectoral) emissions (i.e., repeating the mean for each ensemble member to give the same dimension as $\mathbf{X}_e$). The matrix $\mathbf{P}_e$ should be examined for error correlations between regions (sectors) (see Figure 10.3).

This project has received funding from the European Union's Horizon Europe research and innovation programme under grant agreement No 101081395

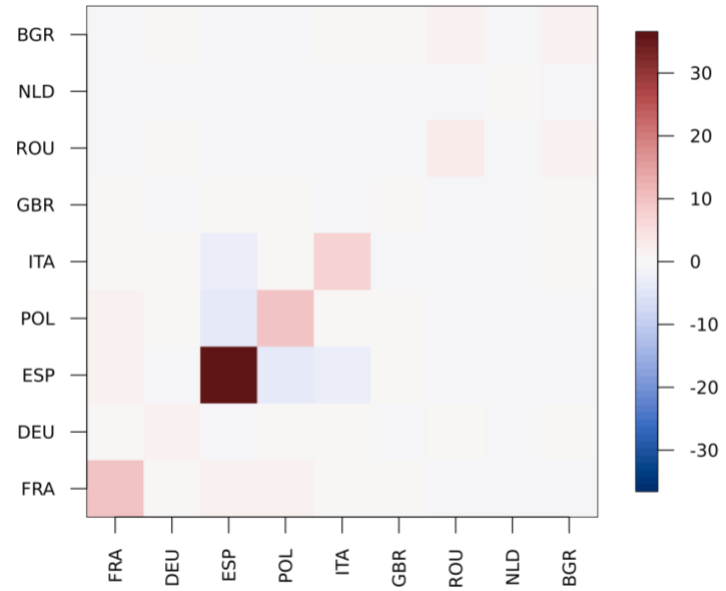


Figure 10.3: Posterior error covariance matrix for N_2O emissions per country derived from an ensemble (same inversion as used in Fig. 10.2). Note, only 9 countries with the largest N_2O emissions in Europe are shown. The error covariance matrix has only weak off-diagonal values, indicating that the country emissions are largely independent from one another, but weak negative correlation is seen between Poland and Spain, and Spain and Italy, likely because these countries are close to the domain boundaries and are more weakly constrained.

As mentioned above, the diagnostics of the difference between the posterior and prior estimates and the uncertainty reduction need to both be considered to get full insights into the information brought by the inversions with respects to the prior estimates.

Another diagnostic can bring a more synthetized and comprehensive characterization of this information as will be described in the following. The posterior fluxes can be considered to be a weighting between the prior and true fluxes, where the weighting depends on the prior and observation uncertainties and how the observations relate to the fluxes (see Section 2.5, equation 2.17). This weighting can be described as a matrix, which is commonly referred to as the *averaging kernel* (AK). Depending on the inversion method, it may be possible to derive the AK directly, but often only approximations of this are possible (Estrada et al., 2025). (Note, it is challenging to derive AKs from high dimensional inversion frameworks, and this remains a relevant area for future work).

AKs support the comparison of posterior fluxes against independent estimates, as they quantify the degree of dependence of the posterior on the prior estimate. By multiplying the AK with the estimate to be compared (such as a flux map derived from a NGHGI) a direct comparison can be made with the posterior minus prior flux differences. (Note the estimate compared needs to be at the same spatiotemporal resolution as the AK). This can be shown based on equation 2.17:

$$\boldsymbol{x_{pos}} = (\mathbf{I} - \mathbf{A})\boldsymbol{x_{pri}} + \mathbf{A}\boldsymbol{x_{true}} + \boldsymbol{\varepsilon} \qquad (10.10)$$

where the matrix $\mathbf{A}$ is the AK, $\mathbf{I}$ is the identity matrix, and $\boldsymbol{\varepsilon}$ is the observational error. An estimate comparable to the posterior fluxes can be derived from the independent flux estimate, $\boldsymbol{x_{ind}}$:

$$\hat{\boldsymbol{x}}_{\boldsymbol{ind}} = (\mathbf{I} - \mathbf{A})\boldsymbol{x_{pri}} + \mathbf{A}\boldsymbol{x_{ind}} \qquad (10.11)$$

This project has received funding from the European Union's Horizon Europe research and innovation programme under grant agreement No 101081395

Thus, comparing $\boldsymbol{x_{pos}}$ and $\widehat{\boldsymbol{x}}_{\boldsymbol{ind}}$ is the same as comparing:

$$\mathbf{A}\boldsymbol{x_{ind}} \Leftrightarrow \boldsymbol{x_{pos}} - (\mathbf{I} - \mathbf{A})\boldsymbol{x_{pri}} \quad (10.12)$$

To summarize, the use of the AK allows an independent estimate to be viewed in the same way the posterior "views" the true fluxes. By applying the AK to the independent estimate it can be directly compared with the posterior flux minus the prior flux weighted by $(\mathbf{I} - \mathbf{A})$ as in (10.12).

11. Epilogue

Rona Thompson

These guidelines attempt to summarize the wealth of knowledge and experience in atmospheric inverse modelling gained over the past approximately three decades. The title "Good Practice Guidelines" was chosen to reflect the fact that this is what is considered to be "good practice" at the present time but is by no means fixed indefinitely. The fields of atmospheric modelling and inverse modelling are evolving all the time and, thus what is "good practice" will evolve as well. Furthermore, this document presents "guidelines", in the sense that it offers advice based on previous studies and experience, but not fixed rules.

As far as the authors are aware, these guidelines are the first to be written for atmospheric inverse modelling and especially pertaining to regional scale inversions. As such, these guidelines should be regarded as a beginning, and the hope is that the international atmospheric inversion community will further contribute to the guidelines and that they will continue to evolve and improve.

12. Acknowledgements

These guidelines were made possible with funding from the European Union's Horizon Europe research and innovation programme under the EYE-CLIMA (grant agreement No. 101081395) and AVENGERS (grant agreement No. 101081322) projects.

This project has received funding from the European Union's Horizon Europe research and innovation programme under grant agreement No 101081395

13. Glossary

IPCC	Intergovernmental Panel on Climate Change
UNFCCC	United Nations Framework Convention on Climate Change
a priori (or prior)	Initial estimate of the state and its uncertainty, based on inventories, climatology, or previous studies
a posteriori (or posterior)	Updated best estimate that combines the *a priori* information with observational data, accounting for their respective uncertainties.
observation operator	A mathematical operator that maps model state variables to observation space. It represents how the model's variables are transformed into what an instrument actually measures.
adjoint operator	The transpose (or adjoint) of the linearised observation or model operator. It propagates information from observation space back to model space.
background mixing ratio	The concentration (mixing ratio) of a tracer that represents large-scale or non-local contributions, excluding local sources within the model domain. It is used as a baseline concentration entering the domain through boundaries.
boundary conditions	Specified values or fluxes of model variables at the edges of the model domain. In atmospheric modelling, boundary conditions control how air masses enter or leave the domain.
background	The model state or estimate that serves as a reference or initial guess before assimilating observations.
analysis	The optimal estimate of the model state obtained by combining background information with observations, weighted by their uncertainties.
condition number	A numerical measure of how sensitive a system is to small perturbations in input data. A high condition number indicates an ill-conditioned problem.
model representation error	Mismatch between reality and what a model can simulate due to structural limitations of the model.
aggregation error	Error introduced when fine-scale processes are represented at coarser spatial or temporal resolution. For example, point observations compared to grid-cell averages can introduce aggregation error.
source receptor relationship (SRR)	A quantitative relationship that describes how sources at one location affect concentrations at another location (receptor).

This project has received funding from the European Union's Horizon Europe research and innovation programme under grant agreement No 101081395

bottom-up	Fluxes (and the methods to derive these) that are independent of atmospheric observations and are derived from process-based or empirical models.
top-down	Fluxes (and the methods to derive these) that are based on atmospheric observations, often through the use of atmospheric inversion.
lateral fluxes	Flows of a given species or element (typically carbon) that are not directly between the surface and the atmosphere but involve horizontal displacement and often lead to an surface-to-atmosphere flux in a different location.
isotopologues	Molecules with the same chemical formula but differ only in their isotopes
source signatures	The characteristic ratio of isotopologues from a particular source.
spin-up	The period in which a forward model is run with prescribed fluxes (and sink) to reach a state representing the actual state of the atmosphere.
kinetic isotope effect (KIE)	The ratio of rate constants for different isotopologues for the same reaction.
footprint	The region over which fluxes have a substantial effect on the observations at a given site, i.e., the site's footprint.
tier	Refers to the one of three methodologies outlined in IPCC Guidelines on national inventories

This project has received funding from the European Union's Horizon Europe research and innovation programme under grant agreement No 101081395

14. References

Aalto, T., Peylin, P., Almut, A., Ma, J., Markkanene, T., Sulkava, H., Bastrikov, V., and Salmon, E.: EYE-CLIMA: High-resolution fluxes and uncertainties of CO2, CH4 and N2O for Europe, EYE-CLIMA Horizon Europe project (grant number 101081395), 2026.

Agustí-Panareda, A., Massart, S., Chevallier, F., Boussetta, S., Balsamo, G., Beljaars, A., Ciais, P., Deutscher, N. M., Engelen, R., Jones, L., Kivi, R., Paris, J.-D., Peuch, V.-H., Sherlock, V., Vermeulen, A. T., Wennberg, P. O., and Wunch, D.: Forecasting global atmospheric CO2, Atmos. Chem. Phys., 14, 11959–11983, https://doi.org/10.5194/acp-14-11959-2014, 2014.

Agustí-Panareda, A., Massart, S., Chevallier, F., Balsamo, G., Boussetta, S., Dutra, E., and Beljaars, A.: A biogenic CO2 flux adjustment scheme for the mitigation of large-scale biases in global atmospheric CO2 analyses and forecasts, Atmos. Chem. Phys., 16, 10399–10418, https://doi.org/10.5194/acp-16-10399-2016, 2016.

Agusti-Panareda, A., Diamantakis, M., Massart, S., Chevallier, F., noz-Sabater, J. M., 'e, J. B., Curcoll, R., Engelen, R., Langerock, B., Law, R., Loh, Z., 'ı, J. A. M., Parrington, M., Peuch, V. H., Ramonet, M., Roehl, C., Vermeulen, A. T., Warneke, T., and Wunch, D.: Modelling CO2 weather - why horizontal resolution matters, Atmospheric Chemistry and Physics, 2019, 1–48, https://doi.org/10.5194/acp-2019-177, 2019.

Agustí-Panareda, A., Barré, J., Massart, S., Inness, A., Aben, I., Ades, M., Baier, B. C., Balsamo, G., Borsdorff, T., Bousserez, N., Boussetta, S., Buchwitz, M., Cantarello, L., Crevoisier, C., Engelen, R., Eskes, H., Flemming, J., Garrigues, S., Hasekamp, O., Huijnen, V., Jones, L., Kipling, Z., Langerock, B., McNorton, J., Meilhac, N., Noël, S., Parrington, M., Peuch, V.-H., Ramonet, M., Razinger, M., Reuter, M., Ribas, R., Suttie, M., Sweeney, C., Tarniewicz, J., and Wu, L.: Technical note: The CAMS greenhouse gas reanalysis from 2003 to 2020, Atmos. Chem. Phys., 23, 3829–3859, https://doi.org/10.5194/acp-23-3829-2023, 2023.

Ahmadov, R., Gerbig, C., Kretschmer, R., Koerner, S., Neininger, B., Dolman, A. J., and Sarrat, C.: Mesoscale covariance of transport and CO2 fluxes: Evidence from observations and simulations using the WRF-VPRM coupled atmosphere-biosphere model, 112, https://doi.org/10.1029/2007jd008552, 2007.

Allan, W., Struthers, H., and Lowe, D. C.: Methane carbon isotope effects caused by atomic chlorine in the marine boundary layer: Global model results compared with Southern Hemisphere measurements, Journal of Geophysical Research: Atmospheres, 112, https://doi.org/10.1029/2006jd007369, 2007.

Alvarez, R. A., Zavala-Araiza, D., Lyon, D. R., Allen, D. T., Barkley, Z. R., Brandt, A. R., Davis, K. J., Herndon, S. C., Jacob, D. J., Karion, A., Kort, E. A., Lamb, B. K., Lauvaux, T., Maasakkers, J. D., Marchese, A. J., Omara, M., Pacala, S. W., Peischl, J., Robinson, A. L., Shepson, P. B., Sweeney, C., Townsend-Small, A., Wofsy, S. C., and Hamburg, S. P.: Assessment of methane emissions from the U.S. oil and gas supply chain, Science, 2, eaar7204, https://doi.org/10.1126/science.aar7204, 2018.

Anderson, D. C., Duncan, B. N., Fiore, A. M., Baublitz, C. B., Follette-Cook, M. B., Nicely, J. M., and Wolfe, G. M.: Spatial and temporal variability of the hydroxyl radical: Understanding the role of large-scale climate features and their influence on OH through its dynamical and photochemical drivers, Atmospheric Chemistry and Physics, 21, 6481–6508, https://doi.org/10.5194/acp-21-6481-2021, 2021.

Andrews, A.: A square root formulation of the Kalman covariance equations., AIAA J., 6, 1165–1166, https://doi.org/10.2514/3.4696, 1968.

Atkinson, R.: Gas-phase tropospheric chemistry of volatile organic compounds: 1. Alkanes and alkenes, Journal of Physical and Chemical Reference Data, 26, 215–290, 1997.

This project has received funding from the European Union's Horizon Europe research and innovation programme under grant agreement No 101081395

Atkinson, R.: Kinetics of the gas-phase reactions of OH radicals with alkanes and cycloalkanes, Atmospheric Chemistry and Physics, 3, 2233–2307, https://doi.org/10.5194/acp-3-2233-2003, 2003.

Bacour, C., MacBean, N., Chevallier, F., Léonard, S., Koffi, E. N., and Peylin, P.: Assimilation of multiple datasets results in large differences in regional- to global-scale NEE and GPP budgets simulated by a terrestrial biosphere model, Biogeosciences, 20, 1089–1111, https://doi.org/10.5194/bg-20-1089-2023, 2023.

Baker, D. F., Bell, E., Davis, K. J., Campbell, J. F., Lin, B., and Dobler, J.: A new exponentially decaying error correlation model for assimilating OCO-2 column-average CO2 data using a length scale computed from airborne lidar measurements, Geosci. Model Dev., 15, 649–668, https://doi.org/10.5194/gmd-15-649-2022, 2021.

Bakkaloglu, S., Lowry, D., Fisher, R. E., France, J. L., and Nisbet, E. G.: Carbon isotopic characterisation and oxidation of UK landfill methane emissions by atmospheric measurements, Waste Manag., 132, 162–175, https://doi.org/10.1016/j.wasman.2021.07.012, 2021.

Bakwin, P. S., Tans, P. P., Hurst, D. F., and Zhao, C.: Measurements of carbon dioxide on very tall towers: results of the NOAA/CMDL program, Tellus, 50B, 401–415, 1998a.

Bakwin, P. S., Tans, P. P., Hurst, D. F., and Zhao, C.: Measurements of carbon dioxide on very tall towers: results of the NOAA/CMDL program, Tellus B, 50, 401–415, https://doi.org/10.3402/tellusb.v50i5.16216, 1998b.

Balsamo, G., Engelen, R., Thiemert, D., Agusti-Panareda, A., Bousserez, N., Broquet, G., Brunner, D., Buchwitz, M., Chevallier, F., Choulga, M., Gon, H. D. V. D., Florentie, L., Haussaire, J.-M., Janssens-Maenhout, G., Jones, M. W., Kaminski, T., Krol, M., Quéré, C. L., Marshall, J., McNorton, J., Prunet, P., Reuter, M., Peters, W., and Scholze, M.: The CO2 Human Emissions (CHE) Project: First Steps Towards a European Operational Capacity to Monitor Anthropogenic CO2 Emissions, Front. Remote Sens., 2, 707247, https://doi.org/10.3389/frsen.2021.707247, 2021.

Baray, S., Jacob, D. J., Maasakkers, J. D., Sheng, J.-X., Sulprizio, M. P., Jones, D. B. A., Bloom, A. A., and McLaren, R.: Estimating 2010–2015 anthropogenic and natural methane emissions in Canada using ECCC surface and GOSAT satellite observations, Atmos Chem Phys, 21, 18101–18121, https://doi.org/10.5194/acp-21-18101-2021, 2021.

Basso, L. S., Wilson, C., Chipperfield, M. P., Tejada, G., Cassol, H. L. G., Arai, E., Williams, M., Smallman, T. L., Peters, W., Naus, S., Miller, J. B., and Gloor, M.: Atmospheric CO2 inversion reveals the Amazon as a minor carbon source caused by fire emissions, with forest uptake offsetting about half of these emissions, Atmos. Chem. Phys., 23, 9685–9723, https://doi.org/10.5194/acp-23-9685-2023, 2023.

Basu, S., Lehman, S. J., Miller, J. B., Andrews, A. E., Sweeney, C., Gurney, K. R., Xu, X., Southon, J., and Tans, P. P.: Estimating US fossil fuel CO2 emissions from measurements of 14C in atmospheric CO2, Proc National Acad Sci, 117, 13300–13307, https://doi.org/10.1073/pnas.1919032117, 2020.

Basu, S., Lan, X., Dlugokencky, E., Michel, S., Schwietzke, S., Miller, J. B., Bruhwiler, L., Oh, Y., Tans, P. P., Apadula, F., Gatti, L. V., Jordan, A., Necki, J., Sasakawa, M., Morimoto, S., Iorio, T. D., Lee, H., Arduini, J., and Manca, G.: Estimating Emissions of Methane Consistent with Atmospheric Measurements of Methane and δ^{13}C of Methane, Atmospheric Chem Phys Discuss, 2022, 1–38, https://doi.org/10.5194/acp-2022-317, 2022a.

Basu, S., Lan, X., Dlugokencky, E., Michel, S., Schwietzke, S., Miller, J. B., Bruhwiler, L., Oh, Y., Tans, P. P., Apadula, F., Gatti, L. V., Jordan, A., Necki, J., Sasakawa, M., Morimoto, S., Iorio, T. D., Lee, H., Arduini, J., and Manca, G.: Estimating emissions of methane consistent with atmospheric measurements of methane and δ13C of methane, Atmos. Chem. Phys., 22, 15351–15377, https://doi.org/10.5194/acp-22-15351-2022, 2022b.

Berchet, A., Pison, I., Chevallier, F., Bousquet, P., Conil, S., Geever, M., Laurila, T., Lavric, J., Lopez, M., Moncrieff, J., Necki, J., Ramonet, M., Schmidt, M., Steinbacher, M., and Tarniewicz, J.: Towards

This project has received funding from the European Union's Horizon Europe research and innovation programme under grant agreement No 101081395

better error statistics for atmospheric inversions of methane surface fluxes, Atmos. Chem. Phys., 13, 7115–7132, https://doi.org/10.5194/acp-13-7115-2013, 2013.

Berchet, A., Pison, I., Chevallier, F., Bousquet, P., Bonne, J. L., and Paris, J. D.: Objectified quantification of uncertainties in Bayesian atmospheric inversions, Geoscientific Model Development, 8, 1525–1546, https://doi.org/10.5194/gmd-8-1525-2015, 2015.

Berchet, A., Sollum, E., Thompson, R. L., Pison, I., Thanwerdas, J., Broquet, G., Chevallier, F., Aalto, T., Berchet, A., Bergamaschi, P., Brunner, D., Engelen, R., Fortems-Cheiney, A., Gerbig, C., Zwaaftink, C. D. G., Haussaire, J.-M., Henne, S., Houweling, S., Karstens, U., Kutsch, W. L., Luijkx, I. T., Monteil, G., Palmer, P. I., Peet, J. C. A. van, Peters, W., Peylin, P., Potier, E., Rödenbeck, C., Saunois, M., Scholze, M., Tsuruta, A., and Zhao, Y.: The Community Inversion Framework v1.0: a unified system for atmospheric inversion studies, Geosci Model Dev, 14, 5331–5354, https://doi.org/10.5194/gmd-14-5331-2021, 2021.

Berchet, A., Thanwerdas, J., Elias, E., Reum, F., and Broquet, G.: CoCO2 Prototype System for a Copernicus CO2 Service: Quantification of transport errors with an ensemble of inversions, 2023.

Bergamaschi, P., Krol, M., Dentener, F., Vermeulen, A., Meinhardt, F., Graul, R., Ramonet, M., Peters, W., and Dlugokencky, E. J.: Inverse modelling of national and European CH_4 emissions using the atmospheric zoom model TM5, Atmos. Chem. Phys., 5, 2431–2460, https://doi.org/10.5194/acp-5-2431-2005, 2005.

Bergamaschi, P., Frankenberg, C., Meirink, J. F., Krol, M., Dentener, F., Wagner, T., Platt, U., Kaplan, J. O., Korner, S., Heimann, M., Dlugokencky, E. J., and Goede, A.: Satellite chartography of atmospheric methane from SCIAMACHY on board ENVISAT: 2. Evaluation based on inverse model simulations, J. Geophys. Res., 112, 2007.

Bergamaschi, P., Frankenberg, C., Meirink, J. F., Krol, M., Villani, M. G., Houweling, S., Dentener, F., Dlugokencky, E. J., Miller, J. B., Gatti, L. V., Engel, A., and Levin, I.: Inverse modeling of global and regional CH4 emissions using SCIAMACHY satellite retrievals, Journal of Geophysical Research: Atmospheres, 114, D22301, https://doi.org/10.1029/2009jd012287, 2009.

Bergamaschi, P., Krol, M., Meirink, J. F., Dentener, F., Segers, A., Aardenne, J. van, Monni, S., Vermeulen, A. T., Schmidt, M., Ramonet, M., Yver, C., Meinhardt, F., Nisbet, E. G., Fisher, R. E., O'Doherty, S., and Dlugokencky, E. J.: Inverse modeling of European CH4 emissions 2001-2006, J. Geophys. Res., 115, D22309, https://doi.org/10.1029/2010jd014180, 2010.

Bergamaschi, P., Houweling, S., Segers, A., Krol, M., Frankenberg, C., Scheepmaker, R. A., Dlugokencky, E., Wofsy, S. C., Kort, E. A., Sweeney, C., Schuck, T., Brenninkmeijer, C., Chen, H., Beck, V., and Gerbig, C.: Atmospheric CH4 in the first decade of the 21st century: Inverse modeling analysis using SCIAMACHY satellite retrievals and NOAA surface measurements, https://doi.org/10.1002/jgrd.50480, 2013.

Bergamaschi, P., Segers, A., Brunner, D., Haussaire, J.-M., Henne, S., Ramonet, M., Arnold, T., Biermann, T., Chen, H., Conil, S., Delmotte, M., Forster, G., Frumau, A., Kubistin, D., Lan, X., Leuenberger, M., Lindauer, M., Lopez, M., Manca, G., Müller-Williams, J., O'Doherty, S., Scheeren, B., Steinbacher, M., Trisolino, P., Vítková, G., and Kwok, C. Y.: High-resolution inverse modelling of European CH4 emissions using the novel FLEXPART-COSMO TM5 4DVAR inverse modelling system, Atmos. Chem. Phys., 22, 13243–13268, https://doi.org/10.5194/acp-22-13243-2022, 2022.

Bernard, J., Prigent, C., Jimenez, C., Fluet-Chouinard, E., Lehner, B., Salmon, E., Ciais, P., Zhang, Z., Peng, S., and Saunois, M.: The GIEMS-MethaneCentric database: a dynamic and comprehensive global product of methane-emitting aquatic areas, Earth Syst. Sci. Data, 17, 2985–3008, https://doi.org/10.5194/essd-17-2985-2025, 2025.

Bindle, L., Martin, R. V., Cooper, M. J., Lundgren, E. W., Eastham, S. D., Auer, B. M., Clune, T. L., Weng, H., Lin, J., Murray, L. T., Meng, J., Keller, C. A., Putman, W. M., Pawson, S., and Jacob, D. J.: Grid-

This project has received funding from the European Union's Horizon Europe research and innovation programme under grant agreement No 101081395

stretching capability for the GEOS-Chem 13.0.0 atmospheric chemistry model, Geosci. Model Dev., 14, 5977–5997, https://doi.org/10.5194/gmd-14-5977-2021, 2021.

Bloom, A. A., Bowman, K. W., Lee, M., Turner, A. J., Schroeder, R., Worden, J. R., Weidner, R., McDonald, K. C., and Jacob, D. J.: A global wetland methane emissions and uncertainty dataset for atmospheric chemical transport models (WetCHARTs version 1.0), Geosci. Model Dev., 10, 2141–2156, https://doi.org/10.5194/gmd-10-2141-2017, 2017.

Bocquet, M., Wu, L., and Chevallier, F.: Bayesian design of control space for optimal assimilation of observations. Part I: Consistent multiscale formalism, Quarterly Journal of the Royal Meteorological Society, 137, 1340–1356, https://doi.org/10.1002/qj.837, 2011.

Börjesson, G., Samuelsson, J., and Chanton, J.: Methane Oxidation in Swedish Landfills Quantified with the Stable Carbon Isotope Technique in Combination with an Optical Method for Emitted Methane, Environ. Sci. Technol., 41, 6684–6690, https://doi.org/10.1021/es062735v, 2007.

Bösch, H., Hilker, M., and Noël, S.: Report on the Evaluation of N2O from satellites, EYE-CLIMA deliverable D1.6, https://eyeclima.eu/products/public-reports/, 2026.

Breon, F. M., Broquet, G., Puygrenier, V., Chevallier, F., Xueref-Remy, I., Ramonet, M., Dieudonné, E., Lopez, M., Schmidt, M., Perrussel, O., and Ciais, P.: An attempt at estimating Paris area CO2 emissions from atmospheric concentration measurements, Atmospheric Chemistry and Physics, 15, 1707–1724, https://doi.org/10.5194/acp-15-1707-2015, 2015.

Broquet, G., Chevallier, F., Rayner, P., Aulagnier, C., Pison, I., Ramonet, M., Schmidt, M., Vermeulen, A. T., and Ciais, P.: A European summertime CO2 biogenic flux inversion at mesoscale from continuous in situ mixing ratio measurements, Journal of Geophysical Research: Atmospheres, 116, 1–22, https://doi.org/10.1029/2011jd016202, 2011.

Broquet, G., Chevallier, F., Bréon, F. M., Alemanno, M., Apadula, F., Hammer, S., Haszpra, L., Meinhardt, F., Necki, J., Piacentino, S., Ramonet, M., Schmidt, M., Thompson, R. L., Vermeulen, A. T., Yver, C., and Ciais, P.: Regional inversion of CO2 ecosystem fluxes from atmospheric measurements: reliability of the uncertainty estimates, Atmos. Chem. Phys., 13, 9039–9056, https://doi.org/10.5194/acp-13-9039-2013, 2013.

Broquet, G., Brunner, D., Koene, E., Kuhlmann, G., Brazidec, J. D. L., Tamminen, J., Kaminski, T., Bousserez, N., Marshall, J., Santaren, D., and Berchet, A.: CoCO2 Prototype System for a Copernicus CO2 Service: Synthesis and Recommendations, D4.8, 2023.

Broquet, G., Berchet, A., Fortems-Cheiney, A., Mengistu, A., Tenkanen, M., Aalto, T., and Krishnankutty, N.: EYE-CLIMA: Final fluxes of CO2, CH4 and N2O at 0.5° from 2005, EYE-CLIMA, Horizon Europe project (grant number 101081395), Norway, 2026.

Brunner, D., Henne, S., Keller, C. A., Reimann, S., Vollmer, M. K., O'Doherty, S., and Maione, M.: An extended Kalman-filter for regional scale inverse emission estimation, Atmospheric Chemistry and Physics, 12, 3455–3478, https://doi.org/10.5194/acp-12-3455-2012, 2012.

Brühl, C. and Crutzen, P.MPIC Two-Dimensional Model, in: The Atmospheric Effects of Stratospheric Aircraft: Report of the 1992 Models and Measurements Workshop, Vol 1, p102, https://ntrs.nasa.gov/api/citations/19930015968/downloads/19930015968.pdf 1993.

Buchwitz, M., Reuter, M., Schneising, O., Boesch, H., Guerlet, S., Dils, B., Aben, I., Armante, R., Bergamaschi, P., Blumenstock, T., Bovensmann, H., Brunner, D., Buchmann, B., Burrows, J. P., Butz, A., Chédin, A., Chevallier, F., Crevoisier, C. D., Deutscher, N. M., Frankenberg, C., Hase, F., Hasekamp, O. P., Heymann, J., Kaminski, T., Laeng, A., Lichtenberg, G., Mazière, M. D., Noël, S., Notholt, J., Orphal, J., Popp, C., Parker, R., Scholze, M., Sussmann, R., Stiller, G. P., Warneke, T., Zehner, C., Bril, A., Crisp, D., Griffith, D. W. T., Kuze, A., O'Dell, C., Oshchepkov, S., Sherlock, V., Suto, H., Wennberg, P., Wunch, D., Yokota, T., and Yoshida, Y.: The Greenhouse Gas Climate Change Initiative (GHG-CCI): Comparison and quality assessment of near-surface-sensitive satellite-derived

This project has received funding from the European Union's Horizon Europe research and innovation programme under grant agreement No 101081395

CO2 and CH4 global data sets, Remote Sens. Environ., 162, 344–362, https://doi.org/10.1016/j.rse.2013.04.024, 2015.

Buendia, E. C., Guendehou, S., Limmeechokchai, B., Pipatti, R., Rojas, Y., Sturgiss, R., Tanabe, K., Wirth, T., Romano, D., Witi, J., Garg, A., Weitz, M. M., Cai, B., Ottinger, D. A., Dong, H., MacDonald, J. D., Ogle, S. M., Rocha, M. T., Sanchez, M. J. S., Bartram, D. M., and Towprayoon, S.: 2019 Refinement to the 2006 IPCC Guidelines for National Greenhous Gas Inventories, 2019.

Burgers, G., Leeuwen, P. J. van, and Evensen, G.: Analysis Scheme in the Ensemble Kalman Filter, Mon. Weather Rev., 126, 1719–1724, https://doi.org/10.1175/1520-0493(1998)126<1719:asitek>2.0.co;2, 1998.

Butterbach-Bahl, K., Baggs, E. M., Dannenmann, M., Kiese, R., and Zechmeister-Boltenstern, S.: Nitrous oxide emissions from soils: how well do we understand the processes and their controls?, Biogeosciences, 368, https://doi.org/10.1098/rstb.2013.0122, 2013.

Byrne, B., Baker, D. F., Basu, S., Bertolacci, M., Bowman, K. W., Carroll, D., Chatterjee, A., Chevallier, F., Ciais, P., Cressie, N., Crisp, D., Crowell, S., Deng, F., Deng, Z., Deutscher, N. M., Dubey, M. K., Feng, S., García, O. E., Griffith, D. W. T., Herkommer, B., Hu, L., Jacobson, A. R., Janardanan, R., Jeong, S., Johnson, M. S., Jones, D. B. A., Kivi, R., Liu, J., Liu, Z., Maksyutov, S., Miller, J. B., Miller, S. M., Morino, I., Notholt, J., Oda, T., O'Dell, C. W., Oh, Y.-S., Ohyama, H., Patra, P. K., Peiro, H., Petri, C., Philip, S., Pollard, D. F., Poulter, B., Remaud, M., Schuh, A., Sha, M. K., Shiomi, K., Strong, K., Sweeney, C., Té, Y., Tian, H., Velazco, V. A., Vrekoussis, M., Warneke, T., Worden, J. R., Wunch, D., Yao, Y., Yun, J., Zammit-Mangion, A., and Zeng, N.: National CO2 budgets (2015–2020) inferred from atmospheric CO2 observations in support of the global stocktake, Earth Syst. Sci. Data, 15, 963–1004, https://doi.org/10.5194/essd-15-963-2023, 2023.

Calle, L. and Poulter, B.: Ecosystem age-class dynamics and distribution in the LPJ-wsl v2.0 global ecosystem model, Geosci. Model Dev., 14, 2575–2601, https://doi.org/10.5194/gmd-14-2575-2021, 2021.

Cantrell, C. A., Shetter, R. E., McDaniel, A. H., Calvert, J. G., Davidson, J. A., Lowe, D. C., Tyler, S. C., Cicerone, R. J., and Greenberg, J. P.: Carbon Kinetic Isotope Effect in the Oxidation of Methane by the Hydroxyl Radical, Journal of Geophysical Research-Atmospheres, 95, 22455–22462, https://doi.org/10.1029/jd095id13p22455, 1990.

Carranza, V., Biggs, B., Meyer, D., Townsend-Small, A., Thiruvenkatachari, R. R., Venkatram, A., Fischer, M. L., and Hopkins, F. M.: Isotopic Signatures of Methane Emissions From Dairy Farms in California's San Joaquin Valley, J. Geophys. Res.: Biogeosciences, 127, https://doi.org/10.1029/2021jg006675, 2022.

Chandra, N., Patra, P. K., Fujita, R., Höglund-Isaksson, L., Umezawa, T., Goto, D., Morimoto, S., Vaughn, B. H., and Röckmann, T.: Methane emissions decreased in fossil fuel exploitation and sustainably increased in microbial source sectors during 1990–2020, Commun. Earth Environ., 5, 147, https://doi.org/10.1038/s43247-024-01286-x, 2024.

Chau, T. T. T., Gehlen, M., and Chevallier, F.: A seamless ensemble-based reconstruction of surface ocean pCO2 and air–sea CO2 fluxes over the global coastal and open oceans, Biogeosciences, 19, 1087–1109, https://doi.org/10.5194/bg-19-1087-2022, 2022.

Chen, Z., Jacob, D. J., Nesser, H., Sulprizio, M. P., Lorente, A., Varon, D. J., Lu, X., Shen, L., Qu, Z., Penn, E., and Yu, X.: Methane emissions from China: a high-resolution inversion of TROPOMI satellite observations, Atmos Chem Phys, 22, 10809–10826, https://doi.org/10.5194/acp-22-10809-2022, 2022.

Chen et al., under review for PNAS, 2026.

Chevallier, F.: Impact of correlated observation errors on inverted CO2 surface fluxes from OCO measurements, Geophysical Research Letters, 34, https://doi.org/10.1029/2007gl030463, 2007a.

This project has received funding from the European Union's Horizon Europe research and innovation programme under grant agreement No 101081395

Chevallier, F., Breon, F. M., and Rayner, P. J.: Contribution of the Orbiting Carbon Observatory to the estimation of CO2 sources and sinks: theoretical study in a variational data assimilation framework, J. Geophys. Res., 112, D09307, doi:10.1029/2006JD007375, 2007b.

Chevallier, F.: Fluxes of Carbon Dioxide From Managed Ecosystems Estimated by National Inventories Compared to Atmospheric Inverse Modeling, Geophys Res Lett, 48, https://doi.org/10.1029/2021gl093565, 2021.

Chevallier, F., Fisher, M., Peylin, P., Serrar, S., Bousquet, P., Breon, F. M., Chédin, A., and Ciais, P.: Inferring CO2 sources and sinks from satellite observations: Method and application to TOVS data, Journal of Geophysical Research-Atmospheres, 110, https://doi.org/10.1029/2005jd006390, 2005.

Chevallier, F., Viovy, N., Reichstein, M., and Ciais, P.: On the assignment of prior errors in Bayesian inversions of CO2 surface fluxes, Geophys Res Lett, 33, https://doi.org/10.1029/2006gl026496, 2006.

Chevallier, F., Ciais, P., Conway, T. J., Aalto, T., Anderson, B. E., Bousquet, P., Brunke, E. G., Ciattaglia, L., Esaki, Y., and Fröhlich, M.: CO2 surface fluxes at grid point scale estimated from a global 21 year reanalysis of atmospheric measurements, Journal of Geophysical Research: Atmospheres, 115, https://doi.org/10.1029/2010jd013887, 2010.

Chevallier, F., Wang, T., Ciais, P., Maignan, F., Bocquet, M., Arain, M. A., Cescatti, A., Chen, J., Dolman, A. J., Law, B. E., Margolis, H. A., Montagnani, L., and Moors, E. J.: What eddy-covariance measurements tell us about prior land flux errors in CO2-flux inversion schemes, Glob. Biogeochem. Cycles, 26, https://doi.org/10.1029/2010gb003974, 2012.

Chib, S. and Greenberg, E.: Understanding the Metropolis-Hastings Algorithm, The American Statistician, 49, 327–335, https://doi.org/10.1080/00031305.1995.10476177, 1995.

Ciais, P., Wang, Y., Andrew, R., Bron, F. M., Chevallier, F., Broquet, G., Nabuurs, G. J., Peters, G., McGrath, M., Meng, W., Zheng, B., and Tao, S.: Biofuel burning and human respiration bias on satellite estimates of fossil fuel CO2 emissions, Environ Res Lett, 15, 074036, https://doi.org/10.1088/1748-9326/ab7835, 2020a.

Ciais, P., Yao, Y., Gasser, T., Baccini, A., Wang, Y., Lauerwald, R., Peng, S., Bastos, A., Li, W., Raymond, P. A., Canadell, J. G., Peters, G. P., Andres, R. J., Chang, J., Yue, C., Dolman, A. J., Haverd, V., Hartmann, J., Laruelle, G., Konings, A. G., King, A. W., Liu, Y., Luyssaert, S., Maignan, F., Patra, P. K., Peregon, A., Regnier, P., Pongratz, J., Poulter, B., Shvidenko, A., Valentini, R., Wang, R., Broquet, G., Yin, Y., Zscheischler, J., Guenet, B., Goll, D. S., Ballantyne, A.-P., Yang, H., Qiu, C., and Zhu, D.: Empirical estimates of regional carbon budgets imply reduced global soil heterotrophic respiration, Natl Sci Rev, 8, nwaa145-, https://doi.org/10.1093/nsr/nwaa145, 2020b.

Ciais, P., Yao, Y., Gasser, T., Baccini, A., Wang, Y., Lauerwald, R., Peng, S., Bastos, A., Li, W., Raymond, P. A., Canadell, J. G., Peters, G. P., Andres, R. J., Chang, J., Yue, C., Dolman, A. J., Haverd, V., Hartmann, J., Laruelle, G., Konings, A. G., King, A. W., Liu, Y., Luyssaert, S., Maignan, F., Patra, P. K., Peregon, A., Regnier, P., Pongratz, J., Poulter, B., Shvidenko, A., Valentini, R., Wang, R., Broquet, G., Yin, Y., Zscheischler, J., Guenet, B., Goll, D. S., Ballantyne, A.-P., Yang, H., Qiu, C., and Zhu, D.: Empirical estimates of regional carbon budgets imply reduced global soil heterotrophic respiration, Natl Sci Rev, 8, nwaa145, https://doi.org/10.1093/nsr/nwaa145, 2020c.

Ciais, P., Bastos, A., Chevallier, F., Lauerwald, R., Poulter, B., Canadell, J. G., Hugelius, G., Jackson, R. B., Jain, A., Jones, M., Kondo, M., Luijkx, I. T., Patra, P. K., Peters, W., Pongratz, J., Petrescu, A. M. R., Piao, S., Qiu, C., Randow, C. V., Regnier, P., Saunois, M., Scholes, R., Shvidenko, A., Tian, H., Yang, H., Wang, X., and Zheng, B.: Definitions and methods to estimate regional land carbon fluxes for the second phase of the REgional Carbon Cycle Assessment and Processes Project (RECCAP-2), Geosci. Model Dev., 15, 1289–1316, https://doi.org/10.5194/gmd-15-1289-2022, 2022.

Corazza, M., Bergamaschi, P., Vermeulen, A. T., Aalto, T., Haszpra, L., Meinhardt, F., O'Doherty, S., Thompson, R., Moncrieff, J., Popa, E., Steinbacher, M., Jordan, A., Dlugokencky, E., Brühl, C., Krol, M., and Dentener, F.: Inverse modelling of European N2O emissions: assimilating observations from

This project has received funding from the European Union's Horizon Europe research and innovation programme under grant agreement No 101081395

different networks, Atmos. Chem. Phys., 11, 2381–2398, https://doi.org/10.5194/acp-11-2381-2011, 2011.

Craig, H.: Isotopic standards for carbon and oxygen and correction factors for mass-spectrometric analysis of carbon dioxide, Geochim. Cosmochim. Acta, 12, 133–149, https://doi.org/10.1016/0016-7037(57)90024-8, 1957.

Crippa, M., Solazzo, E., Huang, G., Guizzardi, D., Koffi, E., Muntean, M., Schieberle, C., Friedrich, R., and Janssens-Maenhout, G.: High resolution temporal profiles in the Emissions Database for Global Atmospheric Research, Sci Data, 7, 121, https://doi.org/10.1038/s41597-020-0462-2, 2020.

Crippa, M., Solazzo, E., Guizzardi, D., Monforti-Ferrario, F., Tubiello, F. N., and Leip, A.: Food systems are responsible for a third of global anthropogenic GHG emissions, Nature Food, 1–12, https://doi.org/10.1038/s43016-021-00225-9, 2021.

Crippa, M., Guizzardi, D., Pagani, F., Schiavina, M., Melchiorri, M., Pisoni, E., Graziosi, F., Muntean, M., Maes, J., Dijkstra, L., Damme, M. V., Clarisse, L., and Coheur, P.: Insights into the spatial distribution of global, national, and subnational greenhouse gas emissions in the Emissions Database for Global Atmospheric Research (EDGAR v8.0), Earth Syst. Sci. Data, 16, 2811–2830, https://doi.org/10.5194/essd-16-2811-2024, 2024.

Crowell, S., Baker, D., Schuh, A., Basu, S., Jacobson, A. R., Chevallier, F., Liu, J., Deng, F., Feng, L., Chatterjee, A., Crisp, D., Eldering, A., Jones, D. B., McKain, K., Miller, J., Nassar, R., Oda, T., O'Dell, C., Palmer, P. I., Schimel, D., Stephens, B., and Sweeney, C.: The 2015-2016 Carbon Cycle As Seen from OCO-2 and the Global In Situ Network, Atmospheric Chemistry and Physics, 2019, 1–79, https://doi.org/10.5194/acp-2019-87, 2019.

Crowley, J. N., Saueressig, G., Bergamaschi, P., Fischer, H., and Harris, G. W.: Carbon kinetic isotope effect in the reaction CH 4+ Cl: a relative rate study using FTIR spectroscopy, Chemical physics letters, 303, 268–274, https://doi.org/10.1016/s0009-2614(99)00243-2, 1999.

Crutzen, P. J.: The influence of nitrogen oxides on the atmospheric ozone content, Q. J. R. Meteorol. Soc., 96, 1970.

Dasgupta, B., Menoud, M., Veen, C. van der, Levin, I., Veidt, C., Moossen, H., Michel, S. E., Sperlich, P., Morimoto, S., Fujita, R., Umezawa, T., Platt, S., Zwaaftink, C. G., Myhre, C. L., Fisher, R., Lowry, D., Nisbet, E. G., France, J., Maisch, C. W., Brailsford, G., Moss, R., Goto, D., Pandey, S., Houweling, S., Warwick, N., and Röckmann, T.: Harmonisation of methane isotope ratio measurements from different laboratories using atmospheric samples, Atmos. Meas. Tech., 18, 6591–6607, https://doi.org/10.5194/amt-18-6591-2025, 2025.

Dasgupta, B., Pandey, S., Houweling, S., Menoud, M., Veen, C. van der, Miller, J., Riddell-Young, B., Michel, S. E., Sperlich, P., Morimoto, S., Fujita, R., Platt, S., Zwaaftink, C. G., Levin, I., Veidt, C., Myhre, C. L., Maisch, C. W., Fisher, R., Nisbet, E. G., France, J., Moss, R., Warwick, N., and Röckmann, T.: Global methane emission estimates from a dual-isotope inversion: new constraints from δD-CH4, Atmos. Chem. Phys., 26, 8601–8616, https://doi.org/10.5194/acp-26-8601-2026, 2026.

Defourny, P.: ESA Land Cover Climate Change Initiative: Global Land Cover Maps, Version 2.0.7. Centre for Environmental Data Analysis, date of citation. https://catalogue.ceda.ac.uk/uuid/b382ebe6679d44b8b0e68ea4ef4b701c, 2019.

Deng, Z., Ciais, P., Tzompa-Sosa, Z. A., Saunois, M., Qiu, C., Tan, C., Sun, T., Ke, P., Cui, Y., Tanaka, K., Lin, X., Thompson, R. L., Tian, H., Yao, Y., Huang, Y., Lauerwald, R., Jain, A. K., Xu, X., Bastos, A., Sitch, S., Palmer, P. I., Lauvaux, T., d'Aspremont, A., Giron, C., Benoit, A., Poulter, B., Chang, J., Petrescu, A. M. R., Davis, S. J., Liu, Z., Grassi, G., Albergel, C., Tubiello, F. N., Perugini, L., Peters, W., and Chevallier, F.: Comparing national greenhouse gas budgets reported in UNFCCC inventories against atmospheric inversions, Earth Syst Sci Data, 14, 1639–1675, https://doi.org/10.5194/essd-14-1639-2022, 2022.

This project has received funding from the European Union's Horizon Europe research and innovation programme under grant agreement No 101081395

Deng, Z., Ciais, P., Hu, L., Martinez, A., Saunois, M., Thompson, R. L., Tibrewal, K., Peters, W., Byrne, B., Grassi, G., Palmer, P. I., Luijkx, I. T., Liu, Z., Liu, J., Fang, X., Wang, T., Tian, H., Tanaka, K., Bastos, A., Sitch, S., Poulter, B., Albergel, C., Tsuruta, A., Maksyutov, S., Janardanan, R., Niwa, Y., Zheng, B., Thanwerdas, J., Belikov, D., Segers, A., and Chevallier, F.: Global Greenhouse Gas Reconciliation 2022, Earth Syst. Sci. Data, 2025, 1–47, https://doi.org/10.5194/essd-17-1121-2025, 2025.

Desroziers, G., Berre, L., Chapnik, B. & Poli, P. Diagnosis of observation, background and analysis-error statistics in observation space. Q. J. R. Meteorol. Soc. 131, 3385–3396 (2005).

Diaz-Isaac, L. I., Lauvuax, T., Bocquet, M., and Davis, K. J.: Calibration of a multi-physics ensemble for greenhouse gas atmospheric transport model uncertainty estimation, Atmos. Chem. Phys., 19, 5695–5718, https://doi.org/10.5194/acp-19-5695-2019, 2019.

Douglas, P. M. J., Stratigopoulos, E., Park, J., and Phan, D.: Global geographic variability in freshwater methane hydrogen isotope ratios and its implications for emissions source apportionment and microbial biogeochemistry, Biogeosciences, 1–35, https://doi.org/10.5194/bg-2020-410, 2020.

East, J. D., Jacob, D. J., Jervis, D., Balasus, N., Estrada, L. A., Hancock, S. E., Sulprizio, M. P., Thomas, J., Wang, X., Chen, Z., Varon, D. J., and Worden, J. R.: Worldwide inference of national methane emissions by inversion of satellite observations with UNFCCC prior estimates, Nat. Commun., 16, 11004, https://doi.org/10.1038/s41467-025-67122-8, 2025.

EEA CORINE Land Cover User Manual; Copernicus Land Monitoring Service: Copenhagen, Denmark, 2021

Emmons, L. K., Walters, S., Hess, P. G., Lamarque, J. F., Pfister, G. G., Fillmore, D., Granier, C., Guenther, A., Kinnison, D., Laepple, T., Orlando, J., Tie, X., Tyndall, G., Wiedinmyer, C., Baughcum, S. L., and Kloster, S.: Description and evaluation of the Model for Ozone and Related chemical Tracers, version 4 (MOZART-4), Geosci. Model Dev., 3, 43–67, https://doi.org/10.5194/gmd-3-43-2010, 2010.

Enting, I. G.: Inverse Problems in Atmospheric Constituent Transport, Cambridge University Press, Cambridge, 2002.

Errico, R. M.: What is an Adjoint Model?, Bull. Am. Meteorol. Soc., 78, 2577–2591, https://doi.org/10.1175/1520-0477(1997)078<2577:wiaam>2.0.co;2, 1997.

Estrada, L. A., Varon, D. J., Sulprizio, M., Nesser, H., Chen, Z., Balasus, N., Hancock, S. E., He, M., East, J. D., Mooring, T. A., Alonso, A. O., Maasakkers, J. D., Aben, I., Baray, S., Bowman, K. W., Worden, J. R., Cardoso-Saldaña, F. J., Reidy, E., and Jacob, D. J.: Integrated Methane Inversion (IMI) 2.0: an improved research and stakeholder tool for monitoring total methane emissions with high resolution worldwide using TROPOMI satellite observations, Geosci. Model Dev., 18, 3311–3330, https://doi.org/10.5194/gmd-18-3311-2025, 2025.

Etiope, G., Ciotoli, G., Schwietzke, S., and Schoell, M.: Gridded maps of geological methane emissions and their isotopic signature, Earth Sys Sci Data, 11, 1–22, https://doi.org/10.5194/essd-11-1-2019, 2019.

Evensen, G.: Sequential data assimilation with a nonlinear quasi-geostrophic model using Monte Carlo methods to forecast error statistics, Journal of Geophysical Research, 99, 10143–10162, 1994.

Feinberg, A. I., Coulon, A., Stenke, A., Schwietzke, S., and Peter, T.: Isotopic source signatures_ Impact of regional variability on the δ13CH4 trend and spatial distribution, Atmospheric Environment, 174, 99–111, https://doi.org/10.1016/j.atmosenv.2017.11.037, 2018.

Firestone, M. K. and Davidson, E. A.: Microbiological basis of NO and N2O production and consumption in soil, edited by: Andreae, M. O. and Schimel, D. S., John Wiley & Sons Ltd, 7–21, 1989.

Fisher: Minimization algorithms for variational data assimilation, in: Seminar on Recent Developments in Numerical Methods for Atmospheric Modelling, 1998.

This project has received funding from the European Union's Horizon Europe research and innovation programme under grant agreement No 101081395

Fisher, M. and Courtier, P.: Estimating the covariances matrices of analysis and forecast error in variational data assimilation, 1995.

Fisher, R. E., France, J. L., Lowry, D., Lanoisellé, M., Brownlow, R., Pyle, J. A., Cain, M., Warwick, N., Skiba, U. M., Drewer, J., Dinsmore, K. J., Leeson, S. R., Bauguitte, S. J. B., Wellpott, A., O'Shea, S. J., Allen, G., Gallagher, M. W., Pitt, J., Percival, C. J., Bower, K., George, C., Hayman, G. D., Aalto, T., Lohila, A., Aurela, M., Laurila, T., Crill, P. M., McCalley, C. K., and Nisbet, E. G.: Measurement of the 13C isotopic signature of methane emissions from Northern European wetlands, Global Biogeochem Cycles, 2016GB005504, https://doi.org/10.1002/2016gb005504, 2017.

Fluet-Chouinard, E., Stocker, B. D., Zhang, Z., Malhotra, A., Melton, J. R., Poulter, B., Kaplan, J. O., Goldewijk, K. K., Siebert, S., Minayeva, T., Hugelius, G., Joosten, H., Barthelmes, A., Prigent, C., Aires, F., Hoyt, A. M., Davidson, N., Finlayson, C. M., Lehner, B., Jackson, R. B., and McIntyre, P. B.: Extensive global wetland loss over the past three centuries, Nature, 614, 281–286, https://doi.org/10.1038/s41586-022-05572-6, 2023.

Forster, P., Storelvmo, T., Armour, K., Collins, W., Dufresne, J. L., Frame, D., Lunt, D. J., Mauritsen, T., Palmer, M. D., Watanabe, M., Wild, M., and Zhang, H.: The Earth's Energy Budget, Climate Feedbacks, and Climate Sensitivity. In: Climate Change 2021: The Physical Science Basis. Contribution of Working Group I to the Sixth Assessment Report of the Intergovernmental Panel on Climate Change, Cambridge University Press, Cambridge, United Kingdom, 2021.

Fortems-Cheiney, A.: EYE-CLIMA: Recommendation on whether CO source of CO2 needs to be accounted for in CO2 inversions, EYE-CLIMA, Horizon Europe project (grant number 101081395), Norway, 2025.

Fortems-Cheiney, A., Pison, I., Broquet, G., Dufour, G., Berchet, A., Potier, E., Coman, A., Siour, G., and Costantino, L.: Variational regional inverse modeling of reactive species emissions with PYVAR-CHIMERE-v2019, Geosci Model Dev, 14, 2939–2957, https://doi.org/10.5194/gmd-14-2939-2021, 2021.

France, J. L., Fisher, R. E., Lowry, D., Allen, G., Andrade, M. F., Bauguitte, S. J.-B., Bower, K., Broderick, T. J., Daly, M. C., Forster, G., Gondwe, M., Helfter, C., Hoyt, A. M., Jones, A. E., Lanoisell, M., Moreno, I., Nisbet-Jones, P. B. R., Oram, D., Pasternak, D., Pitt, J. R., Skiba, U., Stephens, M., Wilde, S. E., and Nisbet, E. G.: 13C methane source signatures from tropical wetland and rice field emissions, Philos. Trans. R. Soc. A, 380, 20200449, https://doi.org/10.1098/rsta.2020.0449, 2022.

Friedlingstein, P., O'Sullivan, M., Jones, M. W., Andrew, R. M., Hauck, J., Landschützer, P., Quéré, C. L., Li, H., Luijkx, I. T., Olsen, A., Peters, G. P., Peters, W., Pongratz, J., Schwingshackl, C., Sitch, S., Canadell, J. G., Ciais, P., Jackson, R. B., Alin, S. R., Arneth, A., Arora, V., Bates, N. R., Becker, M., Bellouin, N., Berghoff, C. F., Bittig, H. C., Bopp, L., Cadule, P., Campbell, K., Chamberlain, M. A., Chandra, N., Chevallier, F., Chini, L. P., Colligan, T., Decayeux, J., Djeutchouang, L. M., Dou, X., Rojas, C. D., Enyo, K., Evans, W., Fay, A. R., Feely, R. A., Ford, D. J., Foster, A., Gasser, T., Gehlen, M., Gkritzalis, T., Grassi, G., Gregor, L., Gruber, N., Gürses, Ö., Harris, I., Hefner, M., Heinke, J., Hurtt, G. C., Iida, Y., Ilyina, T., Jacobson, A. R., Jain, A. K., Jarníková, T., Jersild, A., Jiang, F., Jin, Z., Kato, E., Keeling, R. F., Goldewijk, K. K., Knauer, J., Korsbakken, J. I., Lan, X., Lauvset, S. K., Lefèvre, N., Liu, Z., Liu, J., Ma, L., Maksyutov, S., Marland, G., Mayot, N., McGuire, P. C., Metzl, N., Monacci, N. M., Morgan, E. J., Nakaoka, S.-I., Neill, C., Niwa, Y., Nützel, T., Olivier, L., Ono, T., Palmer, P. I., Pierrot, D., Qin, Z., Resplandy, L., Roobaert, A., Rosan, T. M., Rödenbeck, C., Schwinger, J., Smallman, T. L., Smith, S. M., Sospedra-Alfonso, R., Steinhoff, T., et al.: Global Carbon Budget 2024, Earth Syst. Sci. Data, 17, 965–1039, https://doi.org/10.5194/essd-17-965-2025, 2025.

Fujita, R., Morimoto, S., Maksyutov, S., Kim, H.-S., Arshinov, M., Brailsford, G., Aoki, S., and Nakazawa, T.: Global and regional CH4 emissions for 1995–2013 derived from atmospheric CH 4, δ 13C-CH 4and δD-CH 4observations and a chemical transport model, Journal of Geophysical Research-Atmospheres, n/a, e2020JD032903, https://doi.org/10.1029/2020jd032903, 2020.

This project has received funding from the European Union's Horizon Europe research and innovation programme under grant agreement No 101081395

Fujita, R., Graven, H., Zazzeri, G., Hmiel, B., Petrenko, V. V., Smith, A. M., Michel, S. E., and Morimoto, S.: Global Fossil Methane Emissions Constrained by Multi-Isotopic Atmospheric Methane Histories, J. Geophys. Res.: Atmos., 130, https://doi.org/10.1029/2024jd041266, 2025.

Fung, I., John, J., Lerner, J., Matthews, E., Prather, M., Steele, L. P., and Fraser, P. J.: Three-dimensional model synthesis of the global methane cycle, J. Geophys. Res., 96, 13033–13065, https://doi.org/10.1029/91jd01247, 1991.

Ganesan, A. L., Rigby, M., Zammit-Mangion, A., Manning, A. J., Prinn, R. G., Fraser, P. J., Harth, C. M., Kim, K. R., Krummel, P. B., Li, S., °hle, J. M., O'Doherty, S. J., Park, S., Salameh, P. K., Steele, L. P., and Weiss, R. F.: Characterization of uncertainties in atmospheric trace gas inversions using hierarchical Bayesian methods, Atmos. Chem. Phys., 14, 3855–3864, https://doi.org/10.5194/acp-14-3855-2014, 2014.

Ganesan, A. L., Rigby, M., Lunt, M. F., Parker, R. J., Boesch, H., Goulding, N., Umezawa, T., Zahn, A., Chatterjee, A., Prinn, R. G., Tiwari, Y. K., Schoot, M. van der, and Krummel, P. B.: Atmospheric observations show accurate reporting and little growth in India's methane emissions, Nature communications, 8, 836, https://doi.org/10.1038/s41467-017-00994-7, 2017.

Ganesan, A. L., Stell, A. C., Gedney, N., Comyn-Platt, E., Hayman, G., Rigby, M., Poulter, B., and Hornibrook, E. R. C.: Spatially Resolved Isotopic Source Signatures of Wetland Methane Emissions, Geophys. Res. Lett., 45, 3737–3745, https://doi.org/10.1002/2018gl077536, 2018.

Ganshin, A., Oda, T., Saito, M., Maksyutov, S., Valsala, V., Andres, R. J., Fisher, R. E., Lowry, D., Lukyanov, A., and Matsueda, H.: A global coupled Eulerian-Lagrangian model and 1× 1 km CO 2 surface flux dataset for high-resolution atmospheric CO 2 transport simulations, Geoscientific Model Development, 5, 231–243, https://doi.org/10.5194/gmd-5-231-2012, 2012.

Gaspari, G. and Cohn, S. E.: Construction of correlation functions in two and three dimensions, Q. J. R. Meteorol. Soc., 125, 723–757, https://doi.org/10.1002/qj.49712555417, 1999.

Geels, C., Gloor, M., Ciais, P., Bousquet, P., Peylin, P., Vermeulen, A. T., Dargaville, R., Aalto, T., Brandt, J., Christensen, J. H., Frohn, L. M., Haszpra, L., Karstens, U., Rodenbeck, C., Ramonet, M., Carboni, G., and Santaguida, R.: Comparing atmospheric transport models for future regional inversions over Europe - Part 1: mapping the atmospheric CO2 signals, Atmos. Chem. Phys., 7, 3461–3479, 2007.

Giering, R. and Kaminski, T.: Recipes for adjoint code construction, ACM Transactions on Mathematical Software (TOMS), 24, 437–474, https://doi.org/10.1145/293686.293695, 1998.

Gloor, M., Bakwin, P., Hurst, D., Lock, L., Draxler, R., and Tans, P.: What is the concentration footprint of a tall tower?, J. Geophys. Res., 106, 17831–17840, https://doi.org/10.1029/2001jd900021, 2001.

Gómez-Ortiz, C., Monteil, G., Basu, S., and Scholze, M.: A CO2–Δ14CO2 inversion setup for estimating European fossil CO2 emissions, Atmos. Chem. Phys., 25, 397–424, https://doi.org/10.5194/acp-25-397-2025, 2024.

Grassi, G., Stehfest, E., Rogelj, J., Vuuren, D. van, Cescatti, A., House, J., Nabuurs, G.-J., Rossi, S., Alkama, R., Viñas, R. A., Calvin, K., Ceccherini, G., Federici, S., Fujimori, S., Gusti, M., Hasegawa, T., Havlik, P., Humpenöder, F., Korosuo, A., Perugini, L., Tubiello, F. N., and Popp, A.: Critical adjustment of land mitigation pathways for assessing countries' climate progress, Nat Clim Change, 11, 425–434, https://doi.org/10.1038/s41558-021-01033-6, 2021.

Grassi, G., Schwingshackl, C., Gasser, T., Houghton, R. A., Sitch, S., Canadell, J. G., Cescatti, A., Ciais, P., Federici, S., Friedlingstein, P., Kurz, W. A., Sanchez, M. J. S., Viñas, R. A., Alkama, R., Bultan, S., Ceccherini, G., Falk, S., Kato, E., Kennedy, D., Knauer, J., Korosuo, A., Melo, J., McGrath, M. J., Nabel, J. E. M. S., Poulter, B., Romanovskaya, A. A., Rossi, S., Tian, H., Walker, A. P., Yuan, W., Yue, X., and Pongratz, J.: Harmonising the land-use flux estimates of global models and national inventories for 2000–2020, Earth Syst Sci Data, 15, 1093–1114, https://doi.org/10.5194/essd-15-1093-2023, 2023.

This project has received funding from the European Union's Horizon Europe research and innovation programme under grant agreement No 101081395

Guevara, M., Enciso, S., Tena, C., Jorba, O., Dellaert, S., Gon, H. D. van der, and García-Pando, C. P.: A global catalogue of CO2 emissions and co-emitted species from power plants, including high-resolution vertical and temporal profiles, Earth Syst. Sci. Data, 16, 337–373, https://doi.org/10.5194/essd-16-337-2024, 2023.

Guillevic, M., Vollmer, M. K., Wyss, S. A., Leuenberger, D., Ackermann, A., Pascale, C., Niederhauser, B., and Reimann, S.: Dynamic–gravimetric preparation of metrologically traceable primary calibration standards for halogenated greenhouse gases, Atmos. Meas. Tech., 11, 3351–3372, https://doi.org/10.5194/amt-11-3351-2018, 2018.

Gurney, K. R.: Towards robust regional estimates of CO2 sources and sinks using atmospheric transport models, Nature, 415, 626–630, 2002.

Hagemann, R., Nief, G., and Roth, E.: Absolute isotopic scale for deuterium analysis of natural waters. Absolute D/H ratio for SMOW1, Tellus, 22, 712–715, https://doi.org/10.1111/j.2153-3490.1970.tb00540.x, 1970.

Hall, B. D., Sutton, G. S., and Elkins, J. W.: The NOAA nitrous oxide standard scale for atmospheric observations, Journal of Geophysical Research, 112, https://doi.org/10.1029/2006jd007954, 2007.

Hampson, R. F., Kurylo, M. J., and Sander, S. P.: Evaluated Rate Constants for Selected HCFCs and HFCs with OH and O(1D). NASA, Scientific Assessment of Stratospheric Ozone, 1989.

Harvey, A. C.: Forecasting, structural time series models and the Kalman filter, Cambridge University Press, 554 pp., 1990.

He, J., Naik, V., and Horowitz, L. W.: Hydroxyl radical (OH) response to meteorological forcing and implication for the methane budget, Geophysical Research Letters, https://doi.org/10.1029/2021gl094140, 2021.

Helton, J. C. and Davis, F. J.: Latin hypercube sampling and the propagation of uncertainty in analyses of complex systems, Reliab. Eng. Syst. Saf., 81, 23–69, https://doi.org/10.1016/s0951-8320(03)00058-9, 2003.

Henne, S., Brunner, D., Oney, B., Leuenberger, M., Eugster, W., Bamberger, I., Meinhardt, F., Steinbacher, M., and Emmenegger, L.: Validation of the Swiss methane emission inventory by atmospheric observations and inverse modelling, Atmospheric Chemistry and Physics, 16, 3683–3710, https://doi.org/10.5194/acp-16-3683-2016, 2016.

Hmiel, B., Petrenko, V. V., Dyonisius, M. N., Buizert, C., Smith, A. M., Place, P. F., Harth, C., Beaudette, R., Hua, Q., Yang, B., Vimont, I., Michel, S. E., Severinghaus, J. P., Etheridge, D., Bromley, T., Schmitt, J., Faïn, X., Weiss, R. F., and Dlugokencky, E.: Preindustrial 14 CH 4 indicates greater anthropogenic fossil CH 4 emissions, Nature, 578, 409–412, https://doi.org/10.1038/s41586-020-1991-8, 2020.

Hoesly, R. M., Smith, S. J., Feng, L., Klimont, Z., Janssens-Maenhout, G., Pitkanen, T., Seibert, J. J., Vu, L., Andres, R. J., Bolt, R. M., Bond, T. C., Dawidowski, L., Kholod, N., Kurokawa, J., Li, M., Liu, L., Lu, Z., Moura, M. C. P., O'Rourke, P. R., and Zhang, Q.: Historical (1750–2014) anthropogenic emissions of reactive gases and aerosols from the Community Emissions Data System (CEDS), Geosci. Model Dev., 11, 369–408, https://doi.org/10.5194/gmd-11-369-2018, 2017.

Höglund-Isaksson, L., Gmez-Sanabria, A., Klimont, Z., Rafaj, P., and Schpp, W.: Technical potentials and costs for reducing global anthropogenic methane emissions in the 2050 timeframe results from the GAINS model, Environ Res Commun, 2, 025004, https://doi.org/10.1088/2515-7620/ab7457, 2020.

Houtekamer, P. L. and Mitchell, H. L.: A Sequential Ensemble Kalman Filter for Atmospheric Data Assimilation, Mon. Weather Rev., 129, 123–137, https://doi.org/10.1175/1520-0493(2001)129<0123:asekff>2.0.co;2, 2001.

Houtekamer, P. L. and Zhang, F.: Review of the Ensemble Kalman Filter for Atmospheric Data Assimilation, Mon. Wea. Rev., 144, 4489–4532, https://doi.org/10.1175/mwr-d-15-0440.1, 2016.

This project has received funding from the European Union's Horizon Europe research and innovation programme under grant agreement No 101081395

Houweling, S., Bergamaschi, P., Chevallier, F., Heimann, M., Kaminski, T., Krol, M., Michalak, A. M., and Patra, P.: Global inverse modeling of CH4 sources and sinks: an overview of methods, Atmospheric Chemistry and Physics, 17, 235–256, https://doi.org/10.5194/acp-17-235-2017, 2017.

Hu, L., Keller, C. A., Long, M. S., Sherwen, T., Auer, B., Silva, A. D., Nielsen, J. E., Pawson, S., Thompson, M. A., Trayanov, A. L., Travis, K. R., Grange, S. K., Evans, M. J., and Jacob, D. J.: Global simulation of tropospheric chemistry at 12.5 km resolution: performance and evaluation of the GEOS-Chem chemical module (v10-1) within the NASA GEOS Earth system model (GEOS-5 ESM), Geosci. Model Dev., 11, 4603–4620, https://doi.org/10.5194/gmd-11-4603-2018, 2018.

Huijnen, V., Williams, J., Weele, M. van, Noije, T. van, Krol, M., Dentener, F., Segers, A., Houweling, S., Peters, W., Laat, J. de, Boersma, F., Bergamaschi, P., Velthoven, P. van, Sager, P. L., Eskes, H., Alkemade, F., Scheele, R., Nédélec, P., and Pätz, H.-W.: The global chemistry transport model TM5: description and evaluation of the tropospheric chemistry version 3.0, Geosci. Model Dev., 3, 445–473, https://doi.org/10.5194/gmd-3-445-2010, 2010.

Ide, K., Courtier, P., Ghil, M., and Lorenc, A. C.: Unified Notation for Data Assimilation : Operational, Sequential and Variational, Journal of the Meteorological Society of Japan Ser II, 75, 181–189, 1997.

Inness, A., Ades, M., Agustí-Panareda, A., Barré, J., Benedictow, A., Blechschmidt, A.-M., Dominguez, J. J., Engelen, R., Eskes, H., Flemming, J., Huijnen, V., Jones, L., Kipling, Z., Massart, S., Parrington, M., Peuch, V.-H., Razinger, M., Remy, S., Schulz, M., and Suttie, M.: The CAMS reanalysis of atmospheric composition, Atmos Chem Phys, 19, 3515–3556, https://doi.org/10.5194/acp-19-3515-2019, 2019.

Ishijima, K., Nakazawa, T., and Aoki, S.: Variations of atmospheric nitrous oxide concentration in the northern and western Pacific, Tellus B, 61, 408–415, https://doi.org/10.1111/j.1600-0889.2008.00406.x, 2009.

Ishijima, K., Patra, P. K., Takigawa, M., Machida, T., Matsueda, H., Sawa, Y., Steele, L. P., Krummel, P. B., Langenfelds, R. L., Aoki, S., and Nakazawa, T.: Stratospheric influence on the seasonal cycle of nitrous oxide in the tropospheric as deduced from aircraft observations and model simulations, J. Geophys. Res., 115, https://doi.org/10.1029/2009jd013322, 2010.

Ito, A. and Inatomi, M.: Use of a process-based model for assessing the methane budgets of global terrestrial ecosystems and evaluation of uncertainty, Biogeosciences, 9, 759–773, https://doi.org/10.5194/bg-9-759-2012, 2012.

Jacob, D. J., Turner, A. J., Maasakkers, J. D., Sheng, J., Sun, K., Liu, X., Chance, K., Aben, I., McKeever, J., and Frankenberg, C.: Satellite observations of atmospheric methane and their value for quantifying methane emissions, Atmos Chem Phys, 16, 14371–14396, https://doi.org/10.5194/acp-16-14371-2016, 2016.

Jacob, D. J., Varon, D. J., Cusworth, D. H., Dennison, P. E., Frankenberg, C., Gautam, R., Guanter, L., Kelley, J., McKeever, J., Ott, L. E., Poulter, B., Qu, Z., Thorpe, A. K., Worden, J. R., and Duren, R. M.: Quantifying methane emissions from the global scale down to point sources using satellite observations of atmospheric methane, Atmos. Chem. Phys., 22, 9617–9646, https://doi.org/10.5194/acp-22-9617-2022, 2022.

Janssens-Maenhout, G., Pinty, B., Dowell, M., Zunker, H., Andersson, E., Balsamo, G., Bézy, J. L., Brunhes, T., Bösch, H., Bojkov, B., Brunner, D., Buchwitz, M., Crisp, D., Ciais, P., Counet, P., Dee, D., Gon, H. D. van der, Dolman, H., Drinkwater, M. R., Dubovik, O., Engelen, R., Fehr, T., Fernandez, V., Heimann, M., Holmlund, K., Houweling, S., Husband, R., Juvyns, O., Kentarchos, A., Landgraf, J., Lang, R., Löscher, A., Marshall, J., Meijer, Y., Nakajima, M., Palmer, P. I., Peylin, P., Rayner, P., Scholze, M., Sierk, B., Tamminen, J., and Veefkind, P.: Toward an Operational Anthropogenic CO2 Emissions Monitoring and Verification Support Capacity, Bull. Amer. Meteor. Soc., 101, E1439–E1451, https://doi.org/10.1175/bams-d-19-0017.1, 2020.

This project has received funding from the European Union's Horizon Europe research and innovation programme under grant agreement No 101081395

Jentzsch, K., Männistö, E., Marushchak, M. E., Korrensalo, A., Delden, L. van, Tuittila, E.-S., Knoblauch, C., and Treat, C. C.: Shoulder season controls on methane emissions from a boreal peatland, Biogeosciences, 21, 3761–3788, https://doi.org/10.5194/bg-21-3761-2024, 2024.

Jöckel, P., Tost, H., Pozzer, A., Brühl, C., Buchholz, J., Ganzeveld, L., Hoor, P., Kerkweg, A., Lawrence, M. G., Sander, R., Steil, B., Stiller, G., Tanarhte, M., Taraborrelli, D., Aardenne, J. van, and Lelieveld, J.: The atmospheric chemistry general circulation model ECHAM5/MESSy1: consistent simulation of ozone from the surface to the mesosphere, Atmos. Chem. Phys., 6, 5067–5104, https://doi.org/10.5194/acp-6-5067-2006, 2006.

Joelsson, L. M. T., Schmidt, J. A., Nilsson, E. J. K., Blunier, T., Griffith, D. W. T., Ono, S., and Johnson, M. S.: Kinetic isotope effects of 12CH3D + OH and 13CH3D + OH from 278 to 313 K, Atmos. Chem. Phys., 16, 4439–4449, https://doi.org/10.5194/acp-16-4439-2016, 2016.

Johnson, M. S., Matthews, E., Du, J., Genovese, V., and Bastviken, D.: Methane Emission From Global Lakes: New Spatiotemporal Data and Observation-Driven Modeling of Methane Dynamics Indicates Lower Emissions, J Geophys Res Biogeosciences, 127, e2022JG006793, https://doi.org/10.1029/2022jg006793, 2022.

Kadygrov, N., Broquet, G., Chevallier, F., Rivier, L., Gerbig, C., and Ciais, P.: On the potential of the ICOS atmospheric CO2 measurement network for estimating the biogenic CO2 budget of Europe, Atmos. Chem. Phys., 15, 12765-12787, doi:10.5194/acp-15-12765-2015, 2015.

Kaiser, J. W., Heil, A., Andreae, M. O., Benedetti, A., Chubarova, N., Jones, L., Morcrette, J.-J., Razinger, M., Schultz, M. G., Suttie, M., and Werf, G. R. van der: Biomass burning emissions estimated with a global fire assimilation system based on observed fire radiative power, Biogeosciences, 9, 527–554, https://doi.org/10.5194/bg-9-527-2012, 2012.

Kalman, R. E.: A New Approach to Linear Filtering and Prediction Problems, Journal of Basic Engineering, 82, 35–45, https://doi.org/10.1115/1.3662552, 1960.

Kaminski, T., Rayner, P. J., Heimann, M., and Enting, I. G.: On aggregation errors in atmospheric transport inversions, J. Geophys. Res., 106, 4703–4715, https://doi.org/10.1029/2000jd900581, 2001.

Kaminski, T., Knorr, W., Schürmann, G., Scholze, M., Rayner, P. J., Zaehle, S., Blessing, S., Dorigo, W., Gayler, V., Giering, R., Gobron, N., Grant, J. P., Heimann, M., Hooker-Stroud, A., Houweling, S., Kato, T., Kattge, J., Kelley, D., Kemp, S., Koffi, E. N., Köstler, C., Mathieu, P. -P., Pinty, B., Reick, C. H., Rödenbeck, C., Schnur, R., Scipal, K., Sebald, C., Stacke, T., Scheltinga, A. T. van, Vossbeck, M., Widmann, H., and Ziehn, T.: The BETHY/JSBACH Carbon Cycle Data Assimilation System: experiences and challenges, J. Geophys. Res.: Biogeosciences, 118, 1414–1426, https://doi.org/10.1002/jgrg.20118, 2013.

Kangasaho, V., Tsuruta, A., Backman, L., Mäkinen, P., Houweling, S., Segers, A., Krol, M., Dlugokencky, E. J., Michel, S., White, J. W. C., and Aalto, T.: The Role of Emission Sources and Atmospheric Sink in the Seasonal Cycle of CH4 and δ13-CH4: Analysis Based on the Atmospheric Chemistry Transport Model TM5, Atmosphere, 13, 888, https://doi.org/10.3390/atmos13060888, 2022.

Karstens, U., Schwingshackl, C., Schmithüsen, D., and Levin, I.: A process-based 222radon flux map for Europe and its comparison to long-term observations, Atmos. Chem. Phys., 15, 12845–12865, https://doi.org/10.5194/acp-15-12845-2015, 2015.

Katharopoulos, I., Rust, D., Vollmer, M. K., Brunner, D., Reimann, S., O'Doherty, S. J., Young, D., Stanley, K. M., Schuck, T., Arduini, J., Emmenegger, L., and Henne, S.: Impact of transport model resolution and a priori assumptions on inverse modeling of Swiss F-gas emissions, Atmos. Chem. Phys., 23, 14159–14186, https://doi.org/10.5194/acp-23-14159-2023, 2023.

Ke, P., Ciais, P., Sitch, S., Li, W., Bastos, A., Liu, Z., Xu, Y., Gui, X., Bian, J., Goll, D. S., Xi, Y., Li, W., O'Sullivan, M., Souza, J. G. D., Friedlingstein, P., and Chevallier, F.: Low latency carbon budget

This project has received funding from the European Union's Horizon Europe research and innovation programme under grant agreement No 101081395

analysis reveals a large decline of the land carbon sink in 2023, Natl. Sci. Rev., 11, nwae367, https://doi.org/10.1093/nsr/nwae367, 2024.

Keeling, C. D., Piper, S. C., and Heimann, M.: A three-dimensional model of atmospheric CO2 transport based on observed winds, 4 mean annual gradients and interannual variations, vol. 55, edited by: Peterson, D. H., AGU, 305–363, 1989.

Kiel, M., O'Dell, C. W., Fisher, B., Eldering, A., Nassar, R., MacDonald, C. G., and Wennberg, P. O.: How bias correction goes wrong: measurement of XCO2 affected by erroneous surface pressure estimates, Atmos. Meas. Tech., 12, 2241–2259, https://doi.org/10.5194/amt-12-2241-2019, 2019.

Kim, J., Kim, H. M., and Cho, C.-H.: Influence of CO_2 observations on the optimized CO_2 flux in an ensemble Kalman filter, Atmos. Chem. Phys., 14, 13515–13530, https://doi.org/10.5194/acp-14-13515-2014, 2014.

King, S. L., Quay, P. D., and Lansdown, J. M.: The 13C/12C kinetic isotope effect for soil oxidation of methane at ambient atmospheric concentrations, J. Geophys. Res.: Atmos., 94, 18273–18277, https://doi.org/10.1029/jd094id15p18273, 1989.

Kirschke, S., Bousquet, P., Ciais, P., Saunois, M., Canadell, J. G., Dlugokencky, E. J., Bergamaschi, P., Bergmann, D., Blake, D. R., Bruhwiler, L., Cameron-Smith, P., Castaldi, S., Chevallier, F., Feng, L., Fraser, A., Heimann, M., Hodson, E. L., Houweling, S., Josse, B., Fraser, P. J., Krummel, P. B., Lamarque, J.-F., Langenfelds, R. L., Quere, C. L., Naik, V., O'Doherty, S., Palmer, P. I., Pison, I., Plummer, D., Poulter, B., Prinn, R. G., Rigby, M., Ringeval, B., Santini, M., Schmidt, M., Shindell, D. T., Simpson, I. J., Spahni, R., Steele, L. P., Strode, S. A., Sudo, K., Szopa, S., Werf, G. R. V. der, Voulgarakis, A., Weele, M. van, Weiss, R. F., Williams, J. E., and Zeng, G.: Three decades of global methane sources and sinks, Nature Geosci, 6, 813–823, https://doi.org/10.1038/ngeo1955, 2013.

Kleinen, T., Mikolajewicz, U., and Brovkin, V.: Terrestrial methane emissions from the Last Glacial Maximum to the preindustrial period, Clim Past, 16, 575–595, https://doi.org/10.5194/cp-16-575-2020, 2020.

Ko, M. K. W., Newman, P. A., Reimann, S., and Strahan, S. E.: Lifetimes of Stratospheric Ozone-Depleting Substances, Their Replacements and Related Species, 2013.

Koffi, E. N., Bergamaschi, P., Karstens, U., Krol, M., Segers, A., Schmidt, M., Levin, I., Vermeulen, A. T., Fisher, R. E., and Kazan, V.: Evaluation of the boundary layer dynamics of the TM5 model over Europe, Geoscientific Model Development, 9, 3137, https://doi.org/10.5194/gmd-9-3137-2016, 2016.

Kountouris, P., Gerbig, C., Totsche, K. U., Dolman, A. J., Meesters, A. G. C. A., Broquet, G., Maignan, F., Gioli, B., Montagnani, L., and Helfter, C.: An objective prior error quantification for regional atmospheric inverse applications, Biogeosciences, 12, 7403–7421, https://doi.org/10.5194/bg-12-7403-2015, 2015.

Krinner, G., Viovy, N., Noblet-Ducoudré, N. de, Ogée, J., Polcher, J., Friedlingstein, P., Ciais, P., Sitch, S., and Prentice, I. C.: A dynamic global vegetation model for studies of the coupled atmosphere-biosphere system, Global Biogeochemical Cycles, 19, https://doi.org/10.1029/2003gb002199, 2005.

Krol, M., Bruine, M. de, Killaars, L., Ouwersloot, H., Pozzer, A., Yin, Y., Chevallier, F., Bousquet, P., Patra, P., Belikov, D., Maksyutov, S., Dhomse, S., Feng, W., and Chipperfield, M. P.: Age of air as a diagnostic for transport timescales in global models, Geosci. Model Dev., 11, 3109–3130, https://doi.org/10.5194/gmd-11-3109-2018, 2018.

Krol, M. C., Meirink, J. F., Bergamaschi, P., Mak, J. E., Lowe, D., Jöckel, P., Houweling, S., and Röckmann, T.: What can ^{14}CO measurements tell us about OH?, Atmos. Chem. Phys., 8, 5033–5044, https://doi.org/10.5194/acp-8-5033-2008, 2008.

This project has received funding from the European Union's Horizon Europe research and innovation programme under grant agreement No 101081395

Kuenen, J., Dellaert, S., Visschedijk, A., Jalkanen, J.-P., Super, I., and Gon, H. D. van der: CAMS-REG-v4: a state-of-the-art high-resolution European emission inventory for air quality modelling, Earth Syst. Sci. Data, 14, 491–515, https://doi.org/10.5194/essd-14-491-2022, 2022.

Kuhlmann, G., Brunner, D., Broquet, G., and Meijer, Y.: Quantifying CO2 emissions of a city with the Copernicus Anthropogenic CO2 Monitoring satellite mission, Atmos. Meas. Tech., 13, 6733–6754, https://doi.org/10.5194/amt-13-6733-2020, 2020.

Laan-Luijkx, I. T. van der, Velde, I. R. van der, Veen, E. van der, Tsuruta, A., Stanislawska, K., Babenhauserheide, A., Zhang, H. F., Liu, Y., He, W., Chen, H., Masarie, K. A., Krol, M. C., and Peters, W.: The CarbonTracker Data Assimilation Shell (CTDAS) v1.0: implementation and global carbon balance 2001--2015, Geoscientific Model Development, 10, 2785–2800, https://doi.org/10.5194/gmd-10-2785-2017, 2017.

Lamb, W., Andrew, R., Jones, M., Nicholls, Z., Peters, G., Smith, C., Saunois, M., Grassi, G., Pongratz, J., Smith, S., Tubiello, F., Crippa, M., Gidden, M., Friedlingstein, P., Minx, J., and Forster, P.: Differences in anthropogenic greenhouse gas emissions estimates explained, Earth Syst. Sci. Data Discuss., 2025, 1–28, https://doi.org/10.5194/essd-2025-188, 2025.

Lan, X., Basu, S., Schwietzke, S., Bruhwiler, L. M. P., Dlugokencky, E. J., Michel, S. E., Sherwood, O. A., Tans, P. P., Thoning, K., Etiope, G., Zhuang, Q., Liu, L., Oh, Y., Miller, J. B., Pétron, G., Vaughn, B. H., and Crippa, M.: Improved Constraints on Global Methane Emissions and Sinks Using δ13C-CH4, Global Biogeochem Cy, 35, https://doi.org/10.1029/2021gb007000, 2021.

Lauerwald, R., Regnier, P., Figueiredo, V., Prast, A. E., Bastviken, D., Lehner, B., Maavara, T., and Raymond, P.: Natural Lakes Are a Minor Global Source of N2O to the Atmosphere, Glob. Biogeochem. Cycles, 33, 1564–1581, https://doi.org/10.1029/2019gb006261, 2019.

Lauvaux, T., Schuh, A. E., Uliasz, M., Richardson, S., Miles, N., Andrews, A. E., Sweeney, C., Diaz, L. I., Martins, D., Shepson, P. B., and Davis, K. J.: Constraining the CO2 budget of the corn belt: exploring uncertainties from the assumptions in a mesoscale inverse system, Atmos. Chem. Phys., 12, 337–354, https://doi.org/10.5194/acp-12-337-2012, 2012.

Lauvaux, T., et al., High-resolution atmospheric inversion of urban CO2 emissions during the dormant season of the Indianapolis Flux Experiment (INFLUX), J. Geophys. Res. Atmos., 121, 5213–5236, doi:10.1002/2015JD024473, 2016.

Lawrence, D. M., Fisher, R. A., Koven, C. D., Oleson, K. W., Swenson, S. C., Bonan, G., Collier, N., Ghimire, B., Kampenhout, L., Kennedy, D., Kluzek, E., Lawrence, P. J., Li, F., Li, H., Lombardozzi, D., Riley, W. J., Sacks, W. J., Shi, M., Vertenstein, M., Wieder, W. R., Xu, C., Ali, A. A., Badger, A. M., Bisht, G., Broeke, M., Brunke, M. A., Burns, S. P., Buzan, J., Clark, M., Craig, A., Dahlin, K., Drewniak, B., Fisher, J. B., Flanner, M., Fox, A. M., Gentine, P., Hoffman, F., Keppel-Aleks, G., Knox, R., Kumar, S., Lenaerts, J., Leung, L. R., Lipscomb, W. H., Lu, Y., Pandey, A., Pelletier, J. D., Perket, J., Randerson, J. T., Ricciuto, D. M., Sanderson, B. M., Slater, A., Subin, Z. M., Tang, J., Thomas, R. Q., Martin, M. V., and Zeng, X.: The Community Land Model Version 5: Description of New Features, Benchmarking, and Impact of Forcing Uncertainty, Journal of Advances in Modeling Earth Systems, 11, 4245–4287, https://doi.org/10.1029/2018ms001583, 2019.

Lehner, B., Anand, M., Fluet-Chouinard, E., Tan, F., Aires, F., Allen, G. H., Bousquet, P., Canadell, J. G., Davidson, N., Ding, M., Finlayson, C. M., Gumbricht, T., Hilarides, L., Hugelius, G., Jackson, R. B., Korver, M. C., Liu, L., McIntyre, P. B., Nagy, S., Olefeldt, D., Pavelsky, T. M., Pekel, J.-F., Poulter, B., Prigent, C., Wang, J., Worthington, T. A., Yamazaki, D., Zhang, X., and Thieme, M.: Mapping the world's inland surface waters: an upgrade to the Global Lakes and Wetlands Database (GLWD v2), Earth Syst. Sci. Data, 17, 2277–2329, https://doi.org/10.5194/essd-17-2277-2025, 2025.

Lelieveld, J., Gromov, S., Pozzer, A., and Taraborrelli, D.: Global tropospheric hydroxyl distribution, budget and reactivity, Atmospheric Chemistry and Physics, 16, 12477–12493, https://doi.org/10.5194/acp-16-12477-2016, 2016.

This project has received funding from the European Union's Horizon Europe research and innovation programme under grant agreement No 101081395

Levin, I., Veidt, C., Vaughn, B. H., Brailsford, G., Bromley, T., Heinz, R., Lowe, D., Miller, J. B., Poß, C., and White, J. W. C.: No inter-hemispheric δ13CH4 trend observed., Nature, 486, E3-4-discussion E4, https://doi.org/10.1038/nature11175, 2012.

Li, X., Rinne, J., Tuittila, E., and Vesala, T.: Year-Round δ13C-CH4 Reveals Seasonal Transition in Methane-Related Processes in a Boreal Mire, J. Geophys. Res.: Biogeosciences, 130, https://doi.org/10.1029/2025jg008922, 2025.

Lian, J., Bréon, F.-M., Broquet, G., Lauvaux, T., Zheng, B., Ramonet, M., Xueref-Remy, I., Kotthaus, S., Haeffelin, M., and Ciais, P.: Sensitivity to the sources of uncertainties in the modeling of atmospheric CO2 concentration within and in the vicinity of Paris, Atmos Chem Phys, 21, 10707–10726, https://doi.org/10.5194/acp-21-10707-2021, 2021.

Liang, Q., Chipperfield, M. P., Fleming, E. L., Abraham, N. L., Braesicke, P., Burkholder, J. B., Daniel, J. S., Dhomse, S., Fraser, P. J., Hardiman, S. C., Jackman, C. H., Kinnison, D. E., Krummel, P. B., Montzka, S. A., Morgenstern, O., McCulloch, A., Mühle, J., Newman, P. A., Orkin, V. L., Pitari, G., Prinn, R. G., Rigby, M., Rozanov, E., Stenke, A., Tummon, F., Velders, G. J. M., Visioni, D., and Weiss, R. F.: Deriving Global OH Abundance and Atmospheric Lifetimes for Long-Lived Gases: A Search for CH3CCl3 Alternatives, Journal of Geophysical Research: Atmospheres, 122, 11-914-11–933, https://doi.org/10.1002/2017jd026926, 2017.

Lindqvist, H., Kivimäki, E., Häkkilä, T., Tsuruta, A., Schneising, O., Buchwitz, M., Lorente, A., Velarte, M. M., Borsdorff, T., Alberti, C., Backman, L., Buschmann, M., Chen, H., Dubravica, D., Hase, F., Heikkinen, P., Karppinen, T., Kivi, R., McGee, E., Notholt, J., Rautiainen, K., Roche, S., Simpson, W., Strong, K., Tu, Q., Wunch, D., Aalto, T., and Tamminen, J.: Evaluation of Sentinel-5P TROPOMI Methane Observations at Northern High Latitudes, Remote Sens., 16, 2979, https://doi.org/10.3390/rs16162979, 2024.

Liu, M., Raymond, P. A., Lauerwald, R., Zhang, Q., Trapp-Müller, G., Davis, K. L., Moosdorf, N., Xiao, C., Middelburg, J. J., Bouwman, A. F., Beusen, A. H. W., Peng, C., Lacroix, F., Tian, H., Wang, J., Li, M., Zhu, Q., Cohen, S., Hoek, W. J. van, Li, Y., Li, Y., Yao, Y., and Regnier, P.: Global riverine land-to-ocean carbon export constrained by observations and multi-model assessment, Nat. Geosci., 17, 896–904, https://doi.org/10.1038/s41561-024-01524-z, 2024.

Liu, Z., Ciais, P., Deng, Z., Lei, R., Davis, S. J., Feng, S., Zheng, B., Cui, D., Dou, X., Zhu, B., Guo, R., Ke, P., Sun, T., Lu, C., He, P., Wang, Y., Yue, X., Wang, Y., Lei, Y., Zhou, H., Cai, Z., Wu, Y., Guo, R., Han, T., Xue, J., Boucher, O., Boucher, E., Chevallier, F., Tanaka, K., Wei, Y., Zhong, H., Kang, C., Zhang, N., Chen, B., Xi, F., Liu, M., Bréon, F.-M., Lu, Y., Zhang, Q., Guan, D., Gong, P., Kammen, D. M., He, K., and Schellnhuber, H. J.: Near-real-time monitoring of global CO2 emissions reveals the effects of the COVID-19 pandemic, Nature communications, 1–12, https://doi.org/10.1038/s41467-020-18922-7, 2020.

Lu, X., Jacob, D. J., Wang, H., Maasakkers, J. D., Zhang, Y., Scarpelli, T. R., Shen, L., Qu, Z., Sulprizio, M. P., Nesser, H., Bloom, A. A., Ma, S., Worden, J. R., Fan, S., Parker, R. J., Boesch, H., Gautam, R., Gordon, D., Moran, M. D., Reuland, F., Villasana, C. A. O., and Andrews, A.: Methane emissions in the United States, Canada, and Mexico: evaluation of national methane emission inventories and 2010–2017 sectoral trends by inverse analysis of in situ (GLOBALVIEWplus CH4 ObsPack) and satellite (GOSAT) atmospheric observations, Atmos. Chem. Phys., 22, 395–418, https://doi.org/10.5194/acp-22-395-2022, 2021.

Lucas, D. D., Simpson, M., Cameron-Smith, P., and Baskett, R. L.: Bayesian inverse modeling of the atmospheric transport and emissions of a controlled tracer release from a nuclear power plant, Atmospheric Chemistry and Physics, 17, 13521–13543, https://doi.org/10.5194/acp-17-13521-2017, 2017.

Lueker, T. J., Walker, S. J., Vollmer, M. K., Keeling, R. F., Nevison, C. D., and Weiss, R. F.: Coastal upwelling air-sea fluxes revealed in atmospheric observations of O2/N2, CO2 and N2O, Geophysical Research Letters, 30, 1292–1295, 2003.

This project has received funding from the European Union's Horizon Europe research and innovation programme under grant agreement No 101081395

Lunt, M. F., Rigby, M., Ganesan, A. L., and Manning, A. J.: Estimation of trace gas fluxes with objectively determined basis functions using reversible-jump Markov chain Monte Carlo, Geosci. Model Dev., 9, 3213–3229, https://doi.org/10.5194/gmd-9-3213-2016, 2016.

Maasakkers, J. D., Jacob, D. J., Sulprizio, M. P., Scarpelli, T. R., Nesser, H., Sheng, J. X., Zhang, Y., Hersher, M., Bloom, A. A., Bowman, K. W., Worden, J. R., Janssens-Maenhout, G., and Parker, R. J.: Global distribution of methane emissions, emission trends, and OH concentrations and trends inferred from an inversion of GOSAT satellite data for 2010--2015, Atmospheric Chemistry and Physics, 19, 7859–7881, https://doi.org/10.5194/acp-19-7859-2019, 2019.

Maavara, T., Lauerwald, R., Laruelle, G. G., Akbarzadeh, Z., Bouskill, N. J., Cappellen, P. V., and Regnier, P.: Nitrous oxide emissions from inland waters: Are IPCC estimates too high?, Glob. Chang. Biol., 25, 473–488, https://doi.org/10.1111/gcb.14504, 2019.

MacBean, N., Bacour, C., Raoult, N., Bastrikov, V., Koffi, E. N., Kuppel, S., Maignan, F., Ottlé, C., Peaucelle, M., Santaren, D., and Peylin, P.: Quantifying and Reducing Uncertainty in Global Carbon Cycle Predictions: Lessons and Perspectives From 15 Years of Data Assimilation Studies With the ORCHIDEE Terrestrial Biosphere Model, Glob. Biogeochem. Cycles, 36, https://doi.org/10.1029/2021gb007177, 2022.

Marik, T., Fischer, H., Conen, F., and Smith, K.: Seasonal variations in stable carbon and hydrogen isotope ratios in methane from rice fields, Glob. Biogeochem. Cycles, 16, 41-1-41–11, https://doi.org/10.1029/2001gb001428, 2002.

Marshall, J., Reum, F., Broquet, G., Potier, E., Berchet, A., Fortems-Cheiney, A., Koene, E., Brunner, D., Houweling, S., Ioannidis, E., Segers, A., Kaiser-Weiss, A., Galkowski, M., Sekula, P., Monteil, G., Chen, H., Palmer, P., Scarpeille, T., Mengistu, A., and Aalto, T.: CoCO2 Prototype System for a Copernicus CO2 Service: Intercomparison of national scale inversions, D4.6, 2023.

Mason Earles, J., Yeh, S. and Skog, K.: Timing of carbon emissions from global forest clearance. Nature Clim Change 2, 682–685, https://doi.org/10.1038/nclimate1535, 2012.

McGrath, M. J., Petrescu, A. M. R., Peylin, P., Andrew, R. M., Matthews, B., Dentener, F., Balkovič, J., Bastrikov, V., Becker, M., Broquet, G., Ciais, P., Fortems-Cheiney, A., Ganzenmüller, R., Grassi, G., Harris, I., Jones, M., Knauer, J., Kuhnert, M., Monteil, G., Munassar, S., Palmer, P. I., Peters, G. P., Qiu, C., Schelhaas, M.-J., Tarasova, O., Vizzarri, M., Winkler, K., Balsamo, G., Berchet, A., Briggs, P., Brockmann, P., Chevallier, F., Conchedda, G., Crippa, M., Dellaert, S. N. C., Gon, H. A. C. D. van der, Filipek, S., Friedlingstein, P., Fuchs, R., Gauss, M., Gerbig, C., Guizzardi, D., Günther, D., Houghton, R. A., Janssens-Maenhout, G., Lauerwald, R., Lerink, B., Luijkx, I. T., Moulas, G., Muntean, M., Nabuurs, G.-J., Paquirissamy, A., Perugini, L., Peters, W., Pilli, R., Pongratz, J., Regnier, P., Scholze, M., Serengil, Y., Smith, P., Solazzo, E., Thompson, R. L., Tubiello, F. N., Vesala, T., and Walther, S.: The consolidated European synthesis of CO2 emissions and removals for the European Union and United Kingdom: 1990–2020, Earth Syst. Sci. Data, 15, 4295–4370, https://doi.org/10.5194/essd-15-4295-2023, 2023.

McNorton, J., Wilson, C., Gloor, M., Parker, R., Boesch, H., Feng, W., Hossaini, R., and Chipperfield, M.: Attribution of recent increases in atmospheric methane through 3-D inverse modelling, Atmospheric Chemistry and Physics, 2018, 1–34, https://doi.org/10.5194/acp-2018-474, 2018.

Meirink, J. F., Bergamaschi, P., and Krol, M. C.: Four-dimensional variational data assimilation for inverse modelling of atmospheric methane emissions: method and comparison with synthesis inversion, Atmospheric Chemistry and Physics, 8, 6341–6353, https://doi.org/10.5194/acp-8-6341-2008, 2008.

Mengistu, A. G., Tsuruta, A., Berchet, A., Thompson, R., Tenkanen, M., Lindqvist, H., Markkanen, T., Leppänen, A., Laitinen, A., Martinez, A., Fortems-Cheiney, A., Höglund-Isaksson, L., and Aalto, T.: High-resolution inversion of methane emissions over Europe using the Community Inversion Framework and FLEXPART, EGUsphere, 2026, 1–41, https://doi.org/10.5194/egusphere-2025-5877, 2026.

This project has received funding from the European Union's Horizon Europe research and innovation programme under grant agreement No 101081395

Menoud, M., Veen, C. van der, Lowry, D., Fernandez, J. M., Bakkaloglu, S., France, J. L., Fisher, R. E., Maazallahi, H., Stanisavljević, M., Nęcki, J., Vinkovic, K., Łakomiec, P., Rinne, J., Korbeń, P., Schmidt, M., Defratyka, S., Yver-Kwok, C., Andersen, T., Chen, H., and Röckmann, T.: New contributions of measurements in Europe to the global inventory of the stable isotopic composition of methane, Earth Syst. Sci. Data, 14, 4365–4386, https://doi.org/10.5194/essd-14-4365-2022, 2022.

Michalak, A. M., Hirsch, A., Bruhwiler, L., Gurney, K. R., Peters, W., and Tans, P. P.: Maximum likelihood estimation of covariance parameters for Bayesian atmospheric trace gas surface flux inversions, Journal of Geophysical Research-Atmospheres, 110, https://doi.org/10.1029/2005jd005970, 2005.

Michalak, A. M., Randazzo, N. A., and Chevallier, F.: Diagnostic methods for atmospheric inversions of long-lived greenhouse gases, 17, 7405–7421, https://doi.org/10.5194/acp-17-7405-2017, 2017.

Minschwaner, K., Salawitch, R. J., and McElroy, M. B.: Absorption of Solar Radiation by O2: Implications for O3 and Lifetimes of N2O, CFCl3, and CF2Cl2, J. Geophys. Res., 98, 10-543-10–561, https://doi.org/10.1029/93jd00223, 1993.

Monteil, G., Broquet, G., Scholze, M., Lang, M., Karstens, U., Gerbig, C., Koch, F. T., Smith, N. E., Thompson, R. L., Luijkx, I. T., White, E., Meesters, A., Ciais, P., Ganesan, A. L., Manning, A., Mischurow, M., Peters, W., Peylin, P., Tarniewicz, J., Rigby, M., Rödenbeck, C., Vermeulen, A., and Walton, E. M.: The regional European atmospheric transport inversion comparison, EUROCOM: first results on European-wide terrestrial carbon fluxes for the period 2006--2015, Atmospheric Chemistry and Physics, 20, 12063–12091, https://doi.org/10.5194/acp-20-12063-2020, 2020.

Monteil, G., Kallingal, J. T., and Scholze, M.: CH4 emissions from Northern Europe wetlands: compared data assimilation approaches, Atmos. Chem. Phys., 25, 14251–14277, https://doi.org/10.5194/acp-25-14251-2025, 2025.

Montzka, S. A., Krol, M., Dlugokencky, E., Hall, B., Jöckel, P., and Lelieveld, J.: Small interannual variability of global atmospheric hydroxyl., Science, 331, 67–69, https://doi.org/10.1126/science.1197640, 2011.

Munassar, S., Monteil, G., Scholze, M., Karstens, U., Rödenbeck, C., Koch, F.-T., Totsche, K. U., and Gerbig, C.: Why do inverse models disagree? A case study with two European CO2 inversions, Atmos Chem Phys, 23, 2813–2828, https://doi.org/10.5194/acp-23-2813-2023, 2023.

Munassar, S., Rödenbeck, C., Gałkowski, M., Koch, F.-T., Totsche, K. U., Botía, S., and Gerbig, C.: To what extent does the CO2 diurnal cycle impact flux estimates derived from global and regional inversions?, Atmos. Chem. Phys., 25, 639–656, https://doi.org/10.5194/acp-25-639-2025, 2024.

Murguia-Flores, F., Arndt, S., Ganesan, A. L., Murray-Tortarolo, G., and Hornibrook, E. R. C.: Soil Methanotrophy Model (MeMo v1.0): a process-based model to quantify global uptake of atmospheric methane by soil, Geosci. Model Dev., 11, 2009–2032, https://doi.org/10.5194/gmd-11-2009-2018, 2018.

Naus, S., Montzka, S. A., Patra, P. K., and Krol, M. C.: A 3D-model inversion of methyl chloroform to constrain the atmospheric oxidative capacity, Atmospheric Chemistry and Physics, 2020, 21, https://doi.org/10.5194/acp-21-4809-2021, 2021.

Nesser, H., Bowman, K. W., Thill, M. D., Varon, D. J., Randles, C. A., Tewari, A., Cardoso-Saldaña, F. J., Reidy, E., Maasakkers, J. D., and Jacob, D. J.: Predicting and correcting the influence of boundary conditions in regional inverse analyses, Geosci. Model Dev., 18, 9279–9291, https://doi.org/10.5194/gmd-18-9279-2025, 2025.

Nevison, C. D., Lueker, T. J., and Weiss, R. F.: Quantifying the nitrous oxide source from coastal upwelling, Global Biogeochem. Cycles, 18, https://doi.org/10.1029/2003gb002110, 2004.

Nevison, C. D., Liang, Q., Newman, P. A., Stephens, B. B., Dutton, G., Lan, X., Commane, R., Gonzalez, Y., and Kort, E.: Observational and model evidence for a prominent stratospheric influence

This project has received funding from the European Union's Horizon Europe research and innovation programme under grant agreement No 101081395

on variability in tropospheric nitrous oxide, Atmos. Chem. Phys., 24, 10513–10529, https://doi.org/10.5194/acp-24-10513-2024, 2024.

Nicely, J. M., Salawitch, R. J., Canty, T., Anderson, D. C., Arnold, S. R., Chipperfield, M. P., Emmons, L. K., Flemming, J., Huijnen, V., Kinnison, D. E., Lamarque, J., Mao, J., Monks, S. A., Steenrod, S. D., Tilmes, S., and Turquety, S.: Quantifying the causes of differences in tropospheric OH within global models, J Geophys Res Atmospheres, 122, 1983–2007, https://doi.org/10.1002/2016jd026239, 2017.

Niwa, Y., Tohjima, Y., Terao, Y., Saeki, T., Ito, A., Umezawa, T., Yamada, K., Sasakawa, M., Machida, T., Nakaoka, S.-I., Nara, H., Tanimoto, H., Mukai, H., Yoshida, Y., Morimoto, S., Takatsuji, S., Tsuboi, K., Sawa, Y., Matsueda, H., Ishijima, K., Fujita, R., Goto, D., Lan, X., Schuldt, K., Heliasz, M., Biermann, T., Chmura, L., Necki, J., Xueref-Remy, I., and Sferlazzo, D.: Multi-observational estimation of regional and sectoral emission contributions to the persistent high growth rate of atmospheric CH4 for 2020–2022, Atmos. Chem. Phys., 25, 6757–6785, https://doi.org/10.5194/acp-25-6757-2025, 2025.

Nocedal, J. and Wright, S. J.: Numerical Optimization, Springer, 2006.

Oda, T., Maksyutov, S., and Andres, R. J.: The Open-source Data Inventory for Anthropogenic CO_2, version 2016 (ODIAC2016): a global monthly fossil fuel CO_2 gridded emissions data product for tracer transport simulations and surface flux inversions, Earth System Science Data, 10, 87–107, https://doi.org/10.5194/essd-10-87-2018, 2018.

Ogle, S. M., Domke, G., Kurz, W. A., Rocha, M. T., Huffman, T., Swan, A., Smith, J. E., Woodall, C., and Krug, T.: Delineating managed land for reporting national greenhouse gas emissions and removals to the United Nations framework convention on climate change, Carbon Balance Manag., 13, 9, https://doi.org/10.1186/s13021-018-0095-3, 2018.

Oh, Y., Zhuang, Q., Welp, L. R., Liu, L., Lan, X., Basu, S., Dlugokencky, E. J., Bruhwiler, L., Miller, J. B., Michel, S. E., Schwietzke, S., Tans, P., Ciais, P., and Chanton, J. P.: Improved global wetland carbon isotopic signatures support post-2006 microbial methane emission increase, Commun. Earth Environ., 3, 159, https://doi.org/10.1038/s43247-022-00488-5, 2022.

CarbonTracker CH4 2025: https://doi.org/10.25925/HXKS-V755.

Olefeldt, D., Hovemyr, M., Kuhn, M. A., Bastviken, D., Bohn, T. J., Connolly, J., Crill, P., Euskirchen, E. S., Finkelstein, S. A., Genet, H., Grosse, G., Harris, L. I., Heffernan, L., Helbig, M., Hugelius, G., Hutchins, R., Juutinen, S., Lara, M. J., Malhotra, A., Manies, K., McGuire, A. D., Natali, S. M., O'Donnell, J. A., Parmentier, F.-J. W., Räsänen, A., Schädel, C., Sonnentag, O., Strack, M., Tank, S. E., Treat, C., Varner, R. K., Virtanen, T., Warren, R. K., and Watts, J. D.: The Boreal–Arctic Wetland and Lake Dataset (BAWLD), Earth Syst Sci Data, 13, 5127–5149, https://doi.org/10.5194/essd-13-5127-2021, 2021.

Palmer, P. I., Feng, L., Lunt, M. F., Parker, R. J., Bsch, H., Lan, X., Lorente, A., and Borsdorff, T.: The added value of satellite observations of methane forunderstanding the contemporary methane budget, Philos. Trans. R. Soc. A, 379, 20210106, https://doi.org/10.1098/rsta.2021.0106, 2021.

Pandey, S., Houweling, S., Krol, M., Aben, I., and Rockmann, T.: On the use of satellite-derived CH_4 : CO_2 columns in a joint inversion of CH_4 and CO_2 fluxes, Atmospheric Chemistry and Physics, 15, 8615–8629, https://doi.org/10.5194/acp-15-8615-2015, 2015.

Pandey, S., Houweling, S., and Segers, A.: Order of magnitude wall time improvement of variational methane inversions by physical parallelization: a demonstration using TM5-4DVAR, Geosci. Model Dev., 15, 4555–4567, https://doi.org/10.5194/gmd-15-4555-2022, 2022.

Patra, P. K., Saeki, T., Dlugokencky, E. J., Ishijima, K., Umezawa, T., Ito, A., Aoki, S., Morimoto, S., Kort, E. A., Crotwell, A., KUMAR, K. R., and Nakazawa, T.: Regional Methane Emission Estimation Based on Observed Atmospheric Concentrations (2002-2012), Journal of the Meteorological Society of Japan, 94, 91–113, https://doi.org/10.2151/jmsj.2016-006, 2016.

Patra, P. K., Hajima, T., Saito, R., Chandra, N., Yoshida, Y., Ichii, K., Kawamiya, M., Kondo, M., Ito, A., and Crisp, D.: Evaluation of earth system model and atmospheric inversion using total column CO2

This project has received funding from the European Union's Horizon Europe research and innovation programme under grant agreement No 101081395

observations from GOSAT and OCO-2, Prog. Earth Planet. Sci., 8, 25, https://doi.org/10.1186/s40645-021-00420-z, 2021a.

Patra, P. K., Krol, M. C., Prinn, R. G., Takigawa, M., Mühle, J., Montzka, S. A., Lal, S., Yamashita, Y., Naus, S., Chandra, N., Weiss, R. F., Krummel, P. B., Fraser, P. J., O'Doherty, S., and Elkins, J. W.: Methyl Chloroform Continues to Constrain the Hydroxyl (OH) Variability in the Troposphere, J Geophys Res Atmospheres, 126, https://doi.org/10.1029/2020jd033862, 2021b.

Paustian, K., Ravindranath, N. H., and Amstel, A. van: Agriculture, Forestry and Other Land Use. In: IPCC Guidelines for National Greenhouse Gas Inventories, 2006.

Peng, S., Lin, X., Thompson, R. L., Xi, Y., Liu, G., Hauglustaine, D., Lan, X., Poulter, B., Ramonet, M., Saunois, M., Yin, Y., Zhang, Z., Zheng, B., and Ciais, P.: Wetland emission and atmospheric sink changes explain methane growth in 2020, Nature, 612, 477–482, https://doi.org/10.1038/s41586-022-05447-w, 2022.

Peters, W., Miller, J. B., Whitaker, J., Denning, A. S., Hirsch, A., Krol, M. C., Zupanski, D., Bruhwiler, L., and Tans, P. P.: An ensemble data assimilation system to estimate CO 2surface fluxes from atmospheric trace gas observations, J. Geophys. Res., 110, 419–21, https://doi.org/10.1029/2005jd006157, 2005.

Peters, W., Jacobson, A. R., Sweeney, C., Andrews, A. E., Conway, T. J., Masarie, K., Miller, J. B., Bruhwiler, L. M. P., tron, G. P., Hirsch, A. I., Worthy, D. E. J., Werf, G. R. V. der, Randerson, J. T., Wennberg, P. O., Krol, M. C., and Tans, P. P.: An atmospheric perspective on North American carbon dioxide exchange: CarbonTracker, Proceedings of the National Academy of Sciences, 104, 18925–18930, https://doi.org/10.1073/pnas.0708986104, 2007.

Peters, W., Krol, M. C., Werf, G. R. V. der, Houweling, S., Jones, C. D., Hughes, J., Schaefer, K., Masarie, K. A., Jacobson, A. R., and Miller, J. B.: Seven years of recent European net terrestrial carbon dioxide exchange constrained by atmospheric observations, Global Change Biology, 16, 1317–1337, https://doi.org/10.1111/j.1365-2486.2009.02078.x, 2010.

Petrenko, V. V., Smith, A. M., Schaefer, H., Riedel, K., Brook, E., Baggenstos, D., Harth, C., Hua, Q., Buizert, C., Schilt, A., Fain, X., Mitchell, L., Bauska, T., Orsi, A., Weiss, R. F., and Severinghaus, J. P.: Minimal geological methane emissions during the Younger Dryas–Preboreal abrupt warming event, Nature, 548, 443–446, https://doi.org/10.1038/nature23316, 2017.

Petrescu, A. M. R., Qiu, C., Ciais, P., Thompson, R. L., Peylin, P., McGrath, M. J., Solazzo, E., Janssens-Maenhout, G., Tubiello, F. N., Bergamaschi, P., Brunner, D., Peters, G. P., Höglund-Isaksson, L., Regnier, P., Lauerwald, R., Bastviken, D., Tsuruta, A., Winiwarter, W., Patra, P. K., Kuhnert, M., Oreggioni, G. D., Crippa, M., Saunois, M., Perugini, L., Markkanen, T., Aalto, T., Zwaaftink, C. D. G., Tian, H., Yao, Y., Wilson, C., Conchedda, G., Günther, D., Leip, A., Smith, P., Haussaire, J.-M., Leppänen, A., Manning, A. J., McNorton, J., Brockmann, P., and Dolman, A. J.: The consolidated European synthesis of CH4 and N2O emissions for the European Union and United Kingdom: 1990–2017, Earth Syst Sci Data, 13, 2307–2362, https://doi.org/10.5194/essd-13-2307-2021, 2021.

Peylin, P., Law, R. M., Gurney, K. R., Chevallier, F., Jacobson, A. R., Maki, T., Niwa, Y., Patra, P. K., Peters, W., Rayner, P. J., Rodenbeck, C., Laan-Luijkx, I. T. van der, and Zhang, X.: Global atmospheric carbon budget: results from an ensemble of atmospheric CO2 inversions, Biogeosciences, 10, 6699–6720, https://doi.org/10.5194/bg-10-6699-2013, 2013.

Pillai, D., Gerbig, C., Ahmadov, R., Rodenbeck, C., Kretschmer, R., Koch, T., Thompson, R., Neininger, B., and Lavric, J. V.: High-resolution simulations of atmospheric CO2 over complex terrain - representing the Ochsenkopf mountain tall tower, Atmos. Chem. Phys., 11, 7445–7464, https://doi.org/10.5194/acp-11-7445-2011, 2011.

Pillai, D., Gerbig, C., Kretschmer, R., Beck, V., Karstens, U., Neininger, B., and Heimann, M.: Comparing Lagrangian and Eulerian models for CO 2 transport--a step towards Bayesian inverse

This project has received funding from the European Union's Horizon Europe research and innovation programme under grant agreement No 101081395

modeling using WRF/STILT-VPRM, Atmospheric Chemistry and Physics, 12, 8979–8991, https://doi.org/10.5194/acp-12-8979-2012, 2012.

Pisso, I., Sollum, E., Grythe, H., Kristiansen, N., Cassiani, M., Eckhardt, S., Arnold, D., Morton, D., Thompson, R. L., Zwaaftink, C. D. G., Evangeliou, N., Sodemann, H., Haimberger, L., Henne, S., Brunner, D., Burkhart, J. F., Fouilloux, A., Brioude, J., Philipp, A., Seibert, P., and Stohl, A.: The Lagrangian particle dispersion model FLEXPART version 10.3, Geosci Model Dev, 2019, 1–67, https://doi.org/10.5194/gmd-2018-333, 2019.

Potapov, P., Hansen, M. C., Laestadius, L., Turubanova, S., Yaroshenko, A., Thies, C., Smith, W., Zhuravleva, I., Komarova, A., Minnemeyer, S., and Esipova, E.: The last frontiers of wilderness: Tracking loss of intact forest landscapes from 2000 to 2013, Sci. Adv., 3, e1600821, https://doi.org/10.1126/sciadv.1600821, 2017.

Potier, E., Broquet, G., Wang, Y., Santaren, D., Berchet, A., Pison, I., Marshall, J., Ciais, P., Bréon, F.-M., and Chevallier, F.: Complementing XCO2 imagery with ground-based CO2 and 14CO2 measurements to monitor CO2 emissions from fossil fuels on a regional to local scale, Atmos. Meas. Tech., 15, 5261–5288, https://doi.org/10.5194/amt-15-5261-2022, 2022.

Prather, M. J., Holmes, C. D., and Hsu, J.: Reactive greenhouse gas scenarios: Systematic exploration of uncertainties and the role of atmospheric chemistry, Geophys. Res. Lett., 39, L09803, https://doi.org/10.1029/2012gl051440, 2012.

Prather, M. J., Hsu, J., DeLuca, N. M., Jackman, C. H., Oman, L. D., Douglass, A. R., Fleming, E. L., Strahan, S. E., Steenrod, S. D., Søvde, O. A., Isaksen, I. S. A., Froidevaux, L., and Funke, B.: Measuring and modeling the lifetime of Nitrous Oxide including its variability, Journal of Geophysical Research: Atmospheres, 120, 5693–5705, https://doi.org/10.1002/2015jd023267, 2015.

Prinn, R. G., Cunnold, D., Rasmussen, R., Simmonds, P., Alyea, F., Crawford, A., Fraser, P., and Rosen, R.: Atmospheric emissions and trends of nitrous oxide deduced from 10 years of ALE-GAGE data, J. Geophys. Res., 95, 18-369-18–385, 1990.

Prinn, R. G., Huang, J., Weiss, R. F., Cunnold, D. M., Fraser, P. J., Simmonds, P. G., McCulloch, A., Harth, C., Reimann, S., and Salameh, P.: Evidence for variability of atmospheric hydroxyl radicals over the past quarter century, Geophysical Research Letters, 32, https://doi.org/10.1029/2004gl022228, 2005.

Purohit, P. and Höglund-Isaksson, L.: Global emissions of fluorinated greenhouse gases 2005–2050 with abatement potentials and costs, Atmos. Chem. Phys., 17, 2795–2816, https://doi.org/10.5194/acp-17-2795-2017, 2017.

Püschel, B., Vojta, M., Kandler, L., Crotwell, M., Engel, A., Krummel, P. B., Lunder, C. R., Mühle, J., O'Doherty, S., Prinn, R. G., Stanley, K. M., Vimont, I., Vollmer, M. K., Wagenhäuser, T., Weiss, R. F., Young, D., and Stohl, A.: Global distribution of tetrafluoromethane (CF4) and hexafluoroethane (C2F6) emissions determined by inverse modeling, https://doi.org/10.5194/egusphere-2025-5656, 2025.

Qu, Z., Jacob, D. J., Bloom, A. A., Worden, J. R., Parker, R. J., and Boesch, H.: Inverse modeling of 2010–2022 satellite observations shows that inundation of the wet tropics drove the 2020–2022 methane surge, Proc. Natl. Acad. Sci., 121, e2402730121, https://doi.org/10.1073/pnas.2402730121, 2024.

Quay, P., King, S., White, D., Brockington, M., Plotkin, B., Gammon, R., Gerst, S., and Stutsman, J.: Atmospheric 14CO: A tracer of OH concentration and mixing rates, J. Geophys. Res.: Atmos., 105, 15147–15166, https://doi.org/10.1029/2000jd900122, 2000.

Rabier, F. and Liu, Z.: Variational Data Assimilation: Theory and Overview, 2003.

Raivonen, M., Smolander, S., Backman, L., Susiluoto, J., Aalto, T., Markkanen, T., Mäkelä, J., Rinne, J., Peltola, O., Aurela, M., Lohila, A., Tomasic, M., Li, X., Larmola, T., Juutinen, S., Tuittila, E.-S., Heimann,

This project has received funding from the European Union's Horizon Europe research and innovation programme under grant agreement No 101081395

M., Sevanto, S., Kleinen, T., Brovkin, V., and Vesala, T.: HIMMELI v1.0: HelsinkI Model of MEthane buiLd-up and emIssion for peatlands, Geoscientific Model Development, 10, 4665–4691, https://doi.org/10.5194/gmd-10-4665-2017, 2017.

Ramsden, A. E., Ganesan, A. L., Western, L. M., Rigby, M., Manning, A. J., Foulds, A., France, J. L., Barker, P., Levy, P., Say, D., Wisher, A., Arnold, T., Rennick, C., Stanley, K. M., Young, D., and O'Doherty, S.: Quantifying fossil fuel methane emissions using observations of atmospheric ethane and an uncertain emission ratio, Atmos Chem Phys, 22, 3911–3929, https://doi.org/10.5194/acp-22-3911-2022, 2022.

Rastigejev, Y., Park, R., Brenner, M. P., and Jacob, D. J.: Resolving intercontinental pollution plumes in global models of atmospheric transport, J. Geophys. Res.: Atmos., 115, https://doi.org/10.1029/2009jd012568, 2010.

Ravishankara, A. R., Daniel, J. S., and Portmann, R. W.: Nitrous Oxide (N2O): The Dominant Ozone-Depleting Substance Emitted in the 21st Century, Science, 326, 123–125, https://doi.org/10.1126/science.1176985, 2009.

Rayner, P. J., Enting, I. G., Francey, R. J., and Langenfelds, R.: Reconstructing the recent carbon cycle from atmospheric CO2, δ13C and O2/N2 observations, Tellus B, 51, 213–232, https://doi.org/10.3402/tellusb.v51i2.16273, 1999.

Reeburgh, W. S., Hirsch, A. I., Sansone, F. J., Popp, B. N., and Rust, T. M.: Carbon kinetic isotope effect accompanying microbial oxidation of methane in boreal forest soils, Geochimica et Cosmochimica Acta, 61, 4761–4767, 1997.

Regnier, P., Friedlingstein, P., Ciais, P., Mackenzie, F. T., Gruber, N., Janssens, I. A., Laruelle, G. G., Lauerwald, R., Luyssaert, S., Andersson, A. J., Arndt, S., Arnosti, C., Borges, A. V., Dale, A. W., Gallego-Sala, A., Goddéris, Y., Goossens, N., Hartmann, J., Heinze, C., Ilyina, T., Joos, F., LaRowe, D. E., Leifeld, J., Meysman, F. J. R., Munhoven, G., Raymond, P. A., Spahni, R., Suntharalingam, P., and Thullner, M.: Anthropogenic perturbation of the carbon fluxes from land to ocean, Nat. Geosci., 6, 597–607, https://doi.org/10.1038/ngeo1830, 2013.

Rigby, M., Manning, A. J., and Prinn, R. G.: Inversion of long-lived trace gas emissions using combined Eulerian and Lagrangian chemical transport models, Atmos. Chem. Phys., 11, 9887–9898, https://doi.org/10.5194/acp-11-9887-2011, 2011.

Rijsdijk, P., Eskes, H., Dingemans, A., Boersma, K. F., Sekiya, T., Miyazaki, K., and Houweling, S.: Quantifying uncertainties in satellite NO2 superobservations for data assimilation and model evaluation, Geosci. Model Dev., 18, 483–509, https://doi.org/10.5194/gmd-18-483-2025, 2024.

Rödenbeck, C., Houweling, S., Gloor, M., and Heimann, M.: CO2 flux history 1982-2001 inferred from atmospheric data using a global inversion of atmospheric transport, Atmos. Chem. Phys., 3, 1919–1964, 2003.

Rödenbeck, C., Gerbig, C., Trusilova, K., and Heimann, M.: A two-step scheme for high-resolution regional atmospheric trace gas inversions based on independent models, Atmospheric Chemistry and Physics, 9, 5331–5342, https://doi.org/10.5194/acp-9-5331-2009, 2009.

Rodgers, C. D.: Inverse methods for atmospheric sounding: theory and practice, World Scientific, https://doi.org/10.1142/3171, 2000.

Rodgers, C. D. and Connor, B. J.: Intercomparison of remote sounding instruments, J. Geophys. Res.: Atmos., 108, 4116, https://doi.org/10.1029/2002jd002299, 2003.

Ruckstuhl, A. F., Henne, S., Reimann, S., Steinbacher, M., Vollmer, M. K., O'Doherty, S., Buchmann, B., and Hueglin, C.: Robust extraction of baseline signal of atmospheric trace species using local regression, Atmos. Meas. Tech., 5, 2613–2624, https://doi.org/10.5194/amt-5-2613-2012, 2012.

This project has received funding from the European Union's Horizon Europe research and innovation programme under grant agreement No 101081395

Ruiz, D. J., Prather, M. J., Strahan, S. E., Thompson, R. L., Froidevaux, L., and Steenrod, S. D.: How Atmospheric Chemistry and Transport Drive Surface Variability of N2O and CFC-11, J Geophys Res Atmospheres, 126, https://doi.org/10.1029/2020jd033979, 2021.

Saueressig, G., Crowley, J. N., Bergamaschi, P., Brühl, C., Brenninkmeijer, C. A., and Fischer, H.: Carbon 13 and D kinetic isotope effects in the reactions of CH4 with O (1 D) and OH: new laboratory measurements and their implications for the isotopic composition of stratospheric methane, Journal of Geophysical Research: Atmospheres, 106, 23127–23138, https://doi.org/10.1029/2000jd000120, 2001.

Saunois, M., Stavert, A. R., Poulter, B., Bousquet, P., Canadell, J. G., Jackson, R. B., Raymond, P. A., Dlugokencky, E. J., Houweling, S., Patra, P. K., Ciais, P., Arora, V. K., Bastviken, D., Bergamaschi, P., Blake, D. R., Brailsford, G., Bruhwiler, L., Carlson, K. M., Carrol, M., Castaldi, S., Chandra, N., Crevoisier, C., Crill, P. M., Covey, K., Curry, C. L., Etiope, G., Frankenberg, C., Gedney, N., Hegglin, M. I., oglund-Isakson, L. H., Hugelius, G., Ishizawa, M., Ito, A., Janssens-Maenhout, G., Jensen, K. M., Joos, F., Kleinen, T., Krummel, P. B., Langenfelds, R. L., Laruelle, G. G., Liu, L., Machida, T., Maksyutov, S., McDonald, K. C., McNorton, J., Miller, P. A., Melton, J. R., Morino, I., uller, J. M., Murgia-Flores, F., Naik, V., Niwa, Y., Noce, S., O'Doherty, S., Parker, R. J., Peng, C., Peng, S., Peters, G. P., Prigent, C., Prinn, R., Ramonet, M., Regnier, P., Riley, W. J., Rosentreter, J. A., Segers, A., Simpson, I. J., Shi, H., Smith, S. J., Steele, P. L., Thornton, B. F., Tian, H., Tohjima, Y., Tubiello, F. N., Tsuruta, A., Viovy, N., Voulgarakis, A., Weber, T. S., Weele, M. van, Werf, G. R. V. der, Weiss, R. F., Worthy, D., Wunch, D., Yin, Y., Yoshida, Y., Zhang, W., Zhang, Z., Zhao, Y., Zheng, B., Zhu, Q., and Zhuang, Q.: The Global Methane Budget 2000-2017, Earth Sys Sci Data, 12, 1561–1623, https://doi.org/10.5194/essd-12-1561-2020, 2020.

Saunois, M., Martinez, A., Poulter, B., Zhang, Z., Raymond, P. A., Regnier, P., Canadell, J. G., Jackson, R. B., Patra, P. K., Bousquet, P., Ciais, P., Dlugokencky, E. J., Lan, X., Allen, G. H., Bastviken, D., Beerling, D. J., Belikov, D. A., Blake, D. R., Castaldi, S., Crippa, M., Deemer, B. R., Dennison, F., Etiope, G., Gedney, N., Höglund-Isaksson, L., Holgerson, M. A., Hopcroft, P. O., Hugelius, G., Ito, A., Jain, A. K., Janardanan, R., Johnson, M. S., Kleinen, T., Krummel, P. B., Lauerwald, R., Li, T., Liu, X., McDonald, K. C., Melton, J. R., Mühle, J., Müller, J., Murguia-Flores, F., Niwa, Y., Noce, S., Pan, S., Parker, R. J., Peng, C., Ramonet, M., Riley, W. J., Rocher-Ros, G., Rosentreter, J. A., Sasakawa, M., Segers, A., Smith, S. J., Stanley, E. H., Thanwerdas, J., Tian, H., Tsuruta, A., Tubiello, F. N., Weber, T. S., Werf, G. R. van der, Worthy, D. E. J., Xi, Y., Yoshida, Y., Zhang, W., Zheng, B., Zhu, Q., Zhu, Q., and Zhuang, Q.: Global Methane Budget 2000–2020, Earth Syst. Sci. Data, 17, 1873–1958, https://doi.org/10.5194/essd-17-1873-2025, 2025.

Say, D., Ganesan, A. L., Lunt, M. F., Rigby, M., O'Doherty, S., Harth, C., Manning, A. J., Krummel, P. B., and Bauguitte, S.: Emissions of halocarbons from India inferred through atmospheric measurements, Atmos. Chem. Phys., 19, 9865–9885, https://doi.org/10.5194/acp-19-9865-2019, 2019.

Scarpelli, T. R., Jacob, D. J., Maasakkers, J. D., Sulprizio, M. P., Sheng, J.-X., Rose, K., Romeo, L., Worden, J. R., and Janssens-Maenhout, G.: A global gridded (0.1∘×0.1∘) inventory of methane emissions from oil, gas, and coal exploitation based on national reports to the United Nations Framework Convention on Climate Change, Earth Syst. Sci. Data, 12, 563–575, https://doi.org/10.5194/essd-12-563-2020, 2020.

Schewchuk, J. R.: An Introduction to the Conjugate Gradient Method Without the Agonizing Pain, Carnegie Mellon University, Pittsburg, PA, USA, 1994.

Schneising, O., Buchwitz, M., Reuter, M., Bovensmann, H., Burrows, J. P., Borsdorff, T., Deutscher, N. M., Feist, D. G., Griffith, D. W. T., Hase, F., Hermans, C., Iraci, L. T., Kivi, R., Landgraf, J., Morino, I., Notholt, J., Petri, C., Pollard, D. F., Roche, S., Shiomi, K., Strong, K., Sussmann, R., Velazco, V. A., Warneke, T., and Wunch, D.: A scientific algorithm to simultaneously retrieve carbon monoxide and methane from TROPOMI onboard Sentinel-5 Precursor, Atmos Meas Tech, 12, 6771–6802, https://doi.org/10.5194/amt-12-6771-2019, 2019.

This project has received funding from the European Union's Horizon Europe research and innovation programme under grant agreement No 101081395

Schneising, O., Bovensmann, H., Buchwitz, M., Buschmann, M., Deutscher, N. M., Griffith, D. W. T., Hachmeister, J., Hase, F., Iraci, L. T., Kivi, R., Morino, I., Ohyama, H., Petri, C., Reuter, M., Robinson, J., Roehl, C., Sha, M. K., Shiomi, K., Strong, K., Sussmann, R., Té, Y., Velazco, V. A., Vrekoussis, M., Wang, W., Warneke, T., Weidmann, D., Wunch, D., Zhou, M., and Bösch, H.: TROPOMI/WFMD v2.0: Improved retrievals of XCH_4 and XCO with XGBoost-based quality filtering, EGUsphere, 2025, 1–39, https://doi.org/10.5194/egusphere-2025-5422, 2025.

Schuh, A. E., Jacobson, A. R., Basu, S., Weir, B., Baker, D., Bowman, K., Chevallier, F., Crowell, S., Davis, K. J., Deng, F., Denning, S., Feng, L., Jones, D., Liu, J., and Palmer, P. I.: Quantifying the Impact of Atmospheric Transport Uncertainty on CO 2Surface Flux Estimates, Global Biogeochem. Cycles, 0, 2018GB006086, https://doi.org/10.1029/2018gb006086, 2019.

Seibert, P. and Frank, A.: Source-receptor matrix calculation with a Lagrangian particle dispersion model in backward mode, Atmos Chem Phys, 4, 51–63, https://doi.org/10.5194/acp-4-51-2004, 2004.

Sellmaier, A., Damm, E., Sachs, T., Kirbus, B., Wiekenkamp, I., Rinke, A., Pätzold, F., Nomura, D., Lampert, A., and Rex, M.: New insights in atmospheric methane variability in the Arctic by ship-borne measurements during MOSAiC, Atmos. Chem. Phys., 25, 17685–17700, https://doi.org/10.5194/acp-25-17685-2025, 2025.

Sha, M. K., Langerock, B., Blavier, J.-F. L., Blumenstock, T., Borsdorff, T., Buschmann, M., Dehn, A., Mazière, M. D., Deutscher, N. M., Feist, D. G., García, O. E., Griffith, D. W. T., Grutter, M., Hannigan, J. W., Hase, F., Heikkinen, P., Hermans, C., Iraci, L. T., Jeseck, P., Jones, N., Kivi, R., Kumps, N., Landgraf, J., Lorente, A., Mahieu, E., Makarova, M. V., Mellqvist, J., Metzger, J.-M., Morino, I., Nagahama, T., Notholt, J., Ohyama, H., Ortega, I., Palm, M., Petri, C., Pollard, D. F., Rettinger, M., Robinson, J., Roche, S., Roehl, C. M., Röhling, A. N., Rousogenous, C., Schneider, M., Shiomi, K., Smale, D., Stremme, W., Strong, K., Sussmann, R., Té, Y., Uchino, O., Velazco, V. A., Vigouroux, C., Vrekoussis, M., Wang, P., Warneke, T., Wizenberg, T., Wunch, D., Yamanouchi, S., Yang, Y., and Zhou, M.: Validation of methane and carbon monoxide from Sentinel-5 Precursor using TCCON and NDACC-IRWG stations, Atmos. Meas. Tech., 14, 6249–6304, https://doi.org/10.5194/amt-14-6249-2021, 2021.

Sherwood, O. A., Schwietzke, S., Arling, V. A., and Etiope, G.: Global Inventory of Gas Geochemistry Data from Fossil Fuel, Microbial and Burning Sources, version 2017, Earth Syst. Sci. Data, 9, 639–656, https://doi.org/10.5194/essd-9-639-2017, 2017.

Sicsik-Paré, A., Fortems-Cheiney, A., Pison, I., Broquet, G., Opler, A., Potier, E., Martinez, A., Schneising, O., Buchwitz, M., Maasakkers, J. D., Borsdorff, T., and Berchet, A.: Can we obtain consistent estimates of the emissions in Europe from three different CH_4 TROPOMI products?, EGUsphere, 2025, 1–48, https://doi.org/10.5194/egusphere-2025-2622, 2025.

Simon, D.: Optimal State Estimation: Kalman, H-infinity and Nonlinear Approaches, A John Wiley and Sons, Inc., 552 pp., 2006.

Smith, B., Wårlind, D., Arneth, A., Hickler, T., Leadley, P., Siltberg, J., and Zaehle, S.: Implications of incorporating N cycling and N limitations on primary production in an individual-based dynamic vegetation model, Biogeosciences, 11, 2027–2054, https://doi.org/10.5194/bg-11-2027-2014, 2014.

Snover, A. K. and Quay, P. D.: Hydrogen and carbon kinetic isotope effects during soil uptake of atmospheric methane, Global Biogeochemical Cycles, 14, 25–39, https://doi.org/10.1029/1999gb900089, 2000.

Solazzo, E., Crippa, M., Guizzardi, D., Muntean, M., Choulga, M., and Janssens-Maenhout, G.: Uncertainties in the Emissions Database for Global Atmospheric Research (EDGAR) emission inventory of greenhouse gases, Atmospheric Chemistry and Physics, 21, 5655–5683, https://doi.org/10.5194/acp-21-5655-2021, 2021.

This project has received funding from the European Union's Horizon Europe research and innovation programme under grant agreement No 101081395

Soulie, A., Granier, C., Darras, S., Zilbermann, N., Doumbia, T., Guevara, M., Jalkanen, J.-P., Keita, S., Liousse, C., Crippa, M., Guizzardi, D., Hoesly, R., and Smith, S. J.: Global anthropogenic emissions (CAMS-GLOB-ANT) for the Copernicus Atmosphere Monitoring Service simulations of air quality forecasts and reanalyses, Earth Syst. Sci. Data, 16, 2261–2279, https://doi.org/10.5194/essd-16-2261-2024, 2024.

Spivakovsky, C. M., Logan, J. A., Montzka, S. A., Balkanski, Y. J., Foreman-Fowler, M., Jones, D. B. A., Horowitz, L. W., Fusco, A. C., Brenninkmeijer, C. A. M., and Prather, M. J.: Three-dimensional climatological distribution of tropospheric OH: Update and evaluation, Journal of Geophysical Research: Atmospheres, 105, 8931–8980, https://doi.org/10.1029/1999jd901006, 2000.

Steinbach, J., Gerbig, C., Rodenbeck, C., Karstens, U., Minejima, C., and Mukai, H.: The CO 2 release and Oxygen uptake from Fossil Fuel Emission Estimate (COFFEE) dataset: effects from varying oxidative ratios, Atmospheric Chemistry and Physics, 11, 6855–6870, https://doi.org/10.5194/acp-11-6855-2011, 2011.

Steiner, M., Peters, W., Luijkx, I., Henne, S., Chen, H., Hammer, S., and Brunner, D.: European CH4 inversions with ICON-ART coupled to the CarbonTracker Data Assimilation Shell, Atmos. Chem. Phys., 24, 2759–2782, https://doi.org/10.5194/acp-24-2759-2024, 2024a.

Steiner, M., Cantarello, L., Henne, S., and Brunner, D.: Flow-dependent observation errors for greenhouse gas inversions in an ensemble Kalman smoother, Atmos. Chem. Phys., 24, 12447–12463, https://doi.org/10.5194/acp-24-12447-2024, 2024b.

Stohl, A., Seibert, P., Arduini, J., Eckhardt, S., Fraser, P., Greally, B. R., Lunder, C., Maione, M., ºhle, J. M., O'Doherty, S., Prinn, R. G., Reimann, S., Saito, T., Schmidbauer, N., Simmonds, P. G., Vollmer, M. K., Weiss, R. F., and Yokouchi, Y.: An analytical inversion method for determining regional and global emissions of greenhouse gases: Sensitivity studies and application to halocarbons, Atmos. Chem. Phys., 9, 1597–1620, https://doi.org/10.5194/acp-9-1597-2009, 2009.

Strode, S. A., Wang, J. S., Manyin, M., Duncan, B., Hossaini, R., Keller, C. A., Michel, S. E., and White, J. W. C.: Strong sensitivity of the isotopic composition of methane to the plausible range of tropospheric chlorine, Atmos. Chem. Phys., 20, 8405–8419, https://doi.org/10.5194/acp-20-8405-2020, 2020.

Sun, Q., Joos, F., Lienert, S., Berthet, S., Carroll, D., Gong, C., Ito, A., Jain, A. K., Kou-Giesbrecht, S., Landolfi, A., Manizza, M., Pan, N., Prather, M., Regnier, P., Resplandy, L., Séférian, R., Shi, H., Suntharalingam, P., Thompson, R. L., Tian, H., Vuichard, N., Zaehle, S., and Zhu, Q.: The Modeled Seasonal Cycles of Surface N2O Fluxes and Atmospheric N2O, Glob. Biogeochem. Cycles, 38, https://doi.org/10.1029/2023gb008010, 2024.

Super, I., Mathas, D., Jonkheid, B., Segers, A., and Kuenen, J.: CAMS-REG-UNC-v8.1: a detailed uncertainty product for the gridded CAMS-REG-v8.1 emission inventory, Earth Syst. Sci. Data, 18, 6119–6137, https://doi.org/10.5194/essd-18-6119-2026, 2026.

Szénási, B., Berchet, A., Broquet, G., Segers, A., Gon, H. D. van der, Krol, M., Hullegie, J. J. S., Kiesow, A., Günther, D., Petrescu, A. M. R., Saunois, M., Bousquet, P., and Pison, I.: A pragmatic protocol for characterising errors in atmospheric inversions of methane emissions over Europe, Tellus B Chem Phys Meteorology, 73, 1–23, https://doi.org/10.1080/16000889.2021.1914989, 2021.

Tanneberger, F., Appulo, L., Ewert, S., Lakner, S., Brolcháin, N. Ó., Peters, J., and Wichtmann, W.: The Power of Nature-Based Solutions: How Peatlands Can Help Us to Achieve Key EU Sustainability Objectives, Adv Sustain Syst, 5, 2000146, https://doi.org/10.1002/adsu.202000146, 2021.

Tans, P. P., Conway, T. J., and Nakazawa, T.: Latitudinal distribution of the sources and sinks of atmospheric carbon dioxide derived from surface observations and an atmospheric transport model, Journal of Geophysical Research: Atmospheres (1984--2012), 94, 5151–5172, https://doi.org/10.1029/jd094id04p05151, 1989.

This project has received funding from the European Union's Horizon Europe research and innovation programme under grant agreement No 101081395

Tarantola, A.: Inverse problem theory and methods for model parameter estimation, Society for Industrial and Applied Mathematics, 2005.

Team, M., Nisbet, E. G., Allen, G., Fisher, R. E., France, J. L., Lee, J. D., Lowry, D., Andrade, M. F., Bannan, T. J., Barker, P., Bateson, P., Bauguitte, S. J.-B., Bower, K. N., Broderick, T. J., Chibesakunda, F., Cain, M., Cozens, A. E., Daly, M. C., Ganesan, A. L., Jones, A. E., Lambakasa, M., Lunt, M. F., Mehra, A., Moreno, I., Pasternak, D., Palmer, P. I., Percival, C. J., Pitt, J. R., Riddle, A. J., Rigby, M., Shaw, J. T., Stell, A. C., Vaughan, A. R., Warwick, N. J., and Wilde, S. E.: Isotopic signatures of methane emissions from tropical fires, agriculture and wetlands: the MOYA and ZWAMPS flights, Philos. Trans. R. Soc. A, 380, 20210112, https://doi.org/10.1098/rsta.2021.0112, 2022.

Tegetmeyer, C., Kaiser, M., & Barthelmes, A.: The European Wetland Map ('EWM') [Data set]. Zenodo. https://doi.org/10.5281/zenodo.15302184, 2025.

Tenkanen, M. K., Tsuruta, A., Gon, H. D. van der, Höglund-Isaksson, L., Leppänen, A., Markkanen, T., Petrescu, A. M. R., Raivonen, M., Aaltonen, H., and Aalto, T.: Partitioning anthropogenic and natural methane emissions in Finland during 2000–2021 by combining bottom-up and top-down estimates, Atmos. Chem. Phys., 25, 2181–2206, https://doi.org/10.5194/acp-25-2181-2025, 2024.

Thacker, W. C.: Data assimilation with inequality constraints, Ocean Modelling, 16, 264–276, https://doi.org/10.1016/j.ocemod.2006.11.001, 2007.

Thanwerdas, J., Saunois, M., Pison, I., Hauglustaine, D., Berchet, A., Baier, B., Sweeney, C., and Bousquet, P.: How do Cl concentrations matter for the simulation of CH4 and δ13C(CH4) and estimation of the CH4 budget through atmospheric inversions?, Atmos. Chem. Phys., 22, 15489–15508, https://doi.org/10.5194/acp-22-15489-2022, 2022.

Thanwerdas, J., Saunois, M., Berchet, A., Pison, I., and Bousquet, P.: Investigation of the renewed methane growth post-2007 with high-resolution 3-D variational inverse modeling and isotopic constraints, Atmos. Chem. Phys., 24, 2129–2167, https://doi.org/10.5194/acp-24-2129-2024, 2023.

Thanwerdas, J., Saunois, M., Berchet, A., Pison, I., and Bousquet, P.: Investigation of the renewed methane growth post-2007 with high-resolution 3-D variational inverse modeling and isotopic constraints, Atmos. Chem. Phys., 24, 2129–2167, https://doi.org/10.5194/acp-24-2129-2024, 2024.

Thanwerdas, J., Berchet, A., Constantin, L., Tsuruta, A., Steiner, M., Reum, F., Henne, S., and Brunner, D.: Improving the ensemble square root filter (EnSRF) in the Community Inversion Framework: a case study with ICON-ART 2024.01, Geosci. Model Dev., 18, 1505–1544, https://doi.org/10.5194/gmd-18-1505-2025, 2025.

Thompson, R. L. and Stohl, A.: FLEXINVERT: an atmospheric Bayesian inversion framework for determining surface fluxes of trace species using an optimized grid, Geosci Model Dev, 7, 2223–2242, https://doi.org/10.5194/gmd-7-2223-2014, 2014.

Thompson, R. L., Chevallier, F., Crotwell, A. M., Dutton, G., Langenfelds, R. L., Prinn, R. G., Weiss, R. F., Tohjima, Y., Nakazawa, T., Krummel, P. B., Steele, L. P., Fraser, P., O'Doherty, S., Ishijima, K., and Aoki, S.: Nitrous oxide emissions 1999 to 2009 from a global atmospheric inversion, Atmos. Chem. Phys., 14, 1–17, https://doi.org/10.5194/acp-14-1801-2014, 2014a.

Thompson, R. L., Patra, P. K., Ishijima, K., Saikawa, E., Corazza, M., Karstens, U., Wilson, C., Bergamaschi, P., Dlugokencky, E., and Sweeney, C.: TransCom N2O model inter-comparison-Part 1: Assessing the influence of transport and surface fluxes on tropospheric N2O variability, Atmospheric Chemistry and Physics, 14, 4349–4368, https://doi.org/10.5194/acp-14-4349-2014, 2014b.

Thompson, R. L., Patra, P. K., Chevallier, F., Maksyutov, S., Law, R. M., Ziehn, T., Peters, W., Ganshin, A., Zhuravlev, R., Maki, T., Nakamura, T., Shirai, T., Ishizawa, M., Saeki, T., Machida, T., Poulter, B., Canadell, J. G., and Ciais, P.: Top-down assessment of the Asian carbon budget since the mid 1990s, Nature communications, 7, https://doi.org/10.1038/ncomms10724, 2016.

This project has received funding from the European Union's Horizon Europe research and innovation programme under grant agreement No 101081395

Thompson, R. L., Sasakawa, M., Machida, T., Aalto, T., Worthy, D., Lavric, J. V., Myhre, C. L., and Stohl, A.: Methane fluxes in the high northern latitudes for 2005-2013 estimated using a Bayesian atmospheric inversion, Atmospheric Chemistry and Physics, 17, 3553–3572, https://doi.org/10.5194/acp-17-3553-2017, 2017.

Thompson, R. L., Nisbet, E. G., Pisso, I., Stohl, A., Blake, D., Dlugokencky, E. J., Helmig, D., and White, J. W. C.: Variability in Atmospheric Methane From Fossil Fuel and Microbial Sources Over the Last Three Decades, Geophysical Research Letters, 112, D04306-10, https://doi.org/10.1029/2018gl078127, 2018.

Thompson, R. L., Lassaletta, L., Patra, P. K., Wilson, C., Wells, K. C., Gressent, A., Koffi, E. N., Chipperfield, M. P., Winiwarter, W., Davidson, E. A., Tian, H., and Canadell, J. G.: Acceleration of global N2O emissions seen from two decades of atmospheric inversion, Nature Climate Change, 9, 993–998, https://doi.org/10.1038/s41558-019-0613-7, 2019.

Thompson, R. L., Broquet, G., Gerbig, C., Koch, T., Lang, M., Monteil, G., Munassar, S., Nickless, A., Scholze, M., Ramonet, M., Karstens, U., Schaik, E. van, Wu, Z., and Rodenbeck, C.: Changes in net ecosystem exchange over Europe during the 2018 drought based on atmospheric observations, Philosophical Transactions of the Royal Society B: Biological Sciences, 375, 20190512–10, https://doi.org/10.1098/rstb.2019.0512, 2020.

Thompson, R. L., Montzka, S. A., Vollmer, M. K., Arduini, J., Crotwell, M., Krummel, P. B., Lunder, C., Mühle, J., O'Doherty, S., Prinn, R. G., Reimann, S., Vimont, I., Wang, H., Weiss, R. F., and Young, D.: Estimation of the atmospheric hydroxyl radical oxidative capacity using multiple hydrofluorocarbons (HFCs), Atmos. Chem. Phys., 24, 1415–1427, https://doi.org/10.5194/acp-24-1415-2024, 2023.

Thompson, R. L., Krishnankutty, N., Pisso, I., Schneider, P., Stebel, K., Sasakawa, M., Stohl, A., and Platt, S. M.: Efficient use of a Lagrangian particle dispersion model for atmospheric inversions using satellite observations of column mixing ratios, Atmos. Chem. Phys., 25, 12737–12751, https://doi.org/10.5194/acp-25-12737-2025, 2025.

Tian, H., Yang, J., Xu, R., Lu, C., Canadell, J. G., Davidson, E. A., Jackson, R. B., Arneth, A., Chang, J., Ciais, P., Gerber, S., Ito, A., Joos, F., Lienert, S., Messina, P., Olin, S., Pan, S., Peng, C., Saikawa, E., Thompson, R. L., Vuichard, N., Winiwarter, W., Zaehle, S., and Zhang, B.: Global soil nitrous oxide emissions since the pre-industrial era estimated by an ensemble of Terrestrial Biosphere Models: Magnitude, attribution and uncertainty, Glob. Change Biol., 25, 640–659, https://doi.org/10.1111/gcb.14514, 2019.

Tian, H., Xu, R., Canadell, J. G., Thompson, R. L., Winiwarter, W., Suntharalingam, P., Davidson, E. A., Ciais, P., Jackson, R. B., Janssens-Maenhout, G., Prather, M. J., Regnier, P., Pan, N., Pan, S., Peters, G. P., Shi, H., Tubiello, F. N., Zaehle, S., Zhou, F., Arneth, A., Battaglia, G., Berthet, S., Bopp, L., Bouwman, A. F., Buitenhuis, E. T., Chang, J., Chipperfield, M. P., Dangal, S. R. S., Dlugokencky, E., Elkins, J. W., Eyre, B. D., Fu, B., Hall, B., Ito, A., Joos, F., Krummel, P. B., Landolfi, A., Laruelle, G. G., Lauerwald, R., Li, W., Lienert, S., Maavara, T., MacLeod, M., Millet, D. B., Olin, S., Patra, P. K., Prinn, R. G., Raymond, P. A., Ruiz, D. J., Werf, G. R., Vuichard, N., Wang, J., Weiss, R. F., Wells, K. C., Wilson, C., Yang, J., and Yao, Y.: A comprehensive quantification of global nitrous oxide sources and sinks, Nature, 248–256, https://doi.org/10.1038/s41586-020-2780-0, 2020.

Tian, H., Pan, N., Thompson, R. L., Canadell, J. G., Suntharalingam, P., Regnier, P., Davidson, E. A., Prather, M., Ciais, P., Muntean, M., Pan, S., Winiwarter, W., Zaehle, S., Zhou, F., Jackson, R. B., Bange, H. W., Berthet, S., Bian, Z., Bianchi, D., Bouwman, A. F., Buitenhuis, E. T., Dutton, G., Hu, M., Ito, A., Jain, A. K., Jeltsch-Thömmes, A., Joos, F., Kou-Giesbrecht, S., Krummel, P. B., Lan, X., Landolfi, A., Lauerwald, R., Li, Y., Lu, C., Maavara, T., Manizza, M., Millet, D. B., Mühle, J., Patra, P. K., Peters, G. P., Qin, X., Raymond, P., Resplandy, L., Rosentreter, J. A., Shi, H., Sun, Q., Tonina, D., Tubiello, F. N., Werf, G. R. van der, Vuichard, N., Wang, J., Wells, K. C., Western, L. M., Wilson, C., Yang, J., Yao, Y., You, Y., and Zhu, Q.: Global nitrous oxide budget (1980–2020), Earth Syst. Sci. Data, 16, 2543–2604, https://doi.org/10.5194/essd-16-2543-2024, 2024.

This project has received funding from the European Union's Horizon Europe research and innovation programme under grant agreement No 101081395

Tibrewal, K., Ciais, P., Saunois, M., Martinez, A., Lin, X., Thanwerdas, J., Deng, Z., Chevallier, F., Giron, C., Albergel, C., Tanaka, K., Patra, P., Tsuruta, A., Zheng, B., Belikov, D., Niwa, Y., Janardanan, R., Maksyutov, S., Segers, A., Tzompa-Sosa, Z. A., Bousquet, P., and Sciare, J.: Assessment of methane emissions from oil, gas and coal sectors across inventories and atmospheric inversions, Commun. Earth Environ., 5, 26, https://doi.org/10.1038/s43247-023-01190-w, 2024.

Tikhonov, A. N., and Arsenin, V. Y., Solutions of Ill-Posed Problems, Wiley, New York, 1977.

Tolk, L. F., Dolman, A. J., Meesters, A. G. C. A., and Peters, W.: A comparison of different inverse carbon flux estimation approaches for application on a regional domain, Atmos. Chem. Phys., 11, 10349–10365, https://doi.org/10.5194/acp-11-10349-2011, 2011.

Tsuruta, A., Aalto, T., Backman, L., Hakkarainen, J., Laan-Luijkx, I. T. van der, Krol, M. C., Spahni, R., Houweling, S., Laine, M., Dlugokencky, E., Gomez-Pelaez, A. J., Schoot, M. van der, LANGENFELDS, R., Ellul, R., Arduini, J., Apadula, F., Gerbig, C., Feist, D. G., Kivi, R., Yoshida, Y., and Peters, W.: Global methane emission estimates for 2000–2012 from CarbonTracker Europe-CH_4 v1.0, Geoscientific Model Development, 10, 1261–1289, https://doi.org/10.5194/gmd-10-1261-2017, 2017.

Tsuruta, A., Kivimäki, E., Lindqvist, H., Karppinen, T., Backman, L., Hakkarainen, J., Schneising, O., Buchwitz, M., Lan, X., Kivi, R., Chen, H., Buschmann, M., Herkommer, B., Notholt, J., Roehl, C., Té, Y., Wunch, D., Tamminen, J., and Aalto, T.: CH4 Fluxes Derived from Assimilation of TROPOMI XCH4 in CarbonTracker Europe-CH4: Evaluation of Seasonality and Spatial Distribution in the Northern High Latitudes, Remote Sens., 15, 1620, https://doi.org/10.3390/rs15061620, 2023a.

Tsuruta, A., Kivimäki, E., Lindqvist, H., Karppinen, T., Backman, L., Hakkarainen, J., Schneising, O., Buchwitz, M., Lan, X., Kivi, R., Chen, H., Buschmann, M., Herkommer, B., Notholt, J., Roehl, C., Té, Y., Wunch, D., Tamminen, J., and Aalto, T.: CH4 Fluxes Derived from Assimilation of TROPOMI XCH4 in CarbonTracker Europe-CH4: Evaluation of Seasonality and Spatial Distribution in the Northern High Latitudes, Remote Sens-basel, 15, 1620, https://doi.org/10.3390/rs15061620, 2023b.

Tsuruta, A., Kuze, A., Shiomi, K., Kataoka, F., Kikuchi, N., Aalto, T., Backman, L., Kivimäki, E., Tenkanen, M. K., McKain, K., García, O. E., Hase, F., Kivi, R., Morino, I., Ohyama, H., Pollard, D. F., Sha, M. K., Strong, K., Sussmann, R., Te, Y., Velazco, V. A., Vrekoussis, M., Warneke, T., Zhou, M., and Suto, H.: Global CH4 fluxes derived from JAXA/GOSAT lower-tropospheric partial column data and the CarbonTracker Europe-CH4 atmospheric inverse model, Atmos. Chem. Phys., 25, 7829–7862, https://doi.org/10.5194/acp-25-7829-2025, 2025.

Tyler, S. C., Crill, P. M., and Brailsford, G. W.: 13C12C Fractionation of methane during oxidation in a temperate forested soil, Geochimica et Cosmochimica Acta, 58, 1625–1633, https://doi.org/10.1016/0016-7037(94)90564-9, 1994.

Tyler, S. C., Ajie, H. O., Rice, A. L., Cicerone, R. J., and Tuazon, E. C.: Experimentally determined kinetic isotope effects in the reaction of CH4 with Cl: Implications for atmospheric CH4, Geophys. Res. Lett., 27, 1715–1718, https://doi.org/10.1029/1999gl011168, 2000.

Tyystjärvi, V., Markkanen, T., Backman, L., Raivonen, M., Leppänen, A., Li, X., Ojanen, P., Minkkinen, K., Hautala, R., Peltoniemi, M., Anttila, J., Laiho, R., Lohila, A., Mäkipää, R., and Aalto, T.: Future methane fluxes of peatlands are controlled by management practices and fluctuations in hydrological conditions due to climatic variability, Biogeosciences, 21, 5745–5771, https://doi.org/10.5194/bg-21-5745-2024, 2024.

Umezawa, T., Brenninkmeijer, C. A. M., ockmann, T. R., Veen, C. van der, Tyler, S. C., Fujita, R., Morimoto, S., Aoki, S., Sowers, T., Schmitt, J., Bock, M., Beck, J., Fischer, H., Michel, S. E., Vaughn, B. H., Miller, J. B., White, J. W. C., Brailsford, G., Schaefer, H., Sperlich, P., Brand, W. A., Rothe, M., Blunier, T., Lowry, D., Fisher, R. E., Nisbet, E. G., Rice, A. L., Bergamaschi, P., Veidt, C., and Levin, I.: Interlaboratory comparison of δ13C and δ D measurements of atmospheric CH4 for combined use of data sets from different laboratories, Atmospheric Measurement Techniques, 11, 1207–1231, https://doi.org/10.5194/amt-11-1207-2018, 2018.

This project has received funding from the European Union's Horizon Europe research and innovation programme under grant agreement No 101081395

Umezawa, T., Tohjima, Y., Terao, Y., Sasakawa, M., Müller, A., Saeki, T., Machida, T., Nakaoka, S.-I., Nara, H., Nomura, S., Nishihashi, M., Mukai, H., Frey, M. M., Morino, I., Ohyama, H., Yoshida, Y., Zeng, J., Noda, H., Saito, M., Matsunaga, T., Sugita, T., Tanimoto, H., Niwa, Y., Ito, A., Yamashita, Y., Shirai, T., Ishizawa, M., Ishijima, K., Tsuboi, K., Sawa, Y., and Matsueda, H.: Long-term and interannual variations of atmospheric methane observed by the NIES and collaborative observation networks, Prog. Earth Planet. Sci., 12, 39, https://doi.org/10.1186/s40645-025-00711-9, 2025.

Upton, S., Reichstein, M., Gans, F., Peters, W., Kraft, B., and Bastos, A.: Constraining biospheric carbon dioxide fluxes by combined top-down and bottom-up approaches, Atmos. Chem. Phys., 24, 2555–2582, https://doi.org/10.5194/acp-24-2555-2024, 2024.

Urraca, R., Janssens-Maenhout, G., Álamos, N., Berna-Peña, L., Crippa, M., Darras, S., Dellaert, S., Gon, H. D. van der, Dowell, M., Gobron, N., Granier, C., Grassi, G., Guevara, M., Guizzardi, D., Gurney, K., Huneeus, N., Keita, S., Kuenen, J., Lopez-Noreña, A., Puliafito, E., Roest, G., Rossi, S., Soulie, A., and Visschedijk, A.: CoCO2-MOSAIC 1.0: a global mosaic of regional, gridded, fossil, and biofuel CO 2 emission inventories, Earth Syst. Sci. Data, 16, 501–523, https://doi.org/10.5194/essd-16-501-2024, 2024.

van der Werf, G. R., Randerson, J. T., Giglio, L., Leeuwen, T. T. van, Chen, Y., Rogers, B. M., Mu, M., Marle, M. J. E. van, Morton, D. C., Collatz, G. J., Yokelson, R. J., and Kasibhatla, P. S.: Global fire emissions estimates during 1997–2016, Earth System Science Data, 9, 697–720, https://doi.org/10.5194/essd-9-697-2017, 2017.

van der Werf, G. R., Randerson, J. T., Wees, D. van, Chen, Y., Giglio, L., Hall, J., Vernooij, R., Mu, M., Shahid, S. B., Barsanti, K. C., Yokelson, R., and Morton, D. C.: Landscape fire emissions from the 5th version of the Global Fire Emissions Database (GFED5), Sci. Data, 12, 1870, https://doi.org/10.1038/s41597-025-06127-w, 2025.

Vanderbecken, P. J., Brazidec, J. D. L., Farchi, A., Bocquet, M., Roustan, Y., Potier, É., and Broquet, G.: Accounting for meteorological biases in simulated plumes using smarter metrics, Atmos. Meas. Tech., 16, 1745–1766, https://doi.org/10.5194/amt-16-1745-2023, 2023.

Varon, D. J., Jacob, D. J., Hmiel, B., Gautam, R., Lyon, D. R., Omara, M., Sulprizio, M., Shen, L., Pendergrass, D., Nesser, H., Qu, Z., Barkley, Z. R., Miles, N. L., Richardson, S. J., Davis, K. J., Pandey, S., Lu, X., Lorente, A., Borsdorff, T., Maasakkers, J. D., and Aben, I.: Continuous weekly monitoring of methane emissions from the Permian Basin by inversion of TROPOMI satellite observations, Atmos. Chem. Phys., 23, 7503–7520, https://doi.org/10.5194/acp-23-7503-2023, 2023.

Villalobos, Y., Rayner, P. J., Silver, J. D., Thomas, S., Haverd, V., Knauer, J., Loh, Z. M., Deutscher, N. M., Griffith, D. W. T., and Pollard, D. F.: Was Australia a sink or source of CO2 in 2015? Data assimilation using OCO-2 satellite measurements, Atmos. Chem. Phys., 21, 17453–17494, https://doi.org/10.5194/acp-21-17453-2021, 2021.

Visser, A. and Bousserez, N.: CORSO: Optimized B matrix parameters for IFS greenhouse gas emission inversions, CORSO Horizon Europe project (grant number 101082194), 2024.

Vojta, M., Plach, A., Thompson, R. L., and Stohl, A.: A comprehensive evaluation of the use of Lagrangian particle dispersion models for inverse modeling of greenhouse gas emissions, Geosci Model Dev, 15, 8295–8323, https://doi.org/10.5194/gmd-15-8295-2022, 2022.

Vojta, M., Plach, A., Annadate, S., Park, S., Lee, G., Purohit, P., Lindl, F., Lan, X., Mühle, J., Thompson, R. L., and Stohl, A.: A global re-analysis of regionally resolved emissions and atmospheric mole fractions of SF6 for the period 2005–2021, Atmos. Chem. Phys., 24, 12465–12493, https://doi.org/10.5194/acp-24-12465-2024, 2024.

Vojta, M., Plach, A., Thompson, R. L., Purohit, P., Stanley, K., O'Doherty, S., Young, D., Pitt, J., Arduini, J., Lan, X., and Stohl, A.: Quantifying European SF6 emissions from 2005 to 2021 using a large inversion ensemble, Atmos. Chem. Phys., 25, 15197–15243, https://doi.org/10.5194/acp-25-15197-2025, 2025.

This project has received funding from the European Union's Horizon Europe research and innovation programme under grant agreement No 101081395

Vojta, M., Subramanian, R., Gialesakis, N., Thompson, R. L., Stohl, A., and Kanakidou, M.: Constraining 2020 methane emissions in the Eastern Mediterranean and Middle East using TROPOMI satellite data, EGUsphere, 2026, 1–38, https://doi.org/10.5194/egusphere-2026-3792, 2026.

Voulgarakis, A., Naik, V., Lamarque, J.-F., Shindell, D. T., Young, P. J., Prather, M. J., Wild, O., Field, R. D., Bergmann, D., Cameron-Smith, P., Cionni, I., Collins, W. J., Dalsøren, S. B., Doherty, R. M., Eyring, V., Faluvegi, G., Folberth, G. A., Horowitz, L. W., Josse, B., MacKenzie, I. A., Nagashima, T., Plummer, D. A., Righi, M., Rumbold, S. T., Stevenson, D. S., Strode, S. A., Sudo, K., Szopa, S., and Zeng, G.: Analysis of present day and future OH and methane lifetime in the ACCMIP simulations, Atmos Chem Phys, 13, 2563–2587, https://doi.org/10.5194/acp-13-2563-2013, 2013.

Wang, Y., Broquet, G., Ciais, P., Chevallier, F., Vogel, F., Kadygrov, N., Wu, L., Yin, Y., Wang, R., and Tao, S.: Estimation of observation errors for large-scale atmospheric inversion of CO2 emissions from fossil fuel combustion, Tellus B: Chem. Phys. Meteorol., 69, 1325723, https://doi.org/10.1080/16000889.2017.1325723, 2017.

Wang, F., Maksyutov, S., Janardanan, R., Tsuruta, A., Ito, A., Morino, I., Yoshida, Y., Tohjima, Y., Kaiser, J. W., Lan, X., Zhang, Y., Mammarella, I., Lavric, J. V., and Matsunaga, T.: Atmospheric observations suggest methane emissions in north-eastern China growing with natural gas use, Sci. Rep., 12, 18587, https://doi.org/10.1038/s41598-022-19462-4, 2022.

Wang, J., Feng, L., Palmer, P.I. et al.: Large Chinese land carbon sink estimated from atmospheric carbon dioxide data. Nature, 586, 720–723. https://doi.org/10.1038/s41586-020-2849-9, 2020.

Wang, J., Feng, L., Palmer, P.I. et al. Reply to: The size of the land carbon sink in China. Nature, 603, E10–E12. https://doi.org/10.1038/s41586-021-04256-x, 2022.

Ward, R. H., Sweeney, C., Miller, J. B., Goeckede, M., Laurila, T., Hatakka, J., Ivakov, V., Sasakawa, M., Machida, T., Morimoto, S., Goto, D., and Ganesan, A. L.: Increasing Methane Emissions and Widespread Cold-Season Release From High-Arctic Regions Detected Through Atmospheric Measurements, J. Geophys. Res.: Atmos., 129, https://doi.org/10.1029/2024jd040766, 2024.

Ward, R. H., Western, L. M., Tunnicliffe, R. L., Fillola, E., Tsuruta, A., Aalto, T., and Ganesan, A. L.: Uncertainty and retrieval sensitivity in TROPOMI-based methane inversions over the North Slope of Alaska, EGUsphere, 2025, 1–38, https://doi.org/10.5194/egusphere-2025-4230, 2025.

Warwick, N. J., Cain, M. L., Fisher, R., France, J. L., Lowry, D., Michel, S. E., Nisbet, E. G., Vaughn, B. H., White, J. W. C., and Pyle, J. A.: Using d13C-CH4 and dD-CH4 to constrain Arctic methane emissions, Atmos. Chem. Phys., 16, 14891–14908, https://doi.org/10.5194/acp-2016-408, 2016.

Weber, T., Wiseman, N. A., and Kock, A.: Global ocean methane emissions dominated by shallow coastal waters, Nature communications, 10, 1–10, https://doi.org/10.1038/s41467-019-12541-7, 2019.

Whitaker, J. S., Hamill, T. M., Whitaker, J. S., and Hamill, T. M.: Ensemble Data Assimilation without Perturbed Observations, http://dx.doi.org/10.1175/1520-0493(2002)130<1913:EDAWPO>2.0.CO;2, 130, 1913–1924, https://doi.org/10.1175/1520-0493(2002)130<1913:edawpo>2.0.co;2, 2002.

Wilson, E. W., Hamilton, W. A., Mount, H. R., and DeMore, W. B.: Rate Constants for the Reactions of Hydroxyl Radical with Several Fluoroethers by the Relative Rate Method, J Phys Chem, 111, 1610–1617, https://doi.org/10.1021/jp068355d, 2007.

Winiwarter, W., Lindl, F., Kaltenegger, K., Warnecke, L., Höglund-Isaksson, L., Sanabria, A. G., Purohit, P., and Klimont, Z.: EYE-CLIMA: Anthropogenic emissions and uncertainties of GHGs and BC, EYE-CLIMA Horizon Europe Project (grant number 101081395), 2024.

Wittig, S., Berchet, A., Pison, I., Saunois, M., Thanwerdas, J., Martinez, A., Paris, J.-D., Machida, T., Sasakawa, M., Worthy, D. E. J., Lan, X., Thompson, R. L., Sollum, E., and Arshinov, M.: Estimating Methane Emissions in the Arctic nations using surface observations from 2008 to 2019, Egusphere, 2023, 1–42, https://doi.org/10.5194/egusphere-2022-1257, 2023.

This project has received funding from the European Union's Horizon Europe research and innovation programme under grant agreement No 101081395

WMO: Integrated Global Greenhouse Gas Information System Good Practice Guidance for Estimating National-scale Greenhouse Gas Emissions usingAtmospheric Observations, GAW Report No. 319, Geneva, Switzerland, 2025.

Wolfe, P.: Convergence Conditions for Ascent Methods, SIAM Rev., 11, 226–235, https://doi.org/10.1137/1011036, 1969.

van der Woude, A. M., Kok, R. de, Smith, N., Luijkx, I. T., Botía, S., Karstens, U., Kooijmans, L. M. J., Koren, G., Meijer, H. A. J., Steeneveld, G.-J., Storm, I., Super, I., Scheeren, H. A., Vermeulen, A., and Peters, W.: Near-real-time CO2 fluxes from CarbonTracker Europe for high-resolution atmospheric modeling, Earth Syst. Sci. Data, 15, 579–605, https://doi.org/10.5194/essd-15-579-2023, 2023.

van der Woude, A. M., Luijkx, I. T., Kok, R. J. de, Peters, W., Chevallier, F., Rödenbeck, C., Ciais, P., Chandra, N., Wang, K., Janardanan, R., Asperen, H. van, Bastos, A., Berg, A. van den, Bloom, A. A., Botía, S., Bowman, K., Canadell, J. G., Souza, R. A. F. de, Dias-Junior, C. Q., Feng, L., Friedlingstein, P., Gatti, L. V., Gloor, E., Ishijima, K., Jiang, F., Jin, Z., Ju, W., Lan, X., Liu, J., Liu, Z., Machida, T., Maksyutov, S., Manning, A. C., Martinez, A., Martins, G. A., McKain, K., Miller, J. B., Nayagam, L., Niwa, Y., Palmer, P. I., Patra, P. K., Pickers, P. A., Poulter, B., Stephens, B. B., Sweeney, C., Wofsy, S., Wu, Z., Yang, D., Yun, J., and Zeng, N.: A Top-Down View of Global and Regional Carbon Budgets From an Ensemble of Atmospheric Inversions, Glob. Biogeochem. Cycles, 40, https://doi.org/10.1029/2025gb008779, 2026.

Xu, X., Sharma, P., Shu, S. et al.: Global greenhouse gas emissions from animal-based foods are twice those of plant-based foods, Nat Food 2, 724–732, https://doi.org/10.1038/s43016-021-00358-x, 2021.

Yao, Y., Tian, H., Shi, H., Pan, S., Xu, R., Pan, N., and Canadell, J. G.: Increased global nitrous oxide emissions from streams and rivers in the Anthropocene, Nat Clim Change, 10, 138–142, https://doi.org/10.1038/s41558-019-0665-8, 2019.

Zellweger, C., Emmenegger, L., Firdaus, M., Hatakka, J., Heimann, M., Kozlova, E., Spain, T. G., Steinbacher, M., Schoot, M. V. van der, and Buchmann, B.: Assessment of recent advances in measurement techniques for atmospheric carbon dioxide and methane observations, Atmos. Meas. Tech., 9, 4737–4757, https://doi.org/10.5194/amt-9-4737-2016, 2016.

Zhang, Z., Poulter, B., Knox, S., Stavert, A., McNicol, G., Fluet-Chouinard, E., Feinberg, A., Zhao, Y., Bousquet, P., Canadell, J. G., Ganesan, A., Hugelius, G., Hurtt, G., Jackson, R. B., Patra, P. K., Saunois, M., Höglund-Isaksson, L., Huang, C., Chatterjee, A., and Li, X.: Anthropogenic emission is the main contributor to the rise of atmospheric methane during 1993–2017, Natl. Sci. Rev., 9, nwab200, https://doi.org/10.1093/nsr/nwab200, 2021a.

Zhang, Z., Fluet-Chouinard, E., Jensen, K., McDonald, K., Hugelius, G., Gumbricht, T., Carroll, M., Prigent, C., Bartsch, A., and Poulter, B.: Development of the global dataset of Wetland Area and Dynamics for Methane Modeling (WAD2M), Earth Syst Sci Data, 13, 2001–2023, https://doi.org/10.5194/essd-13-2001-2021, 2021b.

Zhao, Y., Saunois, M., Bousquet, P., Lin, X., Hegglin, M. I., Canadell, J. G., Jackson, R. B., Hauglustaine, D. A., Szopa, S., Stavert, A. R., Abraham, N. L., Archibald, A. T., Bekki, S., Deushi, M., ockel, P. J., Josse, B., Kinnison, D., Kirner, O., 'ecal, V. M., O'Connor, F. M., Plummer, D. A., Revell, L. E., Rozanov, E., Stenke, A., Strode, S., Tilmes, S., Dlugokencky, E. J., and Zheng, B.: Inter-model comparison of global hydroxyl radical (OH) distributions and their impact on atmospheric methane over the 2000--2016 period, Atmospheric Chemistry and Physics, 19, 13701–13723, https://doi.org/10.5194/acp-2019-281, 2019.

Zhao, Y., Saunois, M., Bousquet, P., Lin, X., Berchet, A., Hegglin, M. I., Canadell, J. G., Jackson, R. B., Dlugokencky, E. J., Langenfelds, R. L., Ramonet, M., Worthy, D., and Zheng, B.: Influences of hydroxyl radicals (OH) on top-down estimates of the global and regional methane budgets, Atmos. Chem. Phys., 20, 9525–9546, https://doi.org/10.5194/acp-2019-1208, 2020.

This project has received funding from the European Union's Horizon Europe research and innovation programme under grant agreement No 101081395

Zhao, Y., Saunois, M., Bousquet, P., Lin, X., Hegglin, M. I., Canadell, J. G., Jackson, R. B., and Zheng, B.: Reconciling the bottom-up and top-down estimates of the methane chemical sink using multiple observations, Atmos Chem Phys, 23, 789–807, https://doi.org/10.5194/acp-23-789-2023, 2022.

Zscheischler, J., Mahecha, M. D., Avitabile, V., Calle, L., Carvalhais, N., Ciais, P., Gans, F., Gruber, N., Hartmann, J., Herold, M., Ichii, K., Jung, M., Landschützer, P., Laruelle, G. G., Lauerwald, R., Papale, D., Peylin, P., Poulter, B., Ray, D., Regnier, P., Rodenbeck, C., Roman-Cuesta, R. M., Schwalm, C., Tramontana, G., Tyukavina, A., Valentini, R., Werf, G. van der, West, T. O., Wolf, J. E., and Reichstein, M.: Reviews and syntheses: An empirical spatiotemporal description\hack\newline of the global surface--atmospherecarbon fluxes:\hack\newline opportunities and data limitations, Biogeosciences, 14, 3685–3703, https://doi.org/10.5194/bg-14-3685-2017, 2017.

Zwaaftink, C. D. G., Henne, S., Thompson, R. L., Dlugokencky, E. J., Machida, T., Paris, J.-D., Sasakawa, M., Segers, A., Sweeney, C., and Stohl, A.: Three-dimensional methane distribution simulated with FLEXPART 8-CTM-1.1 constrained with observation data, Geosci. Model Dev., 11, 4469–4487, https://doi.org/10.5194/gmd-11-4469-2018, 2018.

This project has received funding from the European Union's Horizon Europe research and innovation programme under grant agreement No 101081395

2. Good Practice Guidelines for Evaluating Emission Inventories Using Inverse Modelling Results

Authors: Sander Houweling[1,2], Christian Mielke[3], Lukas Häffner[3], Lara Abou Chehade[4], Hannes Witt[5], Margreet van Zanten[5], Marko Scholze[6], Thomas Kaminski[7], Rona Thompson[8]

Responsible partners: 1. VUA, 2. SRON, 3. UBA, 4. CMCC, 5. RIVM, 6. LUND UNIVERSITY, 7. THE INVERSION LAB, 8. NILU

Document History

Version	Date	Comment	Modifications made by
0.1	11-08-2026	First draft	Sander Houweling[1,2], Christian Mielke[3], Lukas Häffner[3], Lara Abou Chehade[4], Hannes Witt[5], Margreet van Zanten[5], Marko Scholze[6], Thomas Kaminski[7]
0.2	19-10-2026	Second draft complete	Sander Houweling[1,2], Christian Mielke[3], Lukas Häffner[3], Lara Abou Chehade[4], Hannes Witt[5], Margreet van Zanten[5], Marko Scholze[6], Thomas Kaminski[7], Rona Thompson[8]
1.0	22-10-2026	Final formatted version	Lara Abou Chehade[4]

This project has received funding from the European Union's Horizon Europe research and innovation programme under grant agreement No 101081322

Table of Contents

DOCUMENT HISTORY 2

1. PURPOSE AND AUDIENCE 4

2. INVERSE MODELLING 4

2.1. Inverse modelling theory 4

2.2. Atmospheric constraints on surface fluxes 8

2.3. A posteriori fluxes 9

2.4. Inversion methods 11

2.4.1. Domain size 11

2.4.2. Control vector size 12

2.4.3. Measurements 13

3. COMPARING INVERSE MODELLING RESULTS TO INVENTORY DATA 14

3.1. Comparison of national total emissions 14

3.2. Emission trends and seasonal variability 16

3.3. Comparison of gridded emissions 17

3.4. Comparison of sectoral information 17

4. TECHNICAL ASPECTS OF USING INVERSE MODELLING RESULTS 18

4.1. Inversion data for inventory compilers 18

4.2. Tools specifically developed and tailored for inventory compilers 18

4.2.1. The AVENGERS Python tools 18

4.2.2. The AVENGERS Flexible Inversion Tool for Inventory Compilers 20

4.3. Overview of open-source tools 22

5. FURTHER READING 24

6. ACKNOWLEDGEMENTS 24

7. REFERENCES 25

This project has received funding from the European Union's Horizon Europe research and innovation programme under grant agreement No 101081322

1. Purpose and Audience

These good practice guidelines support greenhouse gas emission inventory compilers - and experts who want to start using information from atmospheric inverse modelling - to evaluate and improve their inventories. The focus is primarily on national greenhouse gas emissions. However, the methods described and principles explained here also apply to the assessment of greenhouse gas emissions at larger scales (e.g. the EU27) or smaller scales (e.g. cities), as well as to air pollutants. This guideline document assumes that output from atmospheric inverse modelling is available from some external source already and discusses how to use and interpret that information. Readers interested in setting up and performing atmospheric inverse modelling are referred to the companion document "Good Practice Guidelines for Atmospheric Inversions to Support Greenhouse Gas Emission Reporting", which provides guidelines for the implementation of inverse modelling methodology and how to evaluate its results. This document on the use of inverse modelling results starts with an explanation of the basics of inverse modelling (Section 2), covering the essentials needed to understand inverse modelling methods and interpret their results correctly. This introductory section is followed by advice on how to use inversion output (Section 3), which links to Section 10 of the atmospheric inversion guidelines. Section 4 presents open-source tools that have been developed by inverse modellers and inventory compilers to facilitate the analysis of inverse modelling output. They can also be used to learn more about inverse methods and gain hands-on experience. This is followed by suggestions for further reading in Section 5.

2. Inverse Modelling

2.1. Inverse modelling theory

Atmospheric inverse modelling (also called "flux inversions" or "atmospheric transport inversions") refers to the use of atmospheric measurements to support the quantification of surface fluxes of atmospheric constituents. The surface flux is defined as the amount of a constituent that is emitted into the atmosphere (a source) or taken up from it (a sink) per unit area and time. In the context of these guidelines, the constituents are long-lived greenhouse gases. The methods are motivated by the difficulty of directly measuring fluxes at larger scales.

The approach of multiplying activity data by emission factors that emission inventories use is, in essence, an extrapolation of information, obtained for example from laboratory or field experiments (the emission factors), to spatio-temporal scales of interest (e.g. national annual emissions). When scaling up emissions in this way, implicit assumptions have to be made due to missing information, which introduce uncertainties that are difficult to quantify. To assess the validity of the upscaling methodology and evaluate the emission inventory, independent estimates are needed at aggregated scales. The annual emissions of a country would be a useful example of an aggregate scale since it is so important for monitoring policies.

This project has received funding from the European Union's Horizon Europe research and innovation programme under grant agreement No 101081322

Atmospheric measurements of greenhouse gas abundances from regional monitoring networks provide a suitable independent source of information on surface fluxes for the evaluation of emission inventories. This is because they are particularly sensitive to the net surface flux summed over a larger area. This is true not only for sums in space, but also in time, because of the flow and mixing of the atmosphere between the surface fluxes and measurement locations. The mixing ratio is used as a measure of greenhouse gas abundance. It is the ratio between the number of molecules of a greenhouse gas and that of dry air (primarily consisting of N_2 + O_2) in the sampled air volume, often expressed as parts per billion (ppb) or parts per million (ppm).

For an inert gas, the difference between the mixing ratios that are observed upwind and downwind of a region quantifies the net surface flux in that region (see Figure 2.1). This atmospheric constraint on the size of the flux is often referred to as a "top-down" approach, as opposed to the "bottom-up" approach used in emission inventories, which adds up all known sources and sinks in the region.

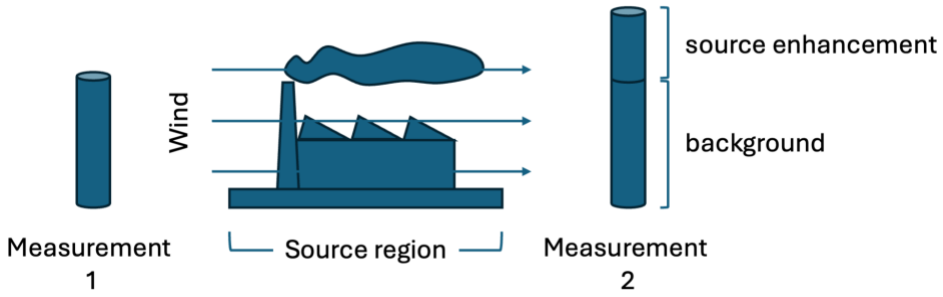


Figure 2.1 A downwind–upwind mixing ratio difference quantifies the integrated emission from a source region located in between.

Most long-lived greenhouse gases are inert on the time scale of regional transport from emission sources to measurement points. Therefore, for simplicity, atmospheric chemical transformation will be ignored in this introduction. The distance between measurement points can be up to several hundred kilometres, resulting in an irregular path across the flux region to the measurement location. Despite this complication, mixing ratio differences observed in a measurement network contain useful information about surface fluxes within the domain of the network. The atmospheric inverse modelling method has been developed to transfer the information in these atmospheric measurements to corresponding constraints on surface fluxes. This requires information on the transport of the gas of interest from the sources to the observation points. For this, we need an atmospheric transport model that simulates the atmospheric dispersion of gases based on meteorological information.

Suppose we use an atmospheric transport model and feed it fluxes from an emission inventory and meteorological information to simulate the corresponding increase in the mixing ratio observed at a measurement site (the so-called mixing ratio enhancement). If the measurement and the simulated atmospheric transport were exact, then a mismatch between the simulated and observed mixing ratio enhancements would point to errors in the emission inventory.

This project has received funding from the European Union's Horizon Europe research and innovation programme under grant agreement No 101081322

In inverse modelling, an optimization algorithm is used to find the flux adjustment that results in the best agreement between the simulated and measured mixing ratios. Here, "inverse" refers to a reversed cause-and-effect relationship between surface fluxes and the mixing ratio changes they cause. If a (forward) model computes the mixing ratio change that is caused by a surface flux, then the inverse model computes the surface flux that explains the mixing ratio change (see Figure 2.2).

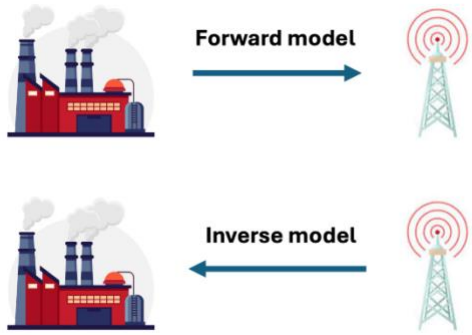


Figure 2.2: Forward and inverse modelling.

In real applications of inverse modelling, the problem is that neither the transport model nor the measurements are exact. To deal with this, the emissions and atmospheric measurements are treated statistically. Each variable (measurement or emission) is represented by a probability density function (PDF). The solution of the inverse problem is then the most plausible combination of mixing ratios and emissions that is consistent with atmospheric transport (as represented by the transport model). Here "most plausible" is defined statistically as the point of the joint emission-measurement PDF constrained by atmospheric transport that has the highest likelihood (see Box 1).

For Gaussian PDFs, the maximum likelihood solution of the inverse problem corresponds to the minimum of the cost function ***J(x)***,

$$J(x) = 1/2(y - \mathrm{H}(x))^{\mathrm{T}}\mathrm{R}^{-1}(y - \mathrm{H}(x)) + 1/2(x - x_0)^{\mathrm{T}}\mathrm{B}^{-1}(x - x_0) \qquad \text{eq. 2.1}$$

where the vector ***x*** contains the fluxes to be estimated using the measurements in vector ***y***. More details about the contents of vector ***x*** will be given in section 2.4. **H** represents the atmospheric transport model mapping ***x*** (fluxes) to ***y*** (measurements). The other variables will be explained later. The first right-hand-side term of equation 2.1 measures the difference between the forward model simulation (**H**(***x***)) and the measurements (***y***). This term is reduced when the model is brought into closer agreement with the measurements. The second right-hand-side term quantifies the deviation of the fluxes ***x*** from a first guess $\boldsymbol{x_0}$, also called a priori fluxes. The first guess is the flux that is expected without considering any atmospheric information. For anthropogenic emissions, it is usually taken from an emission inventory. The second right-hand-side term avoids that the solution of the inversion is inconsistent with the a priori information, as large deviations in ***x*** from $\boldsymbol{x_0}$ increase ***J(x)***, which the inversion tries to minimize.

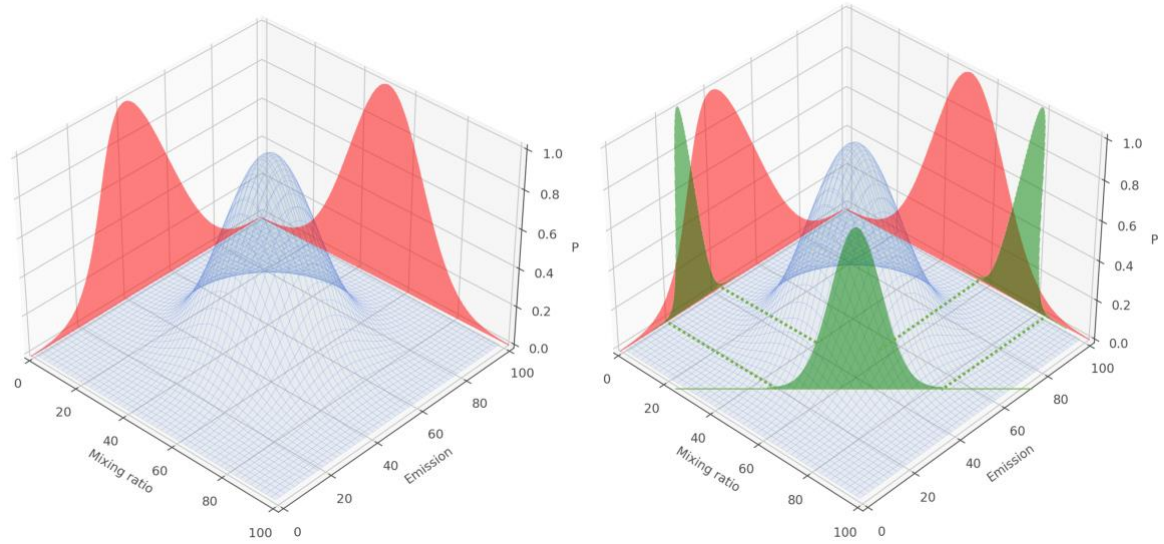
This project has received funding from the European Union's Horizon Europe research and innovation programme under grant agreement No 101081322

Finally, **R** and **B** are covariance matrices that represent the uncertainties of the model-measurement comparison (i.e. the sum of model and measurement uncertainty) and the uncertainty of the a priori emissions, respectively. These matrices weigh the differences in both right-hand-side terms according to their uncertainty (small uncertainty means high weight and vice versa).

The so-called a posteriori fluxes $\boldsymbol{x}_{apos}$ are those that minimize $\boldsymbol{J(x)}$ and are the best compromise between (1) simulating the observed mixing ratios, while (2) deviating as little as possible from the first guess. These a posteriori fluxes represent the statistically most likely solution of the inverse problem. The uncertainty of $\boldsymbol{x}_{apos}$ is quantified by the curvature of $\boldsymbol{J(x)}$ at its minimum (the narrower the cost function minimum, the more precisely $\boldsymbol{x}_{apos}$ is quantified and the smaller its uncertainty). In practice, it is difficult to represent the transport model uncertainties in **R**. The best, but computationally costly, representation of transport model uncertainties is obtained by solving the inverse problem using an ensemble of transport models.

Box 1: A graphical representation of the a posteriori flux as the maximum likelihood point in the transport model constrained joint probability function.

The a posteriori solution of an inverse problem is at the optimum of a probability density function that combines the information in the a priori fluxes, the measurements and the transport model that are used. The minimum of the cost function in equation 2.1 corresponds to this optimum. The figures below provide a graphical representation of the a priori information (left) and the a posteriori solution (right) for the simplified case of a single emission source and a single measurement.



Left: The joint probability (blue) of a priori emission and measurement probabilities (both in red). Right: The transport model constrained joint probability (green cross section of the blue joint probability) and the inferred a posteriori probability of both the emission and the mixing ratio measurement (green projections on the emission and mixing ratio axes). The transport model constrained joint probability represents the combinations of emissions and measurements that are consistent with the atmospheric transport model.

This project has received funding from the European Union's Horizon Europe research and innovation programme under grant agreement No 101081322

Note that mixing ratio enhancements due to emissions are relative to background mixing ratios. Background mixing ratios would be observed in the absence of the emissions that are estimated by the inversion. In regional inverse modelling, these are the mixing ratios that are prescribed at the boundaries of the simulated domain. Usually, they are co-optimized with the emissions. Initial mixing ratios, at the start of the simulation, can be co-optimized too. However, it is more common to use a spin-up (and spin-down) period to remove the ends of inversion-optimized time series. Section 2.3 provides further information on the methods that are used for solving equation 2.1.

2.2. Atmospheric constraints on surface fluxes

Atmospheric inversions for estimating greenhouse gas fluxes use observations from measurement networks and/or satellite remote sensing. Ground-based networks include, e.g., the Integrated Carbon Observing System (ICOS) in Europe or the Global Atmosphere Watch (GAW) program of the World Meteorological Organization (WMO) with measurement sites around the World. Figure 2.3 shows a picture of the measurement tower in Cabauw, the Netherlands, and a map of the ICOS stations in Europe. Since these networks are sparse, sites are selected at large distances from strong local sources so that the measured mixing ratios represent scales that are large enough to avoid unobserved gaps in the network. This approach supports regional flux estimation but limits the spatial resolution that can be achieved (e.g. if one were to measure upwind and downwind of a single farm, the resolution would obviously be higher).



Figure 2.3: The measurement tower in Cabauw, the Netherlands (left) and a map of the locations of the ICOS atmospheric stations across Europe (red dots, right). Source: https://www.icos-cp.eu.

In recent years, a growing number of satellites have been providing a wealth of global data on the abundance of greenhouse gases (e.g., NASA OCO-2/3 for CO_2, and S5P TROPOMI for CH_4), measuring the so-called column-averaged mixing ratio. Here "column" refers to the vertical column of air from the surface to the top of the atmosphere that a satellite sees.

This project has received funding from the European Union's Horizon Europe research and innovation programme under grant agreement No 101081322

Since the vertical column spans the entire atmosphere, local emissions cause only small enhancements in satellite-observed columns (of the order of 1 ppm enhancement in CO_2 for a big city). For this reason, the power of regional satellite measurements to resolve fluxes is rather small. An important exception is high-resolution satellites for detecting methane leakages from single facilities. However, these only work for strong local sources.

The constraint of atmospheric data on surface fluxes is quantified by the uncertainty reduction that an inversion can achieve. If the uncertainties of an a priori and a posteriori flux are σ_0 and σ_{apos}, then this uncertainty reduction is defined as $(\sigma_0 - \sigma_{apos})/\sigma_0$ x 100%. The uncertainty reduction is highest for fluxes that are best observed by the measurement network. Importantly, uncertainty reduction increases with the spatio-temporal scale of the flux that is estimated. This means that larger regions and longer time spans can be better constrained than smaller regions and shorter time spans. This is because emissions from a larger region are detectable in a larger number of measurements and are therefore better observed. In regional inverse modelling, the spatial resolution is limited to a few hundred kilometres for seasonal fluxes in the best observed part of the ICOS network.

The large scales that are resolved by inverse modelling limit its capacity to distinguish between emissions from different source sectors. Sectorial attribution can only work if emission sectors are separated in space or time at scales that the inversion can resolve, which is usually not the case. If the a priori flux uncertainty differs strongly between sectors, then the inversion will attribute emission adjustments by design to the most uncertain sector (see section 2.2). Because of this, CO_2 inverse modelling usually attributes flux adjustments to natural processes or the LULUCF sector, since emissions from fossil fuel burning have a much smaller uncertainty. The combined use of measurements of co-emitted gases or isotopes in inversions is under development, and has the potential to improve the sectoral attribution. In the case of methane, for example, a source that also emits ethane points to a fossil source, and a joint methane-ethane inversion can use this to separate biological and fossil sources of methane. For strong local emissions of methane, high-resolution satellites can reach the resolution needed to uniquely identify emission sources.

2.3. A posteriori fluxes

From the discussion in the previous section, it follows that the results of inverse modelling can only be used to evaluate an emission inventory for fluxes that are sufficiently well detected by the atmospheric measurements. The so-called a posteriori flux uncertainty covariance matrix provides important information on whether this is the case. This matrix contains the a posteriori uncertainty of each flux and how these uncertainties are correlated between fluxes. It is computed from the curvature (second derivative) of the cost-function as explained in Section 2.1. The fluxes should show a significant uncertainty reduction compared to the a priori flux uncertainty; otherwise, the atmospheric measurements did not provide enough information. The a posteriori uncertainty covariances are also important, because they indicate whether the inversion can estimate fluxes in one region independently from fluxes in neighbouring regions. Flux inversions generally cannot resolve country borders. If inversion-derived flux

This project has received funding from the European Union's Horizon Europe research and innovation programme under grant agreement No 101081322

adjustments (the difference between a priori and a posteriori) are sensitive to the country mask that is used to obtain country totals, then this sensitivity adds to the uncertainty of the flux adjustment for a country. This is because the inversion cannot localize a required flux adjustment well enough to tell on which side of the border it is needed.

Due to the use of a priori fluxes, the a posteriori fluxes that are obtained from inversions are not independent estimates of those fluxes. While atmospheric measurements provide independent information on greenhouse gas fluxes, the mapping of this information onto the fluxes depends on the a priori fluxes. The flux adjustment that is needed to match the atmospheric measurements reflects the independent information carried by the measurements and is therefore more independent of the a priori fluxes than the a posteriori flux is. For this reason, the emission inventory to be evaluated should preferably be used as a priori fluxes. If other a priori fluxes are used, then the comparison between the a posteriori fluxes and the inventory is compromised by the difference between the a priori fluxes used in the inversions and the inventory being evaluated.

The spatial or temporal pattern of the a posteriori fluxes below the scale that is resolved by the inversion stems from the a priori fluxes. For this reason, the a posteriori fluxes often reproduce the exact location of local emissions – which might seem impressive but is explained largely by the a priori. A useful measure of inversion performance is the flux uncertainty reduction; the larger the uncertainty reduction, the stronger the influence of the measurements and the more independent the estimated flux is from its a priori starting point.

Because of the importance of transport model uncertainty, it is advisable to compare results of flux inversions that use different transport models to test if flux adjustments are robust to the transport model that is used.

If mixing ratio output is available from a forward model run using a posteriori fluxes (the simulated mixing ratio at the measurement stations, see section 2.1), then it is advised to check the fit of the inversion to measurements at sites in the vicinity of the adjusted emissions. If the inversion fails to reproduce these measurements within their uncertainty, this is a sign that the transport model fails in the transfer of measurement information to the fluxes. This test is useful for independent measurements as well as measurements that are used in the inversion. If the inversion significantly improves the fit to independent data compared with the a priori simulation, then this is a strong indication that there is a problem in the a priori fluxes. As an example, Figure 2.4 shows the time series of the a priori, a posteriori, and measured CO_2 mixing ratios at the Torfhaus station in Germany for the year 2022, from an inversion with the LUMIA system (using FLEXPART as atmospheric tracer transport model). At this site, the fluxes improve the fit to the observations compared with the a priori fluxes.

This project has received funding from the European Union's Horizon Europe research and innovation programme under grant agreement No 101081322

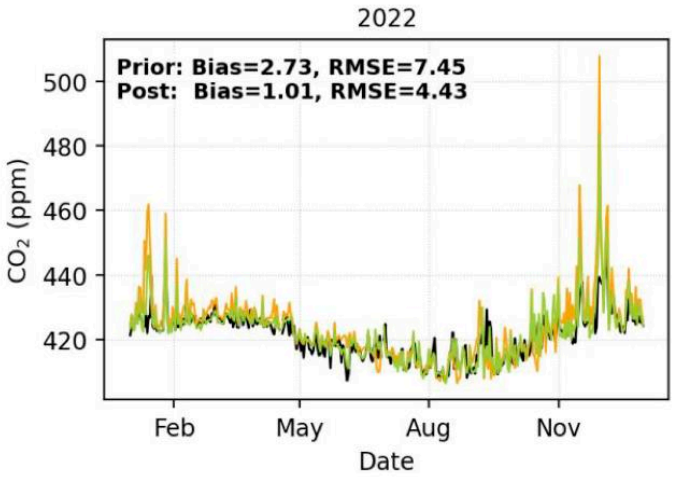


Figure 2.4: Hourly time series of a priori (orange line) and a posteriori (green line) CO_2 mixing ratios simulated by FLEXPART at Torfhaus (TOH) station (German ICOS station) compared with the measured mixing ratios (black line), along with the associated bias and RMSE.

As discussed in section 2.1, inversion-derived flux adjustments address the sum of all emission sectors, unless the inversion setup is designed to obtain sector-specific information (using additional information such as isotopes or co-emitted gases). If the inversion setup distinguishes different sectors without measurements that support their distinction, then the flux adjustment is usually distributed over all sectors weighted by the a priori uncertainty of each sector.

If the target gas has important atmospheric sinks (such as for CH_4) or is removed by atmospheric deposition (e.g. in the case of aerosols), this needs to be accounted for in the atmospheric transport model. The a posteriori flux will be sensitive to errors in the sink term, which are difficult to distinguish from errors in the sources (again, the sum of both errors can be estimated, but process attribution is difficult). Note that in regional inversions of long-lived greenhouse gases such as CH_4, the contribution of the atmospheric sink is often small enough to be neglected.

2.4. Inversion methods

A wide variety of inversion methods exist and can be found in the literature. A comprehensive overview of those methods explaining the technical differences between inversion systems is outside of the scope of this document (more information can be found in Section 2 of the companion document "Good Practice Guidelines for Atmospheric Inversions to Support Greenhouse Gas Emission Reporting"). The aim of this section is to provide general information on inversion methods that is relevant for the use and interpretation of inversion-optimized fluxes.

2.4.1. Domain size

The size of the domain that is used in inverse modelling ranges between that of a single emitting facility and the whole Earth. Because of computational costs, there is a trade-off between the domain size and the spatial resolution of the transport model that is used; the smaller the domain, the higher the resolution that can be achieved. The resolution at which the inversion estimates fluxes is often coarser than the resolution of

This project has received funding from the European Union's Horizon Europe research and innovation programme under grant agreement No 101081322

the transport model that is used. In this case, the flux to be estimated spans several model grid boxes (in space and time). The inversion then scales the flux pattern spanned by these boxes. The pattern comes from the dataset that is used as a priori and is not modified by the inversion. Nevertheless, the details of this pattern matter for the quality of the transport model simulation, which is why inverse modellers are generally keen on obtaining details on emission locations and time profiles at high resolution from inventories.

Global modellers do not need to worry about spatial domain boundaries, which is an important advantage compared with regional models. Mixing ratios at the domain boundaries of regional models are taken from global models and can be optimized further. Subtle differences in atmospheric transport at the domain boundaries between the global model that supplies those boundaries and the regional model that needs them can affect the optimized regional emissions (particularly those in proximity to domain boundaries). To overcome the spatial resolution limitation of global models, zoom models that provide enhanced resolution over a region of interest are used. Below a few kilometres resolution, different physics needs to be included in the model, because it starts to resolve phenomena such as clouds and turbulence that are taken care of by subgrid parameterizations in coarse resolution models. Because of this, there is a limit to the use of global zoom models.

Atmospheric transport models either use precomputed meteorology from a weather forecasting model ("offline" models), compute their own weather ("online models"), or combine these by steering the computed meteorology to that of a weather forecasting model (through a method called nudging). Since the resolution of weather forecasts is limited, the combined option has the advantage that local weather conditions can be simulated more precisely (a high-resolution model nudged to a lower resolution forecast). There is a trade-off with computation time (and hence domain size) since online models are computationally more expensive to run.

Depending on the size of the domain for which inversion-estimated emissions are needed, global, regional, or high-resolution turbulence-resolving models may be required. When comparing inversion results to inventories, it is good to check if a suitable model was used. For example, a typical global inversion without zooming provides insufficient resolution to estimate fluxes from individual European countries.

2.4.2. Control vector size

In inverse modelling computer programs, the control or state vector contains the parameters that are optimized (***x*** in equation 2.1). It consists of parameters representing the flux of a certain region during a certain time interval. The size of the control vector depends on the definition of those regions (in space and time). The more regions and time intervals, the higher the computational costs and the larger the degree of detail at which the inversion can modify the fluxes. A too low degree of detail may compromise the fit to the measurements and may lead to biased a posteriori emission estimates. A too high degree of detail may lead to over-fitting of the measurements and unrealistic fine-scale fluctuations in the emission adjustments (often referred to as dipoles because of upward and downward adjustments that are right next to each other). The optimal compromise depends on the information content of the measurements, which varies with distance

This project has received funding from the European Union's Horizon Europe research and innovation programme under grant agreement No 101081322

from the measurement location. Some inversion methods adapt the region size to the information content within the measurement network. In this case, the region size increases with the distance from the measurement points. Alternatively, emissions can be optimized at the highest spatial resolution (of the model grid) in combination with spatial and temporal correlation length scales. These correlation length scales provide adjustable constraints on the flexibility of the inversion to modify the emission pattern. They are specified in the a priori uncertainty covariance matrix (**B** in equation 2.1). A high correlation between the a priori uncertainties of two neighbouring flux regions means that if one flux is underestimated, then the neighbouring flux is likely to be underestimated also. As a result, these fluxes will likely be modified in the same manner.

When using a posteriori emissions from an inversion to evaluate an emission inventory, it is advised to check that the setup of the inversion and the definition of the state vector are appropriate for the inventory that is evaluated. For example, if the region size exceeds the size of a country, then the inversion cannot resolve the flux from that country.

2.4.3. Measurements

The ground-based measurements used in inversions are usually from measurement networks that provide datasets spanning several years. The global WMO GAW measurement network provides data, predominantly from remote measurement sites that represent background conditions. Ambient air samples are collected in flasks that are sent to central laboratories for analysis. The sampling frequency varies between sites but is usually rather low (about once a week). The global network is designed to monitor large-scale trends in greenhouse gases. Global inversions using these data estimate fluxes over large subcontinental regions.

Inversions for estimating national greenhouse gas fluxes use measurements from regional monitoring networks (such as ICOS in Western Europe). In this case, samples are collected continuously from tall towers (100 m or higher) and are analyzed using locally installed greenhouse gas monitors (see Figure 2.3). This allows short-term mixing ratio variations to be measured, which are critical for estimating regional fluxes. The number of towers in regional networks is limited and unevenly distributed over the domain that is monitored. The performance of regional inversions varies within the domain of the regional network. For countries in the periphery of the network, the gain from using atmospheric measurements will inevitably be less. Without measurement information, the inversion will return the a priori fluxes. In the periphery of the network, however, the a posteriori fluxes might rather deviate from the a priori in compensation for transport errors from elsewhere in the domain.

Satellites improve the measurement coverage in places where surface networks provide insufficient observational constraints. However, inversions using satellite data have their own challenges related to the variable data coverage, because of the cloud free conditions that are required, and retrieval errors that are correlated with the measurement conditions (surface albedo, sun angle, etc.). Currently, the most reliable quantification of emissions using satellites is for large local emissions that are within the detection range of high-resolution satellites.

This project has received funding from the European Union's Horizon Europe research and innovation programme under grant agreement No 101081322

When using a posteriori emissions from an inversion to evaluate an emission inventory, it is advised to verify the source of measurement data that was used, to judge whether it provides suitable information for the inventory being evaluated. For example, using only weekly measurements from background sites of the global monitoring network provides little information on the emission from a western European country.

Table 2.1 lists public archives that provide inversion results. Section 4.2 discusses tools that are available to start using these data.

Table 2.1: Public archives of inversion-optimized emissions.

Archive	Target gas	Target application	URL
CAMS reanalysis	CO_2, CH_4, N_2O	Sub-continental trends and interannual variability	https://ads.atmosphere.copernicus.eu/datasets/cams-global-greenhouse-gas-inversion?tab=overview
CAMS facility scale	CH_4	Facility-scale methane emissions from satellites	https://apps.atmosphere.copernicus.eu/overview?app=methane-explorer
GCP RECCAP2	CO_2, CH_4, N_2O	Sub-continental trends and interannual variability	https://www.globalcarbonproject.org/reccap/overview.htm
ICOS-CP	CO_2, CH_4	National-scale emissions for Europe	For CO_2: https://www.icos-cp.eu/data-products/G068-1T09 For CH_4: https://meta.icos-cp.eu/collections/eqtmTg6COhmsz2YAA_yDuqQy

3. Comparing inverse modelling results to inventory data

The comparison of inverse modelling results to emission inventories may provide valuable insights into the quality of the emission inventory and may indicate points for further development. For inverse modelling data to provide actionable insights, which may lead to an update of the emission inventory, it is necessary to accurately identify the origin of any differences. Therefore, it is helpful to compare the data on different levels, from comparing national total emissions, their spatial distribution, and their variability over time to sectoral disaggregated emissions.

3.1. Comparison of national total emissions

The starting point for most comparisons between national greenhouse gas inventories and inverse modelling results is a comparison of national total emissions. Depending on the format of the inverse modelling output, national total emissions must be calculated by selecting grid cells within the country borders for the country of interest.

This project has received funding from the European Union's Horizon Europe research and innovation programme under grant agreement No 101081322

Although this comparison seems straightforward, there are a couple of points to pay attention to:

- Posterior emissions from inversions are usually provided on a spatially resolved grid and need to be aggregated to the national scale by summing up emissions within the country borders. The same country map should be used for all analyses to ensure consistency. Attention needs to be paid to emission sources that are located close to national borders, as these emissions might be assigned to the wrong country, leading to additional uncertainties (for a more detailed discussion, see Section 10.4.1 of the companion document).
- It is good practice to include the a priori emissions in the comparison between a posteriori emissions and inventory data, as well as the a priori and a posteriori uncertainties (see Figure 3.1). This is because the a posteriori estimate is not independent of the a priori (see Eq. 2.1). The degree of dependence on the a priori is determined by the number of observations and their certainty in relation to the uncertainty in the fluxes that are optimized. It can be gauged from the a posteriori uncertainty and uncertainty reduction (see the discussion on this in Section 2.3). For instance, if there is already a significant discrepancy between a priori and inventory emissions, this might already explain differences between a posteriori and inventory emissions.
- It is good practice to include the outputs of several different inverse modelling setups in the same comparison if available. Discrepancies between a posteriori fluxes of different runs provide useful additional information on the a posteriori flux uncertainties. The individual inversion results should, however, be benchmarked beforehand to determine their quality and suitability for inclusion in the comparison (see also Section 9 of the companion document). The Flexible Inversion Tool for Inventory Compilers, presented in Section 4.2.2, provides examples of different inversion setups and allows the assessment of their impact on the inversion results.
- A posteriori emissions from inverse modelling may include emissions not accounted for in the emission inventory. This might, for example, concern natural emissions of methane or carbon dioxide emissions. It is important to ensure that the comparison is consistent concerning the emission sectors and processes that are accounted for.

Differences between inventory emissions and inverse modelling results may havevarious reasons. Besides over- or underestimation of known emission sources, they could also point to missing emission sources in the inventory. However, it should also be noted that both emission data from inverse modelling as well as emission inventories are estimates with their respective uncertainties, and observed differences do not automatically indicate mistakes in the inventory but may also be caused by uncertainties in the inverse modelling method (for example, due to transport model errors).

This project has received funding from the European Union's Horizon Europe research and innovation programme under grant agreement No 101081322

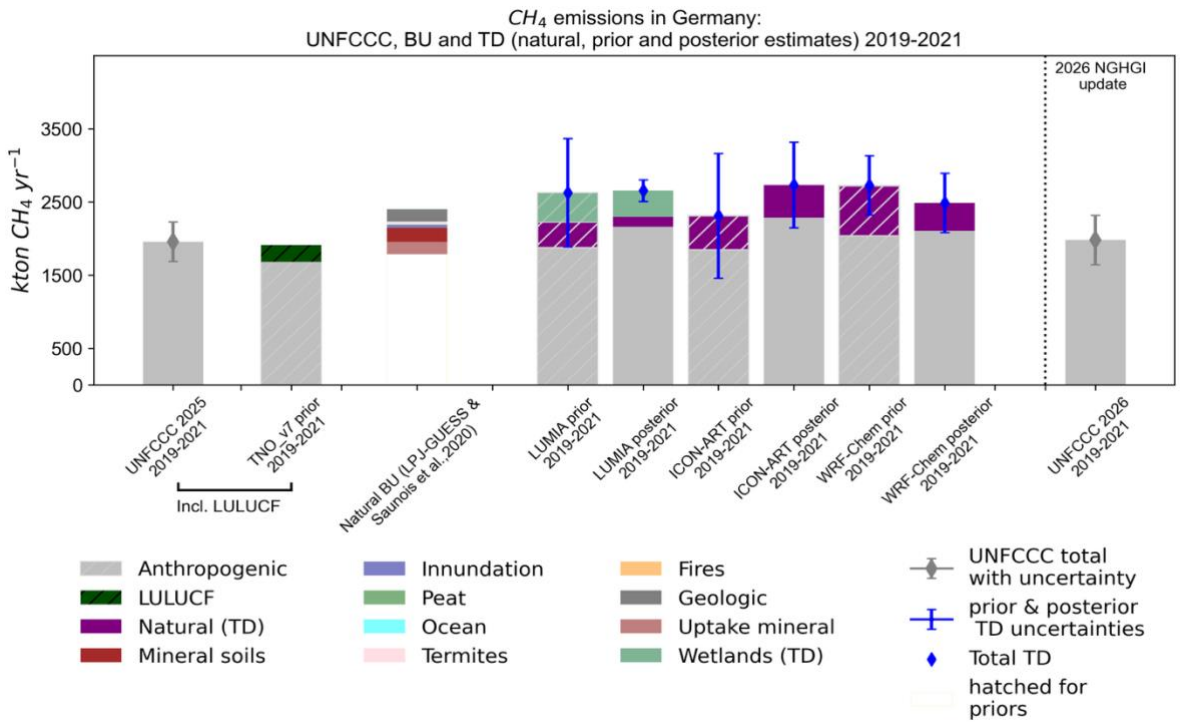


Figure 3.1: Example of a comparison between inventory-reported and inversion-derived methane emissions in Germany, including the official reporting (UNFCCC 2025 and updated 2026 in grey diamonds with reported uncertainties), other inventories (TNO_v7, LPJ-GUESS and Saunois et al., 2020) and the a priori and a posteriori emissions of different inversions (LUMIA, ICON-ART and WRF-Chem) with their sectoral partitions.

3.2. Emission trends and seasonal variability

It may be very instructive to analyse temporal variations in emissions. Comparing the long-term emission trend spanning several years is important as emission inventories and inversions yield more robust results for trends than for means. Trends and percentage changes from year-to-year are also commonly targeted by policies. Trend analyses do require long time series (~10 years), for example because of the inter-annual variability in natural fluxes. However, the consistency of such time series should be checked, as changes in the configuration of the measurement network over time can affect inversion-derived trends. A jump in the uncertainty reduction may be a sign that such changes occurred. It is also useful to compare the year-to-year variability of emissions, which might point to natural fluxes responding to climatological variations or anthropogenic emissions influenced by fluctuations in economic activity.

Next to the annual variability, it is also useful to compare the seasonal cycle of emissions. As most inventories calculate only annual emissions (as this is the required temporal resolution in the reporting), this comparison can be based on process knowledge about major emission sources. Alternatively, one can use temporal emission profiles, as provided for example by CAMS-TEMPO (Guevara et al., 2021), to infer seasonal emissions from an annual inventory. Note that the uncertainty in inverse modelling-derived seasonal cycles can be reduced by averaging multiple years.

This project has received funding from the European Union's Horizon Europe research and innovation programme under grant agreement No 101081322

3.3. Comparison of gridded emissions

Besides emission variations, it is instructive to analyse where emissions take place by comparing the spatial distribution of emissions to identify underlying causes of discrepancies. For example, inverse modelling emissions of sulphur hexafluoride emissions over the Netherlands indicated emissions in the South of the Netherlands, which did not relate to any known emission source but could be linked to AWACS airplanes stationed at the NATO airbase Geilenkirchen in Germany (van der Net et al., 2026). It should be noted that the spatial distribution of the a posteriori emissions can be strongly influenced by the spatial distribution of the prior emissions. Therefore, deviations between the spatial distribution of a posteriori and a priori emissions provide particularly valuable information.

The comparison of spatial emissions is straightforward if the emission inventory provides gridded emissions that may directly be compared to emission maps from inverse modelling. Differences in map projection or resolution might complicate this comparison. In this case, it is helpful to resample both datasets to a common grid. Such maps facilitate the calculation of difference maps or the correlation between the two gridded datasets. It is important to use a regridding algorithm that conserves total emissions.

If national inventory data are not available as gridded maps, then inverse modelling-estimated emission maps can also be compared to proxy data. Projecting a posteriori emissions on a geographical map could also be effective in identifying known sources. Alternatively, global emission datasets can be used such as CAMS-REG-ANT (Kuenen et al. 2022) or CAMS-REG-GLOB (Soulie et al. 2024), which provide gridded data based on national reporting.

Special attention should be paid here to large emission intensities in grid cells crossing national borders. These are usuallydistributed between different countries based on surface area. If the emissions are in reality only occurring on one side of the border, this can lead to discrepancies in the national total emissions. Comparing these emissions to known emission sources in this grid cell can help to identify their origin and improve their attribution (see Section 3.1).

3.4. Comparison of sectoral information

If inverse modelling output provides a sectoral split, this can greatly facilitate the identification of problematic source categories. This requires the consideration of the following points:

- Different sectoral definitions exist that may lead to appreciable deviations in the included emissions. Therefore, it is important to perform a country-specific sector check to ensure a truthful comparison.
- Inverse modelling may provide sectoral information based on co-emitted species, the isotope profile, sectoral differences in the timing of emission, or the sectorial split according to the a priori emissions. When it is based on the sectoral split of the a priori emissions, the sectoral split of a posteriori emissions is not independent of the sectoral split of the inventory and should be considered with

This project has received funding from the European Union's Horizon Europe research and innovation programme under grant agreement No 101081322

caution. Even if isotopes or co-emitted compounds are used, the a priori emission pattern is also used, compromising the independence.

4. Technical aspects of using inverse modelling results

Inventory agencies who would like to use inverse modelling results need an entry point in their annual inventory reporting cycle to do so. The IPCC Refinements (IPCC, 2019) on quality assurance/quality control (QA&QC) offer guidance for inventory compilers on how to approach this. However, the IPCC Refinements do not provide a detailed technical recipe on how to use inversion data for inventory evaluation. This section provides guidance and a description of openly available, pre-developed tools to facilitate the use of inversion data. Depending on the skill set of the user, these tools differ in complexity and required computing experience.

4.1. Inversion data for inventory compilers

There is a technical barrier to the use of the output of atmospheric inverse models directly. Since these data sets have a higher dimensionality (at least two spatial coordinates and a time coordinate), they can become quite large. This led to the adoption of a specialized data format in atmospheric science, NetCDF, which might be unfamiliar to inventory compilers and, hence, may pose an additional barrier towards using inversion results. These files should, in principle, be fully documented and can be read and opened with many commonly used software packages. For example, GIS software can natively process NetCDF files. In addition, Python packages (xarray, gdal) and R libraries (Raster, Terra, Ncdf4) allow using these established data science tools to read and analyze NetCDF files. There are also simpler tools such as Panoply (NASA GISS, 2026) for inspection and visualization of the content of such NetCDF files.

Besides loading the data, the next technical challenge lies in extracting emission data that is comparable to inventory data, i.e., calculating a national yearly emission total instead of daily or monthly fluxes on a spatially resolved grid. These operations might seem straightforward but can have intricate details. For this, we would usually recommend using established software (e.g., GIS software) or Python/R-packages.

As a final note, one needs to pay attention to the units used in the data. While emission inventories report emissions usually in units of weight, like kg, kt or Mg per year, inverse modelling outputs are often reported as particle fluxes in units of mol/m^2/s (but also particle numbers or the mass of carbon in CO_2 or CH_4 are sometimes used). That means one needs to convert them considering the molar mass of the gas, the area of interest and the number of seconds in a year (in the case of mol/m^2/s), where leap years need to be considered as well.

4.2. Tools specifically developed and tailored for inventory compilers

4.2.1. The AVENGERS Python tools

In the Avengers project (https://avengers-project.eu/), the inventory makers involved identified the support that they would need to be able to make use of atmospheric inversion output data (see box 3 of Mielke et al., 2024).

This project has received funding from the European Union's Horizon Europe research and innovation programme under grant agreement No 101081322

This led to the development of the Avengers Analysis Tool for Inventories in PYthon REcipeS (AVANTI-PYRES). These tools support inventory compilers in comparing their data with other third-party data sources such as:

1. Global inversion data products from the atmospheric datastore of CAMS (https://ads.atmosphere.copernicus.eu/datasets/cams-global-greenhouse-gas-inversion?tab=overview),
2. The Emissions Database for Global Atmospheric Research - EDGAR (https://edgar.jrc.ec.europa.eu),
3. Data from the pollution release and transfer register (PRTR) together with data from the industrial emissions data hosted by EEA on the IED portal (https://industry.eea.europa.eu/industrial-emissions/about),
4. Data from emission trading systems(https://www.eea.europa.eu/en/analysis/maps-and-charts/emissions-trading-viewer-1-dashboards).

The tool is available as a repository (see Table 4.1). The repository is fully documented and is accompanied by full walk-through example files in pdf format that illustrate data input and output to the users in order to fully replicate the script input, behaviour and output. Basic knowledge of Python scripting for data analysis is recommended to make the most use of the scripts. Figure 4.1 shows the structural design of these Python tools. The top level of the repository contains Jupyter notebooks that act as a frontend for the data analysis process. The scripts folder contains Python scripts, which carry functions and classes that act as a backend for the Jupyter notebooks. Images and plots are used in markdown cells of the Jupyter notebooks to illustrate the process to the users. The data folder is structured according to the datasets used in the analysis process. Each Jupyter notebook starts with links to data repositories from which data can be downloaded. After the download, the data is moved to the correct folders by the user, which enables the correct data access via the relative path structure of the repository. Each notebook carries out its own analysis of the inventory data and writes the results to an output folder. The output data may be processed further to generate comparisons of national totals and correlations using the “verification” Jupyter notebook.

This project has received funding from the European Union’s Horizon Europe research and innovation programme under grant agreement No 101081322

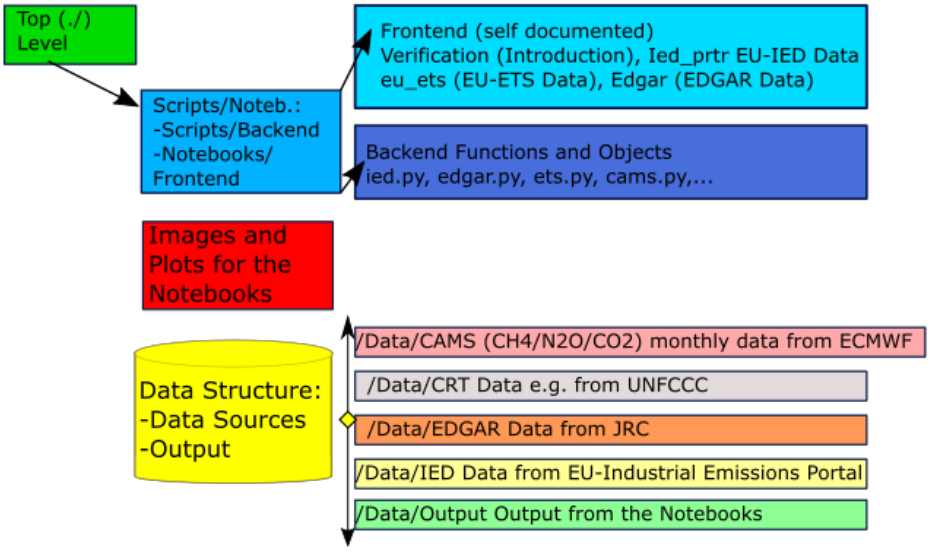


Figure 4.1: Repository structure of the AVENGERS Python tools. Jupyter notebooks contain the basic functionality for comparing inventory data to the four datasets above. Each notebook is annotated and guides the user through the analysis process.

4.2.2. The AVENGERS Flexible Inversion Tool for Inventory Compilers

The Flexible Inversion Tool for Inventory Compilers (FIT-IC, https://fit-ic.inversion-lab.com) is being developed within AVENGERS by a team of inventory compilers and atmospheric inversion experts to bridge the gap between these two communities, with particular focus on educational aspects of atmospheric inverse modelling.

FIT-IC is being designed to answer questions relevant to inventory agencies and such that it can be applied by inventory agencies around the world and by non-atmospheric scientists. The tool features three main functionalities:

1. **forward simulation**: assessing the degree of consistency of atmospheric observations with a given (a priori) emission scenario
2. **inversion**: inferring a (a posteriori) flux scenario that is (in a statistical sense) consistent with the a priori scenario and the atmospheric observations
3. **uncertainty propagation**: provision of uncertainty ranges for the inferred a posteriori flux scenario.

The tool operates on a global domain with a zoom over a target region of interest, e.g., Central Europe, resolving in particular Germany, Switzerland, and the Netherlands. To increase its computational efficiency, it uses pre-computed response functions that quantify the sensitivity of the simulated atmospheric concentration at the measurement station to emissions from anywhere on the globe. To simplify its use, the FIT-IC provides a web frontend based on a Jupyter notebook with an intuitive graphical user interface. Figure 4.2 displays a typical use case for performing forward simulations, and Figure 4.3 for performing an inversion. Note that the output data can be downloaded as a csv file, and all figures can be interactively manipulated and saved as png files.

This project has received funding from the European Union's Horizon Europe research and innovation programme under grant agreement No 101081322

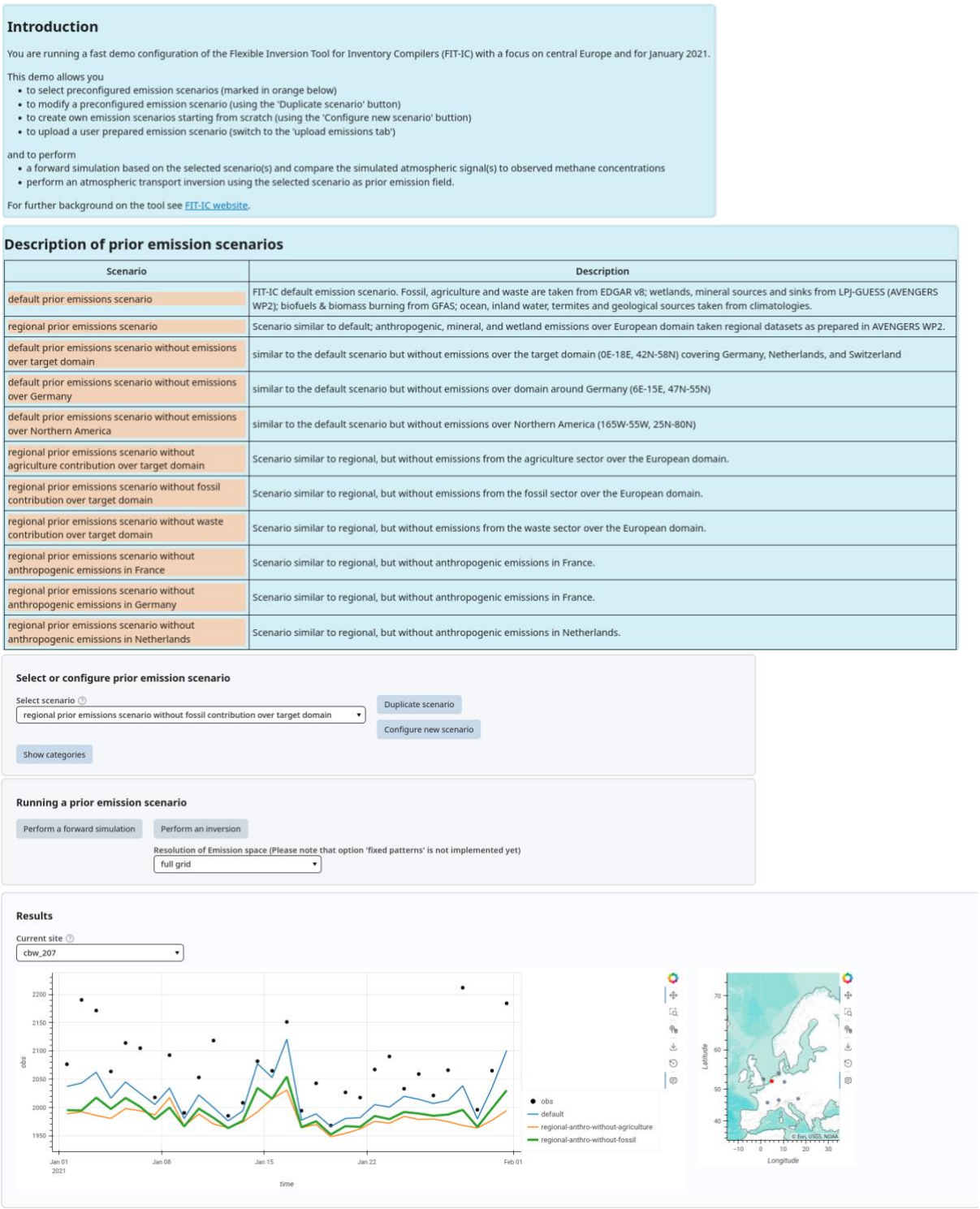
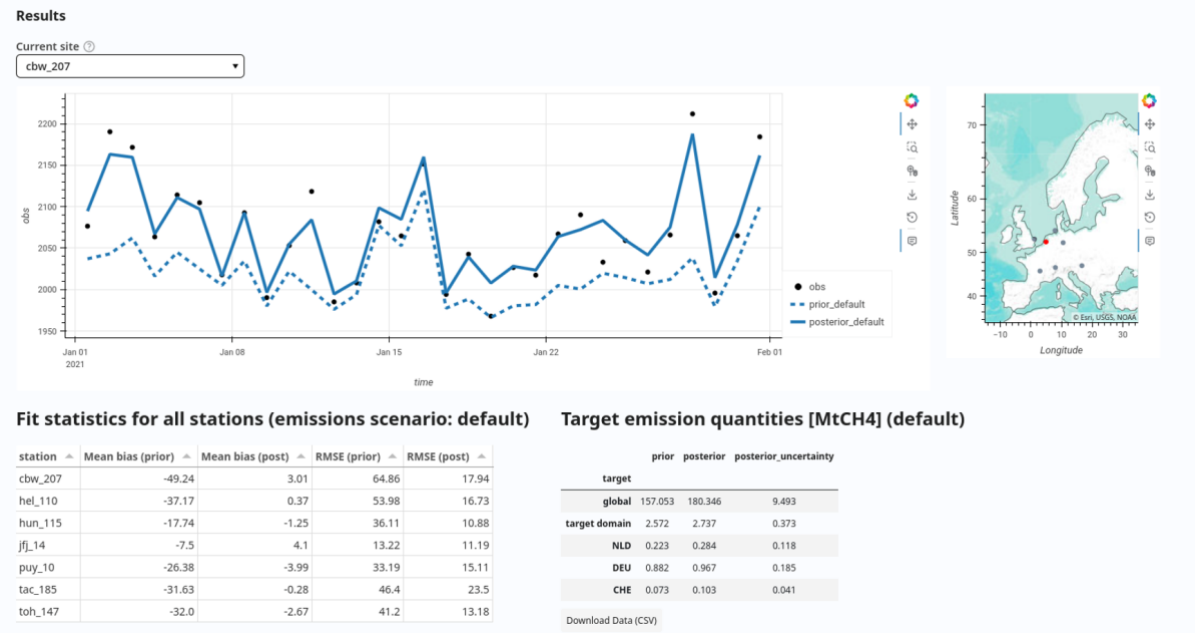


Figure 4.2: An illustration of the FIT-IC GUI for performing forward simulations for a set of different emission scenarios. In the top part, the user can either select an emission scenario from a list of pre-defined scenarios, configure an emission scenario from a number of available sectoral emission fields, or upload their own emission scenario. Next, the user can select to perform either a forward run or an inversion. The results section shows the time series of measured CH_4 concentrations for the selected measurement station as well as the CH_4 concentrations resulting from each of the emission scenarios that were selected during the session (left). The figure on the right highlights the location of the selected station.

This project has received funding from the European Union's Horizon Europe research and innovation programme under grant agreement No 101081322



station	Mean bias (prior)	Mean bias (post)	RMSE (prior)	RMSE (post)
cbw_207	-49.24	3.01	64.86	17.94
hel_110	-37.17	0.37	53.98	16.73
hun_115	-17.74	-1.25	36.11	10.88
jfj_14	-7.5	4.1	13.22	11.19
puy_10	-26.38	-3.99	33.19	15.11
tac_185	-31.63	-0.28	46.4	23.5
toh_147	-32.0	-2.67	41.2	13.18

target	prior	posterior	posterior_uncertainty
global	157.053	180.346	9.493
target domain	2.572	2.737	0.373
NLD	0.223	0.284	0.118
DEU	0.882	0.967	0.185
CHE	0.073	0.103	0.041

Figure 5.3: An illustration of the FIT-IC GUI results section when performing an inversion including the calculation of posterior uncertainties. It shows the time series of measured CH_4 concentrations for the selected measurement station as well as the a priori and a posteriori CH_4 concentrations resulting from each of the emission scenarios that were selected during the session (left). The figure on the right highlights the location of the selected station. The tables at the bottom provide some statistics from the inversion as well as the emission values and their uncertainties.

4.3. Overview of open-source tools

Besides the two tools that are specifically aimed at inventory compilers and described in more detail above, there exists a range of other publicly available open-source tools with different levels of complexity and targeting different communities. A non-exhaustive list including AVANTI-PYRES and FIT-IC is given in Table 4.1. While fluxie is also an analysis tool like AVANTI-PYRES, it is rather aimed at atmospheric inversion experts for the analysis of inversion output and intercomparison of emissions estimates from different atmospheric inverse models. It assumes inversion output provided in a common output format, a NetCDF standard for inverse model output agreed upon by the European inversion community. Like FIT-IC, the Integrated Methane Inversion (IMI) is an open-access tool for performing atmospheric inversions by non-experts. IMI runs on the commercial Amazon Web Services and is set up to infer methane emissions from satellite observations of atmospheric methane. Many of the commonly used inverse modelling systems are openly available. Three examples are listed in Table 4.1 below: i) LUMIA is a Python package employing a specific methodology (variational approach) to solve the inverse problem, ii) the Community Inversion Framework (CIF), which is an expert community tool that has different methodologies implemented for solving the inversion, and iii) FLEXINVERT, which is a Bayesian inversion framework for regional or global inversions and also provides different methodologies for solving the inversion.

This project has received funding from the European Union's Horizon Europe research and innovation programme under grant agreement No 101081322

Table 1.1: A selection of publicly available analysis and inversion tools.

Name	Short description	Requirements	Access
AVANTI-PYRES	The Avengers Analysis Tool for Inventories in PYthon REcipeS (see section 4.2)	JUPYTER Notebook	https://fileshare.icos-cp.eu/s/tFK8bt2qeJ9NFEm
Fluxie	Fluxie is an open-source project developing Python-based scripts for comparing emissions estimates from atmospheric inverse models	JUPYTER Notebook	https://github.com/openghg/fluxie
FIT-IC	The Flexible Inversion Tool for Inventory Compilers (see section 4.3)	JUPYTER Notebook with GUI support	https://fit-ic.inversion-lab.com/
IMI	The Integrated Methane Inversion (IMI) is an open-access cloud-computing inversion tool designed for non-expert users to infer methane emissions	Python scripts with JUPYTER Notebook support	https://carboninversion.com
FLEXINVERT	An open-source Bayesian inversion framework for atmospheric inversions on regional or global scales	Fortran compiler, NetCDF and LAPACK libraries	https://flexinvert.nilu.no/home/ https://git.nilu.no/flexpart/flexinvertplus/-/releases/v1.0.0
LUMIA	The Lund University Modular Inversion Algorithm (LUMIA) is an example of a Python package for performing atmospheric transport inversions	Python scripts	https://lumia.nateko.lu.se
CIF	The Community Inversion Framework (CIF) is an open-source Python package for expert users estimating greenhouse gas (GHG) and air-pollutant surface fluxes from atmospheric observations	Python scripts	http://community-inversion.eu

This project has received funding from the European Union's Horizon Europe research and innovation programme under grant agreement No 101081322

5. Further reading

Topic	Link/Reference
A gentle introduction to the fundamentals of atmospheric inverse modelling	Enting: Inverse Problems in Atmospheric Constituent Transport, 2002
For those who would like to take a deep dive into the math of inverse problems	Tarantola: Inverse problem theory and methods for model parameter estimation,https://www.geologie.ens.fr/~jolivet/Research_files/Tarantola.pdf, 2005
	Rodgers: Inverse methods for atmospheric sounding: theory and practice, 2000
Good practice guidelines for developing and performing atmospheric inversions	Good Practice Guidelines for Atmospheric Inversions to Support Greenhouse Gas Emission Reporting
Special issue on data assimilation in carbon/biogeochemical cycles	https://acp.copernicus.org/articles/special_issue11_192.html
WMO good practice guidelines for estimating national greenhouse gas emissions using atmospheric measurements	https://library.wmo.int/records/item/69714-integrated-global-greenhouse-gas-information-system-good-practice-guidance-for-estimating-national-scale-greenhouse-gas-emissions-using-atmospheric-observations
Copernicus CO_2 Monitoring and Verification Support	https://www.copernicus.eu/sites/default/files/2019-09/CO2_Blue_report_2015.pdf
$CoCO_2$ Decision Support Blueprint	https://coco2-project.eu/sites/default/files/2024-03/CoCO2-D8.5-M30-V0-5%20Decision%20Support%20Blueprint.pdf

6. Acknowledgements

These guidelines were made possible with funding from the European Union's Horizon Europe research and innovation programme under the EYE-CLIMA (grant agreement No. 101081395) and AVENGERS (grant agreement No. 101081322) projects.

7. References

Guevara, M., Jorba, O., Tena, C., Denier van der Gon, H., Kuenen, J., Elguindi, N., Darras, S., Granier, C., and Pérez García-Pando, C.: Copernicus Atmosphere Monitoring Service TEMPOral profiles (CAMS-TEMPO): global and European emission temporal profile maps for atmospheric chemistry modelling, Earth Syst. Sci. Data, 13, 367–404, https://doi.org/10.5194/essd-13-367-2021, 2021.

Mielke, C., Fiore, A., Witt, H. and Kushta, J.: Deliverable Report 1.1 of the Horizon Europe AVENGERS project: AVENGERS User Stories and Case Studies prepared by the AVENGERS Emission Inventory Team, https://avengers-project.eu/wp-content/uploads/2024/09/AVENGERS_deliverable_1_1_user_stories.pdf, 2024

IPCC: Quality assurance/Quality control and Verification, In: 2019 Refinement to the 2006 IPCC Guidelines for National Greenhouse Gas Inventories, edited by: Calvo Buendia, E., Tanabe, K., Kranjc, A., Baasansuren, J., Fukuda, M., Ngarize, S., Osako, A., Pyrozhenko, Y., Shermanau, P., and Federici, S., Vol. 1, Chapter 6, IPCC, Switzerland, https://www.ipcc-nggip.iges.or.jp/public/2019rf/pdf/1_Volume1/19R_V1_Ch06_QA_QC.pdf, 2019

Kuenen, J., Dellaert, S., Visschedijk, A., Jalkanen, J.-P., Super, I., and Denier van der Gon, H.: CAMS-REG-v4: a state-of-the-art high-resolution European emission inventory for air quality modelling, Earth Syst. Sci. Data, 14, 491–515, https://doi.org/10.5194/essd-14-491-2022, 2022.

NASA GISS: Panoply Data Viewer (Version 5.10.1). https://www.giss.nasa.gov/tools/panoply/, last access: 10 August 2026.

Saunois, M., Stavert, A. R., Poulter, B., Bousquet, P., Canadell, J. G., Jackson, R. B., Raymond, P. A., Dlugokencky, E. J., Houweling, S., Patra, P. K., Ciais, P., Arora, V. K., Bastviken, D., Bergamaschi, P., Blake, D. R., Brailsford, G., Bruhwiler, L., Carlson, K. M., Carrol, M., Castaldi, S., Chandra, N., Crevoisier, C., Crill, P. M., Covey, K., Curry, C. L., Etiope, G., Frankenberg, C., Gedney, N., Hegglin, M. I., Höglund-Isaksson, L., Hugelius, G., Ishizawa, M., Ito, A., Janssens-Maenhout, G., Jensen, K. M., Joos, F., Kleinen, T., Krummel, P. B., Langenfelds, R. L., Laruelle, G. G., Liu, L., Machida, T., Maksyutov, S., McDonald, K. C., McNorton, J., Miller, P. A., Melton, J. R., Morino, I., Müller, J., Murguia-Flores, F., Naik, V., Niwa, Y., Noce, S., O'Doherty, S., Parker, R. J., Peng, C., Peng, S., Peters, G. P., Prigent, C., Prinn, R., Ramonet, M., Regnier, P., Riley, W. J., Rosentreter, J. A., Segers, A., Simpson, I. J., Shi, H., Smith, S. J., Steele, P. L., Thornton, B. F., Tian, H., Tohjima, Y., Tubiello, F. N., Tsuruta, A., Viovy, N., Voulgarakis, A., Weber, T. S., van Weele, M., van der Werf, G. R., Weiss, R. F., Worthy, D., Wunch, D., Yin, Y., Yoshida, Y., Zhang, W., Zhang, Z., Zhao, Y., Zheng, B., Zhu, Q., Zhu, Q., and Zhuang, Q.: The Global Methane Budget 2000–2017, Earth Syst. Sci. Data, 12, 1561–1623, https://doi.org/10.5194/essd-12-1561-2020, 2020.

Soulie, A., Granier, C., Darras, S., Zilbermann, N., Doumbia, T., Guevara, M., Jalkanen, J.-P., Keita, S., Liousse, C., Crippa, M., Guizzardi, D., Hoesly, R., and Smith, S. J.: Global anthropogenic emissions (CAMS-GLOB-ANT) for the Copernicus Atmosphere Monitoring Service simulations of air quality forecasts and reanalyses, Earth Syst. Sci. Data, 16, 2261–2279, https://doi.org/10.5194/essd-16-2261-2024, 2024.

van der Net, L., Coenen, P. W. H. G., van Mil, S. E. H., Rienstra, J. D., Zijlema, P. J., Baas, K., van Baren, S. A., Berger Barnett, Y., Dröge, R., Geertjes, K., Honig, E., van Huet, B., te Molder, R. A. B., Montfoort, J. A., van der Zee, T. C., Witt, H. C. H., and van Zanten, M. C.: *National Inventory Document 2026: Greenhouse gas emissions in the Netherlands 1990-2024* (RIVM report; No. 2026-0022). RIVM. https://edepot.wur.nl/715026, 2026.

This project has received funding from the European Union's Horizon Europe research and innovation programme under grant agreement No 101081322

https://eyeclima.eu

https://avengers-project.eu/

Funded by the European Union. Views and opinions expressed are however those of the author(s) only and do not necessarily reflect those of the European Union. Neither the European Union nor the granting authority can be held responsible for them.



The EYE-CLIMA and AVENGERS projects were funded from the European Union's Horizon Europe research and innovation programme under grant agreement No.s 101081395 and 101081322